Modeling and Optimization of High Aspect Ratio Plasma Etching

by

Florian Krüger

A dissertation submitted in partial fulfillment
of the requirements for the degree of
Doctor of Philosophy
(Electrical and Computer Engineering)
in the University of Michigan
2024

Doctoral Committee:

Professor Mark J. Kushner, Chair
Professor Karthik Duraisamy
Associate Professor Bryan R. Goldsmith
Professor L. Jay Guo

Florian Krüger

fkrueger@umich.edu

ORCID iD: 0000-0003-2761-905X

© Florian Krüger 2024

Dedication

To Daria. Obviously.

Acknowledgements

Firstly, I wish to thank my supervisor Mark Kushner who has been a constant and inexhaustible source of knowledge and advice. Scientific rigor, integrity and work ethic are best taught by example, and I can only hope to emulate some of the dedication to those principles I have witnessed over the last years.

Secondly, I would like to thank my thesis committee members Professor Karthik Duraisamy, L. Jay Guo and Bryan R. Goldsmith. I would also like to thank my project collaborators, Hyunjae Lee (Samsung), Sang Ki Nam (Samsung), Mingmei Wang (Lam Research/Tokyo Electron), Du Zhang (Tokyo Electron), Minjoon Park (Tokyo Electron), Andrew Metz (Tokyo Electron) and Pingshan Luan (Tokyo Electron) for their support as well as valuable insight and data.

I am indebted to the entirety of the support staff at the University of Michigan with special thanks Julia Falkovitch-Khain who continually shielded me from all bureaucratic trials and tribulations so I could wholly focus on my academic work.

I wish to acknowledge all fellow members of the Computational Plasma Science and Engineering Group at the University of Michigan, who have shared with me their time, experience and, most important of all, many (probably too long) lunch breaks, some of which helped sustain my sanity more than I care to admit. In alphabetical order: Amanda Lietz, Chenhui Qu, Evan Litch, Eve Lanham, Jordyn Polito, Juliusz Kruszelnicki, Kseniia Konina, Mackenzie Meyer, Sanjana Kerketta, Scott Doyle, Shuo Huang, Tugba Piskin, Xifeng Wang, Yifan Gui.

Because my education did not begin in Michigan, I want to acknowledge my previous advisors Jan Trieschmann, Julian Schulze, Ralf Peter Brinkmann, Sebastian Wilczek and Thomas Mussenbrock who introduced me to the world of science and quite literally, changed my life's trajectory.

Thank you to my parents and family who supported me and made sure that my educational and personal life stayed on track although, at times, I tried my best to derail it.

Last but not least, I must thank my extraordinary wife, Daria, for her love, patience, support and trust without which I would have achieved nothing. While this piece of writing may be the token of one chapter's end, I can't wait for countless more.

Table of Contents

Dedication ii

Acknowledgements iii

Table of Contents v

List of Tables x

List of Figures xi

List of Appendices xvii

List of Abbreviations xviii

List of Symbols xix

Abstract xxii

Chapter 1 : Introduction 1

1.1 The Fourth State of Matter 1

1.2 Basic Properties of Low-Temperature Plasmas 4

1.3 Boltzmann's Equation 4

1.4 Conservation Equations 6

1.4.1 Particle Conservation 6

1.4.2 Momentum Conservation 6

1.4.3 Energy Conservation 7

1.5 Maxwell–Boltzmann Distribution 7

1.6 Thermal Non-Equilibrium 8

1.7 Electron Collision Cross Sections 9

1.8 Rate Coefficients and Collision Rates 9

1.9 Quasineutrality 10
1.10 Ambipolar Diffusion....11
1.11 Plasma Sheath 12
1.12 Capacitively Coupled Plasmas....14
1.13 Electrical Characteristics 15
1.14 Heating Mechanisms 18
1.15 Power Matching 19
1.16 Dual and Multi Frequency RF Power....21
1.17 Plasma Asymmetry and DC self-bias....22
1.18 Generalized Asymmetry 25
1.19 Electrical Asymmetry....27
1.20 Voltage Waveform Tailoring....28
1.21 Ion Energy Distributions....30
1.22 Electronegative Plasmas 32
1.23 Plasma in Semiconductor Processing 34
1.24 Adsorption....39
1.24.1 Physisorption 39
1.24.2 Chemisorption 40
1.25 Etching and Sputtering....40
1.25.1 Direct Sputtering....41
1.25.2 Direct Chemical Etching....42
1.25.3 Ion Enhanced Etching....43
1.26 Aspect Ratio Dependent Etch 44
1.27 Intra Feature Charging....46
1.28 Sidewall Passivation 48

1.29 Computational Modeling 49

1.30 Goals and Scope of this Dissertation 51

1.31 References 53

Chapter 2 : Description of the Models 63

2.1 Hybrid Plasma Equipment 64

2.1.1 Electron Energy Transport Module (EETM) 65

2.1.2 Fluid Kinetics Poisson Module (FKPM) 67

2.1.3 Surface Kinetics Module (SKM) 72

2.1.4 Plasma Chemistry Monte Carlo Module (PCMCM) 73

2.2 Monte Carlo Feature Profile Model (MCFPM) 74

2.2.1 Energetic Particle Surface Reaction 75

2.2.2 Electrostatic Charging 76

2.2.3 Crosslinking Module 77

2.3 References 80

Chapter 3 : Electric Field Reversals Resulting from Voltage Waveform Tailoring in Ar/O_2 Capacitively Coupled Plasmas Sustained in Asymmetric Systems 81

3.1 Introduction 81

3.2 The Ar Base Case 86

3.3 EFR with Ar/O_2 Gas Mixtures 92

3.4 Concluding Remarks 102

3.5 References 105

Chapter 4 : Voltage Waveform Tailoring for High Aspect Ratio Plasma Etching of SiO_2 using $Ar/CF_4/O_2$ Mixtures: Consequences of Ion and Electron Distributions on Etch Profiles 107

4.1 Introduction 107

4.2 Description of the Reactor Scale Model 108

4.3 Description of the Feature Scale Model 110

4.4 Plasma and Etch Properties for 1000 W of VWT Power 113

4.5 Plasma and Etch Properties for 2000 W of VWT Power 127

4.6 Concluding Remarks 135

4.7 References..138

Chapter 5 DC Self-Bias and Ion Energy at Very Low Driving Frequencies. 139

5.1 Introduction..139

5.2 Simulation Setup and Geometry 140

5.2.1 Reactor Scale Setup 140

5.2.2 Feature Scale Setup..142

5.3 Reactor Scale Plasma Properties with Constant Applied Voltage 144

5.4 Reactor Scale Plasma Properties with Constant Applied Power 155

5.5 SiO_2 Etching at Constant Power..163

5.6 Concluding Remarks 166

5.7 References..168

Chapter 6 Autonomous Hybrid Optimization of a SiO_2 Plasma Etching Mechanism...............171

6.1 Introduction..171

6.2 Description of the Optimization Scheme..175

6.3 Reactor Scale Plasma Simulation..177

6.4 Surface Simulation Setup...181

6.5 Target Metrics and Loss Function..186

6.6 Gradient Descent 189

6.7 Nelder-Mead Optimization 195

6.8 Hybrid GD-NM Optimization..198

6.9 Transferability of the Converged Mechanism...203

6.9.1 Variation of O_2 in Flow...204

6.9.2 Variation of Low Frequency Power....207
6.10 Optimization Based on Multiple Features....209
6.11 Concluding Remarks....214
6.12 References....216
Chapter 7 Summary and Outlook....224
7.1 Summary....224
7.2 Future Work....226
Appendices....229

List of Tables

Table 6.1: Base case fluxes to wafer 180

Table 6.2: High-level description of the SiO_2 and AC etch mechanism. 185

Table 6.3: Tuning parameters for gradient descent optimization 191

Table 6.4:Target metrics for gradient descent optimization 191

Table 6.5: Final tuning parameters after coupled optimization. 200

Table 6.6: Final tuning parameters after coupled optimization of feature grid. 211

Table B.1: Complete surface reaction mechanism 232

List of Figures

Figure 1.1: States of matter 2

Figure 1.2. Plasma parameter space [16]. 3

Figure 1.3: Maxwell-Boltzmann distribution corresponding to three different temperatures.........7

Figure 1.4: Electron impact cross sections for e-Ar collisions. Reproduced from Petrović et al....9

Figure 1.5: Schematic of a plasma bounded by two parallel grounded metal plates and the resulting density b) as well as potential c) distribution throughout the gap. 12

Figure 1.6: Schematic of a capacitively coupled plasma and the corresponding potential distribution at 4 different times of the RF period. 14

Figure 1.7: Circuit diagram of capacitively coupled plasma. 18

Figure 1.8: Circuit diagram of the matching network in conjunction with the plasma. 20

Figure 1.9: Schematic of an asymmetric CCP with two different electrode sizes with $A_1 < A_2$ and the blocking capacitor C_B at the powered electrode. 22

Figure 1.10: Voltage waveforms $V_{VWT}(t)$ based on (1.56) for $\varphi = 0, 45, 90, 135$ and $180°$.......29

Figure 1.11 a) IEDs at the powered electrode of a rf CF_4 discharge driven at 13.56 MHz from Kuypers and Hopman [129]. b) Particle in Cell simulation results showing IEDs of helium ions hitting the target electrode of rf discharges driven at frequencies from 1 MHz to 100 MHz. Reproduced from Kawamura et al [130]. 32

Figure 1.12: Schematic representation of a MOSFET 34

Figure 1.13: Manufacturing of strucured integrated circuit devices through deopsition, etch and pattern transfer: a) metal film deposition; b) photoresist deposition; c) patterned optical exposure; d) photoresist development; e) film etch; f) photoresist removal. Based on [16]. 35

Figure 1.14: a) Isotropic etch processes result in an uncontrolled and ultimately undesirable feature. b) Ion bombardment enables anisotropic etching. 37

Figure 1.15: Cross section SEM image of memory channel hole pattern after etching [131]. 38

Figure 1.16: Potential diagram of a generic physisorption and chemisorption process. 39

Figure 1.17: Different types of material removing surface reactions. a) physical sputtering, b) thermal etching, c) chemical removal of ion activated species and d) physical removal of chemically modified species. 41

Figure 1.18: Etching yield of polysilicon and silicon dioxide by 100 eV Ar and Cl as a function of ion incident angles for saturated chlorine fluxes. Reproduced from Chang et al [93]. 42

Figure 1.19: Critical ion angle of incidence for direct hit on the etch front for a) low and b) high aspect ratio feature. 45

Figure 1.20: Surface charge effects responsible for notching, trenching and twisting in HAR etch processes. 46

Figure 1.21: Sidewall passivation during the feature etch process. 48

Figure 2.1: Flowchart of coupled modeling suite consisting of HPEM and MCFPM. 63

Figure 2.2: Schematic representation of the crosslinking process. 78

Figure 3.1: Geometry and circuit used in the model. a) Schematic of the dual frequency capacitively coupled plasma reactor used in this investigation. b) Equivalent circuit diagram of the reactor. Source power at 80 MHz is applied to the top electrode. The 1 MHz tailored waveform is applied to the bottom electrode. 84

Figure 3.2: Plasma properties as a function of phase angle for the pure argon plasma with a constant high frequency power of 100 W and constant bias power of 1 kW. a) Applied voltage amplitudes for the high frequency source (V_{hf}) and amplitude of the low frequency bias (V_0). Top and bottom electrode. b) DC self-bias. 87

Figure 3.3: Plasma properties for the pure argon plasma averaged across the wafer as a function of height above the wafer and time during the low frequency,1 MHz cycle. Values are shown (left-to-right) for phase angles of φ = 0, 45, 90, 135, 180°. a) Axial component of the electric field, b) Ar^+ density, c) electron density and d) applied voltage waveform on the substrate. The Ar^+ and electron densities are plotted on a log-scale spanning 2 decades with the maximum value noted in each image. 88

Figure 3.4: Properties of electrons incident onto the wafer for the pure argon plasma. a) Electron energy and angular distributions for different phase angles plotted on a log-scale spanning 2 decades. b) Mean electron energy and mean electron angle of incidence as a function of phase angles. 91

Figure 3.5: Spatially averaged densities of Ar^+, e^-, O_2^+ and O^-, and electronegativity of Ar/O_2 plasmas as a function of the O_2 mole fraction with a phase angle of $\varphi = 0°$. 93

Figure 3.6: Plasma properties as a function of phase shift φ for different Ar/O_2 ratios when keeping source and bias powers constant. a) DC self-bias produced on the powered substrate. b) Applied voltage amplitude V_0. 94

Figure 3.7: Radial average of the vertical component of the electric field as a function of time during a single 1 MHz cycle and distance from bottom electrode different gas mixtures. Ar/O_2 = a) 100/0, b) 90/10, c) 75/25, d) 50/50. e) Normalized applied voltage V_0. Results are shown for phase shifts of (left-to-right columns) φ = 0, 45, 90, 135 and 180°. The dotted line is for E = 0, the separation between negative electric fields pointing down and positive pointing up. 95

Figure 3.8: Plasma properties for Ar/O_2 = 50/50 and a phase shift of φ = 0°. a) Radial average of the Ar^+ density as a function of time during a single 1 MHz RF cycle plotted on a log-scale over 2-decades. b) O^- density (log-scale, 2-decades) and c) electron density (log-scale 3-decades). The maximum density is noted in each image. d) e) Normalized voltage amplitude V_0.....................98

Figure 3.9: Electron energy and angular distributions incident onto the wafer surface for different Ar/O_2 ratios plotted on a log-scale over 2 decades with phase shifts of a) φ = 0° and b) φ = 180°. The EAD increases in energy and narrows in angle with increasing O_2 fraction, an effect that is most prominent for a) φ = 0°. 100

Figure 3.10: Properties of the electron velocity distribution incident onto the wafer for different Ar/O_2 ratios as a function of phase shifts φ. a) Mean electron energy and b) mean angle of incidence. Decreasing phase angle increases the incident electron energy and narrows the angular distribution, with the effect being most prominent for large O_2 mole fractions........................101

Figure 4.1: Schematics of the reactor. a) The two frequency CCP has the VWT power applied to the lower electrode and a sinusoidal, 80 MHz waveform applied to the top. b) Electrical schematic of the system. From F. Kruger et al, Plasma Sources Sci. Technol. **30**, 085002 (2021). Reproduced by permission of IOP Publishing Ltd. 109

Figure 4.2: Initial geometry used in for feature profile simulations. A 700 nm mask defines a 100 nm opening to 3000 nm thick SiO_2. The simulations are for trench etching, performed in 3-dimensions having a finite depth. 112

Figure 4.3: Voltage amplitudes for the VWT bias (V_{bias}) and top power (V_{top}), and DC self-bias as a function of phase angle. a) P_{VWT} = 1000 W and b) P_{VWT} = 2000 W. 114

Figure 4.4: Vertical electric field component as a function of time and distance from wafer for P_{VWT} = 1000 W for phase angles of a) 0°, b) 45°, c) 90°, d) 135° and e) 180°. The shape of the voltage waveform applied to the bottom electrode is shown in each image. 116

Figure 4.5: Properties of ions and electrons incident onto the wafer for P_{VWT} = 1000 W. a) IEAD and b) EEAD for phase angles of φ = 0°, 45°, 90°, 135° and 180°. The distributions are separately normalized and plotted on a log-scale over 2 decades. c) Mean ion energy as a function of phase angle φ 118

Figure 4.6: Fluxes of reactive species onto the wafer as a function of phase angle φ. a) Neutrals and b) ions. 119

Figure 4.7: Feature properties for P_{VWT} = 1000 W following 15 minutes of etching a) Feature profiles for different phase angles (φ = 0°, 45°, 90°, 135° and 180°). b) Comparison of etch result and electric potential for (left) self-consistent VWT produced EEAD....................................121

Figure 4.8: Spatial distribution of average electron energies incident on the surface of the feature. The feature properties are for P_{VWT} = 1000 W and $\varphi = 0°$ after 15 minutes of etching. Results are shown for initial EEADs produced with VWT and for thermal electron having a temperature. of 3 eV. a) When including acceleration in electric fields produced by feature charging. b) Without acceleration due to feature charging. The view is looking obliquely into the 3-dimensional feature having reflective boundary conditions front-and-back. 126

Figure 4.9: Vertical electric field component as a function of time and distance from wafer for P_{VWT} = 2000 W for phase angles of a) 0°, b) 45°, c) 90°, d) 135° and e) 180°. The shape of the voltage waveform applied to the bottom electrode is shown in each image. 129

Figure 4.10: Electron density for P_{VWT} = 2000 W for phase angle φ of a) 0°, b) 90° and c) 180°). The densities are plotted on a log-scale over 2-decades. 130

Figure 4.11: Energy and angular distributions for charged particles incident onto the wafer for P_{VWT} = 2000 W for phase angles of φ = 0°, 45°, 90°, 135° and 180°. a) Ions and b) electrons. The distributions are separately normalized and plotted on a log-scale over 2 decades............ 131

Figure 4.12: Feature properties for P_{VWT} = 2000 W following 15 minutes of etching a) Feature profiles for different phase angles (φ = 0°, 45°, 90°, 135° and 180°). b) Comparison of profiles obtained with VWT generated EEADs and synthetic thermal electron distribution for phase angles φ of 0°, 90° and 180°. 134

Figure 5.1: Reactor geometry and circuit diagram. 141

Figure 5.2: Feature scale model initial conditions for simulating plasma etching of SiO_2. PR represents photoresist. 144

Figure 5.3: Plasma properties of the $Ar/CF_4/O_2$ CCP base case with V_T = 300 V, V_0 = 1500 V, f_0 = 1 and $\varphi = 0°$. Time averaged a) electron density n_e, b) ionization source by bulk electrons S_b, c) ionization source by secondary electrons S_s, and d) electron temperature, T_e................. 145

Figure 5.4: Average electron density as a function of phase shift φ for fundamental frequencies f_0 = 1 MHz to 10 MHz at constant applied voltage.. 146

Figure 5.5: Power deposition for a) top electrode and b) bottom electrode as a function of phase shift φ for fundamental frequencies f_0 = 1 MHz to 10 MHz. 147

Figure 5.6: Plasma properties as a function of phase shift φ for different fundamental frequencies f_0 = 1 MHz to 10 MHz for constant voltage. a) V_{dc}. b) Mean ion energy incident onto the wafer. 149

Figure 5.7: Sheath properties as a function of fundamental frequency f_0 for $\varphi = 0°$ at constant voltage. a) Sheath thickness ds and b) sheath ion inertia coefficient S..................................... 152

Figure 5.8: Incident average energy of select ion species as a function of mass. 153

Figure 5.9: IEADs as a function of phase shift φ for fundamental frequencies a) f_0 = 1 MHz and b) f_0 = 10 MHz at constant applied voltage. Values are plotted on a 2-decade log scale. 154

Figure 5.10: Applied voltage for constant power (2000 W) as function of phase shift φ for fundamental frequencies f_0 = 1 to 10 MHz applied to the bottom electrode. a) Top electrode and b) bottom electrode. 156

Figure 5.11: Mean electron density as a function of phase shift φ for fundamental frequencies f_0 = 1 MHz to 10 MHz at constant applied power..........157

Figure 5.12: Sheath properties as a function of fundamental frequency f_0 for φ = 0° at constant power. a) Sheath thickness d_s and b) sheath ion inertia coefficient S..........158

Figure 5.13: Plasma parameters as a function of phase shift φ for fundamental frequencies f_0 = 1 MHz to 10 MHz at constant power. a) DC self-bias and b) Mean ion energy delivered to the wafer..........159

Figure 5.14: IEADs as a function of phase shift φ with constant power for fundamental frequencies a) f_0 = 1 and b) 10 MHz. Values are plotted on a 2-decade log scale. 160

Figure 5.15: Fluxes to the wafer as a function of phase shift φ for fundamental frequencies f_0 = 1 to 10 MHz while keeping power constant. a) Total polymerizing flux, b) O-atom flux, c) total ion flux and d) ratio of polymerizing flux to ion flux. 161

Figure 5.16: Predictions for etch profiles in SiO_2 at constant power with fundamental frequency f_0 = 1 MHz and varying phase angles φ. 163

Figure 5.17: Predictions for etch profiles in SiO_2 at constant power with fundamental frequency f_0 = 10 MHz and varying phase angles φ..........165

Figure 6.1: Global schematic of the optimization process. 176

Figure 6.2: CCP reactor geometry and circuit. 177

Figure 6.3: Plasma properties for the base case: a) Electron density [e], b) electron temperature T_e and c) negative fluorine ion Density [F^-], d) ionization rate by bulk electrons, e) ionization rate by secondary electrons..........179

Figure 6.4: Ion Energy-Angular Distribution sampled at the wafer surface during the base case. 181

Figure 6.5: Feature scale simulation setup consisting of a SiO_2 substrate with an amorphous carbon mask. 182

Figure 6.6: Etch features for different O based polymer etch probabilities 0.5% (left) and 2.0% (right)..........184

Figure 6.7: Target metrics used to evaluate the experimental matching..........186

Figure 6.8: SEM image resulting from the base case experiment. 188

Figure 6.9: Outline of the gradient descent method for a 1D parameter space. 189

Figure 6.10: Results from the gradient descent optimization. a) minimal epochal loss. b) values of select metrics as a function of epochs. c) select tuning parameters as a function of epochs. . 192

Figure 6.11: The finite resolution of the loss function leads to convergence issues. 193

Figure 6.12: Evolution of the total loss for different learning rates $\eta = 1x10^{-4}$, $5x10^{-4}$, $1x10^{-3}$ and $5x10^{-3}$.. 194

Figure 6.13: Examples of the geometric transformations of the parameter simplex in a 2D parameter space; reflection, extension; contraction; shrinkage. 195

Figure 6.14: Flow chart describing the Nelder-Mead optimization algorithm. 197

Figure 6.15: Results from the combined gradient descent and Nelder-Mead optimization. a) minimal epochal loss. b) values of select metrics as a function of epochs. c) select model parameters as a function of epochs. 199

Figure 6.16: Final features after etch completion for different parameter sets as a function of epochal evolution and the actual experimental target feature. 201

Figure 6.17: Fluxes incident on the wafer as a function of the O_2/C_4F_6 feedstock gas ratio. 204

Figure 6.18: a) MCFPM features resulting from the O_2/C_4F_6 variation. b) SEM images of the features resulting from the corresponding experiment. 205

Figure 6.19: IEADs resulting from the P_{lf} variation with P_{lf} = 0, 4, 6 and 8 kW. 207

Figure 6.20: a) MCFPM features resulting from the P_{lf} variation. b) SEM images of the features resulting from the corresponding experiment. 208

Figure 6.21: Feature scale simulation setup consisting of a SiO_2 substrate with an amorphous carbon mask and four separate features in a regular grid. 210

Figure 6.22: Results of the feature array optimization. a) minimal epochal loss. b) values of select metrics as a function of epochs. c) select model parameters as a function of epochs. 212

Figure 6.23: Final feature grids after etch completion for different parameter sets as a function of epochal evolution and the actual experimental target feature. 213

Figure A.0.1: Statistical run-to-run variation of the final etch profiles for the P_{VWT} = 1000 W and $\varphi = 0°$ case. a) 15 min run and b) 30 min to produce over etch into the stop layer. For each series of profiles, each case had a different seed for the random number generators, in addition to having the inherent statistical variations in the parallel computing environment. 231

List of Appendices

Appendix A: Statistical Variation in Predicted Feature Profiles 229

Appendix B: Surface Reaction Mechanism 232

List of Abbreviations

DC	Direct Current
AC	Alternating Current
ICP	Inductively Coupled Plasma
CCP	Capacitively Coupled Plasma
RF	Radio Frequency
LF	Low Frequency
HF	High Frequency
LTP	Low Temperature Plasma
IMN	Impedance Matching Network
EAE	Electrical Asymmetry Effect
VWT	Voltage Waveform Tailoring
MOSFET	Metal Oxide Field Effect Transistor
PECVD	Plasma Enhanced Chemical Vapor Deposition
ALD	Atomic Layer Deposition
ALE	Atomic Layer Etching
RIE	Reactive Ion Etching
PR	Photo Resist
AC	Amorphous Carbon
HAR	High Aspect Ratio
ARDE	Aspect Ratio Dependent Etching
HPEM	Hybrid Plasma Equipment Model
EETM	Electron Energy Transport Module
FKPM	Fluid Kinetics Poisson Module
SKM	Surface Kinetics Module
SSBM	Surface Site Balance Model
PCMCM	Plasma Chemistry Monte Carlo Module
MCFPM	Monte Carlo Feature Profile Model
HVM	High Volume Manufacturing

List of Symbols

t	Time
n_e	Electron density
n_i	Ion density
n_g	Neutral gas density
T	Temperature
T_e	Electron temperature
T_i	Ion temperature
T_g	Neutral gas temperature
α	Ionization degree
m	Mass
m_e	Electron mass
m_i	Ion mass
f	Frequency
f_0	Fundamental frequency
ω	Angular frequency
ω_{pe}	Electron plasma frequency
λ_D	Debye length
k_b	Boltzmann constant
e	Elementary charge
ε	Permittivity
ε_0	Vacuum permittivity
ρ	Charge density
Φ	Electric potential
V	Voltage
V_1	Voltage across sheath 1
V_2	Voltage across sheath 2
$\bar{V}_1$	Mean voltage across sheath 1
$\bar{V}_2$	Mean voltage across sheath 2
$\hat{V}_1$	Maximum voltage across sheath 1
$\hat{V}_2$	Maximum voltage across sheath 2
V_{rf}	RF voltage at generator
$\tilde{V}_{max}$	Maximum of applied voltage at generator
$\tilde{V}_{min}$	Minimum of applied voltage at generator
V_{dc}	DC self-bias voltage
V_{VWT}	Tailored voltage waveform
J	Current density

J_1	Current density in sheath 1
J_2	Current density in sheath 2
I	Electric current
I_1	Current in sheath 1
I_2	Current in sheath 2
$\boldsymbol{E}$	Electric field strength
R	Electrical resistance
R_P	Plasma bulk resistance
L	Electrical inductance
L_P	Plasma bulk inductance
C	Electrical capacitance
C_1	Capacitance of sheath 1
C_2	Capacitance of sheath 2
C_B	Capacitance of blocking capacitor
Z	Electrical impedance
Z_L	Total load impedance
Z_0	Generator Output impedance
Q	Electric charge
Q_1	Total electric charge in sheath 1
Q_2	Total electric charge in sheath 2
σ	Electrical conductivity
σ_{dc}	DC conductivity
Γ_R	power reflection coefficient
$\bar{S}_{ohm}$	Time averaged ohmic heating
$\bar{S}_{stoc}$	Time averaged stochastic heating
β	Discharge asymmetry parameter
l	Discharge gap
A	Area
A_1	Area of electrode 1
A_2	Area of electrode 2
s_1	Width of sheath 1
s_2	Width of sheath 2
$\hat{s}_1$	Maximum width of sheath 1
$\hat{s}_2$	Maximum width of sheath 2
Γ	Surface Fluxes
Γ_i	Ion flux to wafer surface
Γ_e	Electron flux to wafer surface
ϕ	Fluxes
E_A	Etch rate of material “A”
$\xi_{A,B}$	Etch selectivity of material “A” vs “B”
k_i	Reaction rate coefficient of reaction i
ν_i	Total rate of collision i
μ	Mobility
μ_e	Electron mobility

μ_i	Ion mobility
D	Diffusion coefficient
D_e	Electron diffusion coefficient
D_i	Ion diffusion coefficient
D_a	Ambipolar diffusion coefficient

Abstract

As critical dimensions of semiconductor devices shrink, feature densities increase and the geometries become more complex, the manufacturing processes are required to consistently improve and innovate. Low temperature plasma based processes are required to etch nanometer scale features with high aspect ratios through multi-material stacks as fast as possible, while maintaining high uniformity and a high yield over a 300 mm wafer. The quality of the surface etch is highly dependent on the energy and angular distribution of the charged particles, ions and electrons originating from the gas phase, incident on the wafer surface.

To control their dynamics, the use of complex tailored voltage waveforms was investigated. The tailored waveform consisted of a sinusoidal harmonic wave and its higher harmonics. Coupled reactor and surface scale simulations were performed to investigate the respective physical regimes. The Hybrid Plasma Equipment Model (HPEM) was utilized to simulate the gas phase and discharge physics in a capacitively coupled plasma operated in the low-pressure regime. Investigated feed gas mixtures include Ar/O_2, $Ar/O_2/CF_4$ as well as $Ar/O_2/C_4F_6$. Based on the HPEM results, the Monte Carlo Feature Profile Model (MCFPM) was used to simulate the feature etch process into SiO_2.

It was found that some degree of control of charged particle dynamics is possible by adjusting the phase of higher harmonics φ through the resulting generation of electrical asymmetry and electric field reversal. These general trends were present in most considered configurations, however the nature of the interaction between ions and the generated DC self-bias were found to

be context dependent with respect to its effects on ion energy. Two distinct regimes were identified. Average ion energy onto the wafer is strongly correlated to the DC self-bias at high f_0, whereas in the low frequency regime this correlation is weak. Average ion energy onto the wafer is instead dominated by dynamic transients in the applied voltage waveforms.

In all cases however, the trends produced in the gas phase translated to significant differences in the feature properties, strongly suggesting that voltage waveform tailoring constitutes a potent concept for etch process control.

Additionally, as many other simulation concepts, the MCFPM is critically dependent on the reaction mechanism representing the physical processes occurring between plasma produced reactant fluxes and the surface represented by the reaction probabilities, yields, rate coefficients, threshold energies etc. The increasing complexity of the structures being fabricated, new materials and novel gas compositions for plasma produced radical fluxes to the wafer also increases the complexity of the reaction mechanism used in feature scale models, and the difficulty in developing the fundamental data required for the mechanism. This challenge is further exacerbated by the fact that acquiring these fundamental data through more complex computational models or experiments is often limited by cost, technical complexity or inadequate models. Methods to automate the selection of fundamental data in a reduced reaction mechanism for feature scale SiO_2 plasma etching using a fluorocarbon gas mixture is discussed. By matching predictions of etch profiles to experimental data using a gradient descent / Nelder-Mead method hybrid optimization scheme these methods produce a reaction mechanism that replicate the experimental training data as well as experimental data using a related but different etch processes.

Chapter 1 : Introduction

Plasma is everywhere. Physically, as the most prevalent state of ordinary matter throughout the universe in the form of stars, lightning and auroras [1–4]; dramatically, but also quietly in terms of how its technological utilization has a seldom recognized presence in all our lives. Parts for furniture, appliances and cars are precisely cut by plasma torches and gas-discharge lasers [5,6]. Machines and tools are hardened by it [7], while it (at least for now) lights streets, offices and train stations [8,9]. Plasma can make water drinkable [10], provide nourishment for plants [11] and treat some of our ills [12–14]. Beyond terrestrial uses, plasma-based propulsion is essential in long-term orbital and interplanetary space fare. Certainly, advances in nuclear fusion research inspire hope that the understanding of plasma can contribute to the creation of a long-term sustainable energy source in a (hopefully) not too distant future. However, undeniably one of the most important contributions of technological plasmas is their established and ever increasingly important role in the manufacturing of advanced semiconductors. Their processing has motivated intense interdisciplinary research endeavors of tens of thousands of scientists as well as engineers (this one included) and directly contributed to the proliferation of ever faster and more efficient electronics and computing devices.

Without technological plasmas there would be no information age!

1.1 The Fourth State of Matter

Plasma is often referred to as the fourth state of matter. State transitions of matter can be understood as responses to energy that is added to a system. The most common states of matter

and respective state transitions are shown in Figure 1.1. Generally, the lowest energy state a substance can occur as is a solid. A solid's structure is defined by the molecules' outer shell electrons interacting over small distances and forming strong chemical bonds, resulting in a materials ability to maintain constant volume, density and a fixed shape. Adding sufficient energy into the system, for example in the form of heat, causes the breaking of these bonds (melting) and a phase transition into the fluid state, losing the ability to withstand shear forces and maintain a fixed shape. At sufficiently high energies molecules are no longer constrained by the cohesive forces and can move freely in a gaseous state (vaporization). If molecules accrue enough energy it can lead to ionization where a neutral particle splits into a charged ion(+) electron(-) pair. A partially or fully ionized gas is called "plasma". Due to the presence of mobile charge carriers, plasmas can react to electromagnetic fields on macroscopic scales and carry electric currents.

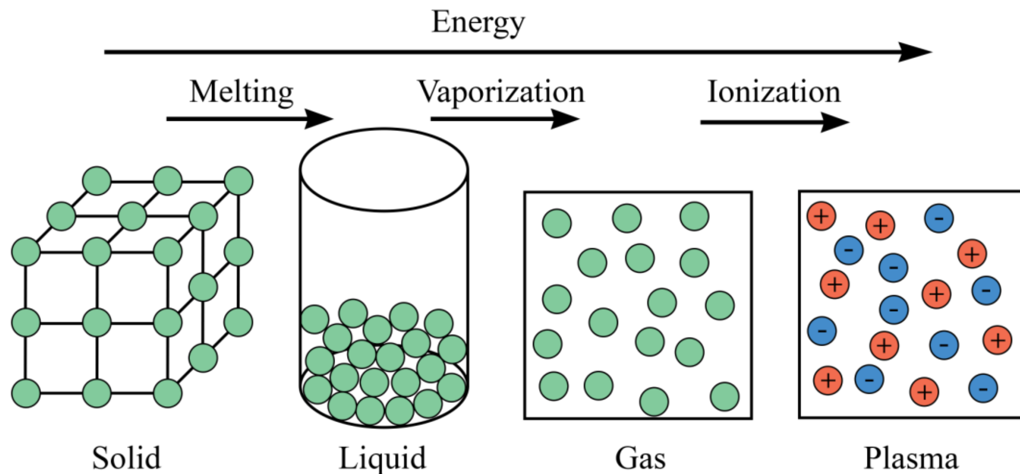

Figure 1.1: States of matter

Beyond these basic characteristics, the plasma state spans an enormous range of physical regimes, each exhibiting drastically different properties. [15,16] A basic categorization is often done based on a plasma's number density and temperature which can range from in space plasmas with low densities (1 cm^{-3}) and low temperatures (1 - 100 eV) to fusion plasmas with high densities

(10^{15} cm^{-3}) and high temperatures (> 10 keV) [17]. An overview of different plasma regimes is depicted in Figure 1.2.

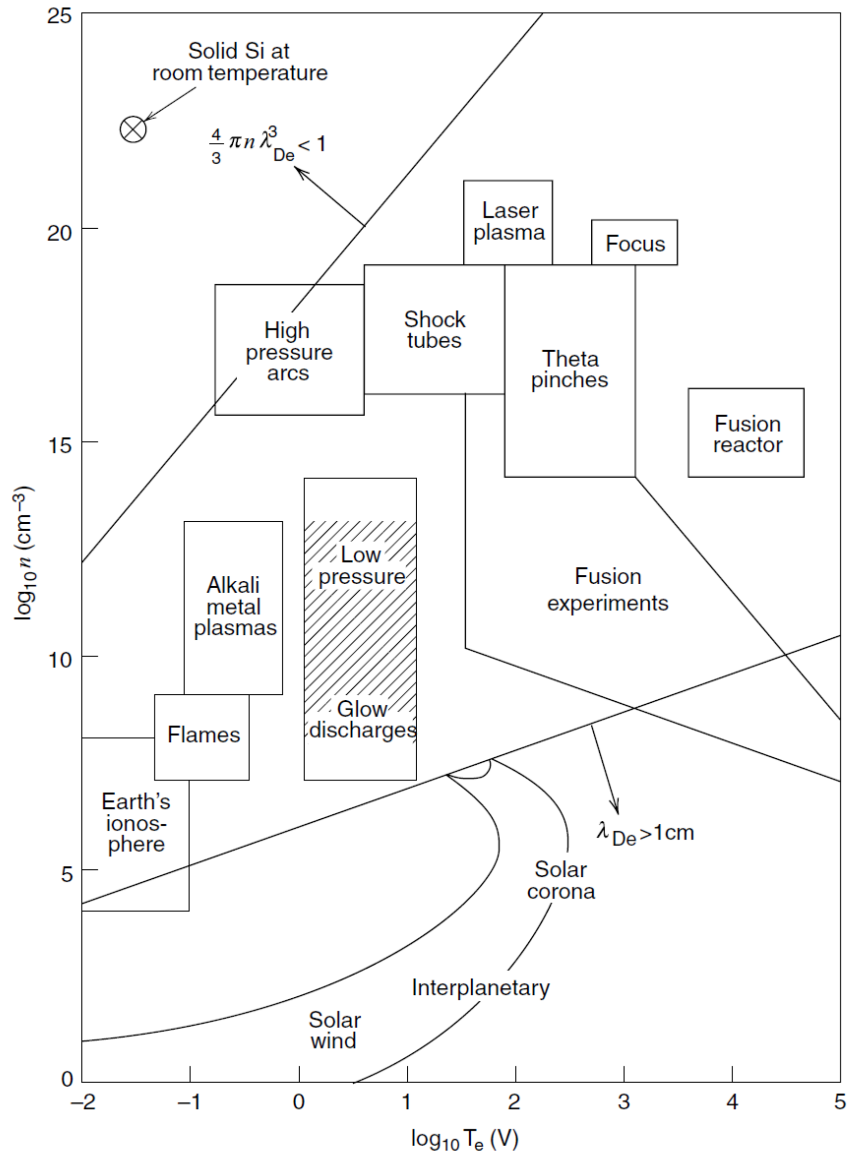

Figure 1.2. Plasma parameter space [16].

The focus of this thesis lies on low temperature plasmas (LTP) with electron temperatures between 1 and 10 eV operated at low pressures (10s of mTorr). These plasmas are often referred to as glow discharges due to their propensity to emit visible light and the fact that they are typically maintained via electric discharge configurations, where the plasma is sustained by coupling energy by electromagnetic or static means.

1.2 Basic Properties of Low-Temperature Plasmas

For plasma to exist, ionization is necessary. The ionization process produces a population of electrons with the number density n_e, one of the most fundamental plasma properties often referred to as simply the plasma density. The degree of ionization α is defined as the ratio of the number densities of ionized to non-ionized neutral gas species, n_i and n_g, respectively.

$$\alpha = \frac{n_i}{n_i + n_g} \tag{1.1}$$

The types of plasmas investigated in this work are considered weakly ionized plasmas with $\alpha < 1\%$. The primary source of ionization in most plasmas is based on electron impacts either directly

$$e + A \rightarrow A^{+} + e + e, \tag{1.2}$$

or as a dissociative ionization

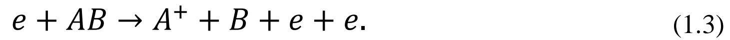

$$e + AB \rightarrow A^{+} + B + e + e. \tag{1.3}$$

Both reactions are highly dependent on the electron's energy which, for a single collision process needs to be greater than the ionization threshold of species A, $\varepsilon_{ion,A}$.

1.3 Boltzmann's Equation

Kinetically, a system of particles is fully described by its distribution function in six-dimensional phase space

$$f(\mathbf{x}, \mathbf{v}, \mathrm{t}) \tag{1.4}$$

with particle positions **x** and velocities **v**. The change to a system's distribution function can be described by 3 major components

$$\frac{\partial f}{\partial t} = \left(\frac{\partial f}{\partial t}\right)_{force} + \left(\frac{\partial f}{\partial t}\right)_{diff} + \left(\frac{\partial f}{\partial t}\right)_{coll} \tag{1.5}$$

where the "force" term corresponds to external forces, for example in the form of external fields exerting a temporal change on the particles. The "diff" term represents the diffusion of particles, and "coll" is the collision term – accounting for the forces acting between particles in collisions. The evolution of this phase space state is described by Boltzmann's Equation:

$$\frac{\partial f}{\partial t} + \mathbf{v}\nabla_r f + \frac{F}{m} \cdot \nabla_v f = \left.\frac{\partial f}{\partial t}\right|_{coll} \tag{1.6}$$

Interparticle collisions can cause rapid, effectively discontinuous, changes in the distribution and are collectively represented in the collision term $\left.\frac{\partial f}{\partial t}\right|_{coll}$. The details of the collision term depend on the specific application but can contain number losses (species absorbing collisions), number gains (species generating reactions), and instantaneous changes to velocity (elastic collisions) or speed (inelastic collisions). In the case of low temperature plasmas, the external force is dominated by electromagnetic fields leading to the commonly used two term approximation:

$$\frac{\partial f}{\partial t} = -\mathbf{v}\nabla_r f - \frac{e(\mathbf{E} + \mathbf{v} \times \mathbf{B})}{m} \cdot \nabla_v f + \left.\frac{\partial f}{\partial t}\right|_{coll} \tag{1.7}$$

Macroscopic quantities can be derived from the distribution function such as the number density

$$n(\mathbf{r}, t) = \int f d^3 v, \tag{1.8}$$

and the particle flux

$$\mathbf{\Gamma}(\mathbf{r}, t) = n\mathbf{u} = \int \mathbf{v} f d^3 v. \tag{1.9}$$

1.4 Conservation Equations

Formulations for fundamental conservation requirements can be obtained through the moments of Boltzmann's equation.

1.4.1 Particle Conservation

The 0th moment yields the continuity equation which governs the particle conservation and by extension the total mass balance of the system.

$$\frac{\partial n}{\partial t} + \nabla \cdot (n\mathbf{u}) = G - L \tag{1.10}$$

A change in local density is the consequence of a divergence of particle flux, i.e., more particles flow into a test location than flow out or due to local generation or loss, given by G and L respectively. G and L originate from the collision operator and are thus linked to the same physical processes that cause a change in particle number.

1.4.2 Momentum Conservation

The first moment yields the momentum conservation equation.

$$mn\left[\frac{\partial \mathbf{u}}{\partial t} + (\mathbf{u} \cdot \nabla)\right] = qn(\mathbf{E} + \mathbf{u} \times \mathbf{B}) - \nabla \cdot \mathbf{\Pi} + f|_{coll} \tag{1.11}$$

Temporal or spatial changes to the momentum carrying flux, $n\mathbf{u}$, described on the left-hand side, are the result the external **E** and **B** fields, the pressure gradients, described by the divergence of the pressure tensor **Π** and the momentum changes because of collisions.

1.4.3 Energy Conservation

The second moment yields the energy conservation equation.

$$\frac{\partial}{\partial t}\left(\frac{3}{2}p\right) + \nabla \cdot \frac{3}{2}p\mathbf{u} + \mathrm{p}\nabla \cdot \mathbf{u} + \nabla \cdot \mathbf{q} = \frac{\partial}{\partial t}\left(\frac{3}{2}p\right)\bigg|_{coll} \tag{1.12}$$

Here $\frac{3}{2}p$ is the thermal energy density and consequently $\frac{3}{2}p\mathbf{u}$ describes the thermal energy flux. $\mathrm{p}\nabla \cdot \mathbf{u}$ is the local heating and cooling due to compression and expansion.

1.5 Maxwell–Boltzmann Distribution

A system that is dominated by elastic momentum transfer collisions will eventually reach a steady state that is represented by the Maxwell–Boltzmann distribution

$$f_B(\mathbf{v}) = \left(\frac{m}{2\pi k_B T}\right)^{3/2} 4\pi v^2 exp\left(-\frac{mv^2}{2k_B T}\right). \tag{1.13}$$

The specific distribution is dependent on the species temperature. Boltzmann distributions corresponding to 3 different temperatures T_1, T_2 and T_3 with $T_1 < T_2 < T_3$ are shown in Figure 1.3.

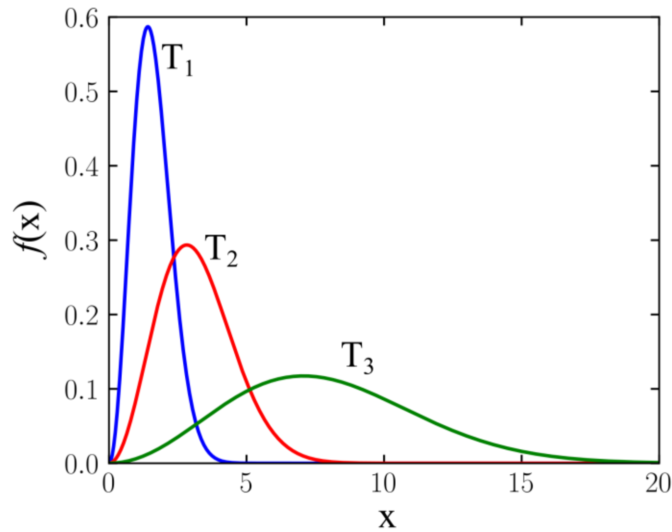

Figure 1.3: Maxwell-Boltzmann distribution corresponding to three different temperatures.

For higher temperatures, the distribution extends further to high velocities, while still containing a finite low temperature component. Systems without external power losses and gains eventually reach this state through mutual interaction of particles, referred to as thermalization i.e., systems in thermal equilibrium generally follow the Maxwell–Boltzmann distribution.

1.6 Thermal Non-Equilibrium

Temperature of a system is directly related to the species' thermal velocities v_{th}.

$$v_{th} = \sqrt{\frac{3k_bT}{m}} \Rightarrow T = \frac{v_{th}^2 m}{3k_b} \qquad (1.14)$$

When power is coupled into plasma via electromagnetic or electrostatic means, it results in heating of the charged particles only. Thermalization i.e., the process of physical bodies reaching thermal equilibrium through mutual interaction, occurs mostly through elastic collisions. Due to the differences in thermal velocity v_{th} and the subsequent difference in collision frequency, electrons thermalize much more rapidly than the heavier ions. Because of this, in the low-pressure regime, electrons are mostly considered in thermal equilibrium with themselves, whereas ions are often not. Energy transfer between electrons and ions through elastic collisions is generally rather inefficient due to the large difference in masses and thus they are not in thermal equilibrium with each other as well. Finally, due to the low collisionality between ions and neutrals because of the low pressure they, too, are generally considered to not be in thermal equilibrium with each other yielding three distinct temperatures of electrons ions and the neutral gas, T_e, T_i, and T_g, respectively, generally with $T_e \gg T_i > T_g$.

1.7 Electron Collision Cross Sections

The probability of electrons to undergo reactions with collision partners is a function of energy which is mostly determined by electron energy. This relation is often represented in the form of energy dependent cross sections $\sigma(\varepsilon)$ like the one presented in Figure 1.4 for electron impact cross sections with Ar. Every type of interaction has its own energy criteria, and thus possesses its own cross section. The most relevant are usually the momentum transfer σ_e, excitation $\sigma_{exc\ i}$, and ionization $\sigma_{ion\ i}$. Notably, momentum transfer can occur at every energy to some degree while excitation and ionization cannot occur below certain thresholds which stem from the atomic/molecular energy level structure.

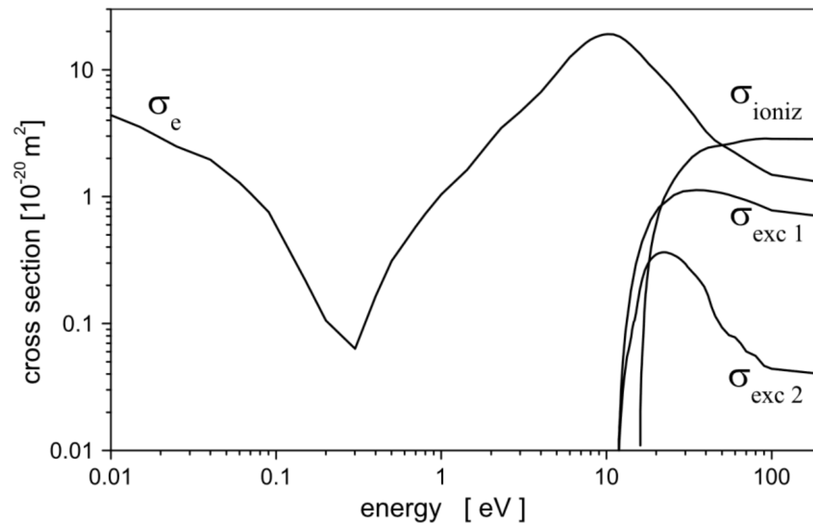

Figure 1.4: Electron impact cross sections for e-Ar collisions. Reproduced from Petrović et al.

1.8 Rate Coefficients and Collision Rates

The effective rate of electron impact reactions is given by its rate coefficient

$$k_i = \int f(\varepsilon)\, v\, \sigma_i(\varepsilon)\, d\varepsilon, \tag{1.15}$$

which is a function of the electron energy distribution $f(\varepsilon)$ as well as the respective energy dependent reaction cross section $\sigma_i(\varepsilon)$. The total rate at which collisions occur is a function of the densities of the respective reactant particles as it is proportional to the mean particle distance and mean free path. The total rate of collision 'i' occurring between electrons and gas species 'j' is then given by

$$\nu_{ji} = n_e \, k_{ji} \, n_j \tag{1.16}$$

1.9 Quasineutrality

Most plasmas are typically quasineutral i.e., the amount of positive charge is equal to the amount of negative charge on macroscopic scales. In terms of the space charge distribution quasineutrality represents the lowest energy state and thus deviations from it are restored in a self-regulating manner. The presence of space charge regions leads to the generation of an electric potential that attracts species of the opposite charge, thus neutralizing the space charge. However, quasineutrality can be broken over small time or length scales [15,16,18] when a force is applied, or an external potential is present. The time scale is defined by the plasma frequency, derived by determining the frequency of electrostatic oscillation of charged species displaced from neutral. In LTPs, the plasma frequency is the electron plasma frequency ω_{pe}, given by

$$\omega_{pe} = \sqrt{\frac{e^2 n_e}{\varepsilon_0 m_e}}, \tag{1.17}$$

where e is the fundamental charge, ε_0 is the permittivity of free space, and m_e is the electron mass. The length scale over which quasineutrality can be broken is the Debye length λ_D, an estimate of the electrostatic shielding distance given by

$$\lambda_D = \sqrt{\frac{\varepsilon_0 k_B T_e}{e^2 n_e}}, \tag{1.18}$$

where k_B is Boltzmann's constant and T_e is electron temperature. The convention in plasma physics is to refer to the electron temperature as $k_B T_e$ in units of eV.

1.10 Ambipolar Diffusion

Macroscopic fluxes can be caused by external fields and or diffusion based on pressure gradients

$$\Gamma = \pm \mu n \mathbf{E} - D \nabla n, \tag{1.19}$$

where μ and D are the macroscopic mobility and diffusion constant, which are unique to each species. The $\mu n \mathbf{E}$ term describes particles being accelerated by an electric field under the influence of collisions and its inertia. The $D \nabla n$ term describes movement down a pressure gradient under the influence of thermal motion. In most plasmas, the positive and negative species have different masses, with the electron dominated negative charge carriers being significantly more agile. This means that the mean velocity of positive charges is different than the mean velocity of negative charges. Charge carrier separation, caused by different diffusion speeds, leads to the generation of an electric field that effectively couples positive and negative charge carrier transport, to a degree. This effect is referred to as ambipolar diffusion and described by

$$\Gamma = -D_a \nabla n, \tag{1.20}$$

with the ambipolar diffusion coefficient

$$D_a = \frac{\mu_i D_e + \mu_e D_i}{\mu_i + \mu_e}. \tag{1.21}$$

1.11 Plasma Sheath

Whenever plasma is in contact with a surface a region of space charge called the "plasma sheath" is generated. This sheath region is of central importance to this work as plasma-surface interactions are critically dependent on its properties. To illustrate its basic structure, it is instructive to consider a simplified case of an electropositive plasma bounded by grounded metal plates depicted in Figure 1.5a.

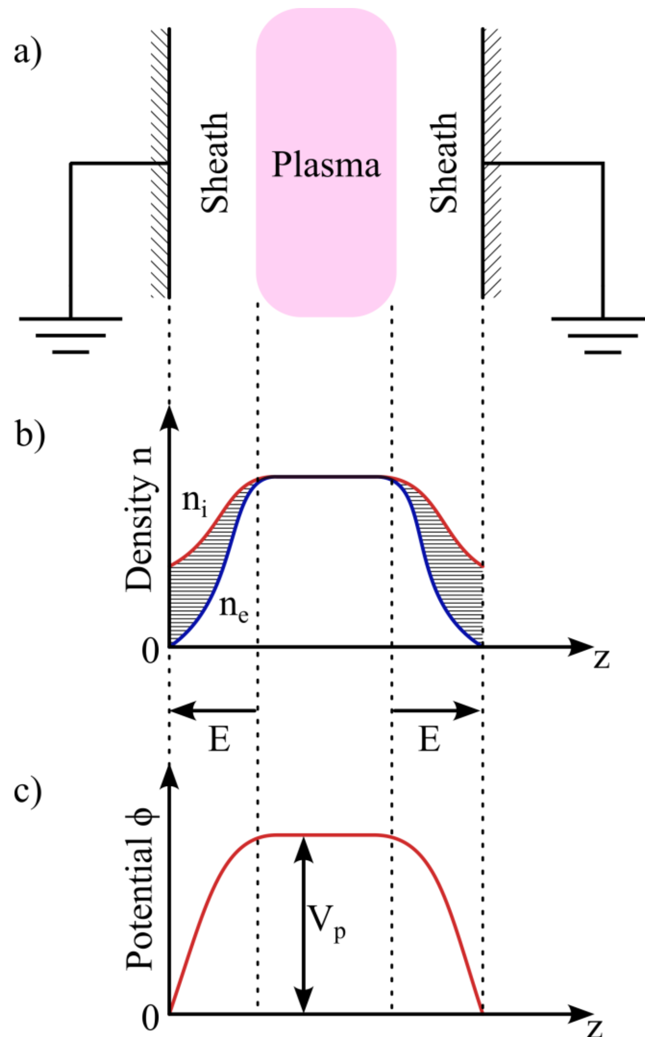

Figure 1.5: Schematic of a plasma bounded by two parallel grounded metal plates and the resulting density b) as well as potential c) distribution throughout the gap.

Losses of charged particle species to the walls occur at different rates. Electrons which are typically much lighter and faster than ions ($m_e/m_i = 7.2 \times 10^{-4}$ in the exemplary case of Argon and $T_e/T_i \geq 10$) are lost to the surface at a significantly higher rate. Typical number densities of ions and electrons as a function of distance are shown in Figure 1.5b. The center region of the plasma, the "bulk", is generally considered to be quasineutral ($n_e \approx n_i$). Because of wall losses, particle densities decrease in proximity to the boundary surfaces with. Due to the electrons' higher loss rate their density n_e in the boundary region is lower than the ions' n_i creating an electron-depleted positive space charge region (shaded area).

The spatial extend of this break in quasineutrality is generally on the order of the Debye length λ_D. This space charge $\rho = n_i - n_e$ causes an electric potential ϕ in accordance with Poisson's equation with the electrical permittivity ε [19–21]:

$$\nabla^2 \phi = -\frac{\rho}{\varepsilon} \tag{1.22}$$

ϕ is depicted in Figure 1.5c. Due to the positive space charge the plasma potential V_p is positive with respect to the ground reference and the corresponding electric field E points from the plasma bulk towards the surface. The sheath electric field in turn accelerates positive ions towards the said surface while simultaneously confining electrons to the bulk. This directional ion acceleration within the plasma sheath is the basis for many technological applications of plasmas, including the anisotropic etching of materials which is a particular focus of this work and introduced in Section 0.

1.12 Capacitively Coupled Plasmas

Since charge is lost to the walls and to ion-electron recombination, a continuous power input is required to sustain plasmas. Although not necessarily thermal in nature, this is generally referred to as plasma heating as it transfers kinetic energy to the charged and neutral species. The magnitude of plasma heating and the underlying mechanism play an essential role in determining basic plasma properties such as plasma density, temperature, potential and a host of downstream properties.

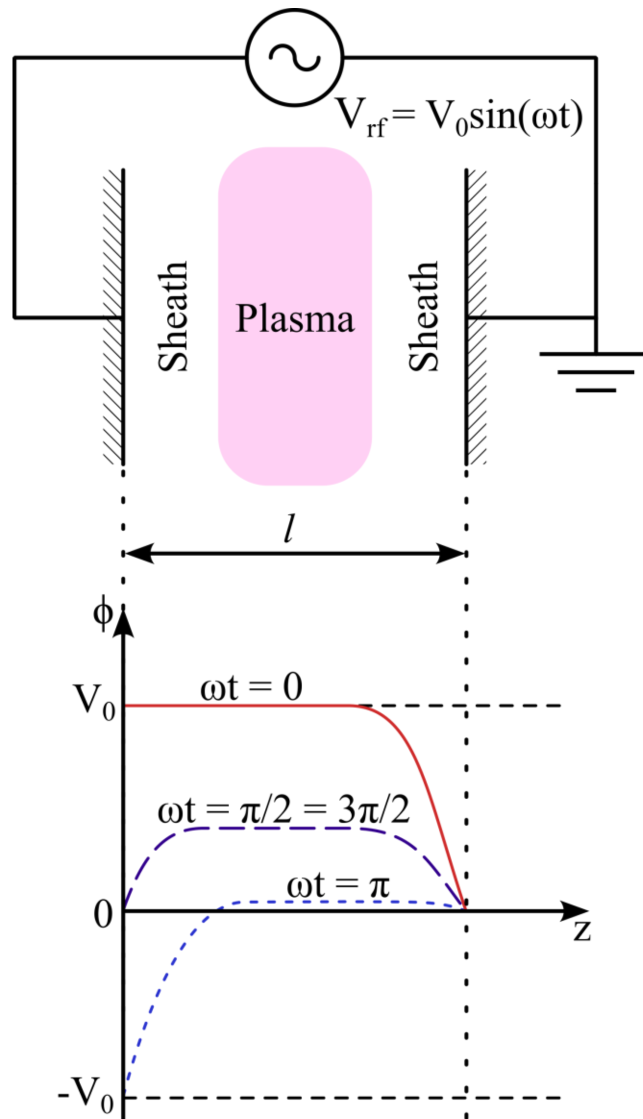

Figure 1.6: Schematic of a capacitively coupled plasma and the corresponding potential distribution at 4 different times of the RF period.

One type of plasma heating with extraordinary technical relevance is through capacitive coupling [22–43]. Capacitively coupled plasmas (CCP) are heated by interfacing with large area electrodes. The simplest setup resembles the planar configuration shown in Figure 1.5a with the exception that a radio frequency (RF) alternating current (AC) voltage is applied to at least one of the electrodes. This setup is schematically depicted in Figure 1.6 where an AC voltage source with $V_{rf}(t) = V_0 \sin(\omega t)$ is connected to the left electrode. Because the plasma potential is always positive with respect to the boundaries the RF oscillation at the electrode propagates to the plasma and sheath potentials leading to oscillations in the sheath potential and thickness. Thus, the plasma potential with respect to the electrodes oscillates while maintaining a mostly flat structure throughout the plasma bulk i.e., the bulk electric field remains negligible. To illustrate this behavior, the plasma potential as a function of gap position z, is shown in Figure 1.6 for two 4 different points in the RF-period with $\omega t = 0, \frac{1}{2}\pi, \pi$ and $\frac{3}{2}\pi$. Note that while always positive with respect to both electrodes, sheath voltages at the grounded and driven electrode are not always identical.

1.13 Electrical Characteristics

In order to examine the behavior of capacitive discharges, a suitable model of its electrical characteristics is imperative. Due to their differences in charge density and potential configuration the bulk and sheath regime are considered separately.

i) The bulk region of the plasma is generally well described by assuming a high electron density, negligible internal electric fields and a conduction current that is much greater than any present displacement current. Its impedance is given by

$$X_p = R_p + j\omega L_p \tag{1.23}$$

which consists of the bulk plasma resistance R_p in series with an inductance L_p. R_p is defined by the bulk's dc conductivity σ_{dc}, its width d and effective electrode facing area A:

$$R_p = \frac{1}{\sigma_{dc}}\frac{d}{A} = \frac{m_e \nu_m}{e^2 n_e}\frac{d}{A} \tag{1.24}$$

analogous to the Drude theory in metals [44,45], with the momentum transfer collision frequency ν_m [16,18]. While the physical origin of the bulk plasma inductance L_p is not in line with the common provenance of inductances i.e., the magnetic self-induction in current carrying coils, it nevertheless resembles the systems response to changes in current based on the electron's inertia. L_p is given by

$$L_p = \frac{R_p}{\nu_m} = \frac{m_e}{e^2 n_e}\frac{d}{A}. \tag{1.25}$$

ii) The sheath region of the plasma is mostly defined by displacement current as the low electron density does not allow for significant amounts of conduction current. Most of the applied voltage is dropped across the two sheaths. While the entire CCP setup resembles a plate capacitor, the sheaths themselves effectively do, too; two areas of high conductivity (electrode and plasma bulk) separated by a low conductivity gap (sheath) across a relatively large area. The capacitances at both sheaths, C_1 and C_2 , respectively, must be considered as non-ideal because the sheath oscillation causes a non-constant gap width and conductivity. Although the conduction current in each sheath is small, it is still determined by the balance between ion and electron contributions. Due to their high mass and inertia, the ion current $\bar{I_i}$ is generally assumed to be static with

$$\bar{I}_i = e n_e u_B A, \tag{1.26}$$

where u_B is the Bohm velocity [46–49]. *While this assumption is specifically challenged as part of this thesis it is still valid in the current context as the ion's inertia is still significantly higher than the electrons' and the ion current is thus much less modulated.*

To balance the continuous ion current, the time averaged electron current must be identical. Because of their low inertia, electron transport in the sheath is strongly dependent on the sheath potentials temporal and spatial dynamics which are depicted in Figure 1.6 for 4 different time points in the RF-cycle, $\omega t = 0,\ \pi/2,\ \pi$ and $3\pi/2$ The electrons are confined by the sheath potential for most of the RF period and thus their current is zero. However, for brief time periods the applied RF voltage causes the plasma potential at the respective sheaths to be small enough to allow for electron current to occur. This moment is referred to as the sheath collapse. In the depicted example it occurs at $\omega t = 0$ at the powered electrode (x = 0) and at $\omega t = \pi$ at the grounded electrode (x $= l$). Since the sheath voltage collapses to zero at the time that the electrons are transferred to the plate, this acts like an ideal diode across the sheath whose preferred direction of current flow is into the plasma. In total, sheaths can be modeled as a non-ideal capacitance, an ideal current source (ion current) and an ideal diode, connected in parallel.

Combining these representations leads to a simplified circuit model shown in Figure 1.7 in which the two sheaths are in series with the bulk conductance and resistance. The voltage V_{rf} is applied across it.

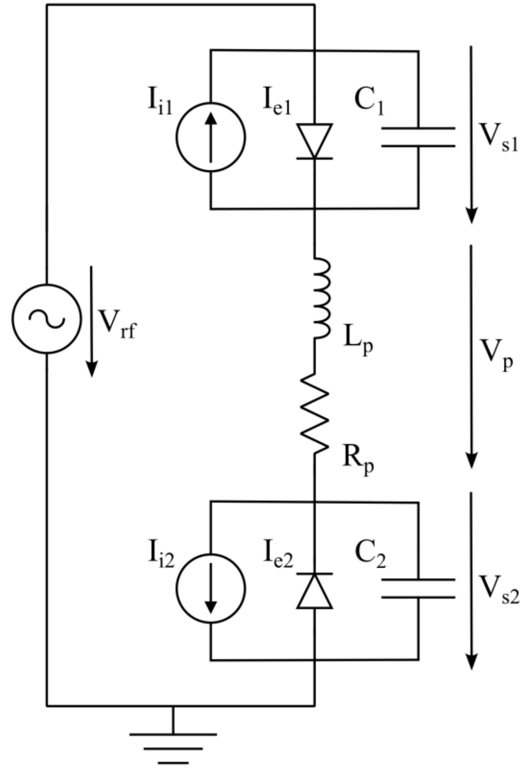

Figure 1.7: Circuit diagram of capacitively coupled plasma.

1.14 Heating Mechanisms

Understanding the electrical properties of CCPs enables some insight into the plasma heating required to sustain the discharge. Two different heating mechanisms are responsible for most of the power coupling in CCPs. While both are ultimately based on the acceleration of electrons in electric potentials and their subsequent momentum transfer collisions, the details have relevant consequences in terms of the involved scaling laws and control capabilities.

i) Ohmic heating – the oscillating voltage across the entire discharge causes an equivalent electron current that, through collisions transfers energy to heavy particles [16]. The time average power deposition per unit area $\bar{S}_{ohm}$ can be described by

$$\bar{S}_{ohm} = \frac{1}{2}J^2 \frac{d}{\sigma_{dc}} = \frac{1}{2}J^2 \frac{m_e \nu_m d}{e^2 n_e} \quad (1.27)$$

with current density J. Because ν_m strongly depends on the gas pressure ohmic heating is not very effective in the low-pressure regime.

ii) Stochastic heating – Due to the changing applied voltage electrons can diffuse into the active sheath area at the powered electrode when the electron confining electric field is at its minimum. When the sheath voltage increases again it accelerates electrons back into the plasma bulk. Because electron heating effectively only occurs during the sheath expansion this heating mode is also known as sheath expansion heating. Assuming a Maxwellian electron distribution and sheath densities according to Child's law the stochastic heating term can be approximated by

$$\bar{S}_{stoc} = \frac{1}{2}\frac{m\,\bar{v}_e}{e^2 n_e}J^2 \quad (1.28)$$

with the mean thermal electron velocity $\bar{v}_e$. Applying Child's law, the current density can be approximated with $J^2 = 1.73e\varepsilon\omega^2\sqrt{T_e V}n_s$ with the applied voltage amplitude V and the RF driving frequency ω, yielding

$$\bar{S}_{stoc} \propto \sqrt{T_e \frac{m}{e}}\varepsilon V \omega^2 \quad (1.29)$$

as the primary scaling behavior [50–55]. Stochastic heating is expected to be sensitive to changes in applied voltage as well as driving frequency.

1.15 Power Matching

When transmitting power from an external source to a load with complex impedance (such as a capacitively coupled plasma), some amount of power can be reflected if the output impedance

of the generator is not matched to that of the plasma system. The power reflection coefficient, Γ_R, is the ratio of power reflected from the plasma reactor relative and power delivered by the power supply through a transmission line and given by

$$\Gamma_R = \frac{Z_L - Z_0}{Z_L + Z_0} \tag{1.30}$$

where Z_L is the impedance of the load (in this case, the combined impedance of the plasma reactor and the plasma) and Z_0 is the output impedance of the power supply and the transmission line [19,56,57]. Typically, to minimize Γ_R an impedance matching network (IMN) (often referred to as match box) between the plasma and the generator is employed. A simple L-type IMN is shown in Figure 1.8.

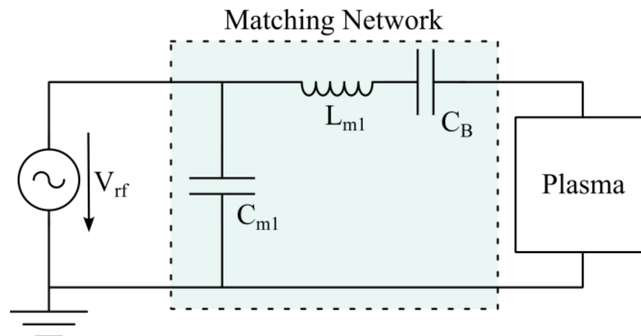

Figure 1.8: Circuit diagram of the matching network in conjunction with the plasma.

It consists of a series inductance L_{m1} as well as a parallel and series capacitance, C_{m1} and C_B, respectively. C_B, called the blocking capacitor as it blocks DC current flow, can affect the plasma dynamics in vital ways by charging up and creating a large negative DC potential at the powered electrode. This effect is induced by a property called asymmetry.

1.16 Dual and Multi Frequency RF Power

The frequency dependence of the capacitive heating modes has inspired the use of dual frequency CCPs, where the power is coupled via two independent low and high frequency components [58,59]. The total applied voltage becomes

$$V_{rf}(t) = V_{lf}\cos(2\pi f_{lf} t) + V_{hf}\cos(2\pi f_{hf} t), \tag{1.31}$$

where V_{lf} and V_{hf} are the voltage amplitudes of the low and high frequency component with respective frequencies of f_{lf} and f_{hf}. The basic idea of using two different frequencies simultaneously was to achieve independent control over both the ion flux and ion bombardment energy onto the substrate electrode. The ion flux is mostly a function of the bulk plasma density whereas the ion energy directly mirrors the sheath voltage. It has been shown that higher driving frequencies generally lead to increased power deposition into the electrons which in turn leads to increased ionization and higher plasma densities and ion fluxes [59–61]. For an equal power deposition, reducing the driving frequency requires an increase in the applied voltage. Since this voltage almost entirely drops across the sheath, an electron starved region, this leads to ion acceleration inside the sheath and consequently allows for some ion energy control. In general, 0.5–13.56 MHz sources are used as the LF source while 27.12– 81.36 MHz sources are used as the HF source [62–64]. While some differential control of ion flux and ion energy can be achieved, in real world application the LF and HF components are not fully independent. They interact indirectly through the respective changes to plasma properties such as plasma density, sheath voltage, sheath width, electron temperature etc. and also create novel non-linear effects that are not present in the single frequency scenario.

1.17 Plasma Asymmetry and DC self-bias

Most capacitive discharges are asymmetric in one or many respects. The simplest and most common one is geometrical asymmetry. Because reactor walls in CCPs are generally grounded, the effective grounded area is larger than the powered area, even if both electrodes have the same dimensions. A schematic of an asymmetrical CCP setup is shown in Figure 1.9, where the powered electrode with area A_1 is on the left-hand side of the discharge gap and the grounded surface with area A_2 is on the right-hand side; note that $A_1 < A_2$.

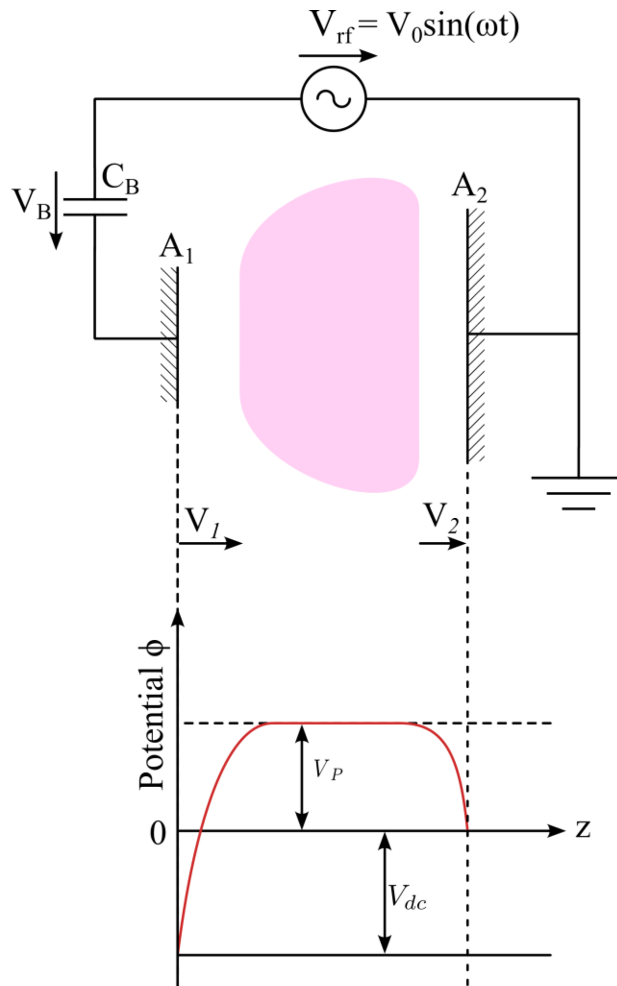

Figure 1.9: Schematic of an asymmetric CCP with two different electrode sizes with $A_1 < A_2$ and the blocking capacitor C_B at the powered electrode.

The most relevant voltages in the system are the voltages across the sheaths, V_1 and V_2, respectively, the voltage across the blocking capacitor V_B as well as the voltage generated by the source $V_{rf} = V_0 \sin(\omega t)$. The time average voltage drop across a sheath is well approximated by its capacitive behavior with

$$\mathrm{V} \propto \frac{\mathrm{Q}}{C}, \tag{1.32}$$

where Q is the total charge contained within the sheath space charge region, and

$$\mathrm{C} = \varepsilon \frac{\mathrm{A}}{d}. \tag{1.33}$$

The conservation of total sheath charge is a fairly good assumption as DC current is not permitted to flow into and out of the system and the bulk region is mostly quasineutral. It thus follows for the two sheaths with (1.32) and (1.33)

$$Q_1 = Q_2 \wedge A_1 < A_2 \;\Rightarrow\; V_1 > V_2. \tag{1.34}$$

Because no DC voltage is generated by the ideal AC source, this leads to a closed loop over which according to Kirchhoff's law [65] the sum of all remaining voltages must equal zero. Accounting for the opposing polarity of the voltages across the sheath this gives:

$$V_1 - V_2 + V_B = 0 \tag{1.35}$$

Considering (1.34), this results in the requirement of a negative voltage across the blocking capacitor called the DC self-bias, V_{dc}.

$$V_{dc} = V_B = -(V_1 - V_2) < 0 \tag{1.36}$$

The presence of this DC self-bias is well documented [66–69] and is of high relevance as effectively increases the total potential drop across the powered sheath, as is depicted in Figure 1.9b. This increased potential directly translates to increased directional acceleration of ions towards the surface, a highly sought after property in CCPs used for semiconductor manufacturing.

This high practical relevance has driven considerable research aimed at understanding and modeling the system's response to asymmetry. In practice, the presented derivation contains some critically weak assumptions such as the assumed constant sheath widths d and consequently the sheath capacitances. Both are, in fact, critically dependent on the sheath voltage itself leading to nonlinear capacitances and time-varying density profiles in the sheaths. Early model descriptions used the Child-Langmuir law [70,71] to describe the sheath behavior [68]. The total rf current in sheath 1 is given by

$$\mathrm{I}_1 = \int_{A_1} \mathrm{J}_1(\boldsymbol{x})\, d^2x. \tag{1.37}$$

Because the rf current density is proportional to the sheath width s_1 and the voltage drop is independent of the position along the surface $\boldsymbol{x}$ with

$$\mathrm{J}_1(\boldsymbol{x}) \propto \frac{\bar{V}_1}{s_1(\boldsymbol{x})} \tag{1.38}$$

and by using an ion density relation derived from Child's law

$$n_{i1}(\boldsymbol{x}) \propto \frac{\bar{V}_1^{3/2}}{s_1^2(\boldsymbol{x})} \tag{1.39}$$

s_1 can be expressed in terms of n_{i1}. Substituting it in (1.38), (1.37) gives

$$\mathrm{I}_1 \propto \bar{V}_1^{1/4} \int_{A_1} n_{i1}^{1/2}(\boldsymbol{x})\, d^2x \tag{1.40}$$

and similarly

$$\mathrm{I}_2 \propto \bar{V}_2^{1/4} \int_{A_2} n_{i2}^{1/2}(\boldsymbol{x})\, d^2x \tag{1.41}$$

for the other sheath. Assuming RF current continuity this gives

$$\frac{\overline{V}_1}{\overline{V}_2} = \left(\frac{\int_{A_2} n_{i2}^{1/2}(\boldsymbol{x})\, d^2x}{\int_{A_1} n_{i1}^{1/2}(\boldsymbol{x})\, d^2x} \right)^4 \qquad (1.42)$$

Making the, admittedly weakly motivated, assumption of a uniform ion density with $n_{i1}(x) = n_{i2}(x) = n_{i0}$ we get

$$\frac{\overline{V}_1}{\overline{V}_2} = \left(\frac{A_2}{A_1} \right)^4 \qquad (1.43)$$

This scaling law clearly shows a non-linear relation of the DC self-bias (which is the difference of $\overline{V}_1$ and $\overline{V}_2$) and the electrode area ratio. However, the model details were not in accordance with many experimental findings [66–69] which typically found

$$\frac{\overline{V}_1}{\overline{V}_2} \approx \left(\frac{A_2}{A_1} \right)^q \qquad (1.44)$$

with $q \leq 2.5$.

1.18 Generalized Asymmetry

The theory of asymmetric discharges was later expanded upon by Heil et al [72] who considered the total unbalanced charge in a sheath given by

$$\frac{Q}{A} = e \int_0^s n_i(z) dz. \qquad (1.45)$$

When sheath 1 is at its maximum extension $\hat{s}_1$ the opposing sheath is at its minimum width and can in good approximation be considered fully collapsed i.e., it contains no charge. This in turn means that all unbalanced charge is contained in sheath and its maximum voltage $\hat{V}_1$ is given by

$$\hat{V}_1 = -\frac{e}{\varepsilon} \int_0^{\hat{s}_1} n_i(z) z\, dz. \qquad (1.46)$$

This maximum charge $\hat{Q}$ can alternatively be expressed as a function of the mean charge density in the sheath

$$\frac{\hat{Q}}{A} = e\hat{s}_1\bar{n}_1, \qquad \text{with} \;\; \bar{n}_1 = \frac{1}{\hat{s}_1}\int_0^{\hat{s}_1} n_i\,(z) z\, dz. \tag{1.47}$$

The maximum sheath voltage can now be expressed as

$$\hat{V}_1 = -\frac{e}{2\varepsilon}\hat{s}_1^2\bar{n}_1 I_s, \tag{1.48}$$

where the sheath integral I_s is a dimensionless quantity that depends only on the normalized profile of the sheath density. Combining (1.47) and (1.48) the two sheath voltages can be expressed as

$$\hat{V}_1 = -\frac{e}{2\varepsilon}\left(\frac{\hat{Q}}{A_1}\right)^2 \frac{I_{s1}}{\bar{n}_1} \tag{1.49}$$

and

$$\hat{V}_2 = -\frac{e}{2\varepsilon}\left(\frac{\hat{Q}}{A_2}\right)^2 \frac{I_{s2}}{\bar{n}_2}. \tag{1.50}$$

The absolute of the sheath voltage ratios yields the asymmetry parameter

$$\beta = \left|\frac{\hat{V}_2}{\hat{V}_1}\right| = \frac{\bar{n}_1}{\bar{n}_2}\left(\frac{\mathrm{A}_1}{\mathrm{A}_2}\right)^2 \frac{I_{s2}}{I_{s1}}. \tag{1.51}$$

In literature this parameter is often also referred to as ε [24,73–78]. To maintain consistency throughout this thesis and in acknowledgement of the fact that the discipline of electrical engineering already has a sufficient number of physical properties being referred to as 'e', 'E' or 'ε', 'β' will be used exclusively. Through the asymmetry parameter, experimentally established scaling laws with respect to the area ratio (with $q \leq 2.5$) are much better represented. Perhaps more notably, this formulation hints at additional factors that can cause asymmetry in a discharge, in addition to the geometric asymmetry of the reactor. A host of different sources for discharge asymmetry are subjects of active research. This includes asymmetry induced by certain

magnetic field configurations, differing electrode material properties such as secondary electron emission coefficients, electron beam injection or special applied RF voltages. Some of these approaches are of particular interest as they are not fixed (in contrast to the reactor geometry) and possibly allow for active discharge control. Asymmetry based on asymmetric applied voltages will play a central role in this thesis.

1.19 Electrical Asymmetry

Under certain conditions asymmetry, i.e., the generation of a DC self-bias voltage, can be induced even in perfectly geometrically symmetric systems by applying asymmetric voltages. Its occurrence is referred to as the electrical asymmetry effect (EAE). While this effect has, quite possibly inadvertently, been present in many multi frequency CCPs, its active consideration and theoretical description goes back to foundational work by Heil, Schulze, Czarnetzki, Brinkmann and Mussenbrock [72–74].

The maximum absolute sheath voltage is defined by the minimum voltage at the powered electrode, keeping in mind the polarity of the sheath voltages i.e. the plasma potential is always positive with respect to the enclosing electrodes, it is a combination of the minimum of the applied RF voltage $\tilde{V}_{min}$ and the DC self-bias:

$$\hat{V}_1 = \tilde{V}_{min} + V_{dc} \tag{1.52}$$

Similar reasoning for the grounded electrode and the maximum of the applied voltage $\tilde{V}_{max}$ leads to a convenient expression for the DC self-bias

$$V_{dc} = -\frac{\tilde{V}_{max} + \beta \tilde{V}_{min}}{1 + \beta} \tag{1.53}$$

which, in the case of a single frequency sinusoidal applied voltage $V_{rf}(t) = V_0 \sin(\omega t)$, reduces to

$$V_{dc} = -\frac{1+\beta}{1+\beta} \quad (1.54)$$

In this scenario, no electrical asymmetry is generated. More general, no time varying applied voltage that is harmonically symmetric ($V_{sym}(\varphi + \pi) = -V_{sym}(\varphi)$) or anti-symmetric ($V_{asym}(\varphi) = -V_{asym}(-\varphi)$) with respect to phase $\varphi = \omega t$ leads to the generation of a DC self-bias in an otherwise symmetric system. Ergo, in order to evoke electrical asymmetry, a voltage that is neither symmetric nor anti-symmetric must be applied.

1.20 Voltage Waveform Tailoring

While there is, technically, an infinite number of functions that mathematically meet these requirements, arbitrary voltage functions can lead to technical difficulties in their generation and impedance matching, especially at high powers. It is for this reason that for technological applications the focus has been on harmonically constructed waveforms where the applied voltage waveform is comprised of a superposition of a fundamental sine wave and its higher harmonics.

$$V_{VWT}(t) = V_{tot} \sum_{k=1}^{N} a_k \cos(k\omega_0 t + \varphi_k) \quad (1.55)$$

Here, $\omega_0 = 2\pi f_0$ is the fundamental frequency, k denotes the harmonic order ($k = 1$ is considered the fundamental), N is the total number of harmonics used, a_k is the relative amplitude of each harmonic, φ_k is the relative phase shift of each harmonic and V_{tot} is the total applied voltage amplitude. Intentional purpose-oriented tailoring of applied voltages or voltage waveform tailoring (VWT) has applications beyond the generation of a DC self-bias, however, in the presented thesis this will be its main purpose, which in turn guides some principles guiding its design and construction. Because odd harmonics do not contribute to the DC self-bias, they are avoided. The technical complexity increases with the number of applied harmonics, so their

number is limited to 5 in this work. Lastly, for a given V_{tot} it exists a solution that optimizes the difference between its extrema, given by

$$V_{VWT}(t) = V_{tot} \sum_{k=1}^{N} \frac{N-k+1}{N(N+k)} \cos(k\omega t + \pi k \varphi). \tag{1.56}$$

The resulting time dependent voltage waveforms are shown in Figure 1.10 for different phase shifts $\varphi = 0, 45, 90, 135$ and $180°$.

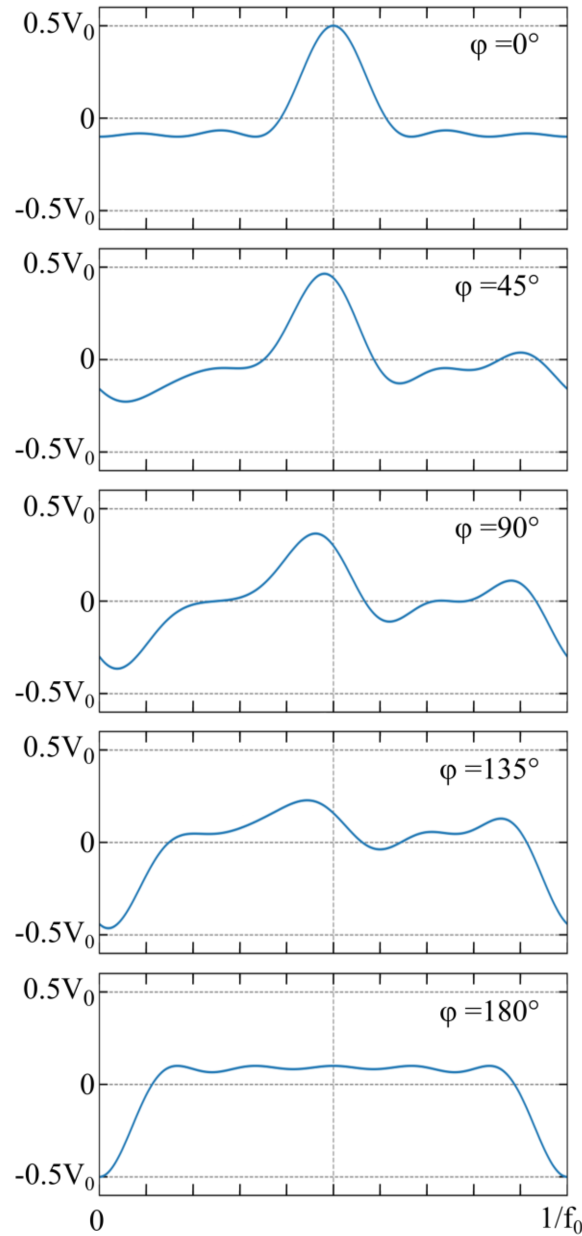

Figure 1.10: Voltage waveforms $V_{VWT}(t)$ based on (1.56) for $\varphi = 0, 45, 90, 135$ and $180°$.

Due to their resemblence the waveform resulting from $\varphi = 0°$ is often reffered to as "peak" waveform whereas the $\varphi = 180°$ case is known as as "valley" waveform. In a geometrically symmetric CCP discharge the peak and valley waverfom have been shown to produce maximum absolute value for V_{dc} with identical magnitude and opposing polarities; negative for $\varphi = 0°$ and positve for $\varphi = 180°$, respectively. The $\varphi = 90°$ waveform is symmetric and thus does not produce a DC self-bias. However, the assumption geometric symmetry is not in line with real reactors and a superposition of geometric and electrical asymmetry is to be expected.

1.21 Ion Energy Distributions

Surface processes, especially ones relevant to the etching of semiconductors, are sensitive to the energy and angle of incidence of ions hitting the surface. For this reason, the control and tailoring of ion angular and energy distributions is of high technical relevance. Ions are generally accelerated to the electrode by the sheath electric field. The maximum energy ions can gain by traversing the sheath is the sheath voltage. However, due to the temporal dynamics of the sheath not all ions gain the same amount of energy but rather obtain a characteristic ion energy and angular distribution IEAD corresponding to the properties of the ion sheath traversal. It is instructive to consider two specific edge cases.

i) The *thick sheath* or *high frequency* limit. Here, the sheath is considered thick enough so that ions can only cross its distance on time scales much larger than the RF period. Without considering ion collisions with the background gas, this idealized conception yields monoenergetic ions corresponding to the mean sheath voltage.

ii) In the *thin sheath* or *low frequency* limit, the ion energy distribution at the surface perfectly matches the temporal behavior of the sheath voltage. Ions are considered to be mobile

enough to traverse the surface on timescales much smaller than the RF period, gaining energy corresponding to the momentary sheath voltage value.

Realistically however, while slow and inert, compared to electrons, ions may possess some limited ability to react to the changing sheath potential. This ability is a function of their weight, the sheath thickness and the driving frequency. For single frequency RF discharges this can result in characteristic bimodal distributions such as those depicted in Figure 1.11 for different particle masses a) and varying driving frequencies b).

Given the use of two or more frequencies, as is the case with voltage waveform tailoring, this simple scaling behavior vanishes, and a more detailed analysis of the sheath dynamics becomes necessary. A detailed analysis of the ion sheath transit behavior resulting from the use of tailored voltage waveforms will be provided in this work.

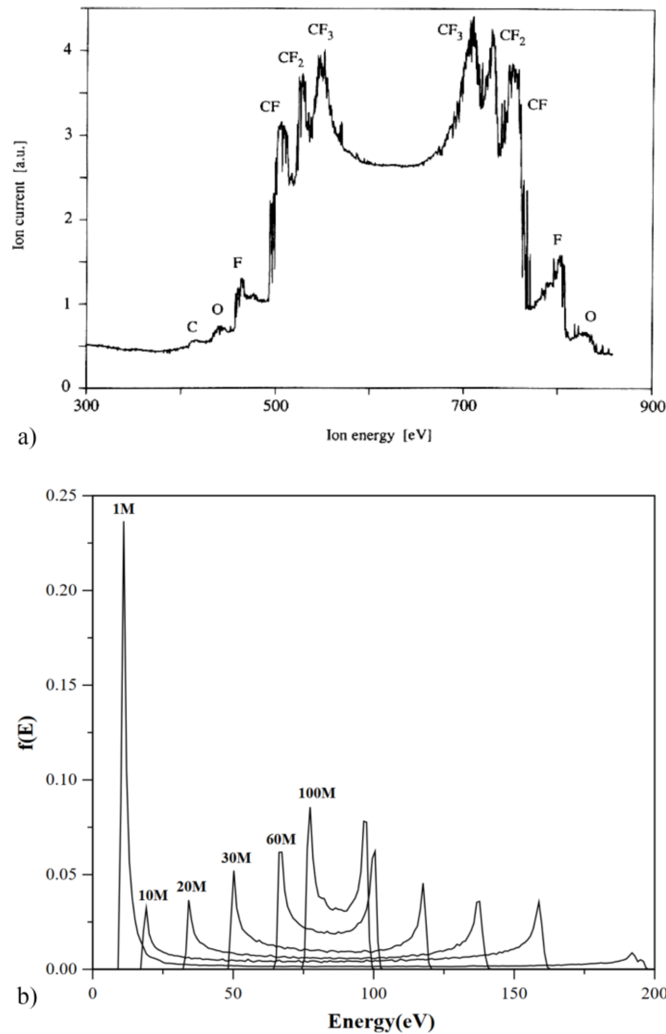

Figure 1.11 a) IEDs at the powered electrode of a rf CF_4 discharge driven at 13.56 MHz from Kuypers and Hopman [129]. b) Particle in Cell simulation results showing IEDs of helium ions hitting the target electrode of rf discharges driven at frequencies from 1 MHz to 100 MHz. Reproduced from Kawamura et al [130].

1.22 Electronegative Plasmas

Some of the theory provided above either directly or indirectly assumes specific relations between the negative charge carries; electrons (light and high energy) the positive charge carriers, ions (heavy and medium to high energy) and neutrals (heavy and low energy) which relied on the presence of only positive ions. Under certain conditions, however, significant amounts of negative ions may be present, depleting electrons, and shifting the mass and inertia ratios of negative and positive charge carriers. The extreme case, in which no electrons are present, and the charge

balance is provided by negative ions, is called an ion-ion plasma. The intermediate regime is characterized by the ratio of negative ions and electrons, called plasma electronegativity. Negative ions are generally produced by direct electron attachment

$$e + A + M \rightarrow A^{-} + M, \tag{1.57}$$

where a third body M is required to conserve energy and momentum, dissociative attachment

$$e + AB \rightarrow A^{-} + B, \tag{1.58}$$

or dissociative ion pair formation

$$e + AB \rightarrow A^{-} + B^{+} + e. \tag{1.59}$$

In either case, the propensity for electron attachment is species specific. The atomic species with the highest specific electronegativity according to the Pauling scale, are F and O, both of which can be expected to be present in relevant quantities due to the usage of oxygen and fluorocarbons as feedstock gases in this thesis.

1.23 Plasma in Semiconductor Processing

Fundamentally, semiconductor devices used as logic (processors), memory, power applications, light emission (LED) or absorption (photovoltaic) are just materials with different electrical properties, some of which are semiconductors, arranged in specific geometric configurations to elicit specific physical behavior. Take for example a (by modern standards) simple device such as a planar metal oxide field effect transistor (MOSFET), shown in Figure 1.12.

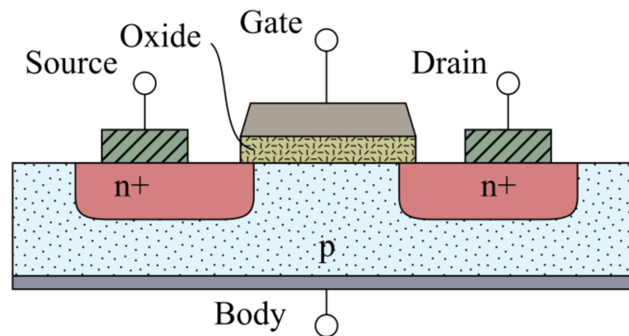

Figure 1.12: Schematic representation of a MOSFET

Doped n-type regions embedded in a p-type substrate are contacted by high conductivity materials and a thin oxide film insulates the gate from the channel region below. Its electrical properties are solely determined by the makeup and geometry of the different materials. Generating these types of structures with suitable precision, repeatability at an appropriate cost and volume is of central importance to the semiconductor industry and by extension to much of the modern world.

The scale of modern devices can be on the order of only several nano meters, and they continue to shrink. Since no mechanical manufacturing can practically be employed on these scales, semiconductor devices are created by means of chemical, thermal and optical processes. Plasmas play a role in a host of these processes such ion implantation used for doping [79], film deposition via sputter processes [80,81], plasma enhanced chemical vapor deposition (PECVD) [82,83] or atomic layer deposition (ALD) [84,85] as well as material removal by direct or

downstream chemical etching, through reactive ion etching (RIE) [86,87] or related processes such as atomic layer etching (ALE) [88–91]. A typical set of steps to create a patterned film is shown in Figure 1.13.

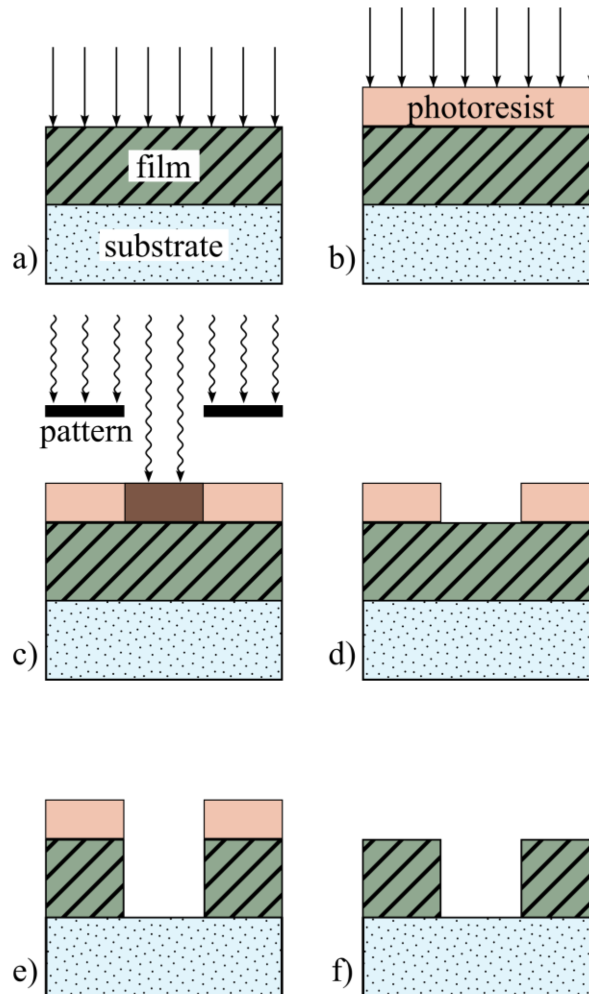

Figure 1.13: Manufacturing of strucured integrated circuit devices through deopsition, etch and pattern transfer: a) metal film deposition; b) photoresist deposition; c) patterned optical exposure; d) photoresist development; e) film etch; f) photoresist removal. Based on [16].

Starting with a blank substrate, a homogeneous film is deposited in a), followed by the deposition of a photoresist (PR) film b). Photoresist is a light sensitive material that changes its chemical structure when it is exposed to certain types of light, making it easier (positive PR) or harder (negative PR) to etch. In c) parts of the photoresist are exposed to light based on a pattern that partially blocks it. The exposed PR is subsequently removed through chemical etching, leaving

behind a patterned mask d). In e), through plasma based anisotropic etch processes this pattern is transferred to the film by removing the material that is no longer covered and protected by the photoresist. Finally, the photoresist is removed, leaving behind only the patterned film in f). While this is an extremely simplified and idealized depiction of the deposition-litho-etch cycle it nevertheless highlights some key requirements:

i) Sufficiently high etch and deposition rates as well as the ability to control them precisely. High rates are highly desirable as this allows for throughput and subsequently a higher production volume.

ii) High etch-selectivity between the different materials, “A” and “B”, $\xi_{A,B}$, which is defined as the ratio of their respective etch rates”, $\xi_{A,B} = \frac{\mathrm{E_A}}{\mathrm{E_B}}$. For example, in the model process discussed above, high selectivity is required between the exposed and non-exposed PR, the PR and the film as well as the film and the substrate.

iii) Controlled anisotropy of the etch process, since a purely isotropic etch process does not allow for precise transfer of mask patterns and as shown in Figure 1.14. An isotropic etch, as depicted in sub-figure a), causes undercut (etching underneath the mask), non-straight sidewalls and overall insufficient control over the shape of the feature.

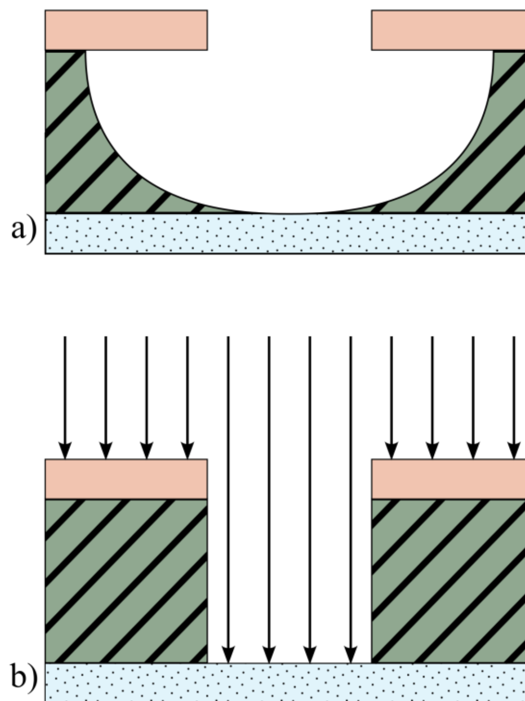

Figure 1.14: a) Isotropic etch processes result in an uncontrolled and ultimately undesirable feature. b) Ion bombardment enables anisotropic etching.

Technological plasmas are a well-established solution that meets these criteria due to some of their fundamental working principles. The plasma's ability to etch is not necessarily native to the used neutral, unexcited gases. Often, (relatively) stable feedstock gases are used, and the reactive components are generated within the etch chamber through dissociation or other modification as a direct result of the highly energetic particles inside the plasma. Because of this, the reactivity and selectivity of the etchant gas can be precisely controlled (including time dependent control) via the electric power deposition into the plasma. Short lived species that otherwise could not be supplied in a stable form can be utilized as they are actively generated on site. Some of the removal processes are synergetic processes requiring high energy ions as well as thermal neutrals. Because ions are non-neutral, their trajectories are sensitive to electric fields. Imparting directionality onto the ions through acceleration in electric fields is the source for anisotropic etching in most plasma systems. While this is not a complete list of reasons, it

nevertheless highlights the utility and relevance of plasmas in semiconductor etch processes. Due to the shrinking dimensions of process nodes and trends toward ever increasingly complex 3-dimensional structures the etching of high aspect ratio (HAR) features has become an area of substantial technological challenges. HAR features in this context are defined as structures in a substrate that possess narrow plasma facing openings with large etch depths. An example of HAR features used for DRAM applications is shown in Figure 1.15. These high aspect ratio features are more susceptible to geometric defects and reductions in etch rate, leading to increased process requirements with respect to variability, ion energy distribution, etch rate etc.

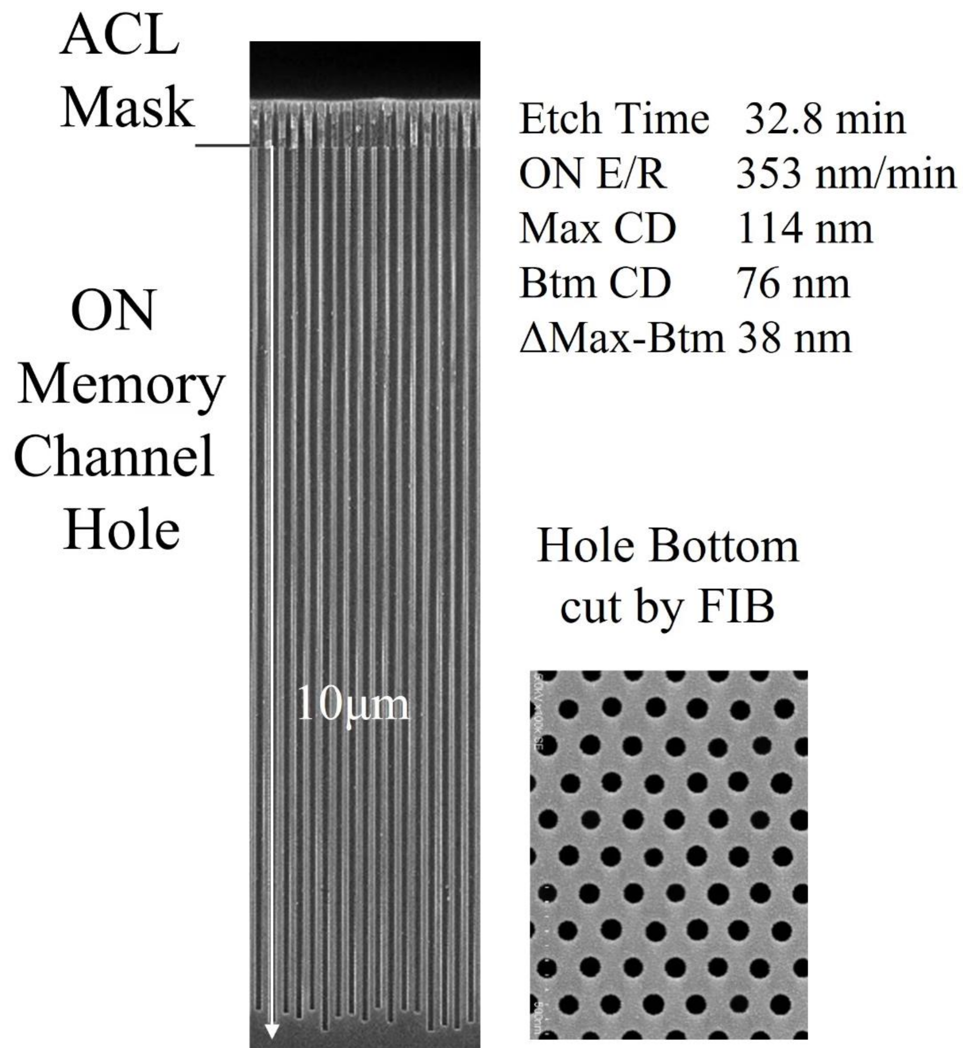

Figure 1.15: Cross section SEM image of memory channel hole pattern after etching [131].

1.24 Adsorption

In the context of this work, *adsorption* is the adhesion of atoms, ions or molecules from a gas to a surface and constitutes the basis for deposition and some surface modification steps. In general, all adsorption processes can be described as an incident particle's capture in a potential well close to the surface. The depth, distance and general shape of that potential are determined by the physical principle on which the adsorption is based. Potential diagrams corresponding to generic physisorption and chemisorption processes are shown in Figure 1.16

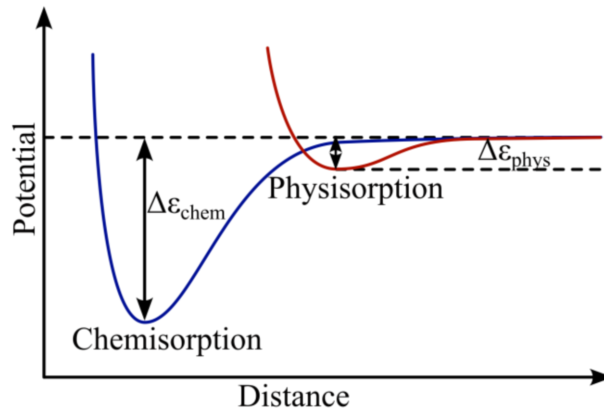

Figure 1.16: Potential diagram of a generic physisorption and chemisorption process.

1.24.1 Physisorption

Physisorption, short for physical adsorption, is a surface adsorption mechanism based on the Van der Waals Force. Physisorption possesses very low binding energy ($\Delta\varepsilon_{phys} = 10 - 100\ \mathrm{meV}$) which means that is generally considered non-permanent as even room temperature thermal energies can cause desorption. However, since this type of bond is rather universal with respect to bonding partners and non-local it allows for significant surface mobility and surface diffusion of physiosorbed species. Through this, physisorption sometimes acts as an intermediate step where the adsorbed particle finds a stronger surface bond type after diffusing to a more appropriate site. [92]

1.24.2 Chemisorption

Chemisorption is based on the formation of chemical bonds between surface and incident species. In contrast to physisorption it is selective with respect to bonding partners as the availability and nature of the bond is determined by the configuration of both partners outer shell electron. Generally, the bonds are much stronger energy ($\Delta\varepsilon_{chem} \geq 500$ meV) and depending on the interacting species, multiple bonds can be formed further increasing the total binding energy.[92]

1.25 Etching and Sputtering

Different mechanisms for the removal of material can be used to achieve desirable etch characteristics and control. Semiconductor manufacturing heavily relies on physical sputtering, chemical etching and a combination of the two in the form of ion enhanced chemical etching. Physical processes such as sputtering are usually anisotropic but fairly slow with very little control over selectivity. Chemical etch processes can be tuned to be very selective, provide high etch rates but usually act almost completely isotopically. The goal is to combine the benefits of multiple fundamental basic mechanism to achieve a reliable, fast and efficient etch process with high control over anisotropy and selectivity. Some basic processes relevant to plasma based material removal processes are depicted in Figure 1.17

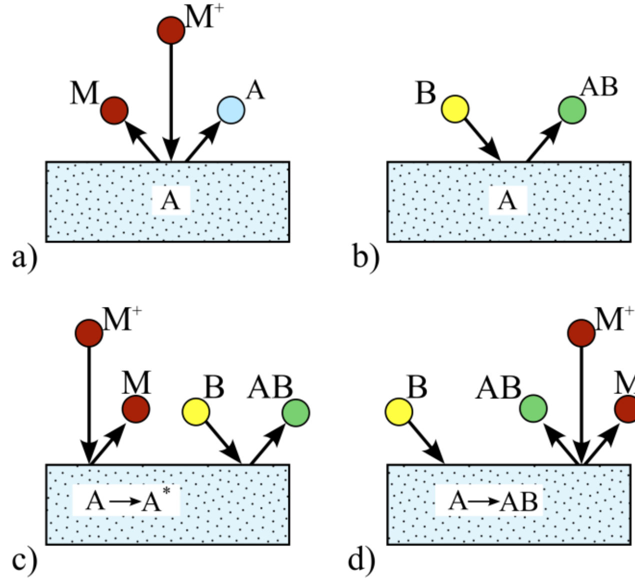

Figure 1.17: Different types of material removing surface reactions. a) physical sputtering, b) thermal etching, c) chemical removal of ion activated species and d) physical removal of chemically modified species.

1.25.1 Direct Sputtering

Sputtering is the ejection of surface species due to the bombardment by ions or fast neutrals. The incident particle collides with the surface and transfers its energy to it. Above a certain threshold energy $\varepsilon_{th,sput}$ this leads to the ejection of on or more surface particles:

$$A_{(s)} + M^{+} \rightarrow A_{(g)} + M_{(g)} \quad (1.60)$$

The ratio of the number of incident and ejected particles is called the sputter yield γ_{sput}, which is generally a function of energy and angle. While angular dependences vary based on specific details such as the incident and sputtered species, crystalline structure or molecular composition, the specific case or Cl sputtering SiO_2, depicted in Figure 1.18 can nevertheless provide some insight. Generally, sputter yield falls off drastically at narrow angles, because very little energy is transferred in these glancing collisions. The maximum sputter yield is generally not a normal incidence, because while it is optimal for energy transfer, it is not guaranteed to provide the best

result in terms of material ejection as the collisional cascade penetrates very deep and energy is lost to a point where the energy transfer to the particles located on the surface is reduced. [16,93,94]

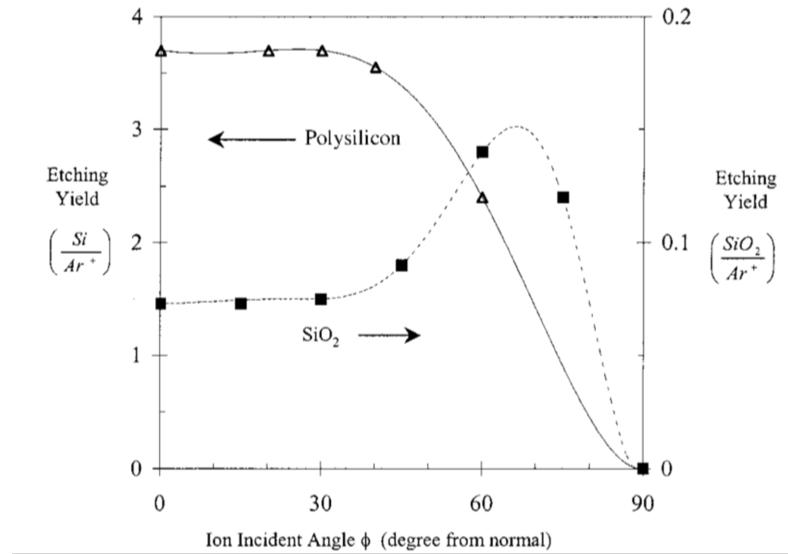

Figure 1.18: Etching yield of polysilicon and silicon dioxide by 100 eV Ar and Cl as a function of ion incident angles for saturated chlorine fluxes. Reproduced from Chang et al [93].

1.25.2 Direct Chemical Etching

The process of a surface species $A_{(s)}$ reacting with a gas phase species $B_{(g)}$ creating a volatile compound $AB_{(g)}$

$$A_{(s)} + B_{(g)} \rightarrow AB_{(g)} \tag{1.61}$$

is referred to as *direct etching* or *thermal etching*. This process is almost invariably isotropic because the relevant etchant species possess a uniform, thermal angular distribution. Thermal etch processes are necessarily confined to a singular step but rather tend to occur in multiple subsequent surface modification steps with the final one only forming a volatile compound:

$$A_{(s)} + B_{(g)} \rightarrow AB_{(s)} \tag{1.62}$$

$$AB_{(s)} + B_{(g)} \rightarrow AB_{2(s)} \tag{1.63}$$

$$AB_{2(s)} + B_{(g)} \rightarrow AB_{3(s)} \tag{1.64}$$

$$AB_{3(s)} + B_{(g)} \rightarrow AB_{4(g)} \tag{1.65}$$

For most processes the rates of reactivity of the surface decreases with increasing attachment, i.e., the rate of reaction of (1.65) is lower than (1.64). Pure, thermal etch processes are predominantly limited by the availability of the educts, given by the reactant fluxes to the surface and density of available surface sites.

1.25.3 Ion Enhanced Etching

Ion enhanced etching or *reactive ion etching* refers to the simultaneous use of ion surface bombardment and chemical etching with the aim to combine the high selectivity and etch rate of chemical processes with the directionality of physical sputtering. This is commonly achieved by using feed gas mixtures that contain or produce chemically active radicals in conjunction with a CCP or CCP-like etch reactor where radicals and highly energetic ions are simultaneously impinging on the wafer surface. In most scenarios, the removal process consists of multiple steps.

$$A_{(s)} + M^{+} \rightarrow A^{*}_{(s)} \tag{1.66}$$

$$A^{*}_{(s)} + B_{(g)} \rightarrow AB_{(g)} \tag{1.67}$$

One of the mechanisms, depicted in Figure 1.17c) relies on ion surface activation. The high energy ions carry and deposit enough energy to activate the surface. The nature of the surface activation can differ, depending on the process, but is generally based on the breaking of bonds, to lower the total surface bonding energy, and increase reactivity through the creation of dangling bonds. The activated surface sites subsequently react with gas phase radicals similar to the mechanism discussed in Section 1.25.2.

Alternatively, the role of the ion bombardment can be the removal of more inert species that were created by prior isotropic processes.

$$A_{(s)} + B_{(g)} \rightarrow AB_{(s)} \quad (1.68)$$

$$AB_{(s)} + M^{+} \rightarrow AB_{(g)} \quad (1.69)$$

As discussed in Section 1.25.2 the reactivity of surface compounds can decrease as they form more saturated species. Often, this process coincides with a reduction of surface bonds, which reduces the total surface bonding energy, making them easier to remove by physical means such as sputtering. In many scenarios, the total etch rate of the combined process can exceed the sum of the individual processes. This synergy is generally highly desirable as it has desirable effects on process times and etch anisotropy.

1.26 Aspect Ratio Dependent Etch

In the context of the ever-increasing requirements for aspect ratio of the etched features, a major technical challenge is posed by aspect ratio dependent etching (ARDE) or RIE-lag. In HAR etch process, as the etch front propagates downwards, a drastic reduction in etch rate is often observed [95–97]. Generally, this is a consequence of transport limitations of neutrals as well as ions. Neutral transport to the bottom of the feature is limited by a host of factors. In scenarios where the mean free path of a neutral thermal particle is on the same scale or larger than geometric restrictions, as is the case in narrow high aspect ratio features, transport is governed by Knudsen diffusion which severely limits neutral gas transport deep into the feature. This is coupled with the loss of radicals during sidewall collisions, the number of which increases with increases etch depth and aspect ratio [98,99]. It has been shown that to some extent the ARDE can be controlled via the gas pressure and substrate temperature [98,100,101]. Through an increase in pressure the lack of

gas transport to the feature bottom can be compensated by simply supplying more total flux, while the lower temperature reduces the surface reactivity and reduces the loss due to surface reactions.

The ion transport effect on ARDE is mostly related to ion losses to the wall. The maximum angle at which an incident ion is able to directly hit the etch front is the critical ion angle Θ_c, shown in Figure 1.19 for a low a) and high b) aspect ratio feature.

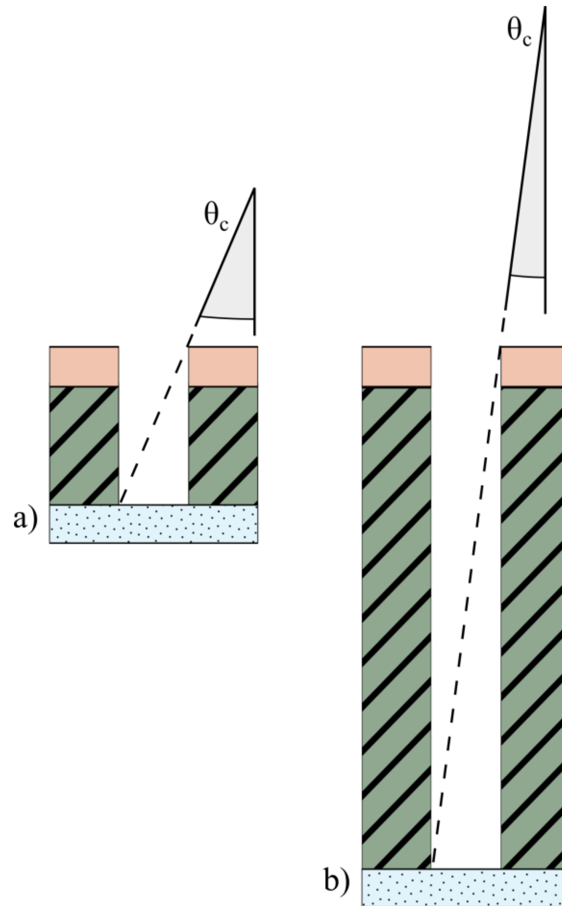

Figure 1.19: Critical ion angle of incidence for direct hit on the etch front for a) low and b) high aspect ratio feature.

As the feature etch progresses, the effective aspect ratio of the feature increases and Θ_c decreases accordingly which in consequence leads to a decrease of total ion flux to the etch front. This dependence on the ion angular distribution for HAR is one key factor for the requirement of narrow ion distributions. The reduction of etch rate due to lack of neutral and ion transport to the bottom of the feature are respectively known as the neutral and ion starved regime.

1.27 Intra Feature Charging

The highly anisotropic, near normal, high-energy ions can penetrate deeply into HAR features whereas the electrons typically have nearly thermal and angularly broad distributions onto the wafer [102]. When etching dielectric (or low conductivity materials), these conditions result in the lower echelons of the feature being charged positively and the upper echelons being charged negatively [103,104]. This differential charging generates electric field components within the feature [103–105] The intra-feature electric fields can deviate ion trajectories from the vertical which can lead to undesired consequences including a reduction of the ion flux at the bottom of the feature [106], and profile distortion such as notching, twisting and bowing [103–105,107–110] as shown in Figure 1.20.

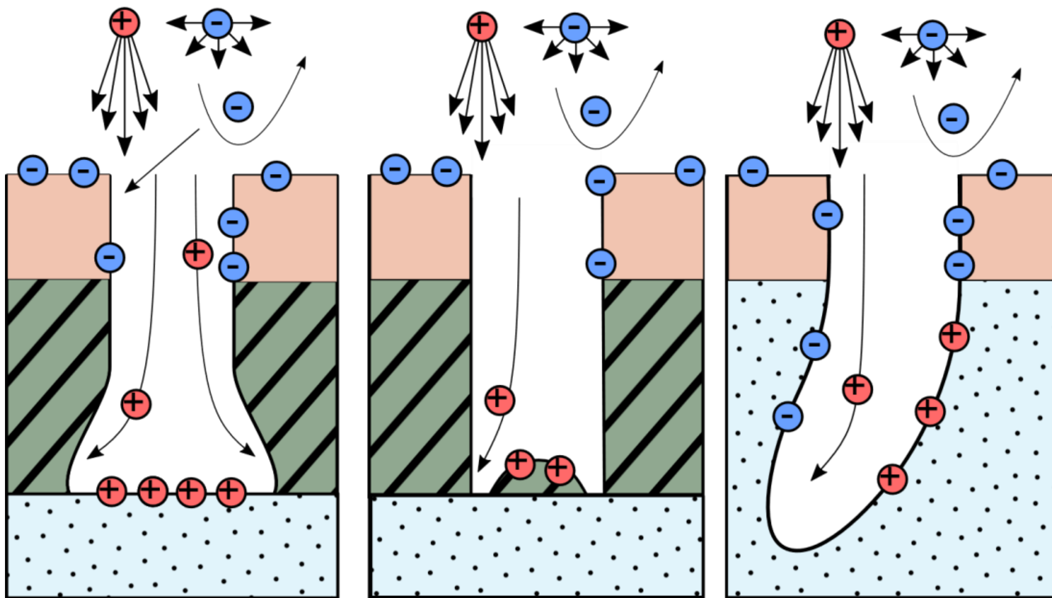

Figure 1.20: Surface charge effects responsible for notching, trenching and twisting in HAR etch processes.

Several remedies have been investigated to minimize differential charging, including operation with ever higher ion energies to minimize the effects of ion deflection. However, this

approach must overcome several challenges. Increasing the ion energy increases the power density at the wafer surface, leading to wafer heating which, unchecked, can stress the thermal budget of the process [22]. In HVM (high volume manufacturing) additional wafer cooling is applied. While this strategy has been very successful it adds technological complexity to the etch system and is ultimately subject to diminishing returns due to the limited heat transport of coolants and the wafer itself.

Another challenge is that the sheath thickness is a function of the sheath voltage and, by extension, is a function of the CCP power. If the source power and plasma density are relatively constant, increasing the incident ion energy by increasing the applied bias voltage will ultimately lead to a thicker and more collisional sheath. The more collisional sheath will produce a lower energy and broader angular distribution of the incident ion flux. The higher ion energies are also incident onto the photoresist or other hard masking materials, resulting in higher physical sputtering rates, which then decrease the selectivity of the dielectric etch with respect to the mask. Maintaining high selectivity is critical during the typically long etch times required for HAR features [111].

Another approach to mediating differential charging is to produce enhanced fluxes of negative charge carriers into the feature. Once such method utilizes power-pulsing to generate an ion-ion plasma during the inter-pulse period. Acceleration of negative ions into the feature during the interpulse period helps alleviate positive charging [112]. This technique is challenged by the difficulty of sustaining a thin sheath during the low-plasma density afterglow, and so the ion acceleration through the sheath is collisional. Another technique utilizes a negative DC bias on the top electrode to generate an electron-beam-like flux of electrons into the feature [102].

1.28 Sidewall Passivation

While ion assisted etch processes possess some intrinsic anisotropy, some etching of the sidewall occurs, nevertheless. This is due to non-ideal ion distributions that hit the sidewalls to some (lesser) degree, a non-zero etch rate even without ions or a combination of the two. Often this is addressed by sidewall passivation, either as an intrinsic part of the process or by intentional design. Adsorption of passivating species on the sidewalls, as depicted in Figure 1.21 can produce a protective layer that slows down or stops the lateral attack of etchant species and reduces undercutting of the mask and bowing. The chemical makeup of this passivation layer is process dependent and can be the result of polymer deposition from Fluorocarbon gas mixtures [113] or the formation of a chemically inert oxide layer [114]. In many scenarios the sidewall passivation mechanism is not self-limiting and excessive deposition of the passivating species causes a reduction of the feature diameter known as *necking* or in extreme cases a complete clog of the feature. This is especially relevant in HAR processes where the diameter of the opening is very limited to begin with.

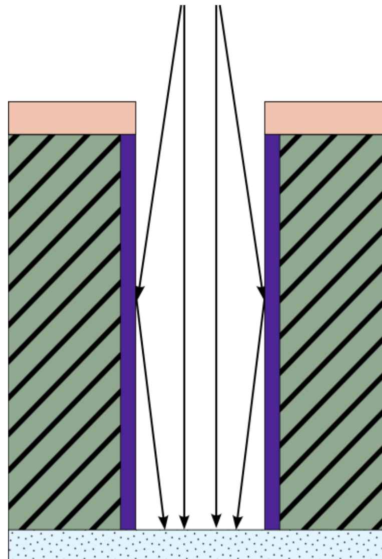

Figure 1.21: Sidewall passivation during the feature etch process.

1.29 Computational Modeling

Plasma processes are complex systems, usually operated in very controlled environments that are sensitive to changes in geometry, materials and operating conditions which makes direct measurements notoriously difficult. The measurement of some of the most fundamental plasma properties is often performed using probes such as Langmuir probes [115,116], resonant probes [117,118] or retarding field analyzers [119,120], which perturb the plasma and generally lack fine spatial or temporal resolution. While some non-invasive techniques like optical measurements [121–127], or electrical analysis exist, they can lead to significantly increased technical complexity as well as cost and may still not capture all relevant quantities. Some of the plasmas fundamental mechanisms may never be directly measured in a reasonable processing setup which has for a long time been a major driver behind the development of computational models that aim to accurately represent the inner workings of plasma processes, allowing for functional and most importantly, flexible insight into otherwise opaque plasma processes. This culminates in the ultimate vision of "digital twins" where entire etch processes are perfectly reproduced in simulations, allowing their development and optimization to be performed on their digital counterpart ahead of or in tandem with the actual physical entity, saving time, cost and providing absolute insight [128]. While this vision has not fully materialized, computational modeling has nevertheless become an integral part of academic and industrial research efforts in the field of low temperature plasmas and semiconductor manufacturing processes. In reality, both surface and gas phase properties and behavior are fundamentally defined by atomic or molecular interactions which, due to the sheer number of particles, cannot be reasonably modeled in a direct approach on macroscopic scales such as reactor or wafer dimensions, which are on the order of tens of cm. Because of this, the particle interactions must either be reduced by clustering similar particles into superparticles on

static cells (kinetic approach) or reducing their transport behavior to idealized quantities such as densities, fluxes, temperatures etc. (fluid approach). While the nature of the assumptions made differ in detail and derivation, they nevertheless require the usage of condensed macroscopic interaction parameters such as rates and probabilities which are ultimately supplied to the simulation in the form of external datasets, either based on experimental data or from mor complex ab initio models. The quality of these datasets can critically affect the validity of simulation results and thus great care must be taken to ensure that they accurately reflect real world behavior.

1.30 Goals and Scope of this Dissertation

This work aims to identify and computationally test techniques to improve upon critical aspects of HAR feature etch processes into SiO_2 using fluorocarbon gas mixtures. This includes the usage of special tailored voltage waveforms as a source of plasma heating and how they affect neutral and charged particle dynamics as well as subsequent effects on feature etch performance and wafer charging. Previous work has shown that the use of voltage waveform tailoring can be used to control the DC self-bias and ion as well as electron incident energy onto the surface. The motivation of these investigations was the control of HAR etching and mediation of feature charge effects, but it has thus far not been applied to 2D systems or relevant gas compositions and neither has the direct link to etch behavior been causally verified. To that end, this thesis employs well tested computational models to

i. Verify the occurrence of the electrical asymmetry effect and electric field reversal, induced by the usage of tailored voltage waveforms, in a different computational model.

ii. Explore effects of the VWT that require a 2-dimensional setup such as effects on discharge homogeneity, self-consistent treatment of geometry (especially geometric asymmetry) and radial structures in plasma properties.

iii. Expand the tested range of gas chemistries to include electronegative gases and fluorocarbons used in semiconductor fabrication.

iv. Provide a direct causal link between charged particle dynamics and etch behavior by simulating HAR surface etch processes directly coupled to the gas phase simulations.

v. Test the established and extended theories of the link between ion energy and DC self-bias in technologically relevant low frequency regimes.

vi. Additionally, to address the stated issue of a model's dependence on physical parameters, this thesis provides a framework for the tuning and optimization of model parameters by developing a semi-autonomous physics informed hybrid optimization scheme and employing it to optimize a fluorocarbon based SiO_2 etch mechanism.

In Chapter 2, the computational models used in this thesis are described. The Hybrid Plasma Equipment Model (HPEM) was used to model the gas phase plasma phenomena and the Monte Carlo Feature Scale Model (MCFPM) was used to represent the surface etch processes.

The use of tailored voltage waveforms for the generation of directional electrons and ions is investigated in Chapter 3 with special focus on the gas composition in terms of electronegativity.

Building on the findings of Chapter 3, the investigation is expanded to appropriate etch gas mixtures and includes the examination of feature etch processes. The results are presented in Chapter 4.

The link between the ion energy control through plasma asymmetry and resulting DC-self bias is investigated for the low frequency regime in Chapter 5.

Chapter 6 introduces and investigates the use of an automatic optimization scheme for surface processes.

A summary of the studies in this thesis is presented in Chapter 7. Improvements to the models and potential future studies to expand upon the work in this thesis are also discussed.

1.31 References

[1] Michael. Zeilik, E. v. P. (Elske van P. Smith and E. v. P. (Elske van P. Smith, *Introductory astronomy and astrophysics*, Saunders College Pub (1987).

[2] P. Schneider, Extragalactic Astronomy and Cosmology *Extragalactic Astronomy and Cosmology*, Springer Berlin Heidelberg (2015).

[3] A. R. Choudhuri, Astrophysics for Physicists *Astrophysics for physicists*, Cambridge University Press (2010).

[4] B. W. Carroll and D. A. Ostlie, An Introduction to Modern Astrophysics, Second Edition *An Introduction to Modern Astrophysics, Second Edition*, Cambridge University Press (2019).

[5] M. Boulos, P. Fauchais and E. Pfender, *Thermal Plasmas: Fundamentals and Applications*, (1994).

[6] V. A. Nemchinsky and W. S. Severance, J Phys D Appl Phys **39,** R423 (2006).

[7] E. Menthe, K. T. Rie, J. W. Schultze and S. Simson, Surf Coat Technol **74–75,** 412 (1995).

[8] J. F. Waymouth and F. Bitter, J Appl Phys **27,** 122 (1956).

[9] A. Reatti, IEEE Trans Power Electron **15,** 361 (2000).

[10] A. Kumar, N. Kumar, G. N. Pandey, al -, R. Gao, S. Mosquera-Romero, E. Ntagia, N. Takeuchi and K. Yasuoka, Jpn J Appl Phys **60,** SA0801 (2020).

[11] N. Puač, M. Gherardi and M. Shiratani, Plasma Processes and Polymers **15,** 1700174 (2018).

[12] T. Von Woedtke, A. Schmidt, S. Bekeschus, K. Wende and K. D. Weltmann, In Vivo (Brooklyn) **33,** 1011 (2019).

[13] S. Bekeschus, T. von Woedtke, S. Emmert and A. Schmidt, Redox Biol **46,** 102116 (2021).

[14] Z. Chen, G. Garcia, V. Arumugaswami and R. E. Wirz, Physics of Fluids **32,** 111702 (2020).

[15] F. F. Chen, *Introduction to Plasma Physics and Controlled Fusion*, Springer (2006).

[16] M. A. Lieberman and A. J. Lichtenberg, Principles of Plasma Discharges and Materials Processing: Second Edition *Principles of Plasma Discharges and Materials Processing: Second Edition*, John Wiley and Sons (2005).

[17] P. M. Bellan, *Fundamentals of Plasma Physics*, Cambridge University Press (2006).

[18] P. Chabert, T. V. Tsankov and U. Czarnetzki, Plasma Sources Sci Technol **30,** 024001 (2021).

[19] John David Jackson, *Classical Electrodynamics*, Wiley (1998).

[20] D. J. Griffiths, Introduction to Electrodynamics *Introduction to Electrodynamics*, Cambridge University Press (2017).

[21] E. M. Purcell and D. J. Morin, (2013).

[22] B. Wu, A. Kumar and S. Pamarthy, Journal of Applied Physics **108,** 51101 (2010).

[23] S. J. Doyle, A. R. Gibson, R. W. Boswell, C. Charles and J. P. Dedrick, Plasma Sources Sci Technol **29,** 124002 (2020).

[24] P. Saikia, H. Bhuyan, M. Escalona, M. Favre, B. Bora, M. Kakati, E. Wyndham, R. S. Rawat and J. Schulze, J Appl Phys **123,** 183303 (2018).

[25] E. Kawamura, V. Vahedi, M. A. Lieberman and C. K. Birdsall, Plasma Sources Sci. Technol **8,** (1999).

[26] D. Levko, R. R. Upadhyay, K. Suzuki and L. L. Raja, Journal of Vacuum Science & Technology B **41,** 12205 (2023).

[27] E. Kawamura, V. Vahedi, M. A. Lieberman and C. K. Birdsall, Plasma Sources Sci Technol **8,** R45 (1999).

[28] S. D. Baalrud, B. Scheiner, B. T. Yee, M. M. Hopkins and E. Barnat, Plasma Sources Sci Technol **29,** 053001 (2020).

[29] M. S. Benilov and N. A. Almeida, Phys Plasmas **26,** 123505 (2019).

[30] O. Murillo, A. S. Mustafaev and V. S. Sukhomlinov, Technical Physics **64,** 1308 (2019).

[31] I. Adamovich, S. D. Baalrud, A. Bogaerts, P. J. Bruggeman, M. Cappelli, V. Colombo, U. Czarnetzki, U. Ebert, J. G. Eden, P. Favia, D. B. Graves, S. Hamaguchi, G. Hieftje, M. Hori, I. D. Kaganovich, U. Kortshagen, M. J. Kushner, N. J. Mason, S. Mazouffre, S. M. Thagard, H. R. Metelmann, A. Mizuno, E. Moreau, A. B. Murphy, B. A. Niemira, G. S. Oehrlein, Z. L. Petrovic, L. C. Pitchford, Y. K. Pu, S. Rauf, O. Sakai, S. Samukawa, S. Starikovskaia, J. Tennyson, K. Terashima, M. M. Turner, M. C. M. Van De Sanden and A. Vardelle, Journal of Physics D: Applied Physics **50,** 323001 (2017).

[32] S.-J. Chung, P. Luan, M. Park, A. Metz and G. S. Oehrlein, Journal of Vacuum Science & Technology B **41,** 062201 (2023).

[33] Z. H. Bi, Y. X. Liu, W. Jiang, X. Xu and Y. N. Wang, Current Applied Physics **11,** S2 (2011).

[34] Z. Donkó, A. Derzsi, I. Korolov, P. Hartmann, S. Brandt, J. Schulze, B. Berger, M. Koepke, B. Bruneau, E. Johnson, T. Lafleur, J. P. Booth, A. R. Gibson, D. O'Connell and T. Gans, Plasma Phys Control Fusion **60,** 014010 (2017).

[35] T. Gans, J. Schulze, D. O'Connell, U. Czarnetzki, R. Faulkner, A. R. Ellingboe and M. M. Turner, Appl Phys Lett **89,** 261502 (2006).

[36] S. Rauf, K. Bera and K. Collins, Plasma Sources Sci Technol **19,** 015014 (2009).

[37] W. Jiang, X. Xu, Z. L. Dai and Y. N. Wang, Phys Plasmas **15,** 33502 (2008).

[38] T. Kitajima, Y. Takeo, N. Nakano and T. Makabe, J Appl Phys **84,** 5928 (1998).

[39] J.-K. Liu, E. Kawamura, M. A. Lieberman, al - and S. Rauf, Plasma Sources Sci Technol **29,** 095019 (2020).

[40] S. Rauf, K. Bera and K. Collins, Plasma Sources Sci Technol **17,** 035003 (2008).

[41] G. Alcouffe, M. Cavarroc, G. Cernogora, F. Ouni, A. Jolly, L. Boufendi and C. Szopa, Plasma Sources Sci Technol **19,** 015008 (2009).

[42] A. Agarwal, S. Rauf and K. Collins, Plasma Sources Sci Technol **21,** 055012 (2012).

[43] T. Lafleur, P. Chabert and J. P. Booth, Plasma Sources Sci Technol **23,** 035010 (2014).

[44] P. Drude, Ann Phys **308,** 369 (1900).

[45] P. Drude, Ann Phys **306,** 566 (1900).

[46] R. P. Brinkmann, J Phys D Appl Phys **44,** 042002 (2011).

[47] I. Langmuir, Physical Review **33,** 954 (1929).

[48] L. S. Hall, Phys Fluids **4,** 388 (1961).

[49] K. U. Riemann, J Phys D Appl Phys **24,** 493 (1991).

[50] M. A. Lieberman, IEEE Transactions on Plasma Science **26,** 955 (1998).

[51] E. Kawamura, M. A. Lieberman and A. J. Lichtenberg, Phys Plasmas **21,** 123505 (2014).

[52] Z. Wang, A. J. Lichtenberg and R. H. Cohen, IEEE Transactions on Plasma Science **26,** 59 (1998).

[53] M. A. Lieberman, IEEE Transactions on Plasma Science **16,** 638 (1988).

[54] J. Schulze, B. G. Heil, D. Luggenhölscher, R. P. Brinkmann and U. Czarnetzki, J Phys D Appl Phys **41,** 195212 (2008).

[55] E. Kawamura, M. A. Lieberman and A. J. Lichtenberg, Phys Plasmas **13,** 53506 (2006).

[56] C. Qu, S. J. Lanham, S. C. Shannon, S. K. Nam and M. J. Kushner, J Appl Phys **127,** 133302 (2020).

[57] K. Kurokawa, IEEE Trans Microw Theory Tech **13,** 194 (1965).

[58] Z. H. Bi, Y. X. Liu, W. Jiang, X. Xu and Y. N. Wang, Current Applied Physics **11,** S2 (2011).

[59] H. H. Goto, H.-D. Löwe, T. Ohmi and H.-D. Lowe, Journal of Vacuum Science & Technology A **10,** 3048 (1992).

[60] W. Tsai, ; G Mueller, ; R Lindquist, ; B Frazier, ; V Vahedi,) G Mueller, R. Lindquist, B. Frazier and V. Vahedi, Journal of Vacuum Science & Technology B: Microelectronics and Nanometer Structures Processing, Measurement, and Phenomena **14,** 3276 (1996).

[61] H. H. Goto, H. D. Lowe and T. Ohmi, IEEE Transactions on Semiconductor Manufacturing **6,** 58 (1993).

[62] A. Derzsi, E. Schüngel, Z. Donkó and J. Schulze, Open Chem **13,** 346 (2015).

[63] Y. Xu, 徐铁君, X. Wu, 吴雪梅, C. Ye and 叶超, Plasma Science and Technology **15,** 1066 (2013).

[64] S. Rauf, P. Tian, J. Kenney and L. Dorf, Journal of Vacuum Science & Technology B **40,** 32202 (2022).

[65] S. Kirchhoff, Ann Phys **140,** 497 (1845).

[66] R. A. Gottscho, G. R. Scheller, D. Stoneback and T. Intrator, J Appl Phys **66,** 492 (1989).

[67] T. Kaneda, T. Kubota, M. Ohuchi and J. S. Chang, J Phys D Appl Phys **23,** 1642 (1990).

[68] S. Maniv, J Appl Phys **63,** 1022 (1988).

[69] R. A. Gottscho, G. R. Scheller, D. Stoneback and T. Intrator, J Appl Phys **66,** 492 (1989).

[70] C. D. Child, Physical Review (Series I) **32,** 492 (1911).

[71] I. Langmuir, Physical Review **2,** 450 (1913).

[72] B. G. Heil, U. Czarnetzki, R. P. Brinkmann and T. Mussenbrock, J Phys D Appl Phys **41,** 165202 (2008).

[73] J. Schulze, E. Schüngel, Z. Donkó and U. Czarnetzki, Plasma Sources Sci Technol **20,** 15017 (2011).

[74] U. Czarnetzki, J. Schulze, E. Schüngel and Z. Donkó, Plasma Sources Sci Technol **20,** 024010 (2011).

[75] J. Schulze, Z. Donkó, B. G. Heil, D. Luggenhölscher, T. Mussenbrock, R. P. Brinkmann and U. Czarnetzki, J Phys D Appl Phys **41,** 105214 (2008).

[76] P. Hartmann, L. Wang, K. Nösges, B. Berger, S. Wilczek, R. P. Brinkmann, T. Mussenbrock, Z. Juhasz, Z. Donkó, A. Derzsi, E. Lee and J. Schulze, J Phys D Appl Phys **54,** 255202 (2021).

[77] J. Schulze, E. Schüngel and U. Czarnetzki, J Phys D Appl Phys **42,** 092005 (2009).

[78] T. Lafleur, Plasma Sources Sci Technol **25,** 013001 (2015).

[79] S. Qin, Proceedings of the International Conference on Ion Implantation Technology (2014).

[80] P. J. Kelly and R. D. Arnell, Vacuum **56,** 159 (2000).

[81] Y. Yamamura and H. Tawara, At Data Nucl Data Tables **62,** 149 (1996).

[82] G. Lucovsky, Adv Funct Mater **6,** 55 (1996).

[83] L. Martinu, O. Zabeida and J. E. Klemberg-Sapieha, Handbook of Deposition Technologies for Films and Coatings: Science, Applications and Technology 392 (2010).

[84] M. Leskelä and M. Ritala, Angewandte Chemie International Edition **42,** 5548 (2003).

[85] R. W. Johnson, A. Hultqvist and S. F. Bent, Materials Today **17,** 236 (2014).

[86] M. Huff, L. Romano and K. Jefimovs, Micromachines 2021, Vol. 12, Page 991 **12,** 991 (2021).

[87] F. Laermer, S. Franssila, L. Sainiemi and K. Kolari, Handbook of Silicon Based MEMS Materials and Technologies 417 (2020).

[88] C. M. Huard, Y. Zhang, S. Sriraman, A. Paterson, K. J. Kanarik and M. J. Kushner, Journal of Vacuum Science & Technology A: Vacuum, Surfaces, and Films **35,** 031306 (2017).

[89] G. Antoun, T. Tillocher, P. Lefaucheux, J. Faguet, K. Maekawa and R. Dussart, Scientific Reports 2021 11:1 **11,** 1 (2021).

[90] J. K. Kim, S. Il Cho, S. H. Lee, C. K. Kim, K. S. Min and G. Y. Yeom, Journal of Vacuum Science & Technology A: Vacuum, Surfaces, and Films **31,** 061302 (2013).

[91] S. Dallorto, A. Goodyear, M. Cooke, J. E. Szornel, C. Ward, C. Kastl, A. Schwartzberg, I. W. Rangelow and S. Cabrini, Plasma Processes and Polymers **16,** 1900051 (2019).

[92] P. W. Atkins, J. De Paula and J. Keeler, Oxford University Press, Oxford *Physical Chemistry*, (2017).

[93] J. P. Chang and H. H. Sawin, Journal of Vacuum Science & Technology B: Microelectronics and Nanometer Structures Processing, Measurement, and Phenomena **19,** 1319 (2001).

[94] G. Packard, A. Rosenfeld, G. S. Oehrlein and S. Hamaguchi, Plasma Sources Sci Technol **27,** 023001 (2018).

[95] C. M. Huard, Y. Zhang, S. Sriraman, A. Paterson and M. J. Kushner, Journal of Vacuum Science & Technology A: Vacuum, Surfaces, and Films **35,** 5 (2017).

[96] R. L. Bates, M. J. Goeckner and Lawrence. J. Overzet, Journal of Vacuum Science & Technology A: Vacuum, Surfaces, and Films **32,** 51302 (2014).

[97] L. Meng, J. Li, C. Zhao and J. Yan, ECS Solid State Letters **3,** Q25 (2014).

[98] T. Panagopoulos and T. Lill, Journal of Vacuum Science & Technology A **41,** 33006 (2023).

[99] S. Gruener and P. Huber, Phys Rev Lett **100,** 064502 (2008).

[100] T. Lill, ; M Grimbergen, ; D Mui,) M Grimbergen and D. Mui, Journal of Vacuum Science & Technology B: Microelectronics and Nanometer Structures Processing, Measurement, and Phenomena **19,** 2123 (2001).

[101] (2002).

[102] V. M. Donnelly and A. Kornblit, Journal of Vacuum Science & Technology A: Vacuum, Surfaces, and Films **31,** 050825 (2013).

[103] B. Radjenović and M. Radmilović-Radjenović, Engineering **06,** 1 (2014).

[104] C. Han, Z. Wu, C. Yang, L. Xie, B. Xu, L. Liu, Z. Yin, L. Jin and Z. Huo, Semicond Sci Technol **35,** 045003 (2020).

[105] B. M. Radjenović, M. D. Radmilović-Radjenović and Z. L. Petrović, IEEE Transactions on Plasma Science **36,** 874 (2008).

[106] H. Jansen, M. De Boer, R. Wiegerink, N. Tas, E. Smulders, C. Neagu and M. Elwenspoek, Microelectron Eng **35,** 45 (1997).

[107] R. J. Belen, S. Gomez, M. Kiehlbauch and E. S. Aydil, Journal of Vacuum Science & Technology A: Vacuum, Surfaces, and Films **24,** 350 (2006).

[108] N. Negishi, M. Miyake, K. Yokogawa, M. Oyama, T. Kanekiyo and M. Izawa, Journal of Vacuum Science & Technology B, Nanotechnology and Microelectronics: Materials, Processing, Measurement, and Phenomena **35,** 051205 (2017).

[109] G. S. Hwang, Journal of Vacuum Science & Technology B: Microelectronics and Nanometer Structures **15,** 70 (1997).

[110] T. Nozawa, T. Kinoshita, T. Nishizuka, A. Narai, T. Inoue and A. Nakaue, Jpn J Appl Phys **34,** 2107 (1995).

[111] D. Zhang, S. Rauf and T. Sparks, IEEE Transactions on Plasma Science **30,** 114 (2002).

[112] A. Agarwal, S. Rauf and K. Collins, J Appl Phys **112,** 33303 (2012).

[113] G. S. Oehrlein and Y. Kurogi, Materials Science and Engineering: R: Reports **24,** 153 (1998).

[114] M. Haverlag, ; G S Oehrlein, ; D Vender, G. S. Oehrlein and D. Vender, Journal of Vacuum Science & Technology B: Microelectronics and Nanometer Structures Processing, Measurement, and Phenomena **12,** 96 (1994).

[115] J. Hopwood, C. R. Guarnieri, S. J. Whitehair and J. J. Cuomo, Journal of Vacuum Science & Technology A **11,** 152 (1993).

[116] R. L. Merlino, Am J Phys **75,** 1078 (2007).

[117] J. Oberrath, M. Friedrichs, J. Gong, M. Oberberg, D. Pohle, C. Schulz, C. Wang, P. Awakowicz, R. P. Brinkmann, M. Lapke, T. Mussenbrock, T. Musch and I. Rolfes, IEEE Transactions on Plasma Science **49,** 3293 (2021).

[118] N. S. J. Braithwaite and R. N. Franklin, Plasma Sources Sci Technol **18,** 014008 (2008).

[119] Y. X. Wei, S. Q. Liu, X. X. Li, H. L. Shen, M. G. Huang and P. K. Liu, Nucl Instrum Methods Phys Res A **785,** 123 (2015).

[120] Y. Yuan, J. Bansky, J. Engemann and A. Brockhaus, Surf Coat Technol **74–75,** 534 (1995).

[121] E. Slikboer, K. Acharya, A. Sobota, E. Garcia-Caurel and O. Guaitella, Sci Rep **10,** 2712 (2020).

[122] B. Huang, C. Zhang, I. Adamovich, Y. Akishev and T. Shao, Plasma Sources Sci Technol **10,** 044001 (2020).

[123] T. Darny, G. Bauville, M. Fleury, S. Pasquiers and J. Santos Sousa, Plasma Sources Sci Technol **30,** 105021 (2021).

[124] L. Invernizzi, N. Sadeghi, F. P. Sainct and P. Guillot, Plasma Sources Sci Technol **31,** 035002 (2022).

[125] S. Schröter, A. Wijaikhum, A. R. Gibson, A. West, H. L. Davies, N. Minesi, J. Dedrick, E. Wagenaars, N. De Oliveira, L. Nahon, M. J. Kushner, J. P. Booth, K. Niemi, T. Gans and D. O'Connell, Physical Chemistry Chemical Physics **20,** 24263 (2018).

[126] C. Y. T. Tschang, R. Bergert, S. Mitic and M. Thoma, J Phys D Appl Phys **53,** 215202 (2020).

[127] G. Nayak, M. S. Simeni, J. Rosato, N. Sadeghi and P. J. Bruggeman, J Appl Phys **128,** 243302 (2020).

[128] D. R. Gunasegaram, A. B. Murphy, A. Barnard, T. DebRoy, M. J. Matthews, L. Ladani and D. Gu, Addit Manuf **46,** 102089 (2021).

[129] A. D. Kuypers and H. J. Hopman, J Appl Phys **67,** 1229 (1990).

[130] E. Kawamura, V. Vahedi, M. A. Lieberman and C. K. Birdsall, Plasma Sources Sci Technol **8,** R45 (1999).

[131] Y. Kihara, M. Tomura, W. Sakamoto, M. Honda and M. Kojima, 2023 Symposium on VLSI Technology and Circuits, (2023).

Chapter 2 : Description of the Models

This thesis is based on computational models that capture the gas phase dynamics and surface evolution of the coupled etch process. Due to the significant difference in relevant time and length scales, the coupled system consists of two discrete models representing the gas phase and surface evolution separately. The modeling suite used in this work is schematically shown in Figure 2.1.

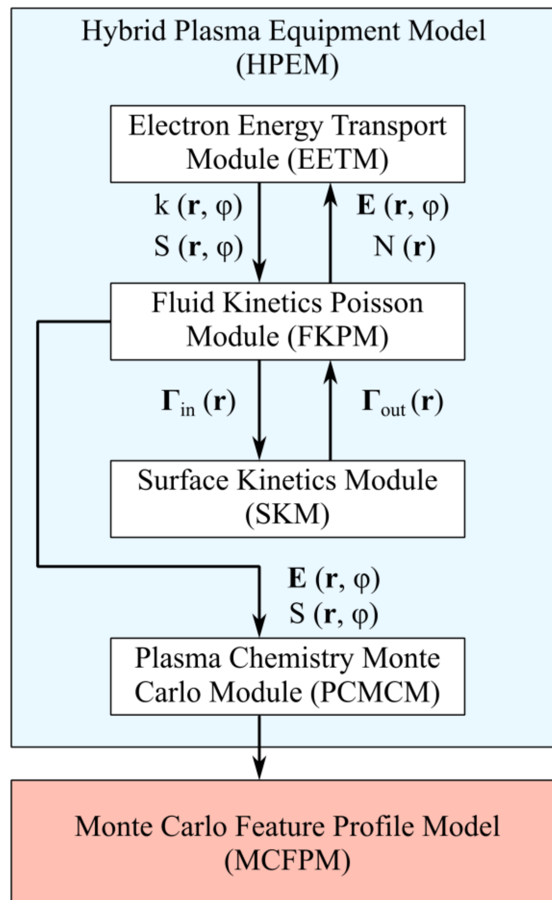

Figure 2.1: Flowchart of coupled modeling suite consisting of HPEM and MCFPM.

The Hybrid Plasma Equipment Model (HPEM) is used to simulate the reactor scale gas phase and is described in Section 2.1. The surface incident fluxes of electrons, ions and neutrals as well as their energy and angular distribution are generated by the HPEM and used as input for the feature scale surface model. The Monte Carlo Feature Scale Model (MCFPM) simulates the actual etch process in three dimensions and generates, among others, the temporal evolution of the feature geometry, composition and electric potential within it. It is described in Section 2.2.

2.1 Hybrid Plasma Equipment

The Hybrid Plasma Equipment Model (HPEM) is a 2-dimensional model which resolves plasma phenomena in a time-slicing approach and incorporates fluid treatment for all species with the option for limit kinetic representation of charged species. HPEM as a whole is based on a modular paradigm where each module addresses specific physical regime and is coupled to others by exchanging physical quantities – electric and magnetic fields, densities, rate coefficients etc. The major modules used in this work are the Fluid Kinetics Poisson Module (FKPM), the Electron Energy Transport Module (EETM), and the Plasma Chemistry Monte Carlo Module (PCMCM) [1].

The coarse program flow is depicted in Figure 2.1. The electron distributions relevant to their impact reactions are obtained in the EETM, by employing a kinetic description using a Monte Carlo approach. The electron impact reaction rates $k(\vec{r},\varphi)$ are used to determine source terms for electron impact reaction $S(\vec{r},\varphi)$. The spatially resolved source terms are used as inputs to the Fluid Kinetics Poisson Module (FKPM). FKPM calculates the densities $N(\vec{r})$, velocities $\vec{v}(\vec{r})$, and the temperatures $T(\vec{r})$ of the heavy as well as their reaction rate coefficients and source functions. The charged particle species densities are used to determine the local space charge density and based

on this, and the boundary conditions set by the metals (grounded or driven) Poisson's equation is solved to provide the electrostatic electric field $\overrightarrow{E_S}(\vec{r},\varphi)$ and the potential $\Phi_P(\vec{r},\varphi)$. The spatial field configuration is passed to the Plasma Chemistry Monte Carlo Module (PCMCM). PCMCM tracks the trajectories of select species using a kinetic Monte Carlo method and records their energy and angular distribution with which they hit certain surfaces (In this thesis it is exclusively used for the bottom mounted wafer).

The specific time step requirements of the respective modules can be different, so the A time slicing approach is employed in which the submodules communicate on the basis of a global iteration which is generally defined by the longest required timestep.

2.1.1 Electron Energy Transport Module (EETM)

The EETM calculates the rate coefficient from electron impact reactions $k(\vec{r},\varphi)$ and corresponding source function $S(\vec{r},\varphi)$ by using the electrostatic electric field $\vec{E}_S(\vec{r},\varphi)$, as well as heavy particle densities $N(\vec{r})$ provided by the FKPM. In this thesis The EETM then obtains the electron properties by using the electron Monte Carlo Simulation (eMCS) to compute electron energy distribution functions (EEDFs). This includes the treatment of secondary electrons that are emitted from surfaces subject to ion bombardment.

The eMCS is a fully kinetic approach in which electrons are represented by pseudoparticles. Pseudoparticle refers to an infinitesimally small cluster of particles that has physical properties (mass, charge etc.) that correspond to a large number of particles. This allows for kinetic treatment without the need to simulate every individual electron while still effectively reproducing macroscopic quantities such as number density charge density etc. The electrons are initialized according to a Maxwellian distribution. Spatially they are initially distributed according

to the background fluid ion density. In the electrostatic scenario, electrons are acted upon by the electric fields

$$\frac{d\vec{v}_e}{dt} = \frac{e}{m_e}\vec{E}, \tag{2.15}$$

where $\vec{v}_e$ is the electron velocity and $\vec{E}$ is the total local electric fields (electromagnetic and static). The electrons are first sectioned by energy into coarse non uniform bins, e.g., 0-5, 5-10, 10-50, 50-300, and 300-1000 eV. the lower energy ranges (< 10 eV) are typically associated with bulk electrons while the higher ones correspond to beam or secondary electrons which were accelerated by sheath electric field. Following the coarse sorting, the collision frequency is calculated on a finer bin resolution according to

$$\nu_i = \left(\frac{3\varepsilon_i}{m_e}\right)^{1/2} \sum_{j,k} \sigma_{ijk} N_j , \tag{2.16}$$

where ε_i is the average energy in bin *i*, σ_{ijk} is the cross-section of the species *j* of process *k* at energy ε_i, and N_j is the density of the species *j*. To ensure a constant time step without collision rate dependence, a null collision approach is applied in the eMCS, which yields a constant timestep $\Delta t = -\ln(r)/\nu_{mj}$, where *r* is a random number distributed within (0, 1) and is the maximum collision frequency in energy range *j*. A null collision frequency is defined as the difference between the maximum collision rate and the real collision frequency. Each timestep, based on a random number, the occurrence of a collision is checked. In the absence of a collision (a null collision) the electron velocity and energy remain unchanged. Otherwise, the electron energy is modified according to the inelastic or elastic nature of the collision and the electron trajectory is scattered [2]. To obtain the EEDFs, electron energies are recorded and binned by energy (i) and space (l)

$$F_{il}=\sum_j w_j \delta\left[\left(\varepsilon_i \pm \frac{1}{2}\Delta\varepsilon_i\right)-\varepsilon_i\right]\delta\left[\left(\vec{r}_l \pm \Delta r\right)-\vec{r}_l\right], \qquad (2.17)$$

where w_j is the relative particle weight, which is determined by

- the weight of the pseudoparticle i.e. the number of actual particles it represents,
- the time step used to advance the particle trajectory and
- spatial weighting.

After each time step the obtained EEDFs $f_e(\varepsilon,\vec{r})$ are normalized according to

$$\sum_i F_{ij}\Delta\varepsilon_i = \sum_i f_e\left(\varepsilon,\vec{r}\right)\varepsilon_i^{1/2}\Delta\varepsilon_i = 1. \qquad (2.18)$$

While the kinetic treatment for bulk electrons is optional, it is always performed for beam and secondary electrons as their distributions are always assumed to be non-Maxwellian and highly directional. They are tracked until they are removed via gas phase or surface collisions or until their energy falls below the lowest inelastic collision threshold in which case, they are transformed into bulk electrons by adding them to the bulk electron source term.

Kinetic treatment allows for highly precise tracking of electron properties that is entirely self-consistent and does not require any assumptions about their distribution. The quality of the kinetic approach is strongly dependent on the statistical quality which generally means that a large number of pseudoparticles is required. This can lead to high computational cost which, fortunately, is very compatible with parallel treatment which has been implemented into HPEM using the OpenMP API [3].

2.1.2 Fluid Kinetics Poisson Module (FKPM)

The Fluid Kinetics Poisson Module (FKPM) is responsible for the handling of the heavy particle densities, electron energy equation and the electrostatic potential. If the kinetic treatment of electrons is not required, alternatively the FKPM determines electron transport properties and

the electron rate coefficients by solving Boltzmann's equation for a range of values of the reduced electric field (E/N). The electron distribution function $f_e(\varepsilon, \vec{r}, \varphi)$ is obtained by solving the Boltzmann equation using the two-term approximation given by equation (1.7). A table is generated and its interpolated values are referenced during the execution of the code. Consequently, the electron temperature (T_e) is obtained using the electron power balance equation

$$\frac{\partial(\frac{3}{2}n_e k_B T_e)}{\partial t} = \nabla \kappa \nabla T_e + \nabla \cdot (\vec{\phi}_e T_e) = P_e \,, \tag{2.20}$$

with the Boltzmann constant k_B , the thermal conductivity κ the electron flux $\vec{\phi}_e$ and the total power deposited into electrons

$$P_e = \vec{j}_e \cdot \vec{E} = e\vec{\phi}_e \cdot \vec{E} \,. \tag{2.21}$$

The electron continuity equation (see Eq 1.10) is solved in either a drift-diffusion formulation given by

$$\vec{\phi}_e = e\mu_e n_e \vec{E} - D_e \nabla n_e \,, \tag{2.22}$$

where μ_e is electron mobility, and D_e is the electron diffusion coefficient or in the Scharfetter-Gummel (S-G) expression. The S-G method is widely used to describe the transport of charged particles in the fluid model [4–6]. With a S-G expression, the flux between the mesh points i and i+1 is

$$\vec{\phi}_{i+1/2} = \frac{\alpha \bar{D}[n_{i+1} - n_i \exp(\alpha \Delta x)]}{1 - \exp(\alpha \Delta x)} \,, \tag{2.23}$$

with

$$\alpha = -e\bar{\mu}\left(\frac{\Phi_{i+1} - \Phi_i}{\Delta x}\right), \tag{2.24}$$

where $\bar{D}$ is the averaged diffusion coefficient between vertex i and i+1, $\bar{\mu}$ and Δx are the averaged mobility and the length of this interval, and Φ_i is the potential on vortex i. To attain the heavy particle densities, the coupled system consisting of the continuity, momentum, and energy equations is solved. For species i with a source term S_i

$$\frac{\partial N_i}{\partial t} = -\nabla \cdot \vec{\phi}_i + S_i, \tag{2.25}$$

$$\frac{\partial \vec{\phi}_i}{\partial t} = \frac{\partial (N_i \vec{v}_i)}{\partial t} = -\frac{1}{m_i}\nabla(kN_i T_i) - \nabla \cdot (N_i \vec{v}_i \vec{v}_i) + \frac{q_i}{m_i} N_i (\vec{E}_s + \vec{v}_i \times \vec{B})$$

$$-\nabla \cdot \bar{\bar{\mu}}_i - \sum_j \frac{m_j}{m_i + m_j} N_i N_j (\vec{v}_i - \vec{v}_j) \nu_{ij}, \tag{2.26}$$

$$\frac{\partial N_i \varepsilon_i}{\partial t} = -\nabla \cdot \bar{\bar{\kappa}} \nabla T_i - p_i \nabla \cdot \vec{v}_i - \nabla \cdot (N_i \vec{v}_i \varepsilon_i) + q_i \vec{\varphi}_i \vec{E} - (\bar{\bar{\mu}}_i \nabla \cdot \nabla \vec{v}_i)$$

$$-\sum_{m,j} k_{mij} N_i N_j \varepsilon_i + \sum_{m,j,l} k_{mjl} N_j N_l \Delta \varepsilon_{mjl}, \tag{2.27}$$

where $\vec{\phi}$ is the flux, N is the density, $\vec{v}$ is the velocity, m is the mass, T is the temperature, $\bar{\bar{\mu}}$ is the viscosity, p is the pressure, and ε is the energy. Since the electrostatic potential is solely determined by the charge density and the boundary conditions, it is solved for using Poisson's equation

$$\nabla \cdot \left[\varepsilon \nabla \Phi(t + \Delta t) \right] = -\rho(t + \Delta t) = -\rho(t) - \Delta t \left. \frac{\partial \rho}{\partial t} \right|_{t+\Delta t}, \tag{2.28}$$

where ρ is the charge density. The total charge density is comprised of the surface charge on materials and the sum of all gas phase charge carries,

$$\rho(t) = \rho_m(t) + \sum_i q_i N_i(t), \tag{2.29}$$

where the first term is the charge density from the solid material, and the second term is the charge from the plasma. Employing a semi-implicit approach for solving Poisson's equation, allows the use of time steps Δt larger than the dielectric relaxation time, which would otherwise be required by explicit methods [7]. If Scharfetter-Gummel fluxes are used, the $\left.\frac{\partial \rho}{\partial t}\right|_{t+\Delta t}$ term can be written as

$$\left.\frac{\partial \rho}{\partial t}\right|_{t+\Delta t} = \frac{\partial \rho_m(t')}{\partial t} - q_{e,j}\nabla\cdot\left(\vec{\phi}_e(t) + \frac{\partial \vec{\phi}_e}{\partial \Phi}[\Phi_s(t+\Delta t) - \Phi_s(t)]\right)$$

$$-\sum_i q_i \nabla\cdot\left(\vec{\phi}_i(t) + \frac{\Delta t}{2}\frac{\partial \vec{\phi}_i(t)}{\partial t}\right), \tag{2.30}$$

where $q_{e,j}$ represents the charge of electrons and ions, respectively, Φ_S is the electrostatic potential. *t*' means that the charge density is evaluated at the current time step *t*, but the potential is evaluated at the time step $t+\Delta t$.

The Jacobian term $\frac{\partial \vec{\phi}_e}{\partial \Phi}$ from Eq. (2.30) is addressed via a perturbation method, where a small fractional potential change (typically = 5%) $\Delta\Phi$ is applied within Δt by solving two first-order partial derivatives of the electron flux with respect to the potential

$$\frac{\partial \vec{\phi}_{i,j}}{\partial \Phi_{i+1,j}} = \frac{\vec{\phi}_{i,j}(\Phi_{i+1,j} + \Delta\Phi_{i+1,j}) - \vec{\phi}_{i,j}(\Phi_{i+1,j})}{\Phi_{i+1,j}}, \tag{2.31}$$

where *i* and *j* are the coordinates of the mesh in the radial and axial direction. The discretized equations mentioned above are solved using either Successive-Over-Relaxation or direct sparse matrix method [8,9].

In addition to the plasma, the potential calculation includes all solid materials. The FKPM discriminates between two types of materials. *Dielectrics* are included in the solution or the potential and are thus defined by their charge density, conductivity and permittivity. The total

material charge is defined by the sum of charged particle fluxes impinging on it, the secondary electrons emitted from the surface, and the conduction current within the material.

Metals are considered to be free of internal electric fields and perfectly equipotential throughout their entire volume. Metal materials effectively act as Dirichlet boundary conditions where the magnitude of the potential is externally defined. On grounded metals it is set to 0 while the potential on powered materials is defined by the applied potential and, if directly connected to the blocking capacitor, the DC self-bias V_{dc}.

$$V\left(t+\Delta t\right)=V_{RF}(t)+V_{dc}\,, \tag{2.32}$$

where $V_{RF}(t)$ is the rf potential at time t. As discussed in the Introduction, V_{dc} is a function of the systems total asymmetry and is numerically determined by evaluating the total accumulated charge on the capacitor

$$V_{dc}=\frac{1}{C}\int\sum_{i}m_{i}\left[\sum_{j}\vec{\phi}_{j}(q_{j}+q\gamma_{ij})\cdot\hat{n}+\frac{\partial(\varepsilon\vec{E}\cdot\hat{n})}{\partial t}\right]dt\,, \tag{2.33}$$

where C is the magnitude of the blocking capacitance, i is the index of the materials, and j is the index of the particles. The first term on the right-hand side is the conduction current carried by ion and secondary electron fluxes. γ_{ij} is the secondary electron emission coefficient of material i when bombarded with particle j. $\hat{n}$ is the normal vector of the electrode surface. The second term is the displacement current on the electrode. The contribution of each metal surface is defined by whether it is directly connected to the grounded ($m_i = -1$) or powered side ($m_i = 1$) of the circuit. The power on the electrode is

$$\overline{P}_{rf}=\frac{1}{\tau}\iint V(t)\left[j\left(\vec{r},t\right)+\frac{d\left(\varepsilon\vec{E}\left(\vec{r},t\right)\right)}{dt}\right]dtdA\,, \tag{2.34}$$

where $V(t)$ is the time-dependent voltage, j is the conduction current density, τ is the rf integration time, and A is the surface area of the electrode. The second term in Eq. (2.34) is the displacement current on the electrode, where ε is the electrode permittivity and $\vec{E}$ is the time-varying electric field.

2.1.3 Surface Kinetics Module (SKM)

Surface interactions can significantly affect the discharge composition and by extension its dynamics as a whole either in the form of surface losses or chemical interaction. This is especially relevant for reactor setups with high surface to volume ratios as is the case with most CCP setups. Simple surface reactions can be addressed using the Surface Kinetics Module (SKM). Lasting surface modification and resulting changes to reactivity can be included via the Surface Site Balance Model (SSBM) within SKM. The SSBM tracks fractional surface site coverage and implements it into the reaction rate equations in the form of a variable sticking coefficient. Modification of the surface, for example by attachment and subsequential site blocking changes the local site coverage and sticking coefficient. [10]

The flux ($\vec{\phi}_{in}$) incident to a surface is provided by FKPM. A surface reaction generally has the form

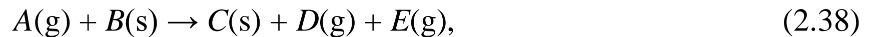

$$A(\mathrm{g}) + B(\mathrm{s}) \rightarrow C(\mathrm{s}) + D(\mathrm{g}) + E(\mathrm{g}), \quad (2.38)$$

where g stands for gas phase species, and s denotes the surface sites. The rate of ith reaction between gas phase species A and surface sites B on material m is:

$$R_{im} = \alpha_i \phi_{Am} \theta_{Bm}, \quad (2.39)$$

where α_i is the reaction rate of ith reaction, ϕ_{Am} is the flux of gas phase species A on material m, θ_{Bm} is the fractional coverage of surface site B on material m which is updated according to the sum of all relevant reaction rates.

The surface coverage ratio, of all the surface sites, is attained by integrating the rate equations of the corresponding sites using a third-order Runge-Kutta technique. The fractional surface coverage along with the gas phase fluxes from the surface, $\vec{\phi}_{out}$, is returned to the FKPM, through which the surface reactions feedback to the plasma. The reaction probability of gas phase species on the surface is the summation of the rates of reactions with it as a reactant.

2.1.4 Plasma Chemistry Monte Carlo Module (PCMCM)

The Plasma Chemistry Monte Carlo Module (PCMCM) is used to record the energy angular distributions of neutrals as well as ions incident on predefined relevant surfaces, most notably the wafer surface in this thesis. In the present scenario it is executed at the end of the simulation, after the plasma has reached a quasi-steady state and thus does not couple its information back into the gas phase simulation, though it can also be executed throughout the simulation when necessary. The PCMCM takes as input the particle densities and field configuration. As the name suggests, it is based on a kinetic Monte Carlo approach. Pseudoparticles are launched spatially distributed according to their density and at velocities based on their Maxwellian temperature distribution obtained from the FKPM. The particles are tracked until they hit a surface and are, if they are charged, subject to the forces of the electric field. Similar to the eMCS, collisions in the PCMCM are also handled using the null-collision technique.

The time step used to integrate the trajectory is based on the time to traverse a grid cell, the mean time between collisions and the RF period. It is set to be a fraction of the smallest of the aforementioned time scales; the fraction is usually between 0.2 and 0.5 within the plasma bulk.

Because the charged particles are accelerated to high energies as they cross the sheath potential this technique ensures an accurate representation of particle velocity and energy. Although generally, neutrals are close to thermally distributed as they make contact with the surface, it is possible to encounter ‘hot neutrals’ which can result from a highly energetic ion neutralizing in a charge exchange collision while maintaining most of its kinetic energy. As both ions and hot neutrals can carry a significant amount of energy to the surface both are recorded as the Ion/Neutral energy angular distribution (IEAD and NEAD respectively).

2.2 Monte Carlo Feature Profile Model (MCFPM)

The Monte Carlo Feature Profile Model (MCFPM) is a voxel-based feature scale simulator used to investigate the physics of feature scale etch processes. It has the option to model 2D and 3D processes, while in this thesis, only the 3D geometry is used [11,12]. In the MCFPM, the surface material is represented by cubic voxels. Each voxel preserves its assigned material properties. Pseudoparticles representing gas phase species are launched with energies and angles sampled from the EADs obtained from the HPEM. The trajectories of the incoming particles are integrated with charged particles subject to acceleration by electric fields, until a collision with a surface occurs. Based on the species of the colliding pair, the incident energy of the gas phase species, and the reaction probability, the outcome of the bombardment is determined. The specific surface reaction is chosen based on a stochastic Monte Carlo approach. Depending on the reaction, the voxel representing the surface site is removed (physical or chemical sputtering), chemically modified (passivation), or a voxel is added on top of the site (deposition). Species reflected from or produced at the surface, such as a sputter or chemical etch product, are returned to the gas phase, and their trajectories are tracked until they are consumed in a subsequent reaction at a surface or leave the feature. Although the capability exists in the MCFPM to have electron stimulated surface

chemistry or electron implantation, in this thesis, electrons do not modify the surface other than by depositing their charge.

Apart from the state of material identities, the MCFPM tracks a variety of other quantities such as the position of the etch front, the spatially resolved magnitude of surface fluxes, the change to energy and angular particle distribution as a function of feature height, the flux into and out of the simulation domain, the electric charge and potential (see 2.2.2) as well as the state of surface cross linking (see 2.2.3). The boundaries in r and y direction (horizontal as well as normal to the viewing plane, respectively) can be reflective or periodic while the top and bottom act as perfect sinks with the added caveat that the simulation is stopped once a particle reaches the lower boundary.

2.2.1 Energetic Particle Surface Reaction

For reactions between thermal neutrals and surface sites the reaction probability is usually assumed to be independent or the angular dependence and carried kinetic energy because it is negligibly small compared to relevant energy thresholds. However, for highly energetic particles, such as ions and hot neutrals, properties such as the rate of reaction, sputter yield and details of the scattering can strongly depend on the specific incident energy and angle [13–17]. In MCFPM this dependence is implemented by scaling the respective reaction probabilities with functional representations of angle and energy

$$p(E_i,\theta) = p_0\left(\frac{E_i - E_{th}}{E_r - E_{th}}\right)^n f(\theta), \tag{2.40}$$

where E_i is the particle energy, θ is the incident angle, p_0 is the reference probability, E_r is the reference energy, E_{th} is the threshold energy, and $f(\theta)$ is the angular dependent function. When

bombarding on the surface, energetic particles can cause physical sputtering or chemical enhanced etching, any of which may have different angular dependence.

In high aspect ratio features, energetic particles are likely to undergo collisions with the sidewall, during which they lose a fraction of their kinetic energy and are scattered. The energy of a particle after a surface collision E_s is

$$E_s(\theta) = E_i\left(\frac{E_i - E_c}{E_{ts} - E_c}\right)\left(\frac{\theta - \theta_c}{90^\circ - \theta_c}\right), \tag{2.41}$$

where E_{ts} is the threshold energy for specular scattering, E_c is the cut off energy of diffusive scattering, and θ_c is the lower angular boundary for specular scattering. Particles with $E_i > E_{ts}$ undergo a purely specular scattering event, i.e., the preserve all the energy and the exit angle equals the angle of incidence. Particles with $E_i < E_c$, or $\theta < \theta_c$ are treated as partially or fully be diffusively scattered, that is to say, they lose a fraction of their energy and gain a randomly assigned diffusive angular component.

2.2.2 Electrostatic Charging

Electrostatic charging of features results from ions or neutrals which neutralize upon striking surfaces and deposit their charge at the impact site. Charge is then retained on the voxel upon which it is deposited until neutralized by an opposing charge or transported via conductive charge transport. In the case of the removal of a charged voxel, the charge is retained in the mesh by redistributing it to the adjacent mesh cells. At sufficiently spatially disparate charge distribution, the resulting electric potential and electric fields affect the trajectories of charged particles via the addition of a Lorentz force term.

Based on the assumption that the time averaged flux of charged species onto the surface is net neutral, the electron flux is adjusted accordingly to enforce that criterion globally. Local charge

transport is not balanced explicitly and is computed self consistently. A detailed description of the MCFPM charging mechanism is given in Wang et al [18] and briefly summarized below. The time rate of change of charge density in numerical cell k, ρ_k (C/cm^3) is

$$\frac{d\rho_k}{dt} = \sum_i \frac{q_i w_i}{\Delta V_k} - \nabla \cdot \rho_k \mu_k \vec{E}, \quad (2.35)$$

where $\vec{E} = -\nabla\Phi$ is the electric field, Φ is the electric potential, and the sum is over incident particles i having weighting w_i and carrying charge q_i. The numerical cell has volume ΔV_k and the charge has electrical mobility μ_k in that cell. The electric potential is obtained by implicitly solving Poisson's equation, $-\nabla \cdot \varepsilon \nabla \Phi = \rho$, using finite volume techniques. Computationally, this is performed using the Successive-Over-Relaxation algorithm employing a parallel red-black technique. Each material included in the simulation is assigned a dielectric constant and mobilities for positive and negative charge transport, corresponding to the hole and electron mobilities. Compared to the other aspects of the simulation, directly solving Poisson's equation is extremely computationally expensive. In order to reduce the computational cost, the evaluation of the charge and potential is only performed after a large amount of charged particles have deposited their charge. Reflective boundary conditions for electric potential are used in the lateral (x-y) dimensions and a zero-gradient boundary condition is used on the top surface of the computational domain. The bottom of the computational domain is grounded. All positive ions neutralize upon their first collision with a surface and return as a hot neutral that, apart from no longer being affected by the electric field usually behave identically to their ion counterpart.

2.2.3 Crosslinking Module

A surface species' (especially polymer's) physical and chemical properties can be dependent on mutual links with neighboring species. This can result in changes to the reactivity

due to a lack of available bonds or more resistance to physical processes due to increases in total surface bond strength. Since these bonds can be broken by exposure to highly energetic particles or radiation, for example through exposure to plasma, this spatially discriminate activation can result in anisotropic shapes if deposits in the neck area of the feature. The general workings of the implanted crosslinking model are shown in Figure 2.2; the crosslink creation during the polymer deposition is depicted in the left column (a-d) and the removal in the right (e-g).

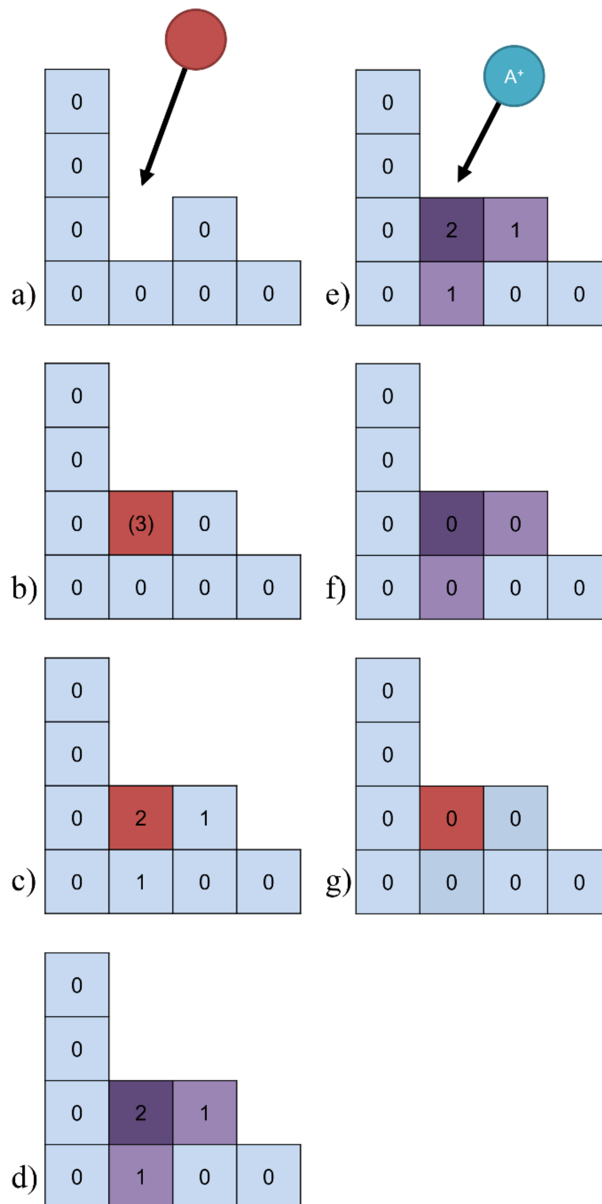

Figure 2.2: Schematic representation of the crosslinking process.

Crosslinking occurs during the deposition of eligible materials (Figure 2.2a) and b). Each material has a maximum number of crosslink partners associated with it, which is based on the number of available bonds (3 in the example depicted in Figure 2.2). During deposition bonds to random eligible cell neighbors can be formed, increasing the respective crosslink number, which is tacked for every cell (Figure 2.2c). If crosslinking occurred, the respective cell identities are changed to represent the physical differences and incur the changes to the physical properties cell (Figure 2.2d).

Crosslinks can be broken by impinging particles such as ions, hot neutrals and photons (Figure 2.2e) The bond breaking is represented by incrementing the affects surface cell's bond number (Figure 2.2f) and its reversion back to an unlinked state (Figure 2.2g).

2.3 References

[1] M. J. Kushner, J Phys D Appl Phys **42,** 194013 (2009).

[2] S. H. Song and M. J. Kushner, Plasma Sources Sci Technol **21,** 055028 (2012).

[3] L. Dagum and R. Menon, IEEE Computational Science and Engineering **5,** 46 (1998).

[4] R. Chandra, Morgan Kaufmann (2001).

[5] C. M. Snowden, Published in **1986** in Singapore by World scientific 222 (1986).

[6] D. L. Scharfetter and H. K. Gummel, IEEE Trans Electron Devices **16,** 64 (1969).

[7] P. L. G. Ventzek, T. J. Sommerer, R. J. Hoekstra and M. J. Kushner, Appl Phys Lett **63,** 605 (1993).

[9] W. H. Press, S. A. Teukolsky, W. T. Vetterling and B. P. Flannery,

[10] D. Zhang and M. J. Kushner, Journal of Vacuum Science & Technology A **19,** 524 (2001).

[11] A. Sankaran and M. J. Kushner, Journal of Vacuum Science & Technology A **22,** 1242 (2004).

[12] C. M. Huard, Y. Zhang, S. Sriraman, A. Paterson, K. J. Kanarik and M. J. Kushner, Journal of Vacuum Science & Technology A: Vacuum, Surfaces, and Films **35,** 031306 (2017).

[13] C. F. Abrams and D. B. Graves, J Appl Phys **86,** 2263 (1999).

[14] C. F. Abrams and D. B. Graves, J Appl Phys **86,** 5938 (1999).

[15] G. S. Oehrlein, P. J. Matsuo, M. F. Doemling, N. R. Rueger, B. E. E. Kastenmeier, M. Schaepkens, T. Standaert and J. J. Beulens, Plasma Sources Sci Technol **5,** 193 (1996).

[16] Y. Yamamura and H. Tawara, At Data Nucl Data Tables **62,** 149 (1996).

[17] P. J. Kelly and R. D. Arnell, Vacuum **56,** 159 (2000).

[18] M. Wang and M. J. Kushner, J Appl Phys **107,** 023309 (2010).

Chapter 3 : Electric Field Reversals Resulting from Voltage Waveform Tailoring in Ar/O_2 Capacitively Coupled Plasmas Sustained in Asymmetric Systems

3.1 Introduction

As described in Chapter 1, plasma etching of dielectrics such as SiO_2 and Si_3N_4 is an integral process in nearly all micro- and nanometer scale electronics fabrication [1] and the etching of high aspect ratio (HAR) features is becoming an increasingly critical process due to the development of 3-dimensional structures such as 3D-NAND memory which requires contact holes through more than 256 alternating layers of SiO_2 and Si_3N_4 with a total aspect ratio of up to 100.[2,3] Typical operating conditions are tens of mTorr gas pressure with hundreds of watts to many kW power deposition over a 30 cm diameter wafer. [4,5] These conditions produce ion fluxes to the wafer of 10^{15}-10^{16} $cm^{-2}s^{-1}$.[6] To enable these ion fluxes (or hot neutral fluxes after ion scattering from sidewalls) to reach the bottom of HAR features with sufficient energy and narrow angular distribution to continue the etch, applied voltages to the substrate are as high as 5 kV while endeavoring to minimize ion collisions inside the sheath.[7]

The electric field in the sheath above the wafer points towards the wafer surface during the majority of the RF cycle, accelerating positive ions to high energies and narrow angular spreads. This same electric field confines electrons to the bulk plasma. It is only during a small fraction of the RF cycle at which time the sheath collapses that electron flux from the bulk plasma reaches the wafer.

In a CCP of the type used for plasma etching of dielectrics in microelectronics fabrication (pressures of tens of mTorr, frequencies of 1 – 100 MHz), the net charged flux to dielectric surfaces in contact with the plasma must sum to zero over the RF cycle in the steady state,

$$\int_0^T \left(\Gamma_e(t) - \Gamma_i(t)\right) dt = 0 \qquad (1)$$

where, T is the RF period. $\Gamma_e(t)$ and $\Gamma_i(t)$ are the time dependent fluxes to the surface of electrons and positive ions, acknowledging that the flux of negative ions is negligible in the absence of pulsing. The electric field in the sheath and presheath usually point towards surfaces to accelerate ions out of the plasma and confine electrons. It is only during a small portion of the anodic part of the RF cycle that the sheath voltage decreases sufficiently to enable electrons to reach the substrate. These electrons arrive at the substrate with largely thermal, isotropic velocity distributions. Voltage waveform tailoring (VWT) is technique that is able to generate directional (anisotropic), high energy electron fluxes onto the substrate through promoting an electric field reversal (EFR) in the presheath above the substrate [8,9]. EFR refers to the electric field in the presheath pointing into the plasma, as opposed to pointing towards the surface. In VWT, a non-sinusoidal voltage is applied to the substrate, typically using several harmonics of a fundamental frequency.[8] EFR in the presheath ultimately results from the requirement that the time average of positive and negative fluxes to the substrate must balance. Only during the sheath collapse during the anodic part of the cycle are electrons able to diffuse to the surface. Under certain conditions, this diffusive electron transport may not be sufficient to satisfy the local charge balance. This lack of ability for diffusive electrons to reach the surface in sufficient numbers may be due to short sheath collapse times, thick sheaths, or magnetically or collisionally hindered transport. For these conditions, negative space charge in the presheath produces an EFR, which slows the transport of ions and speeds the transport of electrons towards the wafer. Electric field reversal has been observed computationally

as well as experimentally.[8–11]

With its ability to produce anisotropic energy and angular distributions (EADs) of electrons onto the substrate which can penetrate deeply into HAR features, EFR produced by voltage waveform tailoring has been proposed as a (partial) remedy for charging inside HAR features.[8] In principle, if the flux of positive ions and negative electrons that penetrate deeply into features can be balanced, the detrimental effects of intra-feature charging can be minimized. Since the production of EFR requires manipulating the sheath potential during the RF cycle, the ion EADs are also affected, and so independent control of the EADs of both electrons and ions is a challenge.

The dynamics of VWT, and EFR in particular, are sensitive to the geometry of the plasma reactor and the electronegativity of the plasma. In this chapter, we discuss results from a computational investigation of electric field reversal in electronegative CCPs sustained in Ar/O_2 mixtures in a plasma reactor similar to those used in HVM. In these simulations, the power deposition is held constant as frequency content is varied to acknowledge that in HVM, power (and not voltage) is usually what is controlled in HAR etching. The consequences of EFR on the EADs of ions and electrons onto the wafer surface are discussed. We found that the consequences of VWT are not limited to electron dynamics but also affect the EADs of ions mainly through the electrical asymmetry effect and the resulting change in the DC self-bias. The observed electric field reversal is almost entirely due to the inertia limited lack of electron conduction current and the decrease in sheath collapse time.

The computational platform used in this investigation, the Hybrid Plasma Equipment Model (HPEM) and has been previously discussed in Chapter 2. The outcome of the investigation for the Ar-only base case is discussed in Section 3.2 with a focus on the influence of the phase angle φ as of the harmonic components of the waveform. In Section 3.3 the influence on EFR of

added oxygen, an electronegative species, to the gas mixture is discussed. Concluding remarks are in Section 3.4.

The reaction mechanism used for pure Ar plasmas is the same as that described in Ref. [12]. The mechanism for Ar/O_2 plasmas is a subset of that described in Ref. [13] which involves only Ar and O containing species. The mechanism for reactions between only O, O_2 and its excited and ion species is described in Ref. [14]. To decrease computational cost, excited states for O and O_2 were lumped into a single state.

A schematic of the cylindrically symmetric CCP reactor used in this investigation is shown in Figure 3.1a).

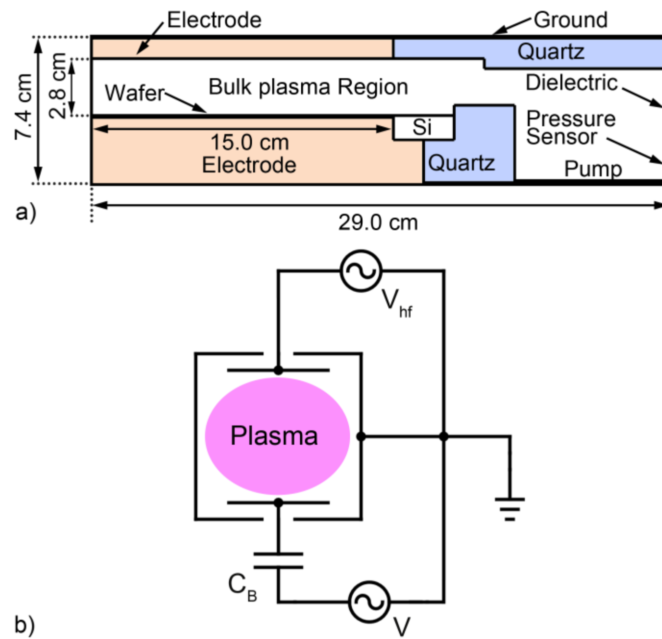

Figure 3.1: Geometry and circuit used in the model. a) Schematic of the dual frequency capacitively coupled plasma reactor used in this investigation. b) Equivalent circuit diagram of the reactor. Source power at 80 MHz is applied to the top electrode. The 1 MHz tailored waveform is applied to the bottom electrode.

The reactor, modeled after multi-frequency CCPs used in in industrial etch applications, consists of two parallel plate electrodes with a diameter of 300 mm separated by a 2.8 cm gap. The

top electrode also serves as a showerhead gas inlet. A 0.7 mm thick silicon wafer is mounted on the bottom electrode. A focus ring made of silicon and quartz to improve discharge uniformity surrounds the wafer. The dielectric constants of these components are $\varepsilon/\varepsilon_0 = 4$ for the outer quartz ring and $\varepsilon/\varepsilon_0 = 11.8$ for the Si ring. While the conductivity of the quartz is negligible, that of the Si wafer is 0.05/Ω-cm. The feedstock gas is a mixture of Ar and O_2 flowing at 500 sccm through the top electrode, with oxygen fractions of 0 to 50%. The reactor pressure is held constant at 40 mTorr at the location of the pressure sensor near the pump port. This is accomplished by throttling the rate of pumping. Secondary electron emission due to ion bombardment of surfaces is included with a coefficient of 0.15.

The wafer is naturally included in the self-consistent electric potential and current calculations by specifying its permittivity and conductivity, whose values are adjusted during execution of the model to accurately represent the actual thickness of the wafer. The conductivity of the wafer is large enough that the voltage drop across the wafer is only a few volts, and does not meaningfully affect the DC bias.

A general electric circuit diagram is shown in Figure 3.1b. The VWT power supply is connected to the bottom electrode through a blocking capacitor C_B of 500 nF. In principle, in the quasi-steady state, the DC bias should be independent of the value of the blocking capacitor provided that the RC time constant of the plasma-capacitor series impedance is large compared to transients in current. The capacitance used here is a balance of there being an acceptably short charging time and long enough RC time constant so that there is little variation in the DC bias during the RF cycle. It may appear in the reactor schematic that the high frequency electrode is touching a grounded metal. Computationally, a zero-conductivity dielectric lies between the two metal materials. As a result, only displacement current flows between the metals that are separated

by what appears to be a perfect capacitor. This is analogous to a dark-space shield. Averaged over a radio frequency cycle, there is no net power transfer nor net current passing between the two metals.

To maintain a relatively constant plasma density, 100 W of power is coupled into the discharge through the top electrode using a sinusoidal voltage V_{hf} with a frequency of 80 MHz. To control the dynamics of charged particles impinging on the wafer surface, a customized voltage waveform, V(t), is applied to the bottom electrode. The waveform is described by equation (1.56) with frequency f_0 = 1 MHz and N = 4 consecutive higher harmonics. The power coupled through the bottom electrode was held constant at 1 kW by adjusting V_0.

3.2 The Ar Base Case

V_{hf} and V_0 are shown in Figure 3.2a as a function of the phase angle φ. The voltage waveforms for these cases are shown in Figure 3.3d for phase shifts of φ = 0°, 45°, 90°, 135° and 180°. The high frequency power is constant at 100 W. Since the phase shift only applies to the tailored waveform on the bottom electrode and the plasma density remains fairly constant, V_{hf} also remains relatively constant for all φ, varying by less than 10%. Even with the low frequency power being constant at 1 kW, due to the changes to the electron dynamics in the sheath region, there is some variation in V_0, increasing from 1296 V to 1650 V or about 27%.

The DC self-bias as a function of the phase angle φ is shown in Figure 3.2b for the argon base case conditions. The decrease in the magnitude of the DC self-biases (less negative) with increasing phase angle φ can be directly attributed to the EAE. At φ = 0° with $|V_{max}| > |V_{min}|$ (see Figure 3.3d) the electrical asymmetry of the applied voltage is at its maximum, and the contribution of the EAE to the DC bias is most negative. The asymmetry is zero when φ = 90° with $|V_{max}| = |V_{min}|$ (Figure 3.3d) where the contribution of the EAE to the dc bias is also zero. The asymmetry is at

its minimum at $\varphi = 180°$ with $|V_{max}| < |V_{min}|$ (see Figure 3.3d), at which point the contribution of the EAE to the DC bias is most positive.

The axial components of the electric field between the two electrodes, $E_z(z, t)$, radially averaged across the wafer, are shown in Figure 3.3a for phase shifts of $\varphi = 0°$, 45°, 90°, 135° and 180°. The electric fields are plotted as a function of time during a single 1 MHz cycle. The dotted line in the images is the $E_z(z, t) = 0$ contour. The respective voltage waveforms are shown in Figure 3.3d.

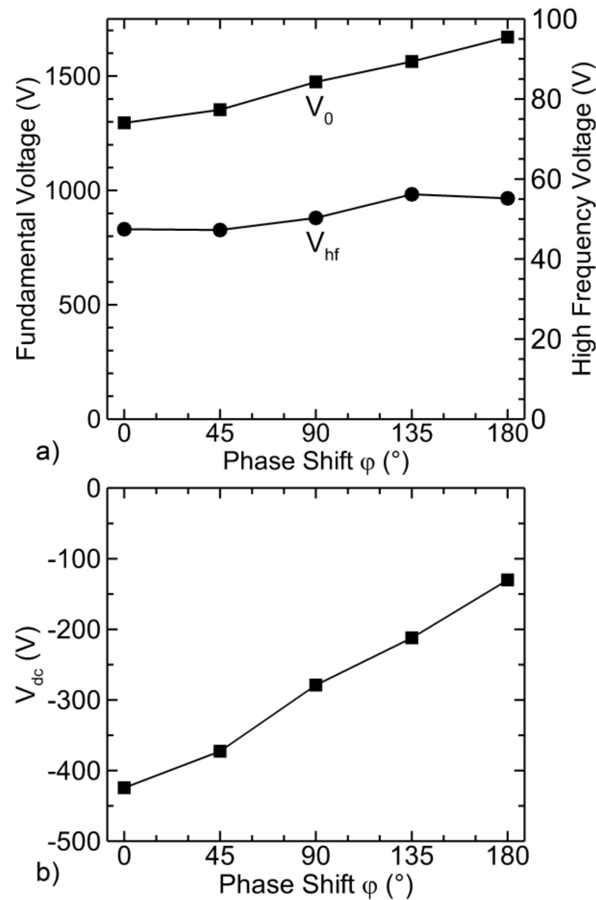

Figure 3.2: Plasma properties as a function of phase angle for the pure argon plasma with a constant high frequency power of 100 W and constant bias power of 1 kW. a) Applied voltage amplitudes for the high frequency source (V_{hf}) and amplitude of the low frequency bias (V_0). Top and bottom electrode. b) DC self-bias.

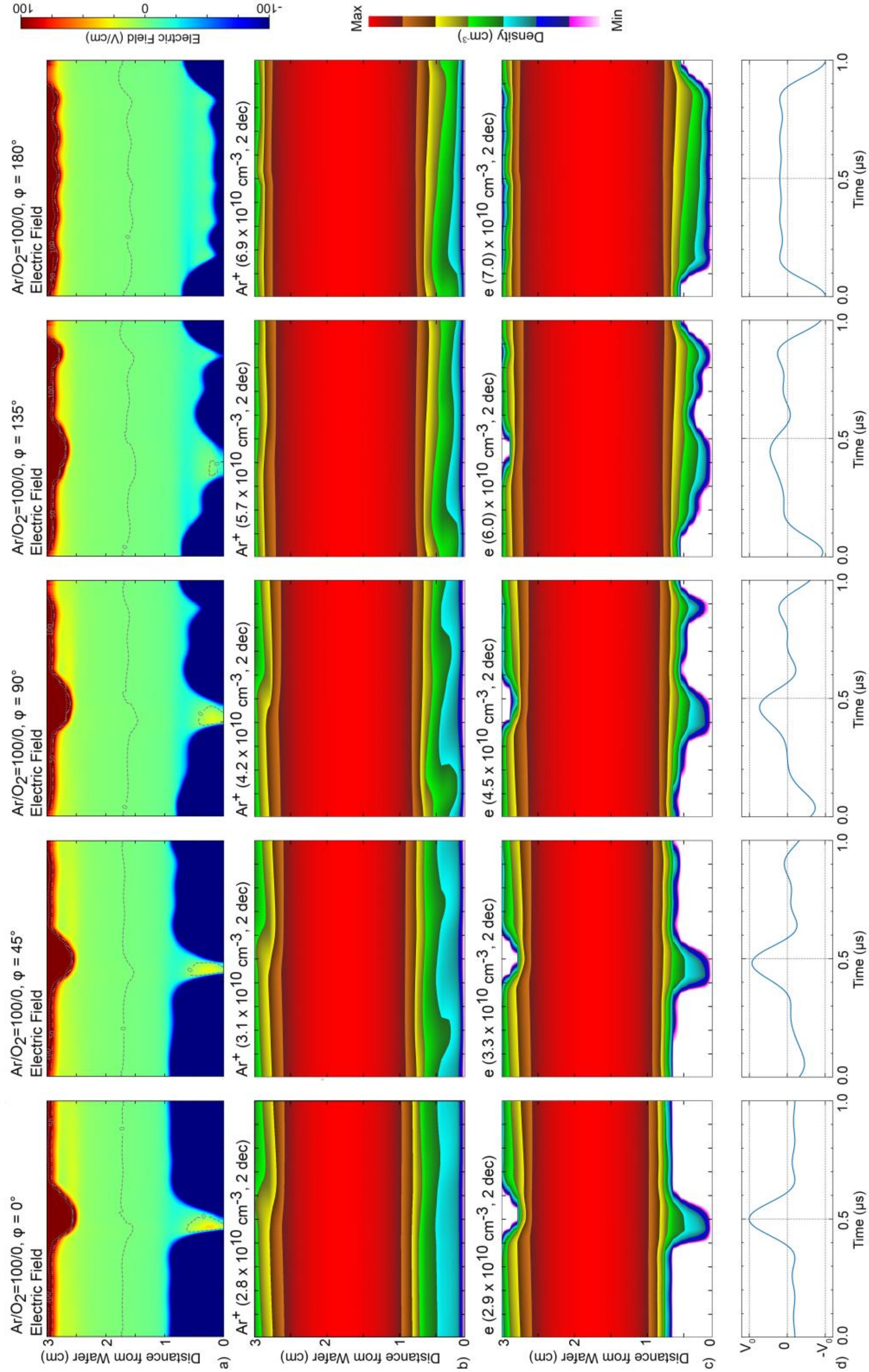

Figure 3.3: Plasma properties for the pure argon plasma averaged across the wafer as a function of height above the wafer and time during the low frequency,1 MHz cycle. Values are shown (left-to-right) for phase angles of $\varphi = 0$, 45, 90, 135, 180°. a) Axial component of the electric field, b) Ar^+ density, c) electron density and d) applied voltage waveform on the substrate. The Ar^+ and electron densities are plotted on a log-scale spanning 2 decades with the maximum value noted in each image.

In plasmas which do not have EFR, $E_z(z, t)$ in the sheath at the bottom electrode will point towards the electrode at all times, which corresponds to a negative value of E_z in these images. However, even with pure argon, there can be an EFR at the peak of the positive excursion of the applied voltage waveform. With $\varphi = 0°$ the EFR occurs during the sheath collapse at around 0.5 μs when the applied voltage is at its maximum positive value and a positive electric field component (pointing in +z direction) is present. This EFR results, in part, from the short duration of the positive voltage excursion of the waveform. During more than 80% of the RF cycle, the applied voltage is negative, with there being less than 20% of the RF cycle being amenable to electron collection. Given that the electrons are mostly thermal, diffusion alone would not provide sufficient current to the wafer to balance the ion current during this short period. An additional drift component is required, which for electrons requires a net electric field pointing upwards (positively), away from the electrode. The reversal in the electric field provides additional electron acceleration to overcome the confining potential and inertial effects to enable the charge and current balance conditions. The generation of the EFR is a natural outcome of the calculation due to solution of Poisson's equation and the charge transport equations.

The densities of Ar^+ and electrons as a function of height averaged across the wafer are shown in the Figure 3.3b and Figure 3.3c as a function of time and for different values of φ. Maximum ion densities increase from 2.8×10^{10} cm^{-3} for $\varphi = 0°$ to 6.9×10^{10} cm^{-3} for $\varphi = 180°$. Recall that the power deposition at both frequencies is being held constant. With a decrease in the magnitude of V_{dc} (less negative) with increasing φ (see Figure 3.2), less fractional power is dissipated by ion acceleration through the sheath. The response of the system is to increase V_0 and V_{hf} (the latter being a small increase) to increase plasma density to maintain a constant power. In spite of its large mass, there is a small response of the Ar^+ density profile to the sheath dynamics,

with ions being accelerated into the lower sheath during the local maxima of the cathodic portion of the low frequency RF cycle. Ions are accelerated into the upper sheath during the local maxima of the anodic cycle. These responses are afforded, in part, by the low fundamental frequency of 1 MHz. Such responses would not be expected, for example, at 13.56 MHz. In contrast, the spatial distribution of electron density in the sheaths is strongly modulated during both the RF cycle and with different values of φ. Electrons are excluded from the lower sheath during the local maxima of the cathodic portion of the low frequency RF cycle and excluded from the upper sheath during local maxima of the anodic portion of the cycle.

A phase angle of $\varphi = 0°$ produces the "peak" waveform (Figure 3.3d, left-most sub-image) which approximates a delta function for higher harmonic orders ($N \rightarrow \infty$). As such, it creates the shortest period of sheath collapse having the largest time derivate in electric field (dE_z/dt), both of which favor EFR. With larger phase angles, this abrupt sheath collapse becomes more gradual and longer, providing electrons with more time to diffuse to the surface, which reduces the need for EFR to balance current. With $\varphi = 180°$, the voltage waveform resembles the "valley" waveform (Figure 3.3d, right-most sub-image) which results in a plasma sheath that is at its minimum voltage and width most of the time – the opposite of the $\varphi = 0$ waveform. This change in φ from 0 to 180° produces a decrease of the EFR, with its elimination for $\varphi = 180°$. A portion of this reduction (and eventual elimination) of the EFR with increasing phase angle is due to the decrease of the magnitude of the DC self-bias (less negative) which reduces electron repulsion from the sheath. Although the instantaneous electron diffusion flux from the bulk plasma may appear to be sufficient to balance current, that flux is actually limited by the ambipolar-like electric fields in the presheath and by the finite time required for electrons to cross the sheath. The secondary electrons emitted from the surface generate a net positive current into the wafer when the sheath expands,

increasing the requirements to balance current by the bulk electrons during sheath collapse.

The EADs of electrons incident onto the wafer for the pure argon plasma for different phase angles φ are shown in Figure 3.4a. The mean electron energy and angle of incidence are shown in Figure 3.4b as a function of phase angle.

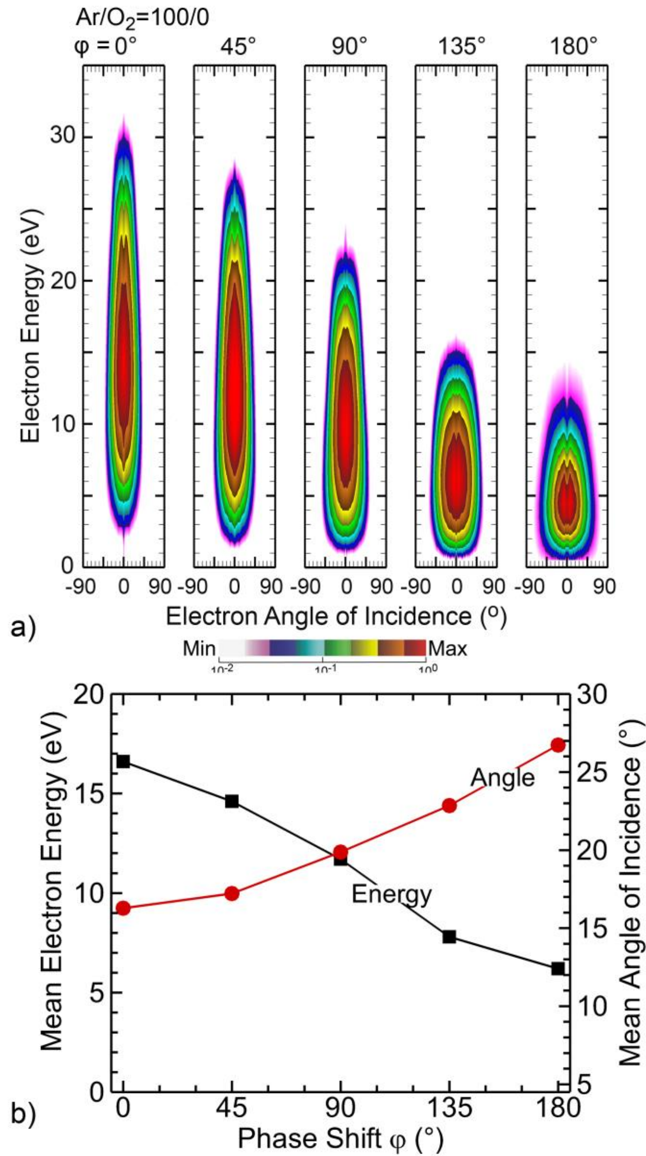

Figure 3.4: Properties of electrons incident onto the wafer for the pure argon plasma. a) Electron energy and angular distributions for different phase angles plotted on a log-scale spanning 2 decades. b) Mean electron energy and mean electron angle of incidence as a function of phase angles.

The trends in the maximum strength of the EFR translate to the EADs. The electron temperature in the bulk plasma is 3.1- 3.3 eV, which is approximately the temperature of the electrons incident onto the wafer for $\varphi = 180°$ which has the minimum EFR. This similarity, including the broad angular distribution, indicates that the electrons are simply diffusing into the sheath with there being little drift component. With decreasing φ, conditions which increase the EFR, there is an increase in directional electron acceleration onto the wafer. With decreasing phase angle φ, the EADs increase in energy while becoming more narrow in angle. As the phase angle decreases from $\varphi = 180°$ to 0°, the mean energy of electrons incident onto the wafer increases from 7.1 eV to 17.3 eV, while the mean angle of incidence decreases from 26.8° to 15.1°. These results suggest that high fluxes of directional electrons onto the substrate can be generated by EFR.

3.3 EFR with Ar/O_2 Gas Mixtures

The addition of oxygen to the argon gas mixture enables the generation of negative ions and the transition of the electropositive Ar discharge to an electronegative plasma. The densities of Ar^+, O_2^+, O^- and electrons, as well as the discharge electronegativity are shown in Figure 3.5 as a function of the O_2 mole fraction in the inlet flow for otherwise the base-case conditions with $\varphi = 0°$. Electronegativity in this case is the ratio of densities of [O^-]/[e].

Through dominantly dissociative electron attachment of O_2 to form O^-, the electron density decreases with increasing O_2 inflow while that of O^- increases. At 50% O_2, the total negative charge in the plasma bulk is nearly equally due to O^- and electrons. Total positive ion density decreases from 2×10^{10} cm^{-3}, for the pure Ar discharge to 1.4×10^{10} cm^{-3} at 50% O_2, a consequence of more power being dissipated in non-ionizing collisions with the increase in O_2 fraction. The total discharge electronegativity increases from to 1.05 at 50% O_2.

Due to the change in electron density and the subsequent changes in power deposition, the DC self-bias is a sensitive function of the Ar/O_2 ratio. V_{dc} as a function of the voltage phase angle φ for Ar/O_2 ratios of 100/0, 90/10, 75/25 and 50/50 is shown in Figure 3.6a. The general trend of decreasing magnitude of V_{dc} (less negative) with increasing phase angle φ occurs for all gas mixtures. This trend is a result of the EAE.

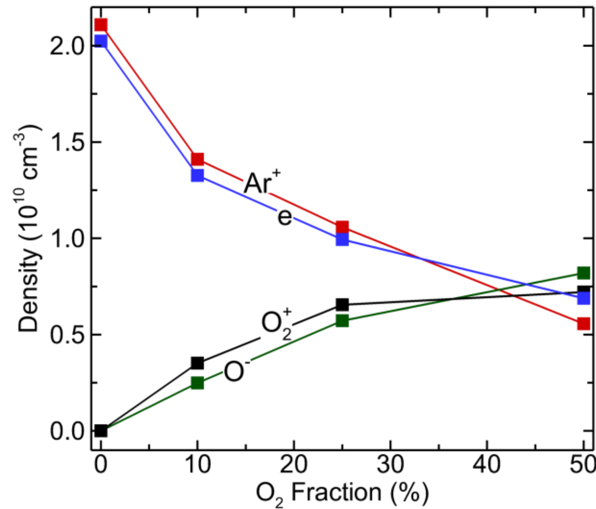

Figure 3.5: Spatially averaged densities of Ar^+, e^-, O_2^+ and O^-, and electronegativity of Ar/O_2 plasmas as a function of the O_2 mole fraction with a phase angle of $\varphi = 0°$.

A second major trend is an increase of the magnitude of V_{dc} (more negative) with increasing O_2 mole fraction. Due to the electronegativity of O_2 containing plasmas and dissipation of power in non-ionizing collisions with O_2, increasing the mole fraction of O_2 requires higher applied voltages to maintain a constant power deposition. The total voltage amplitude V_0 as a function of the phase angle φ for different Ar/O_2 ratios is shown in Figure 3.6b. At $\varphi = 0°$, V_0 increases by approximately 18% from 1300 V with Ar/O_2 = 100/0 to 1545 V at Ar/O_2 = 50/50. For a given electrical or geometrical asymmetry V_{dc} is proportional to V_0, and so on this basis alone, the magnitude of the V_{dc} should increase (become more negative) with increasing O_2 mole fraction.

The axial component of the electric field between the two electrodes, $E_z(z, t)$, radially

averaged across the wafer is shown in Figure 3.7. Each column represents a constant phase angle with φ = 0°, 45°, 90°, 135° and 180°. Each row in turn represents cases at constant gas ratio and varying phase angle with for Ar/O_2 = 100/0 (Figure 3.7a), 90/10 (Figure 3.7b), 75/25 (Figure 3.7c) and 50/50 (Figure 3.7d). The voltage waveforms are shown in the bottom row (Figure 3.7e). The dotted line in the images is the $E_z(z, t) = 0$ contour.

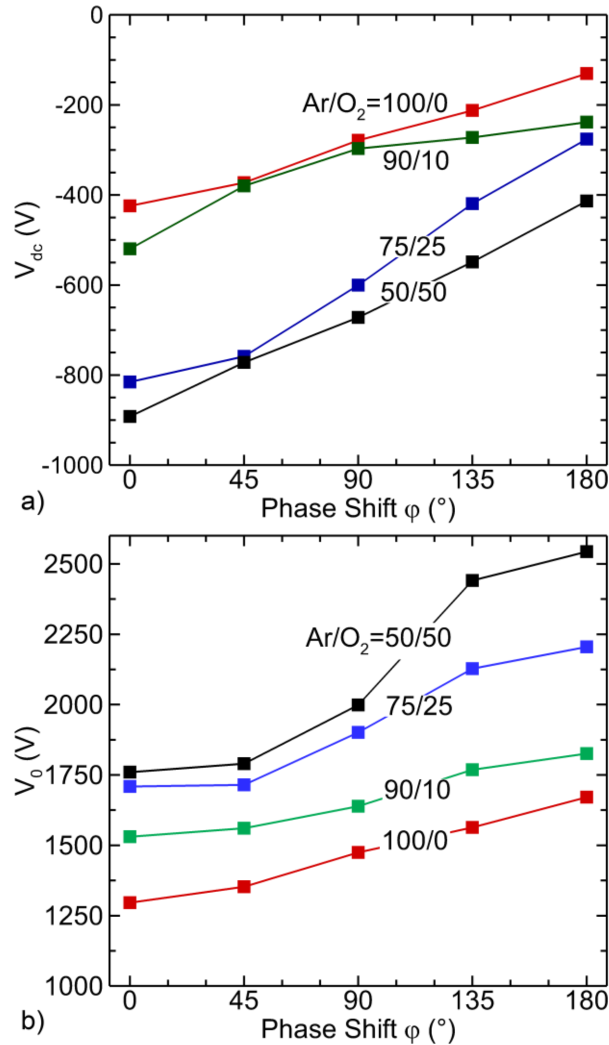

Figure 3.6: Plasma properties as a function of phase shift φ for different Ar/O_2 ratios when keeping source and bias powers constant. a) DC self-bias produced on the powered substrate. b) Applied voltage amplitude V_0.

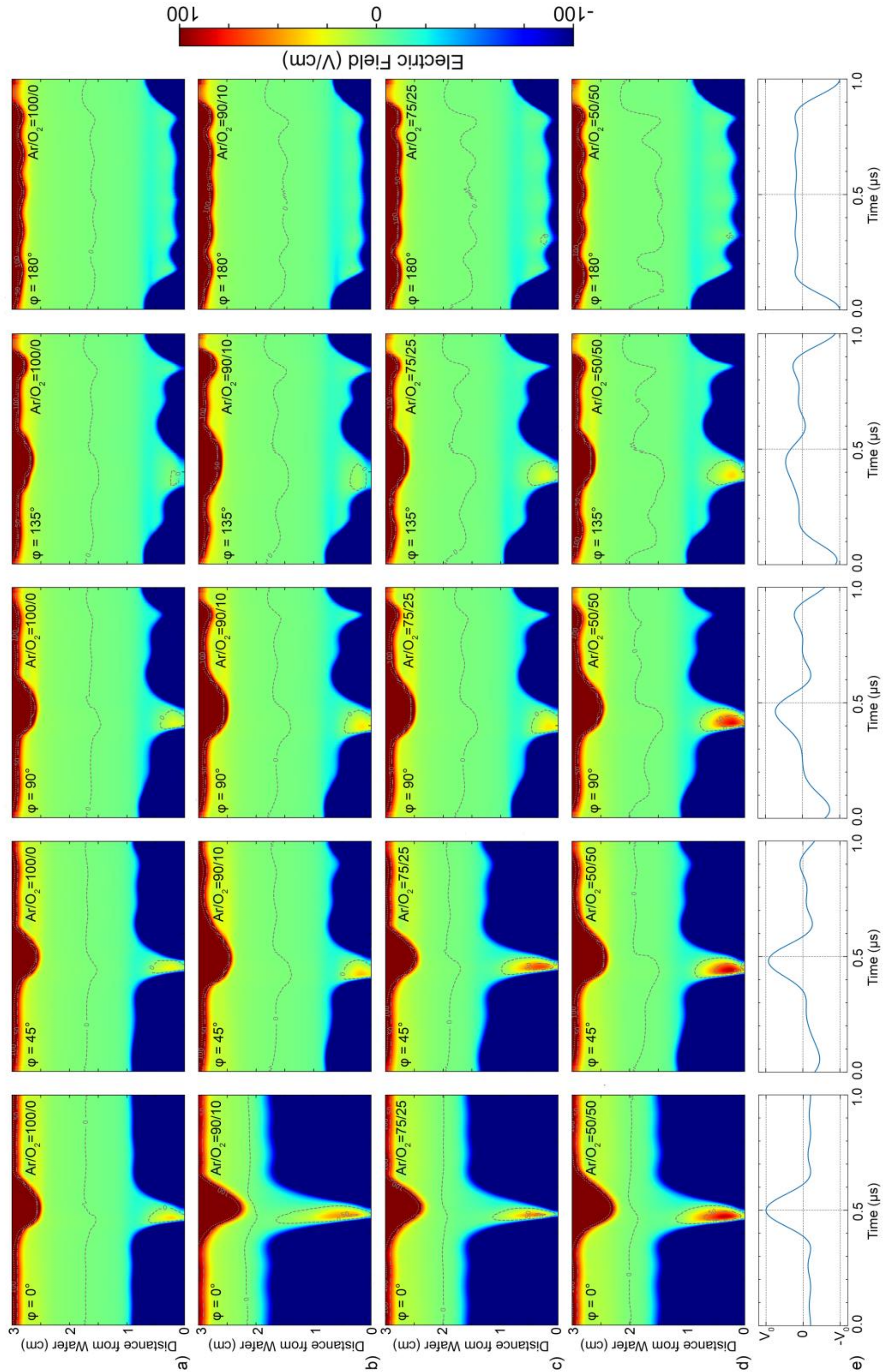

Figure 3.7: Radial average of the vertical component of the electric field as a function of time during a single 1 MHz cycle and distance from bottom electrode different gas mixtures. Ar/O_2 = a) 100/0, b) 90/10, c) 75/25, d) 50/50. e) Normalized applied voltage V_0. Results are shown for phase shifts of (left-to-right columns) φ = 0, 45, 90, 135 and 180°. The dotted line is for E = 0, the separation between negative electric fields pointing down and positive pointing up.

The magnitude of the EFR increases with increasing oxygen mole fraction for all phase angles φ. The EFR has a peak magnitude of 47 V/cm (E/N = 3650 Td, 1 Td = 10^{-17} V-cm^2) in the absence of oxygen for φ =0, and a peak value of 94 V/cm (7300 Td) with Ar/O_2 = 50/50 while the EFR extends deeper into the plasma. In pure argon, the sheath thickness during the cathodic phase is 9.5 mm and the extent of the EFR from the substrate during the anodic phase is 6 mm. For Ar/O_2 = 50/50, the sheath thickness is 15 mm and the extent of the EFR is 12 mm. Due to the lower applied sinusoidal voltage no electric field reversal occurs at the top electrode. In general, EFR occurs when electron transport to the surface has a limited time window during the anodic portion of the RF cycle or is impeded by other means. Since mobility μ_i is inversely proportional to mass and the generation of negative O^- ions produces a decrease in the electron density, the average mobility of negative charge carriers decreases. This decrease in mobility then requires a larger extracting electric field in the form of the EFR. With increase in O_2 fraction from zero to 50%, the electron density decreases to about 40% of that in pure argon. With the sum of the positive ion fluxes decreasing to 80% of their values with pure argon, the EFR increases by a factor of 2 (47 V/cm to 94 V/cm) to extract the needed electron current.

As with the pure argon base cases, the magnitude of the EFR decreases with increasing phase angle for all Ar/O_2 gas mixtures. The temporal modulation of the zero electric field contour in the bulk plasma also varies with phase angle. This modulation indicates that the effects of the VWT are not limited to the sheath and could be responsible for small modulation that occurs in electron temperature. To some degree, this modulation is required by current continuity. Displacement current through the sheath is proportional to dE/dt – current which must be matched largely by conduction current in the bulk plasma. As dE/dt in the sheath varies with phase angle, there must be variation in conduction current in the bulk plasma which in turn requires modulation

in the bulk electric field. The modulation of the E=0 contour is more pronounced at higher Ar/O_2 ratios, indicating that the changes to the sheath potential structure (leading to more displacement current) which increase with the O_2 content extend beyond the immediate sheath region to modulate conduction current in the bulk plasma.

The time dependent densities of Ar^+, O^- and electrons are shown in Figure 3.8 for $\varphi = 0°$ and Ar/O_2 = 50/50. Due to their low mobility and their being trapped in the positive plasma potential, the O^- ions (Figure 3.8b) do not follow the modulated sheath and are confined to the bulk plasma at all times. There is some perturbation of the O^- density at the peak of the cathodic cycle at the top electrode, however the negative ions do not significantly contribute to the transport of negative charge to the surface. In contrast to the stationary O^- density profiles, the electron density profile, shown in Figure 3.8c, responds quickly to the applied potential. The electrons are confined to the plasma bulk during most of the RF period and only extend to the surface at the time of sheath collapse at 0.5 μs. As a result of this discrepancy in dynamic behavior between electrons and O^-, increasing the mole fraction of O^- in the system effectively reduces the transport of negative charges to the surface, thereby necessitating a larger EFR during the portion of the RF cycle during which there is sheath collapse.

With an increase of the magnitude of the DC self-bias V_{dc} and the applied voltage V_0, the sheath potential and sheath width increase. The maximum width of the sheath increases from approximately 9 mm for pure argon to 15 mm for Ar/O_2 = 50/50. This increase in sheath width increases collisionality (reducing electron mobility) and increases the distance electrons need to traverse during the sheath collapse in order to reach the surface. Both effects limit electron transport and increase the need for and magnitude of the EFR.

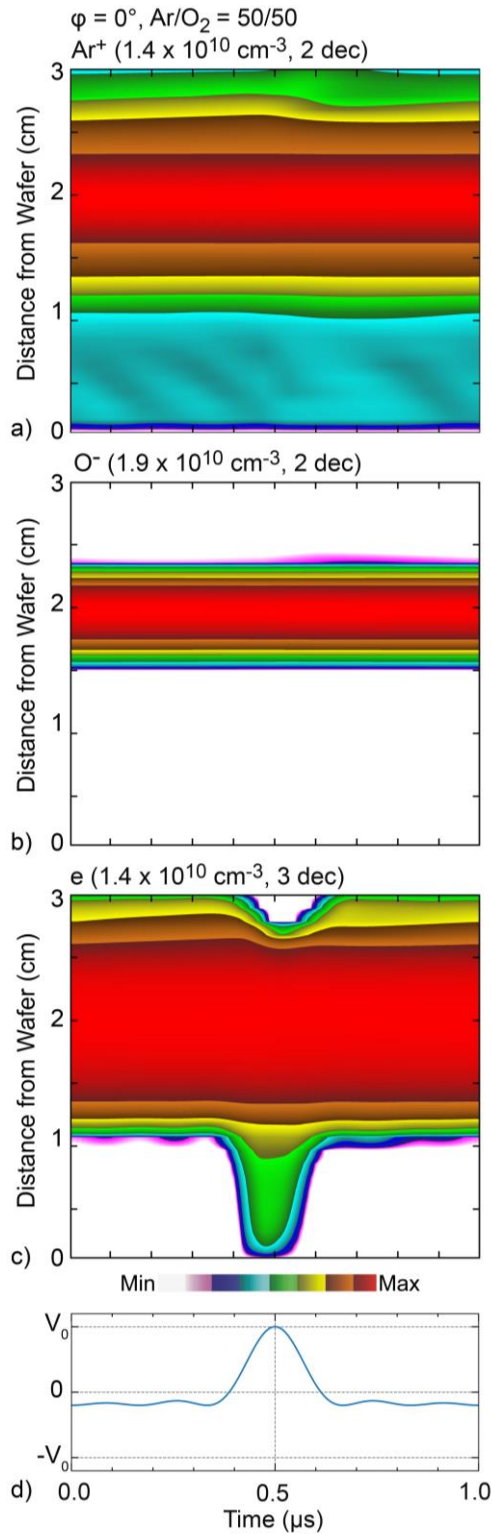

Figure 3.8: Plasma properties for Ar/O_2 = 50/50 and a phase shift of $\varphi = 0°$. a) Radial average of the Ar^+ density as a function of time during a single 1 MHz RF cycle plotted on a log-scale over 2-decades. b) O^- density (log-scale, 2-decades) and c) electron density (log-scale 3-decades). The maximum density is noted in each image. d) e) Normalized voltage amplitude V_0

These two mechanisms (the reduction in the density of mobile charge carriers by the increasing negative ion density and the confinement of electrons by the applied tailored voltage waveform) at least partially add, thereby increasing the magnitude and extent of spatial penetration of the EFR. Comparing the electric field configurations over the range of phase angles reveals a strong dependence of the EFR on gas mixture. With Ar/O_2 = 50/50, the magnitude of the EFR decreases with increasing phase angle – decreasing from 94 V/cm at $\varphi = 0°$ to 11 V/cm at $\varphi = 180°$, a total change of 83 V/cm. For the same phase angle shift for the pure argon plasma, the change in magnitude of the EFR is only 11 V/cm.

The interaction between the two mechanisms producing EFR also results in enhanced electron acceleration towards the wafer. The electron EADs incident onto the wafer are shown in Figure 3.9 for $\varphi = 0°$ (maximum EFR) and for $\varphi = 180°$ (minimum EFR) for different Ar/O_2 feedstock mixtures. With $\varphi = 180°$, the EFR is nominal, resulting in the electron EADs being largely thermal with average energies < 10 eV for bulk electron temperatures of 3.2 – 3.5 eV. There is a small increase in incident electron energy and narrowing of angular distribution for Ar/O_2 = 50/50 where the magnitude of the EFR begins to increase. With $\varphi = 180°$ when most of the negative charge is carried by heavy O^- ions, electron transport is still sufficient to balance positive ion transport due to the sheath being collapsed during most of the RF cycle. There is little additional electron acceleration by an EFR necessary to balance the positive ion flux.

With $\varphi = 0°$, the EFR is well established with peak magnitudes reaching nearly 100 V/cm for Ar/O_2 = 50/50. The maximum electron energy incident onto the wafer extends from 30 eV for pure argon to 100 eV for Ar/O_2 = 50/50. The angular distribution narrows from ±45 degrees for pure argon to a ±20 degree spread for Ar/O_2 = 50/50. The wide range of electron energy, while the minimum energy is nearly constant for oxygen containing mixtures, suggests that the electron

attracting sheath is the equivalent of the thin-sheath-limit for accelerating ions into the electrode. That is, the electron transit time across the sheath is short compared to the RF period, and so electrons are accelerated to the instantaneous sheath potential. The lower energy component of the EAD is likely sustained by continuing thermalization of electrons through collisions inside the sheath.

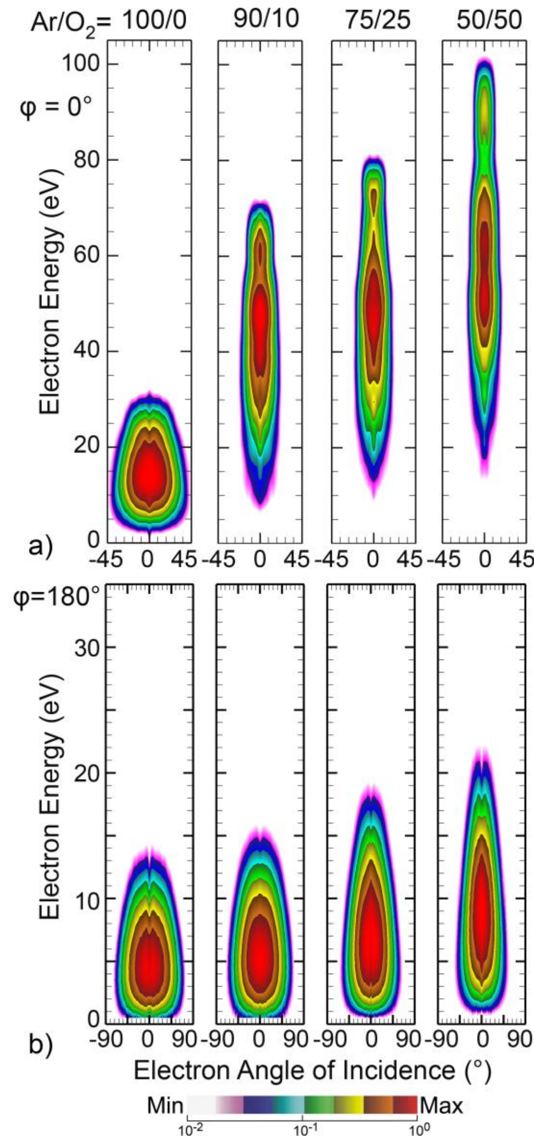

Figure 3.9: Electron energy and angular distributions incident onto the wafer surface for different Ar/O_2 ratios plotted on a log-scale over 2 decades with phase shifts of a) $\varphi = 0°$ and b) $\varphi = 180°$. The EAD increases in energy and narrows in angle with increasing O_2 fraction, an effect that is most prominent for a) $\varphi = 0°$.

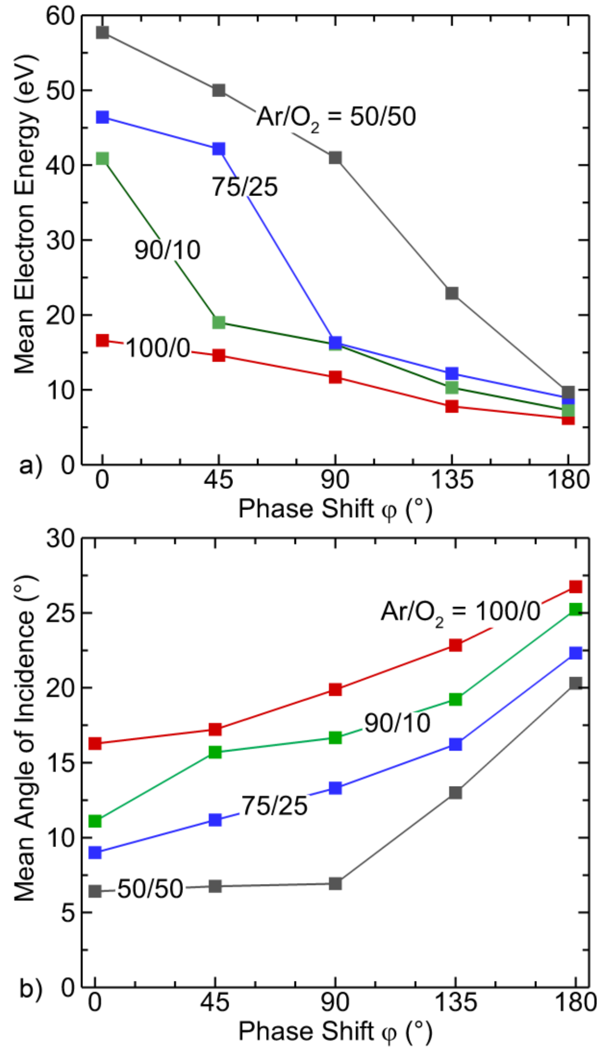

Figure 3.10: Properties of the electron velocity distribution incident onto the wafer for different Ar/O_2 ratios as a function of phase shifts φ. a) Mean electron energy and b) mean angle of incidence. Decreasing phase angle increases the incident electron energy and narrows the angular distribution, with the effect being most prominent for large O_2 mole fractions.

The mean electron energies at the wafer surface as a function of the phase angle, $\bar{\varepsilon}(\varphi)$, for different Ar/$O_2$ mixtures are shown in Figure 3.10a. As with the EADs, the trends correlate with the magnitude and depth into the plasma of the EFR. Mean energies for φ = 180° have a nominal dependence on gas mixture, extending from 6.2 eV for pure argon to 9.7 eV for Ar/O_2 = 50/50. Although this is a change of a factor of 1.5, the absolute change is only 3.5 eV. Mean energies for

φ = 0° extend from 16.7 eV for pure argon to 57.7 eV for Ar/O_2 = 50/50, an increase by a factor of 3.4 and absolute change of 41 eV. The same mechanisms producing a decrease in mean energy produces a decrease in the mean angle with which electrons strike the waver, as shown in Figure 3.10b as a function of the phase angle and gas mixture. For a given Ar/O_2 mixture, the mean angle increases with increasing φ. As with the mean energy, these changes are most pronounced at the highest oxygen content. For Ar/O_2 = 50/50 the mean angle increases from 6.4° at φ = 0° to 20.3° at φ = 180°, a 3-fold increase.

3.4 Concluding Remarks

The use of voltage waveform tailoring (VWT) to generate and control electric field reversals (EFRs) during the sheath collapse in low pressure capacitively coupled RF plasmas sustained in Ar/O_2 mixtures was computationally investigated. The purpose of this investigation is to assess the potential of this technique to accelerate electrons into sub-micron HAR etch features to compensate positive surface charging inside these structures. The effects of the Ar/O_2 feed gas ratio as well as voltage waveforms on the electron energy-angular distributions (EAD) incident onto the wafer surface were investigated while keeping the power deposition constant, as would be the practice in industry. To maintain the plasma density and reduce its dependence on the voltage waveform, a high frequency RF voltage was applied to the top electrode. The substrate bias waveform consisted of a sinusoidal signal and its first 4 harmonics with the even harmonics having a variable phase shift φ. The strength of the EFR increases with the O_2 mole fraction and with a decrease in φ. The correlation with the O_2 mole fraction is a consequence of the electronegative nature of the oxygen. The increase in O_2 mode fraction reduces the electron density while increasing negative ion density, which results in a decrease in the average negative charge carrier mobility. To maintain constant power, a larger applied voltage is required.

The consequences of the phase angle on EFR can be attributed to two major effects: i) the electrical asymmetry effect is maximum at $\varphi = 0°$ ("peak" waveform), leading to a large DC self-bias (most negative) and thick sheath and ii) the time that the sheath collapses is minimized at $\varphi = 0°$ and maximized at $\varphi = 180°$. Both of these effects enhance the EFR. Since the ion flux to the substrate must be balanced by electrons on a time average while electron transport to the substrate by diffusion is insufficient to do so in the presence of these transport limiting factors.

For a fundamental driving frequency of 1 MHz and a power of 1 kW applied to substrate, the bias waveform enables significant control of the electron energy and angle distributions onto the wafer surface. The relative and absolute changes in mean electron energy were strong functions of the Ar/O_2 feed gas ratio and most pronounced in the Ar/O_2 =50/50 mixture, while being significant in all configurations that were investigated. The fact that electronegative gases increase the magnitude of the EFR, and its ability to accelerate electrons into the wafer, suggests that process gas compositions used in semiconductor plasma etching processes, which often contain strongly electronegative species, can potentially profit from this mechanism as well.

The details of plasma etching processes critically depend on the ion energy and angular distributions onto the wafer. Although VWT is able to control the electron EADs onto the wafer, this cannot be done independently of also changing the ion EADs. Changes in the VWT configuration change the DC bias which translates into changing the average ion energy onto the wafer. The shape of the ion EAD will depend on the number of harmonics and the phase angle. Nevertheless, some of the scaling of the EAD described in this work could allow for favorable synergies with current trends in semiconductor manufacturing. Higher applied voltages, as used in plasma etching of HAR features, combined with a voltage waveform resembling the peak-waveform, will produce high energy, narrow angle fluxes of electrons into the wafer surfaces.

These fluxes have the properties required to address intra-feature charging.

To evaluate the efficacy of VWT in the context of actual plasma etching processes, it is important to investigate relevant process conditions using halogen containing gas mixtures combined with feature scale simulations that include the effects of the electron and ion EADs on charge accumulation, feature deformation and depth limited etch rates. There are still open questions with respect to the feasibility of plasmas sustained by complex waveforms at very high powers and the technical difficulties related to power matching, filtering, phase locking and metrology as well as economic considerations.

Due to its potential versatility, future implementations of VWT may be not limited to conventional CCPs but could find application in different contexts such as in inductively coupled plasmas. These applications could be for similar surface charge remediation on biased electrodes or the prevention of material erosion near the antennas caused by high energy ions in E-mode operation during pulsed operation. A broader set of waveform configurations should be investigated as the physical mechanisms discussed here are, in principle, not dependent on any specific waveform. These investigations may include the use of non-consecutive harmonics, pulsed higher harmonics, transient phase shifts or entirely non-harmonic waveforms.

3.5 References

[1] V. M. Donnelly and A. Kornblit, Journal of Vacuum Science & Technology A: Vacuum, Surfaces, and Films **31,** 050825 (2013).

[2] H. Tanaka, M. Kido, K. Yahashi, M. Oomura, R. Katsumata, M. Kito, Y. Fukuzumi, M. Sato, Y. Nagata, Y. Matsuoka, Y. Iwata, H. Aochi and A. Nitayama, Digest of Technical Papers - Symposium on VLSI Technology 14 (2007).

[3] Y. Li, IEEE Solid-State Circuits Magazine **12,** 56 (2020).

[4] B. Wu, A. Kumar and S. Pamarthy, Journal of Applied Physics **108,** 51101 (2010).

[5] S. Rauf and A. Balakrishna, Journal of Vacuum Science & Technology A: Vacuum, Surfaces, and Films **35,** 021308 (2017).

[6] G. Le Dain, A. Rhallabi, C. Cardinaud, A. Girard, M.-C. Fernandez, M. Boufnichel and F. Roqueta, Journal of Vacuum Science & Technology A **36,** 03E109 (2018).

[7] J. C. Wang, W. Tian, S. Rauf, S. Sadighi, J. Kenney, P. Stout, V. S. Vidyarthi, J. Guo, T. Zhou, K. Delfin, N. Lundy, S. C. Pandey, S. Guo and G. S. Sandhu, Plasma Sources Sci Technol **27,** 94003 (2018).

[8] P. Hartmann, L. Wang, K. Nösges, B. Berger, S. Wilczek, R. P. Brinkmann, T. Mussenbrock, Z. Juhasz, Z. Donkó, A. Derzsi, E. Lee and J. Schulze, J Phys D Appl Phys **54,** 255202 (2021).

[9] U. Czarnetzki, D. Luggenhölscher and H. F. Döbele, Plasma Sources Sci Technol **8,** 230 (1999).

[10] Y. X. Liu, Q. Z. Zhang, J. Liu, Y. H. Song, A. Bogaerts and Y. N. Wang, Appl Phys Lett **101,** 114101 (2012).

[11] S. Sharma and M. M. Turner, J Phys D Appl Phys **47,** 285201 (2014).

[12] P. Tian and M. J. Kushner, Plasma Sources Sci Technol **24,** 34017 (2015).

[13] S. Huang, C. Huard, S. Shim, S. K. Nam, I.-C. Song, S. Lu and M. J. Kushner, Journal of Vacuum Science & Technology A **37,** 031304 (2019).

[14] D. S. Stafford and M. J. Kushner, J Appl Phys **96,** (2004).

Chapter 4 : Voltage Waveform Tailoring for High Aspect Ratio Plasma Etching of SiO_2 using $Ar/CF_4/O_2$ Mixtures: Consequences of Ion and Electron Distributions on Etch Profiles

4.1 Introduction

In this Chapter we discuss results from a computational investigation of a multi-frequency CCP sustained in an $Ar/CF_4/O_2$ mixture using a geometry similar to those found in HVM. High frequency power applied to the top electrode is used to sustain the plasma while VWT is used to define the low-frequency bias voltage applied to the bottom electrode. The consequences of the electrical asymmetry effect and the electric field reversal on the IEADs and EEADs onto the wafer surface are discussed. The resulting charged and neutral particle fluxes and distributions are then used in self-consistent simulations of etching a HAR feature into SiO_2 to investigate the ability of VWT to control feature properties.

We found that in spite of the complicating factors of geometry, gas mixture and multiple frequencies, VWT allowed for effective control of IEADs and EEADs onto the wafer, though this control could not be produced independently. Optimizing the waveform to produce a desired EEAD inevitably affects the IEAD. Peak and mean energies of positive ions and of electrons onto the wafer are strong functions of the shape of the applied voltage waveform. With the narrow angle and energetic EEADs produced by VWT, our investigation did show a decrease in intra-feature charging, as measured by a decrease in the positive electrical potential. However, the overall characteristics of the final etch feature were dominated by the ion dynamics.

Synthetic changes to only the EEADs resulted in minor changes of the final etched feature.

For example, there were not significant differences in feature quality between an isotropic, thermal EEAD onto the wafer corresponding to an electron temperature of a 3-4 eV, and the narrow, energetic EEAD produced by VWT. We attribute this result to the fact that thermal electrons are accelerated into the feature by the electric fields produced by the positive, in-feature electric potential. Ultimately, in a quasi-steady state, the flux of positive and negative charge into the feature must be equal. This is achieved by producing a positive potential in the feature, which then accelerates thermal electrons into the feature. The narrow energetic EEADs produced by VWT are also accelerated into the feature. However, their initially higher wafer directed velocities require a smaller positive potential in the feature to achieve the needed flux balance. The end result is a decrease in the intra-feature potential relative to that produced with thermal electrons that is approximately equal to the average energy of the VWT produced EEAD.

The computational platform used for the reactor scale plasma transport, the Hybrid Plasma Equipment Model (HPEM) and the feature scale model, the Monte Carlo Feature Profile Model are described in Chapter 2. The reactor scale setup is described in Section 4.2 and the feature scale setup is described in Section 4.3. The influence of phase angle φ of the voltage waveform on charged particle distributions onto the wafer and etch profiles with low bias power is discussed in Section 4.4 and with high bias power is discussed in Section 4.5. Concluding remarks are in Section 0.

4.2 Description of the Reactor Scale Model

A schematic of the cylindrically symmetric CCP reactor used in this investigation is shown in Figure 4.1. The reactor, modeled after multi-frequency CCPs used in industrial HVM applications, consists of two parallel plate electrodes with a diameter of 300 mm separated by a 2.8 cm gap. A silicon wafer is mounted on the bottom electrode and a showerhead gas inlet is

distributed across the top electrode. A focus ring made of silicon and quartz to improve discharge uniformity surrounds the wafer. The dielectric constants of these components are $\varepsilon/\varepsilon_0 = 4$ for the outer quartz ring and $\varepsilon/\varepsilon_0 = 11.8$ for the Si ring. While the conductivity of the quartz is negligible, that of the Si wafer is 0.05/Ω-cm. The feedstock gas $Ar/CF_4/O_2$ = 75,/15/10 flows at 500 sccm through the top electrode. The reactor pressure is held constant at 40 mTorr at the location of the pressure sensor near the pump port by throttling the rate of pumping.

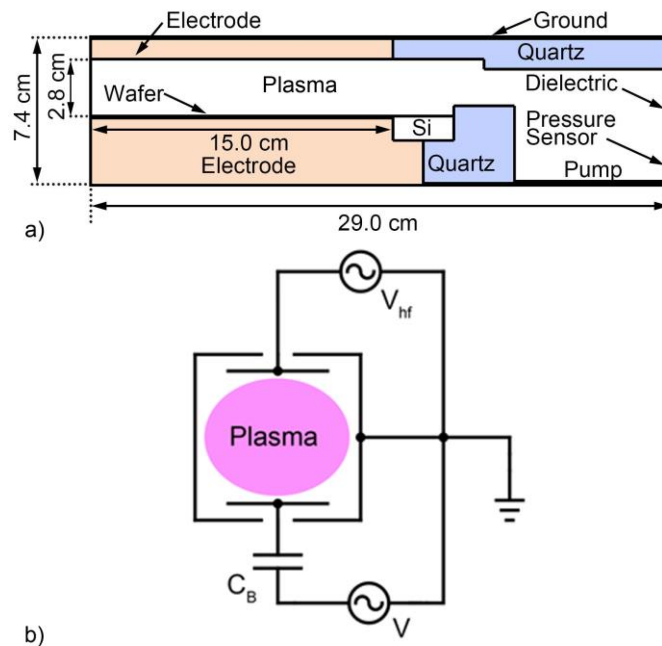

Figure 4.1: Schematics of the reactor. a) The two frequency CCP has the VWT power applied to the lower electrode and a sinusoidal, 80 MHz waveform applied to the top. b) Electrical schematic of the system. From F. Kruger et al, Plasma Sources Sci. Technol. **30**, 085002 (2021). Reproduced by permission of IOP Publishing Ltd.

The VWT power supply is connected to the bottom electrode through a blocking capacitor of 500 nF. In principle, in the quasi-steady state, the DC bias should be independent of the value of the blocking capacitor provided that the RC time constant of the plasma-capacitor series impedance is large compared to transients in current. The capacitance used here is a balance of there being an acceptably short charging time and long enough RC time constant so that there is

little variation in the DC bias during the RF cycle.

Sheath properties are in part a function of plasma density at the edge of the sheath which then determines sheath thickness. To maintain a relatively constant plasma density and to minimize sheath variation based on changes in plasma density, 500 W is coupled into the plasma through the top electrode using a sinusoidal voltage waveform with a frequency of 80 MHz. This power was maintained by continually adjusting the amplitude of the voltage at 80 MHz.

To control the dynamics of charged particles impinging on the wafer surface, a customized voltage waveform, V(t), was applied to the bottom electrode. The waveform is described by equation (1.56) with frequency f_0 = 1 MHz and N = 4 consecutive higher harmonics,

Here, V_0 is the total applied voltage amplitude, k is the harmonic order, N is the total number of frequencies, and the relative phase shift of each harmonic frequency k is φ_k. In this work the number of harmonics is N = 5. The consequences of VWT were investigated by varying the phase shift of the even harmonics φ for k = 2, 4. The power coupled through the bottom electrode, P_0, was initially held constant at 1 kW by adjusting V_0.

4.3 Description of the Feature Scale Model

In this study, we investigated the plasma etching of SiO_2 in a $Ar/O_2/CF_4$ gas mixture using the MCFPM which is described in Chapter 2. A detailed description of the reaction mechanism is given by Huang et al. [1]. Generally, all incoming ions or hot neutrals resulting from neutralization of ions when striking surfaces can physically sputter every material according to the incident particles mass, angle and energy as well as the surface binding energy of the material. Radical C_xF_y species can lead to the deposition of polymer, the main contributor to sidewall passivation, which in turn is removed by sputtering and etching by oxygen radicals. C_xF_y radicals can react with the SiO_2 surface to create a layer of $SiO_2C_xF_y$ complexes, significantly lowering the binding

energy and making the complex easier to chemically sputter.

The electric potential in the feature was computed by collecting charge on surfaces and solving Poisson's equation. The relative permittivity for SiO_2 used in solution of Poisson's equation was $\varepsilon_r = 4.0$, and for photoresist, polymer and $SiO_2C_xF_y$ complexes was $\varepsilon_r = 3.0$. The electric potential then provides electric fields used to advance the trajectories of charged particles. All positive ions neutralized when striking a surface, and if reflected, continued as a neutral. Electrons were collected on surfaces with unity probability. For this study, the SiO_2 and photoresist had essentially zero conductivity (10^{-10}/Ω-cm). Polymer (5×10^{-6}/Ω-cm) and $SiO_2C_xF_y$ complexes (1×10^{-6}/Ω-cm) had finite but small conductivity. These conditions generally resulted in charge being resident only on surfaces or buried under polymer or redeposited etch products if deposition occurred on top of charged surfaces.

The geometry used for the feature evolution is shown in Figure 4.2. The feature is a trench consisting of a 3000 nm thick SiO_2 layer over a Si stop-layer, covered by 100 nm thick photoresist with a 100 nm opening. This geometry produces an aspect ratio of about 30 for an etched trench down to the stop layer. The simulation was performed in 3-dimensions as a finite depth trench. The mesh consists of 60 cells wide by 750 cells tall by 10 cells deep, producing cubic voxels with 5 nm edge length. Reflective boundary conditions are used along the y-axis normal to the geometry shown in Figure 4.2. Although we are simulating a nominally 2-dimensional feature (a trench), performing the simulation in 3-dimensions results in a more realistic representation of sidewall roughness. When simulating a trench in 2-dimensions, sidewall roughness is effectively uniform (and infinite) in the unresolved depth. In 3-dimensions, sidewall roughness is finite. The etching was performed for a fixed process time of 15 minutes.

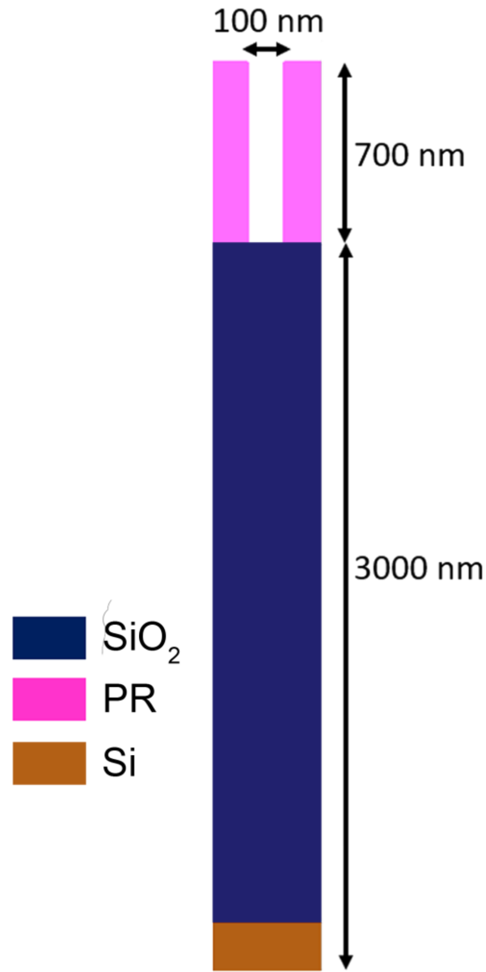

Figure 4.2: Initial geometry used in for feature profile simulations. A 700 nm mask defines a 100 nm opening to 3000 nm thick SiO_2. The simulations are for trench etching, performed in 3-dimensions having a finite depth.

The Monte-Carlo method which is used in the MCFPM inherently produces statistical variation in the details of the features that are produced. This run-to-tun variation can occur naturally in parallel computations by differences in the timings of the processors. The statistical variation features can be demonstrated by changing the seeds for the random number generators on separate runs. The features shown here are typical, average features in which outliers due to statistical variation have been excluded. The statistical run-to-run differences in features are discussed in Appendix A.

4.4 Plasma and Etch Properties for 1000 W of VWT Power

In industrial applications of plasma etching, it is most common to control power deposition in the plasma as opposed to voltage amplitude. To make more direct connection to these applications, the power applied through the VWT on the bottom electrode was first held constant at P_{VWT} = 1000 W by adjusting the voltage amplitude V_0 while varying the phase φ from 0 – 180°. Although this power appears large, by industrial processing standards for HAR etching of 30 cm diameter wafers, 1000 W is a moderately small power [1–3]. The applied voltage amplitudes necessary to maintain constant power coupling through the top electrode (500 W), bottom electrode (P_{VWT} = 1000 W) and the resulting DC self-bias on the bottom electrode are shown in Figure 4.3 as a function of phase angle. At constant power, the amplitude of the high frequency voltage applied to the top electrode is a weak function of the phase angle and is nearly constant at V_{hf} = 120 V. The DC self-bias, however, is strongly coupled to φ with its magnitude decreasing (becoming more positive) by 88% from V_{dc}= -2480 at φ=0° to V_{dc}= -290 at φ=0°.

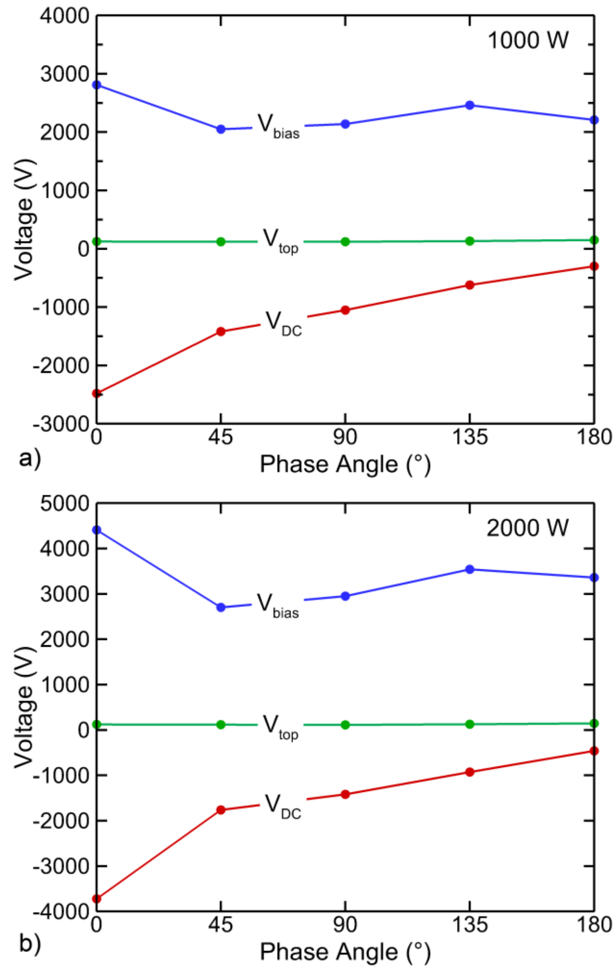

Figure 4.3: Voltage amplitudes for the VWT bias (V_{bias}) and top power (V_{top}), and DC self-bias as a function of phase angle. a) P_{VWT} = 1000 W and b) P_{VWT} = 2000 W.

Earlier works have described the trend of how DC bias depends of the shape of the applied waveform through the generation of the electrical asymmetry effect (EAE) [4,5]. (See Sections 1.17 and 1.18 for details). The formulation for the EAE does not specifically account for a second powered electrode having a unique frequency, such as used here. However, due to the higher frequency and lower power of this second RF bias, the voltage amplitude applied to the top electrode is smaller than that applied to the lower electrode. Sinusoidal voltages alone do not induce electrical asymmetry effects and so we do not expect large perturbations to the EAE process by the high frequency source. With the phase shift applying only to the tailored waveform on the

bottom electrode, V_{hf} remains relatively constant for all φ, varying by less than 10%. Due to the changes to the electron dynamics in the sheath region some variation does occur in V_0, decreasing from 2800 V to 2200 V or about 27% from $\varphi = 0$ to 180°.

The DC self-bias on the lower electrode, V_{dc}, is an important parameter in determining the energy of incident positive ions. For high frequency excitation where the energy width of the IEAD is small compared to the RF voltage amplitude, the centroid in energy of the IEAD typically increases with the magnitude of V_{dc}. With low fundamental frequencies (thin sheath limit), ions transiting the sheath respond to the sheath dynamics during the RF period. (This is nearly always true for electrons.) In this low frequency limit, the correlation between IEAD and V_{dc} is not straight forward. The radially averaged axial electric field as a function of time and distance from the substrate, $E_z(z, t)$, is shown in Figure 4.4 for phase shifts of $\varphi = 0°$ to 180°. In CCPs without an electric field reversal, $E_z(z, t)$ near the bottom electrode sheath will point towards the electrode (negative z direction) at all times. However, with $\varphi = 0°$, an EFR occurs during the sheath collapse at around 0.5 μs when the applied voltage is at its maximum positive value and there is a positive electric field component (pointing in +z direction). This EFR results, in part, from the short duration of the positive voltage excursion of the voltage waveform and the correspondingly short time during which the sheath collapses. In order to produce the required electron flux to the surface to maintain a charge-neutral flux to the substrate, an EFR occurs to accelerate electrons towards the surface. This field reversal is most pronounced in the $\varphi = 0°$ case (69 V/cm) as this phase has the shortest sheath collapse and so requires the largest instantaneous electron flux to the surface. As the duration of the sheath collapse increases with increasing φ and becomes less abrupt, the magnitude of the instantaneous electron flux that is required to balance charge decreases, and so the magnitude of the EFR reversal also decreases.

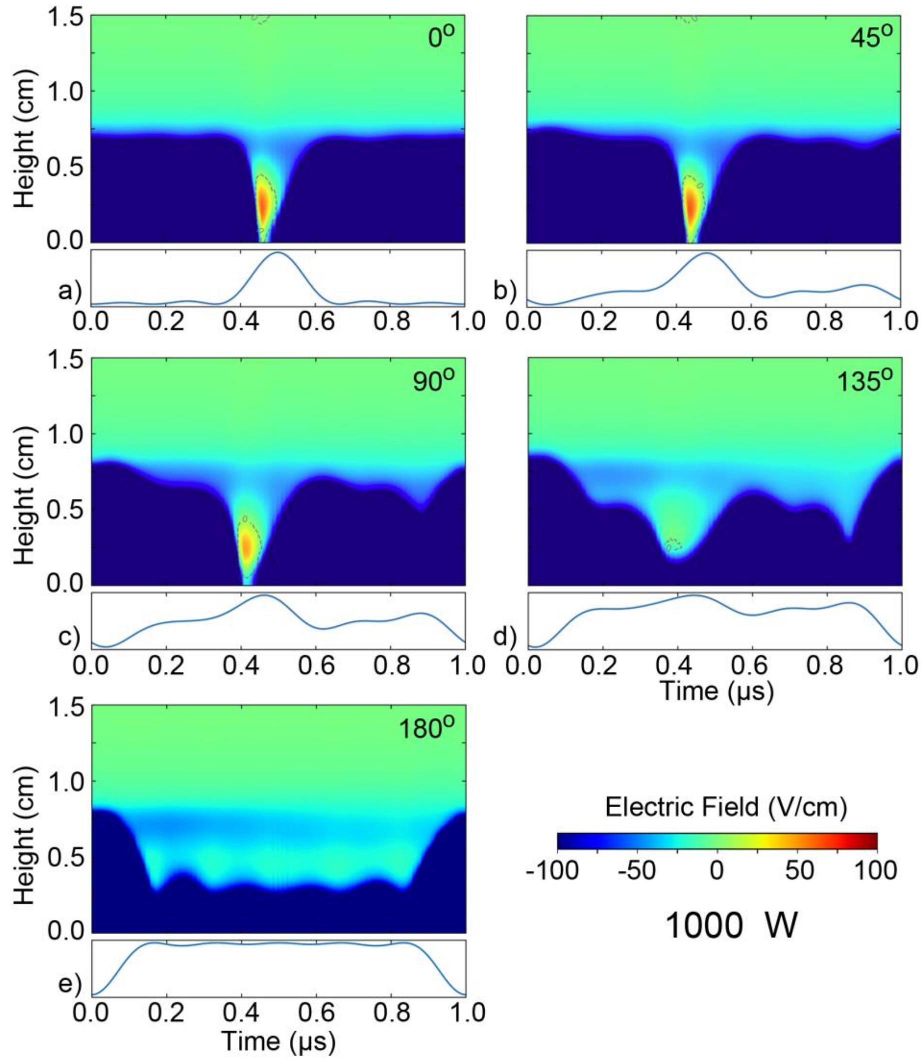

Figure 4.4: Vertical electric field component as a function of time and distance from wafer for P_{VWT} = 1000 W for phase angles of a) 0°, b) 45°, c) 90°, d) 135° and e) 180°. The shape of the voltage waveform applied to the bottom electrode is shown in each image.

The modulation of the sheath as a function of the phase of the harmonics translates into significant variation of IEADs incident onto the wafer, as shown in Figure 4.5a. These IEADs are collected by summing over all ions striking the wafer for φ = 0° to 180°. The IEADs generally decrease in maximum energy with increasing φ, following the trend in V_{dc}. The mean energy of the ions also decreases with increasing φ, as shown in Figure 4.5c. Aside from the general decrease in energy, the shape of the IEADs reflect the temporal dynamics of the sheath. The IEAD for φ =

0° contains a dominant peak at 3000 eV, a result of the sheath maintaining a nearly constant potential and thickness for the majority of the RF cycle. (See Figure 4.4.) The IEADs for φ = 45°, 90° and 135° contain more complex multi-modal structures with broader spreads in energy. The structure in the IEADs reflects the length of time the sheath is maintained at a given potential and thickness. The IEAD for φ = 180 ° has a single dominant peak at approximately 400 eV, as the sheath has one of two quasi-binary states – fully collapsed or fully expanded.

The EEADs incident onto the wafer surface are shown in Figure 4.5b for φ = 0° to 180°. The electric field reversal for small values of φ produces a significant acceleration of electrons normal to the surface, generating an EEAD with a higher energy and narrower angular distribution that might occur with low frequency, sinusoidal waveforms. (Recall that for a purely thermal distribution of electrons onto the surface, the mean energy will be about the electron temperature, 3-4 eV, and the angular spread would span -90° to +90°.) The EEAD for φ = 0°, where the EFR has is largest magnitude, extends to 125 eV, considerably higher than the thermal bulk temperature of about 3.2 eV. (Although the electron energy distribution is non-Maxwellian in the bulk plasma, for convenience we will refer to the electron flux incident onto the electrode in the absence of significant EFR as being the thermal electron flux or resulting from thermal electrons.) The downward trend of the magnitude of the electric field reversal with increasing φ in turn leads to a decrease in the electron acceleration normal to the surface, and so to an overall reduction in electron energy incident onto the surface. With φ = 180°, the EEADs incident onto the surface closely resemble a thermal distribution, though with a somewhat narrower angular distribution. The high energy, low angle electrons are likely the result of electrons accelerated in the sheath at the opposing electrode. Due to the two-decade log scale of the image, these structures are visually overemphasized.

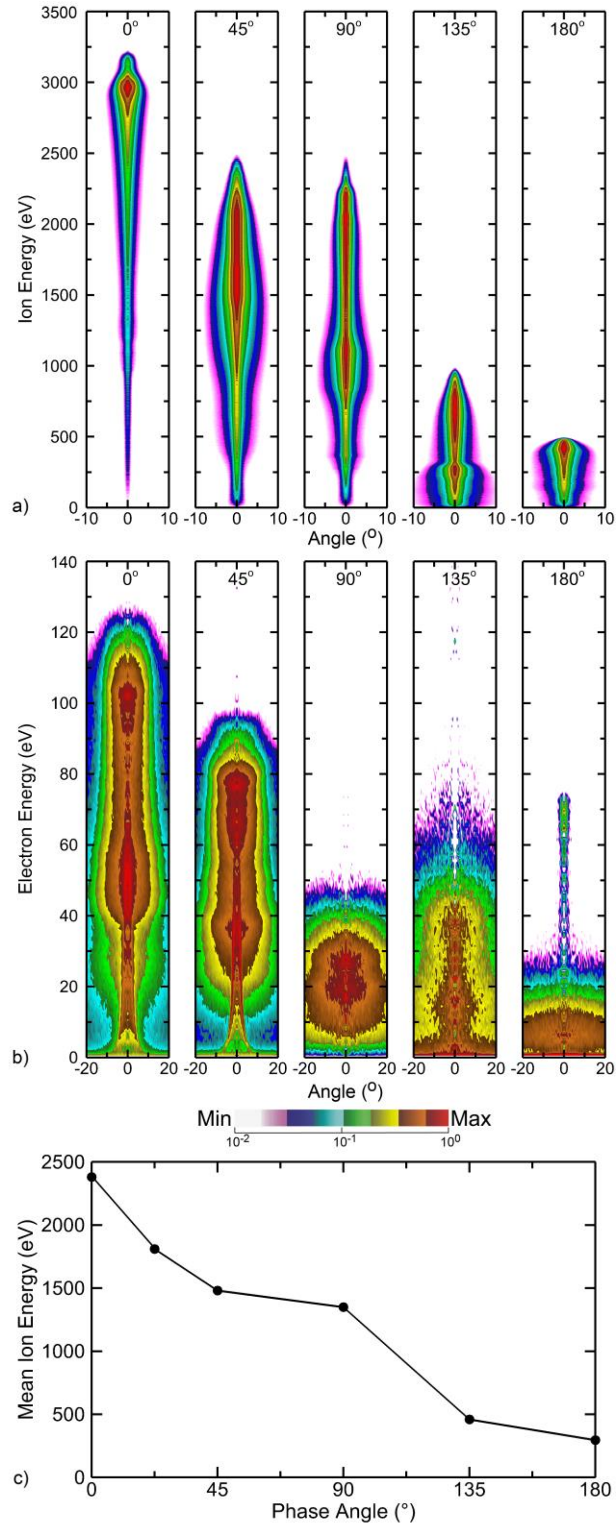

Figure 4.5: Properties of ions and electrons incident onto the wafer for P_{VWT} = 1000 W. a) IEAD and b) EEAD for phase angles of φ = 0°, 45°, 90°, 135° and 180°. The distributions are separately normalized and plotted on a log-scale over 2 decades. c) Mean ion energy as a function of phase angle φ

In addition to the charged particle EADs onto the surface, the silicon-dioxide etching mechanism depends on the magnitude of the individual fluxes of charged and neutral species onto the wafer. In particular, the ratio of polymer depositing and polymer removing species is important in dielectric etching in fluorocarbon containing plasmas. The time averaged fluxes of neutral and ion species onto the wafer as a function φ are shown in Figure 4.6.

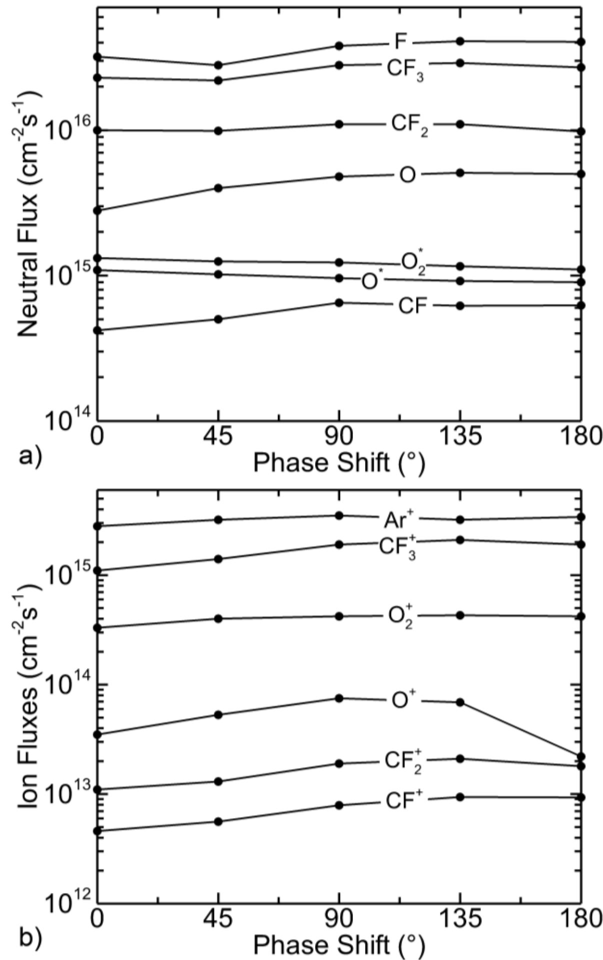

Figure 4.6: Fluxes of reactive species onto the wafer as a function of phase angle φ. a) Neutrals and b) ions.

With changes in φ there are systematic changes in EADs of charged particles onto the surface. However, the neutral fluxes are fairly stable with moderate variation with changes in phase φ for most species. With the high frequency power being held constant, the rates of electron impact dissociation and ionization are nearly constant, producing nearly constant fluxes. The small

variation in neutral fluxes with φ can be attributed to the contribution to dissociation by secondary electrons emitted from the wafer and accelerated by the sheath into the bulk plasma. With the electron energy distribution of the secondary electrons being functions of sheath dynamics, rates of dissociation will also vary.

Similar trends apply for the fluxes of ions to the wafer as a function of φ, which also show little variation with phase both in terms of overall magnitude as well as the relative ratios of ion fluxes. The one notable exception is the flux of O^+ which increases for intermediate values of φ. The atomic weight of O^+ is the lightest of ions having a significant flux to the surface and so will respond more quickly to changes in the sheath (and presheath) compared to other ions. There is also likely a component of ionization of atomic oxygen by high energy secondary electrons. Given that the fluxes of Ar^+ and CF_3^+ are 2 orders of magnitude higher than that of O^+, we do not expect this sensitivity of the flux of O^+ on phase angle to have a large effect on etch properties.

The feature profiles for trenches in SiO_2 after 15 min of plasma etching are shown in Figure 4.7a for phase angles of φ = 0° to 180°. Varying φ for constant power produces significant differences in etch depth, ranging from 1750 nm for φ = 0° to an immediate etch stop due to excessive polymer buildup at φ = 180°. Due to the similar absolute fluxes of reactants for all phase angles, this trend in etch depth is a consequence of the differences in charged particle energy distributions onto the wafer resulting from the change in applied voltage waveforms. The higher energy of the incident ions at low phase angles produces higher rates of removal of passivating polymer films and higher rates of sputtering of SiO_2, directly or by chemically assisted processes. The etch stop at φ = 180° is a consequence of the lower ion energies that are unable to balance the deposition of polymer by removal of polymer by sputtering. A net etch at φ = 180° would be possible for lower rates of polymer deposition (lower incident fluxes of CF_x radicals).

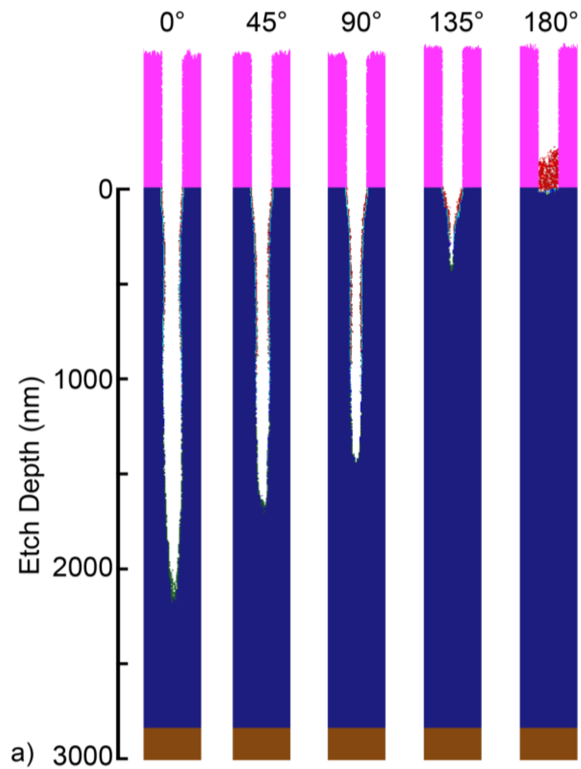

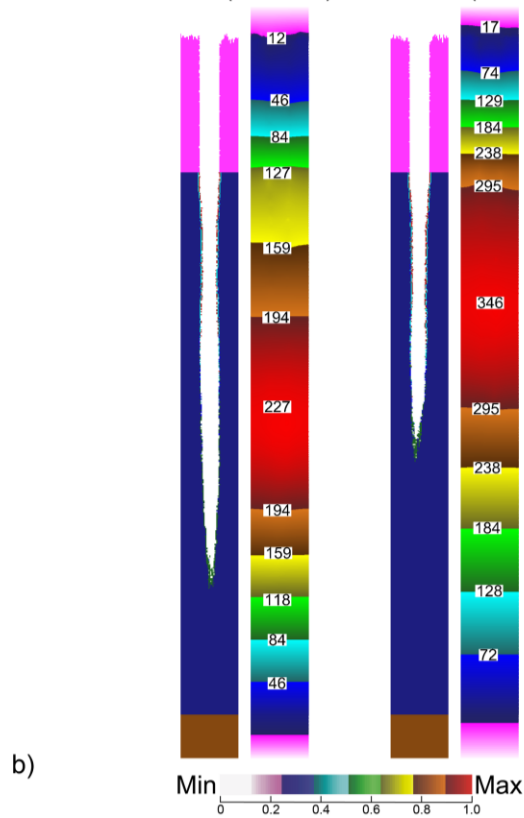

Figure 4.7: Feature properties for P_{VWT} = 1000 W following 15 minutes of etching a) Feature profiles for different phase angles (φ = 0°, 45°, 90°, 135° and 180°). b) Comparison of etch result and electric potential for (left) self-consistent VWT produced EEAD

The higher incident energies of the positive ions also enable them to partially overcome positive electrical potential that builds up inside features. This positive potential slows ions, thereby reducing their sputter yield with possible deflection of their trajectories inside the features, which leads to twisting. One of the original motivations for VWT was to promote in-feature charge neutralization on surfaces by narrowing the angular distribution of electrons to better match that of the ions. These narrow and energetic EEADs presumably would penetrate deeper into the feature than is possible by the broad, low energy thermal EEADs produced by conventional CCPs. The desired end result would be a charge neutral feature.

To test this hypothesis, one would need to perform reactor scale simulations where the ion and neutral fluxes, and IEADs remain the same, while the EEADs varied from low energy, broad angle to high energy, narrow angle. From our attempts to find such conditions, we conclude that the likelihood is small of being able to hold the IEAD constant while varying the EEAD. The very conditions that modify the EEADs also modify the IEADs. A large set of computational experiments were performed to find combinations of voltage, power and waveforms that would maintain the same IEAD while toggling between a nearly thermal EEAD, and an EFR enhanced EEAD. We were not able to find such conditions.

Instead, to test the hypothesis that EEADs produced by electric field reversals can decrease the magnitude of positive charge in the feature the following process was used. Etch profiles were compared when using EEADs produced from using VWT and a synthetic thermal EEAD having a 3 eV electron temperature. The fluxes of radicals and ions, and IEADs, were the same for both cases. These reference simulations were performed for $\varphi = 0°$. For these conditions, the differences in EEADs between those generated by VWT and synthetic thermal distributions are the greatest. The VWT case, $\varphi = 0°$ also resulted in the overall most desirable feature profile.

The etch profiles and corresponding final electric potential are shown in Figure 4.7b for the (left) self consistently generated VWT produced EEAD and (right) for the synthetic thermal EEAD. Both cases have both negative and positive charge distributed throughout the feature, though with net negative charge at the top of the features and net positive charge deeper in the feature. The end result is positive potential inside the feature. The maximum potential with the VWT produced EEAD is 227 V and the maximum potential produced with thermal electrons is 346 V. The larger positive potential with thermal electrons reduces the final etch depth by 30% by slowing the positive ions incident into the feature. This result confirms the initial hypothesis that directional electrons produced by the EFR can be utilized to at least partially neutralize intra-feature surface charging and lessen the decrease in etch rate resulting from that charging.

The maximum ion energy incident into the feature exceeds 3000 eV. If there was no electron neutralization of positive charge in the feature, the positive potential would increase to nearly this maximum value to prevent positive charge from being continually collected. Even when using the thermal electron EEAD, the potential inside the feature is significantly smaller than the maximum ion energy. The thermal electrons initially have isotropic trajectories which dominantly strike the top of the feature. However, the buildup of positive potential in the feature produces electric fields directed upwards that then accelerate these thermal electrons into the feature. The thermal electrons accelerated into the feature then produce significant neutralization of positive charge on the sidewalls.

In the steady state, the positive potential inside the feature increases to a large enough magnitude so that the thermal electrons accelerated into the feature are able to neutralize incremental additions to positive charge. This transient is directly analogous to the charging of a dielectric surface in contact with a plasma to a negative potential that balances the flux of electrons

and ions. The use of the VWT produced EEAD, with its initially higher energy and velocities towards the wafer, and narrower angular distribution, enables this balance of electron and ion fluxes to be achieved with a lower positive potential. The difference in electric maximum potential in the features between the thermal EEAD and the VWT produced EEAD, 120 V, corresponds to approximately the difference in the maximum energy of the VWT produced and thermal EEADs. Although this is not a general result, the difference in potential would not be expected to exceed this value.

When using the VWT generated and thermal EEADs, the location of maximum potential is not at the bottom of the feature but at depths of 1.2 μm for the VWT EEAD and 0.77 μm for the thermal EEAD. The charging of the mask is nominal compared to the energies of ions and EFR accelerated electrons. The mask charging may be more important for low aspect ratio (AR) features where the voltages and powers are lower. However, for HAR features, this is typically not an issue. The maximum of the positive potential is a function of AR. As the feature is etched deeper and the AR increases, the maximum in positive potential transitions from the bottom of the feature at low AR to the side of the feature as the AR increases [1]. For small AR, ions even with a finite angular spread can directly strike the bottom of the feature, and so the maximum positive potential is on the bottom of the feature. For HAR features, ions having a finite angular spread will strike the sidewalls, and positive charging will occur dominantly on the sidewalls. The neutralized particles then proceed as hot neutrals deeper into the feature. The shadowing by the fairly thick photoresist produces a view angle of 3.8° (VWT) to 4.3° (thermal) which is in line with the ion angular spreads.

The charging of the feature occurs over many RF cycles. There are no specific in-feature, intra-cycle dynamics of the electric field as the charging and electric fields are the results of

averaging charged particle fluxes over these many RF cycles. For bias frequencies of many MHz and above, distinct cyclic in-feature electric field dynamics will likely only occur when using pulsed power.

Electron trajectories inside the feature depend on their initial distribution in energy and angle as well as the acceleration resulting from electric fields in the feature produced by charge deposition. In the case with the highest electron energy incident onto the wafer ($\varphi = 0°$) the mean energy of the EEAD is 62 eV. Given the maximum electric potential in the feature is 280 V, the electron trajectories are still likely dominated by the electric fields produced by charging. To verify this likelihood, electron energies incident onto the surface inside the feature were spatially sampled. To enable a side-by-side comparison of these energies, the following process was followed. The feature shape and potential configuration resulting from the $\varphi = 0°$ case after 15 minutes of etching was used and kept constant. (That is, no further evolution of the feature or potential was allowed.) Initial electron trajectories were sampled from the EEAD produced by VWT or from a thermal distribution having an electron temperature of 3 eV. The electron trajectories were followed into the feature, and the electron energies striking the surface were recorded and averaged at each spatial location. Tests were performed for VWT produced EEAD and thermal distributions when including acceleration from the charge produced electrics fields, and when excluding that acceleration.

Figure 4.8: Spatial distribution of average electron energies incident on the surface of the feature. The feature properties are for P_{VWT} = 1000 W and $\varphi = 0°$ after 15 minutes of etching. Results are shown for initial EEADs produced with VWT and for thermal electron having a temperature. of 3 eV. a) When including acceleration in electric fields produced by feature charging. b) Without acceleration due to feature charging. The view is looking obliquely into the 3-dimensional feature having reflective boundary conditions front-and-back.

The resulting spatially resolved average electron energies incident on the feature surface are shown in Figure 4.8. The average energies shown in Figure 4.8a are for initial EEADs (VWT and thermal) when including acceleration in the electric fields produced by charging. The average energies striking the surface for VWT and thermal distributions are spatially similar and

qualitatively resemble the electric potential shown in Figure 4.7b. These distributions largely result from acceleration of the incident electrons by the in-feature electric fields. The average energy of the electrons striking the surface for the initially thermal electrons is maximum at about 240 eV, which corresponds to the maximum positive potential inside the feature. The average energy for the electrons launched from the VWT produced EEAD is maximum at about 275 eV. This value is larger than for the thermal electrons by 35-40 eV due to the electrons selected from the VWT produced EEAD beginning their trajectories with significant initial velocities.

To reinforce this finding, average electron energies striking the surface of the feature were computed for the VWT produced EEAD and for thermal electrons when excluding acceleration by electric fields, as shown in Figure 4.8b. The average energies for the VWT produced EEAD range up to 35 eV and those for the thermal EEAD range up to 6 eV, both values largely reflecting the initial distributions.

These findings suggest that for reasonably large positive potentials produced inside features, the high energy VWT produced EEADs will not dominate the resulting feature properties compared to EEADs produced using conventional waveforms. In both cases, in the steady state electrons are accelerated into the feature in such a manner as to neutralize the incremental charge produced by fluxes of positive ions. This is particularly true for positive potentials that are much larger than the average energy of the incident EEADs.

4.5 Plasma and Etch Properties for 2000 W of VWT Power

While maintaining 500 W of power on the top electrode, the power delivered by the bottom electrode was increased to P_{VWT} = 2000 W to be more aligned with industrial processes. The resulting voltage amplitudes for the top and bottom electrodes, and the DC self-bias are shown in Figure 4.3b as a function of phase angle. The top electrode voltage amplitude remains nearly

unchanged compared to the P_{VWT} = 1000 W cases with there being little variation with phase angle φ. In order to accommodate the increase in power, the bottom electrode voltage amplitude increased by a factor of 1.5-2 compared to the P_{VWT} = 1000 W cases. The low- and high-power cases have nearly identical trends with phase angle, which suggests that these trends are the result of the sheath dynamics rather than being of stochastic origin. Similar to the 1000 W cases, V_{dc} decreases with increasing phase angle as a consequence of the EAE. The large magnitude of V_{dc} correlates to the larger applied voltage amplitude.

The radially averaged, axial electric fields as a function of time during the RF cycle for P_{VWT} = 2000 W are shown in Figure 4.9 for different phase angles φ. Overall, the sheath dynamics and electric field reversals as a function of phase angle are similar to the P_{VWT} = 1000 W cases (Figure 4.4) with the EFR decreasing with phase. One exception is the $\varphi = 0°$ case whose EFR is reduced compared to $\varphi = 45°$ at same power and also reduced compared to the $\varphi = 0°$ case at 1000 W. This apparent outlier is the result of the geometrical constraints of the plasma reactor and of the finite electrode gap (distance between bottom and top electrodes). For example, the spatially resolved electron densities averaged over the RF period are shown in Figure 4.10 for $\varphi = 0°$, 90° and 180°. While the peak electron densities vary by only about 10% the spatial distributions vary considerably with change in φ.

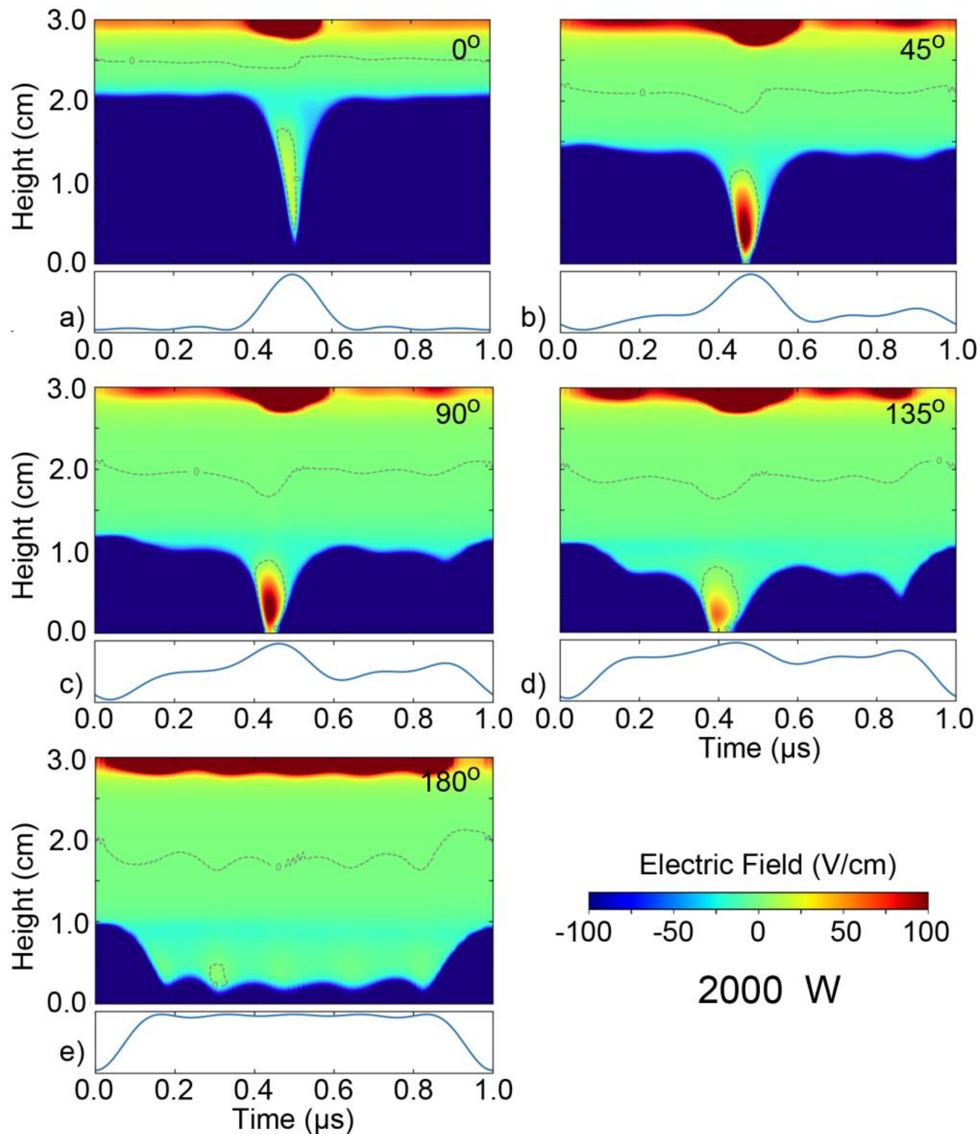

Figure 4.9: Vertical electric field component as a function of time and distance from wafer for P_{VWT} = 2000 W for phase angles of a) 0°, b) 45°, c) 90°, d) 135° and e) 180°. The shape of the voltage waveform applied to the bottom electrode is shown in each image.

With low values of φ, the time averaged sheath thickness is larger, which reflects the larger (more negative) DC bias and voltage amplitude. The sheath thickness then occupies a significant fraction of the gap. The compressed bulk plasma is then more sensitive to, for example, discontinuities between the top electrode and the bounding dielectric insulator where electric field enhancements occurs. The end result is a less spatially uniform plasma. We acknowledge that, if

unaddressed, this expansion of the sheath could potentially affect the spatial uniformity of the wafer processing, and that this effect may be amplified by this particular reactor configuration. Several reactor configurations were investigated (e.g., adjusting the shape and diameter of the focus rings, and top electrode) to confirm that the VWT scaling discussed here, and sheath expansion and plasma compression are general trends. There are many actions, such as adjusting the process parameters (gas composition, gas pressure, flow rates, power) and/or reactor geometry that could be used to recoup the trends with phase angle that were obtained at the lower power. This optimization is beyond the scope of this work. That said, this demonstration emphasizes the concept that design of plasma processing reactors must be performed from a systems perspective. Optimizing one aspect of the design, such as EFR, may ultimately be limited by other aspects of the design, such as gap dimension.

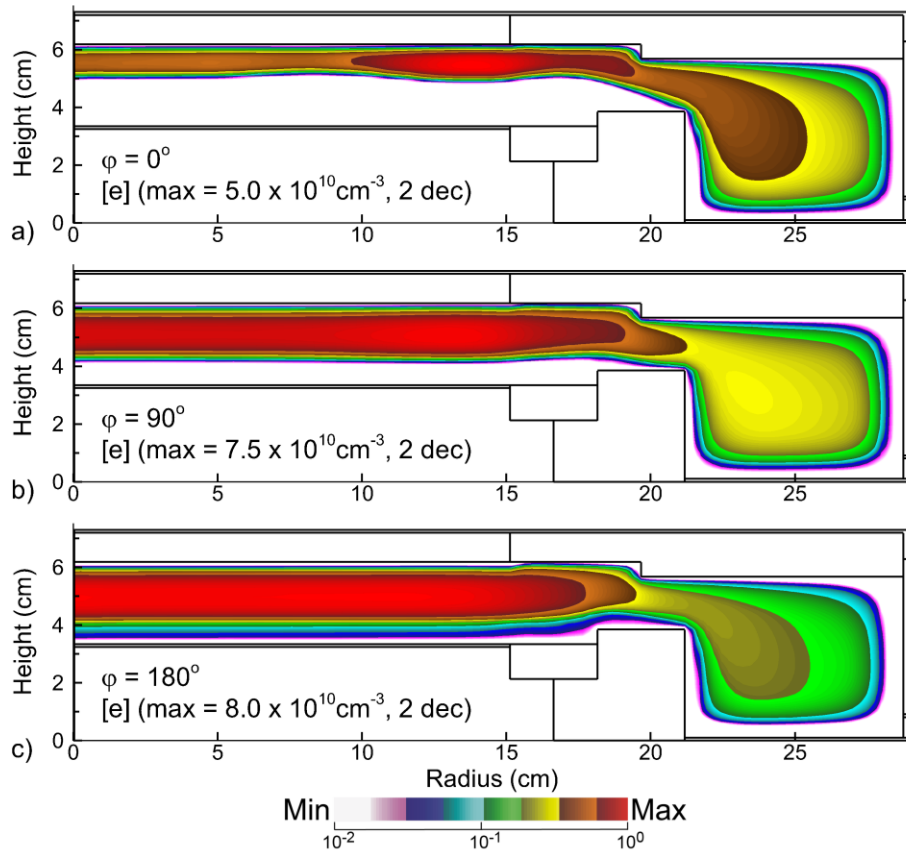

Figure 4.10: Electron density for P_{VWT} = 2000 W for phase angle φ of a) 0°, b) 90° and c) 180°). The densities are plotted on a log-scale over 2-decades.

The similarities to the trends of the lower power cases are also reflected in the IEADs to the wafer as a function of phase angle, are shown in Figure 4.11a.

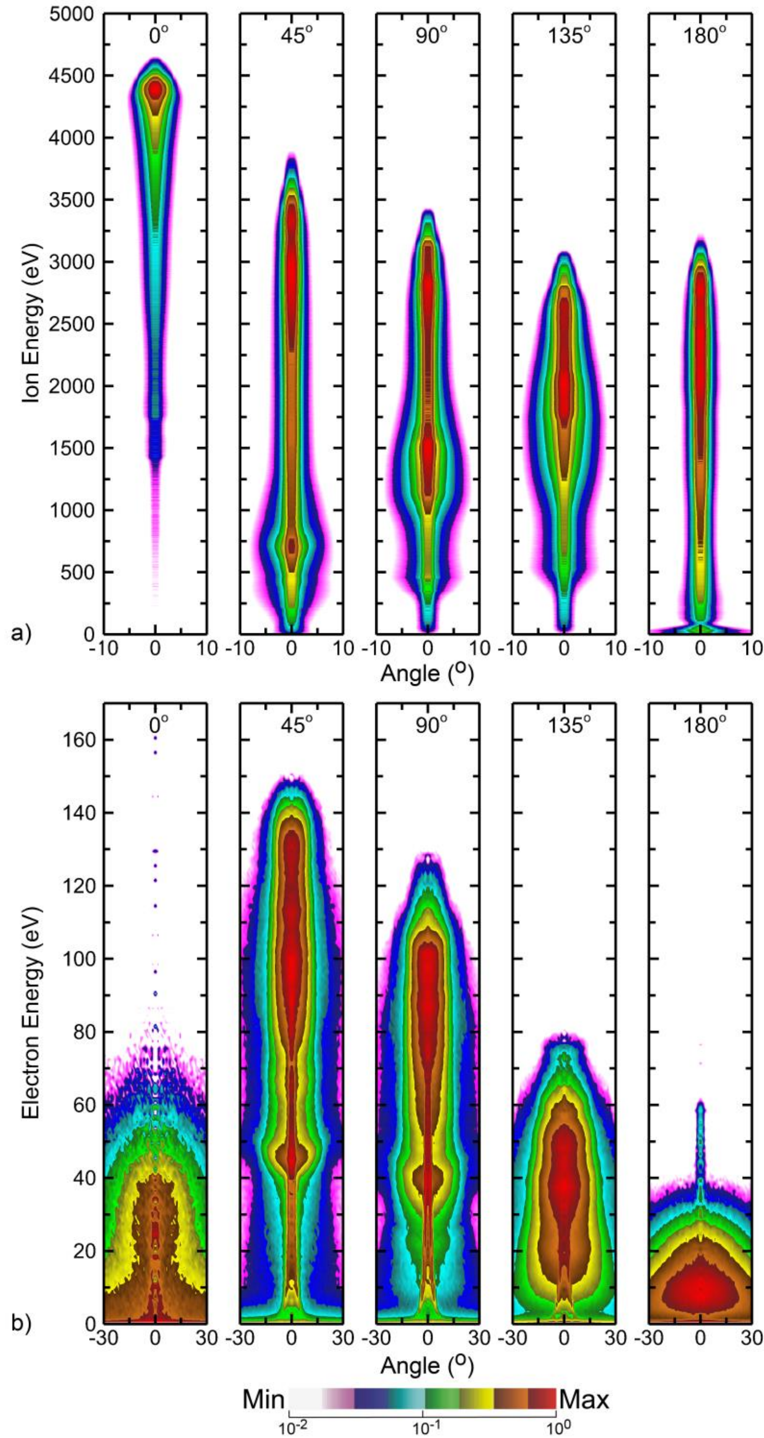

Figure 4.11: Energy and angular distributions for charged particles incident onto the wafer for P_{VWT} = 2000 W for phase angles of φ = 0°, 45°, 90°, 135° and 180°. a) Ions and b) electrons. The distributions are separately normalized and plotted on a log-scale over 2 decades.

While compared to the lower power cases, the ion energies are higher overall due to the larger voltage amplitudes, the peak energies still decline with increase in the phase angle from a maximum of about 4500 eV for $\varphi = 0°$ to 3000 eV at $\varphi = 180°$. Comparing the cases with highest and lowest ion energies ($\varphi = 0°$ and $\varphi = 180°$), the peak ion energy was reduced by approximately 85% at 1000 W and reduced by 38% for 2000 W. This degree of ion energy control should enable some degree of customizing fluxes for energy-sensitive surface processes. In particular, the distribution of high-energy ions compared to low energy ions within the IEAD is sensitive to phase angle.

These trends for the IEADs are in contrast to the much lighter and more agile electrons, whose EEADs to the wafer are shown in Figure 4.11b. The EEADs display the same general trends as in the low power case. The EEADs have high energies and narrow angular spreads for low values of φ compared to thermal distributions due to the electric field reversal produced by VWT. The energies decrease and angular spread increases with increasing phase angle φ. The $\varphi = 0°$ case is, again, a notable exception, having a lower peak energy than a larger phase angle. This exception correlates with the smaller EFR described above. The suppressed electric field reversal due to geometric confinement of the sheath leads to reduced electron acceleration, resulting is the comparatively lower electron energy.

The IEADs, EEADs and fluxes for different phase angles for 2000 W bias power were used as input to otherwise identical MCFPM simulations. The final etch profiles are shown in Figure 4.12a. Significant etch depths were reached for all phases, in deference to the P_{VWT} = 1000 W cases where an etch stop occurred due to excessive fluxes of polymer forming radicals, or lack of polymer sputtering ions, at large phase angle. There are, however, significant differences in etch depth and overall feature quality. The $\varphi = 0°$ case produces the deepest overall etch while having

perhaps a tolerable amount of bowing. The $\varphi = 45°$ case has less bowing but lower etch rate. These trends result from $\varphi = 0°$ case having the higher ion energies (faster overall etch rate) while the $\varphi = 45°$ has a narrower ion angular distribution (less bowing), albeit at a lower energy. Some component of the narrower feature could be a result of the EEAD at $\varphi = 45°$ being more energetic which enables some non-negligible decrease in in-feature charging. The shape of the EEAD is important to moderately increasing etch rate and moderately modifying sidewall slope through neutralizing charge. However, the final feature quality is dominated by the EAD of ions rather than the electrons.

Analogous to the low power case, MCFPM simulations using synthetic thermal EEADs were performed, and the resulting profiles are compared to etch profiles resulting from VWT produced EEADs in Figure 4.12b for $\varphi = 0°$, 90° and 180°. In the $\varphi = 0°$ and 180° cases the differences between the profiles obtained with thermal and VWT EEADs are small and below the statistical threshold discussed in Appendix A. The profile obtained with the VWT EEAD for $\varphi = 90°$ is deeper with a similar amount of tapering compared to the thermal EEAD. These trends result from the EEADs onto the wafer for these conditions having the highest energy and lowest angular spread for intermediate values of φ. This correlation between the improvement of the final etched feature and the energy and directionality of the electrons reinforces the conclusion that these directional electrons enhance the natural neutralization of charge that is produced by acceleration of thermal electrons into the feature. However, the properties of the EEADs do not dominate the shape of the feature.

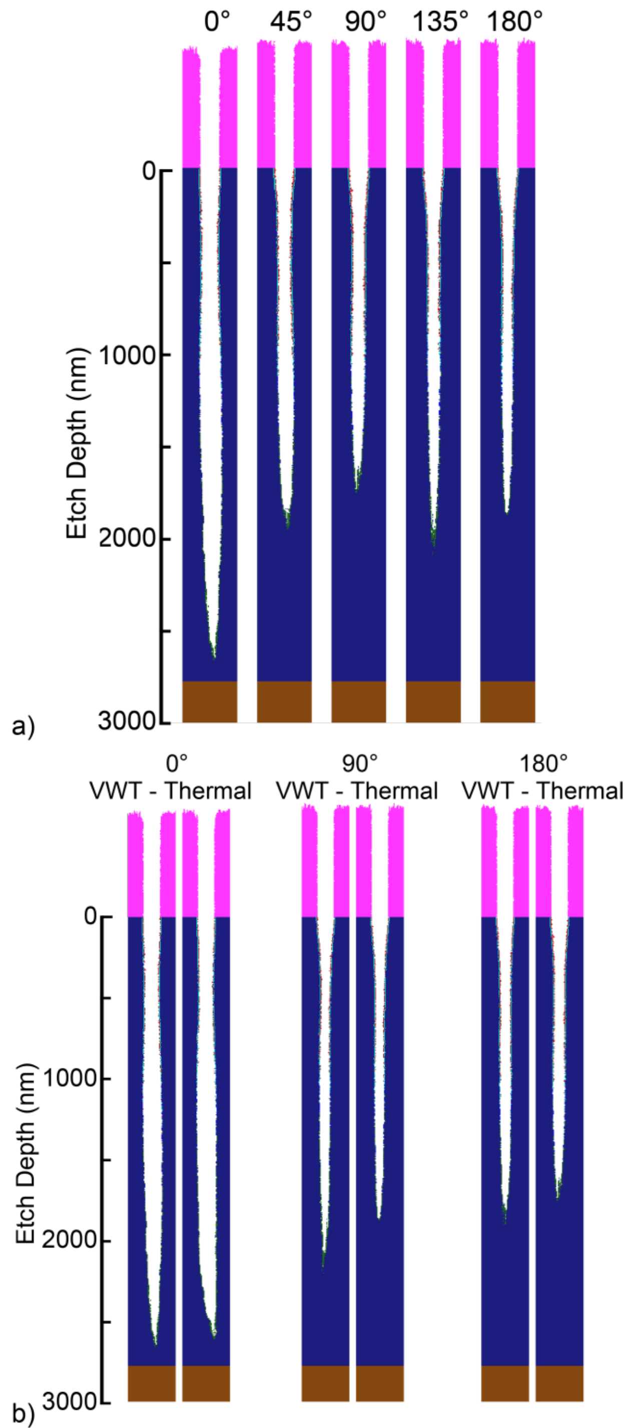

Figure 4.12: Feature properties for P_{VWT} = 2000 W following 15 minutes of etching a) Feature profiles for different phase angles (φ = 0°, 45°, 90°, 135° and 180°). b) Comparison of profiles obtained with VWT generated EEADs and synthetic thermal electron distribution for phase angles φ of 0°, 90° and 180°.

4.6 Concluding Remarks

To investigate the consequences of voltage waveform tailoring (VWT) on etching of SiO_2 using a capacitively coupled $Ar/CF_4/O_2$ plasma, computational investigations of the reactor scale and feature scale processes were performed. While applying 500 W at 80 MHz to the top electrode with the goal of sustaining a constant plasma density, the bottom electrode was driven using VWT composed of consecutive harmonics with a fundamental frequency of 1 MHz at powers of 1000 W and 2000 W. The phase of the even harmonics φ was varied in order to generate electrical asymmetry as well as electric field reversal in the bottom sheath. It was found that changing φ enables control of charged particle dynamics incident onto the wafer surface which in turn translates to significant changes in etch profiles. At low phase angle the EAE as well as the EFR are most significant, which leads to increased energy and directionality of ions as well as electrons onto the wafer.

These favorable distributions in energy and angle increase etch rate by partially reducing the negative effects of intra-feature charging. The directional electrons are better able to reach the lower echelons of the feature and partially neutralize positive charges. The higher energy ions have larger rates of chemical sputtering while also being more able overcome the remaining deflecting electric fields produced by in-feature charging. Overall, for otherwise equal processing conditions and time, low φ cases produced higher etch rates and more favorable sidewall slope. For low bias power, the reduction in ion energy with large values of phase angle resulted in an etch stop due to the large incident flux of polymerizing radicals. At low bias power, having higher ion energies, sputtering of the polymer enabled competitive etching even at high phase angle.

A key finding of this investigation is the VWT produced EEADs having large energy and narrow angle do not produce the expected significant reductions of in-feature charging compared

to thermal EEADs. The VWT produced EEADs did produce somewhat higher etch rates and lower in-feature potentials. However, the buildup of positive charge in the feature accelerates thermal electrons into the feature to energies commensurate with that of the positive potential. The VWT produced EEADs are also accelerated into the feature by this positive potential. If the positive potential is significantly larger than the average energy of the VWT produced EEAD, there is little difference in feature properties between having thermal or VWT generated EEADs. Both are accelerated into the feature by the positive charge to sufficient energy to neutralize, in the steady state, the incremental positive charge brought into the feature by ions.

Another key finding is the need for a systems perspective in process design and in employing VWT in particular. The results of this study showed that at low power, the VWT generated EEADs produced a beneficial effect, enabling higher etch rates for a given power compared to conventional sinusoidal excitation. Conversely, the same etch rate could be sustained at a lower power. We also found that this benefit was not universal. At higher powers, we found that the gap dimension (distance between wafer and top electrode) ultimately limited the ability of VWT to generate electric field reversal and energetic fluxes to the wafer. Low phase angle produces a larger (more negative) DC bias, which thickens the sheath. For a narrow gap CCP, the sheath may consume a large fraction of the gap, which then interferes with the formation of EFR. The fundamental physics of VWT generated EEADs applies to a wide range of powers. However, as with many excitation schemes in plasma etching, the benefits of VWT are likely process dependent, being sensitive to geometry, frequency, pressure and gas mixture.

In the ideal, one would like to tailor an IEAD to best produce the desired etch feature, and then tune the feature profile by tailoring the EEAD. Unfortunately, independently producing specified IEAD and EEAD with the same waveform is difficult. Changing the waveform to

generate, for example, the desired EEAD will also affect the IEAD. There may be opportunity to separately tailor the IEAD and EEAD by using binary-pulsed system. The system would consist of two separate waveforms alternately applied, with one waveform optimized to produce the desired IEAD and the second to produce the desired EEAD.

4.7 References

[1] S. Huang, C. Huard, S. Shim, S. K. Nam, I.-C. Song, S. Lu and M. J. Kushner, Journal of Vacuum Science & Technology A **37,** 031304 (2019).

[2] J. K. Kim, S. Il Cho, S. H. Lee, C. K. Kim, K. S. Min and G. Y. Yeom, Journal of Vacuum Science & Technology A: Vacuum, Surfaces, and Films **31,** 061302 (2013).

[3] J. K. Kim, S. H. Lee, S. Il Cho and G. Y. Yeom, Journal of Vacuum Science & Technology A: Vacuum, Surfaces, and Films **33,** 021303 (2014).

[4] U. Czarnetzki, J. Schulze, E. Schüngel and Z. Donkó, Plasma Sources Sci Technol **20,** 024010 (2011).

[5] J. Schulze, Z. Donkó, B. G. Heil, D. Luggenhölscher, T. Mussenbrock, R. P. Brinkmann and U. Czarnetzki, J Phys D Appl Phys **41,** 105214 (2008).

Chapter 5 DC Self-Bias and Ion Energy at Very Low Driving Frequencies.

5.1 Introduction

Recent industry trends have favored the use of very low frequency (VLF) biases. VLF, typically frequencies below 1-2 MHz, correspond to the thin sheath limit in which the ion entering the sheath will cross the sheath in a small fraction of the RF cycle. In this regime, maximum ion energies incident onto the wafer extend to V_{rf}-V_{dc}, where V_{rf} is the amplitude of a sinusoidal bias and V_{dc} is the negative self-bias on the blocking capacitor. At the same time, the use of voltage waveform tailoring (VWT), is being investigated to customize those ion energy distributions. VWT consists of a bias which is the sum of multiple harmonic frequencies on a single electrode. Due to the added technical complexity and lack of fundamental understanding of its role in modifying ion and electron dynamics in and near the plasma sheath, VWT is only now being broadly adopted by industry [1–7].

The direct measurement of ion energies during industrial plasma etching processes is usually not performed due to the added technical complexity or to avoid disturbing the plasma. As a result, the DC self-bias, V_{dc} is frequently used as a proxy for ion energy onto the wafer. This is a good approximation if the sheath is collisionless and the system is operating in the thick sheath limit, where the ion requires many RF cycles to cross the sheath. For these conditions, the ion energy distribution (IED) striking the wafer has a narrow width in energy centered on -V_{dc}. This is typically the condition intended for control of the IED through VWT.

In this chapter, we discuss results from a computational investigation into the relationship

between V_{dc} and the IED for capacitively coupled plasmas employing VWT over a large range of fundamental bias frequencies. The computed reactive fluxes to the substrate and their energy distributions were used as input to a profile simulator to assess their influences of these reactive fluxes on HAR features etched into SiO_2. We found that at very low frequencies the ions are able to dynamically react to the applied potential and as a consequence incident ion energy onto the wafer can decouple from the trends suggested by V_{dc}.

The reactor and feature scale models (HPEM and MCFPM) are described in Chapter 2 Brief descriptions of reactor and feature scale simulation setup and geometry employed in this investigation are in Section 5.2. The results of the reactor scale gas phase simulations are presented and discussed for constant bias voltage amplitude in Section 5.3 and for constant bias power in Section 5.4. Results are discussed for simulated profiles of HAR trenches etched in SiO_2 using the reactive fluxes produced by these waveforms are discussed in Section 5.5. Concluding remarks are in Section 5.6.

5.2 Simulation Setup and Geometry

5.2.1 Reactor Scale Setup

The investigation of the reactor scale plasma dynamics was performed using the Hybrid Plasma Equipment Model (HPEM) [8–10] which is described in Section 2.1. The reaction mechanism used for $Ar/O_2/CF_4$ plasmas is described by Huang et al [11].

A schematic of the cylindrically symmetric CCP reactor used in this investigation is shown in Figure 5.1. The reactor, modeled after multi-frequency CCPs used in industrial plasma etching applications, consists of two parallel plate electrodes with a diameter of 30 cm separated by a 2.8 cm gap. A silicon wafer is mounted on the bottom electrode and a showerhead gas inlet is distributed across the top electrode. A focus ring made of quartz to improve uniformity of fluxes

to the wafer surrounds the substrate. The dielectric constant of the quartz ring is $\varepsilon/\varepsilon_0 = 4$. While the conductivity of the quartz ring is negligible, that of the Si wafer is 0.05/Ω-cm. The feedstock gas is an $Ar/CF_4/O_2$ =75/15/10 mixture flowing at 500 sccm through the showerhead. The reactor pressure is held constant at 40 mTorr at the location of a pressure sensor near the pump port. This is accomplished by throttling the rate of pumping.

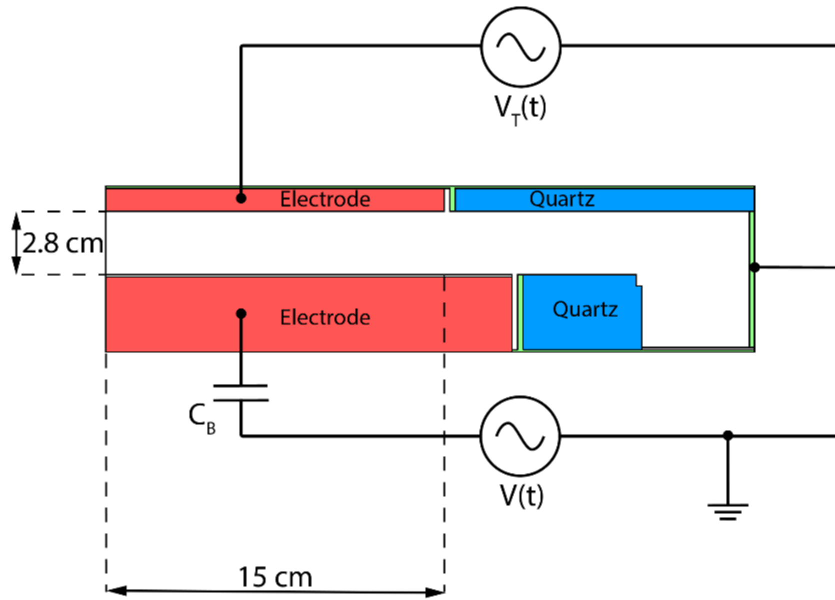

Figure 5.1: Reactor geometry and circuit diagram.

Voltage Waveform Tailoring (VWT) is provided by a power supply connected to the bottom electrode through a blocking capacitor of 100 nF. As such, we are not addressing distortion of the waveform originating from the power supply that may occur by the impedance of the transmission line and substrate. In quasi-steady state operation, the value of V_{dc} should be independent of the value of the blocking capacitor provided that the RC time constant of the plasma-capacitor series impedance is large compared to transients in current. The capacitance used here is a balance of there being an acceptably short charging time and long enough RC time constant so that there is little variation in the V_{dc} during the RF cycle.

The plasma is largely sustained by a sinusoidal voltage with amplitude V_T applied to the top electrode with a fundamental frequency of 80 MHz. To control the dynamics of charged particles impinging on the wafer surface, a customized voltage waveform, V(t), is applied to the bottom electrode. The waveform consists of a fundamental sine wave with a frequency f_0 = 1 MHz to 10 MHz and consecutive harmonics according to (1.56):

In this work the number of harmonics is N = 5. The consequences of VWT were investigated by varying the phase shift of the even harmonics φ for k = 2, 4. The resulting waveforms are equivalent to those shown in Figure 1.14 for phase shifts of φ = 0°, 45°, 90°, 135° and 180°. With the shape and frequency of the applied voltage being closely linked to the plasma properties, two scenarios were investigated:

a) Voltages are held constant at V_T = 300 V and V_0 = 1500 V, as phase shift φ and fundamental frequency f_0 are varied.

b) Applied voltages are dynamically adjusted to maintain a constant power deposition of P_T = P_B = 2000 W, as phase shift φ and fundamental frequency f_0 are varied.

5.2.2 Feature Scale Setup

The fluxes and particle energy and angular distributions to the wafer obtained from HPEM are used as input to the Monte Carlo Feature Profile Model (MCFPM) to simulate the evolution of etch features in semiconductor device materials [11,12]. The MCFM is described in Chapter 2.

The mechanism for etching SiO_2 in an $Ar/O_2/CF_4$ gas mixture used in this work is described in Ref. [11]. All incoming ions or hot neutrals resulting from neutralization of ions striking surfaces can physically sputter all materials according to the incident particle's mass, angle and energy as well as the surface binding energy of the material. Formation of a complex between fluorocarbon radicals and SiO_2 lowers the binding surface energy, thereby reducing the chemical sputtering

threshold. C_xF_y radicals deposit a thin polymer layer (at most a few nm) which is the primary source of sidewall passivation within the feature, whose thickness is controlled by etching with oxygen radicals.

To demonstrate the consequences of changes ion energy and angular distributions (IEADs) resulting from varying f_0 and phase angle, simulations were performed of etching a trench through 3000 nm of SiO_2 covered by a 700 nm thick mask with a 100 nm opening; and terminated by a 100 nm thick Si stop layer. The total aspect ratio is approximately 30. The geometry used for the feature evolution is shown in Figure 5.2. The simulation was performed in 3-dimensions with a mesh consisting of 60 cells wide by 750 cells tall by 20 cells deep using periodic boundary conditions, producing cubic voxels with a 5 nm side length. The etching was performed for a fixed time of 10 minutes.

The intent of the simulation is a uniform trench perpendicular to the plane shown in Figure 5.2 which could, in principle, be performed in 2-dimensions. However, we have found that more robust results are produced when performing a finite depth 3-dimensional simulation. In 2-dimensions, roughness or statistical variation in surface properties are extended infinitely into the third dimension, which can systematically prejudice the outcome, for example, overemphasizing twisting. The finite depth 3D simulations, even with periodic boundary conditions, largely removes these systemic biases.

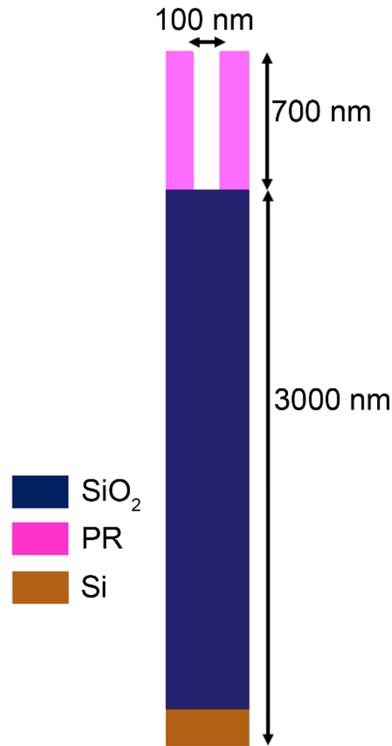

Figure 5.2: Feature scale model initial conditions for simulating plasma etching of SiO_2. PR represents photoresist.

5.3 Reactor Scale Plasma Properties with Constant Applied Voltage

With constant applied voltage amplitudes of V_T = 300 V and V_0 = 1500 V, the fundamental frequency f_0 was varied from 1 MHz to 10 MHz. For each frequency a sweep across the phase angle φ was performed with φ = 0°, 45°, 90°, 135° and 180°. The electron density for the base case with f_0 = 1 MHz and φ = 0° is shown in Figure 5.3a. The cycle averaged electron density at mid-gap is 3.9×10^{10} cm^{-3}, sustained by an electron temperature of 3.1 eV. Ionization at mid-gap is approximately 90% by bulk electrons and 10% by secondary, sheath accelerated electrons. The electronegativity (negative ion density/electron density) at mid-gap is 0.3. Electron density n_e and temperature T_e are fairly homogeneous as a function of radius as shown in Figure 5.3a and d. The ionization is dominated by the bulk electrons. The spatial electron source distribution, generated

by bulk electrons S_b. closely resembles those of n_e and T_e, as shown in Figure 5.3b. The smaller, but still significant amount of ionization by secondary electrons S_s is shown in Figure 5.3c. Since the bulk ionization source is mostly a consequence of electrons accelerated by sheath motion, its maximum is located at the sheath edges. S_s results from electrons accelerated by the total sheath potential and is maximum close to the bottom electrode.

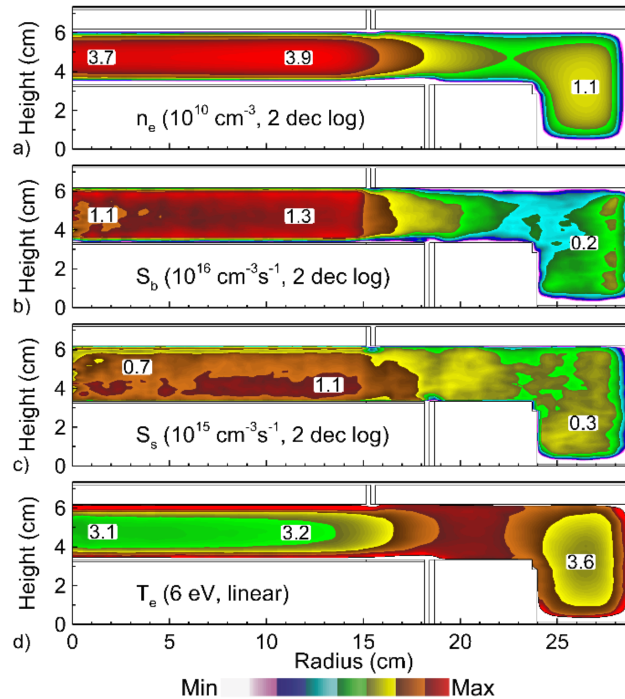

Figure 5.3: Plasma properties of the Ar/CF_4/O_2 CCP base case with V_T = 300 V, V_0 = 1500 V, f_0 = 1 and $\varphi = 0°$. Time averaged a) electron density n_e, b) ionization source by bulk electrons S_b, c) ionization source by secondary electrons S_s, and d) electron temperature, T_e.

The different voltage waveforms that result from changing the phase angle φ can alter the discharge dynamics through differences in sheath expansion heating, electron confinement and modifying surface processes such as ion and electron induced secondary electron emission. While the constant sinusoidal voltage applied to the top electrode is meant to provide a constant background ionization and electron heating, some variation in electron density n_e as a function of φ nevertheless occurs and is shown in Figure 5.4 for fundamental frequencies f_0 = 1 MHz to 10

MHz. Generally, n_e is a function of the total input power at frequencies that produce electron heating. With the top electrode powered at 80 MHz, the majority of this power is expended in electron heating. With varying harmonic content with changing φ on the bottom electrode, power deposition into electrons also varies, directly translating to changes in electron heating and ionization.

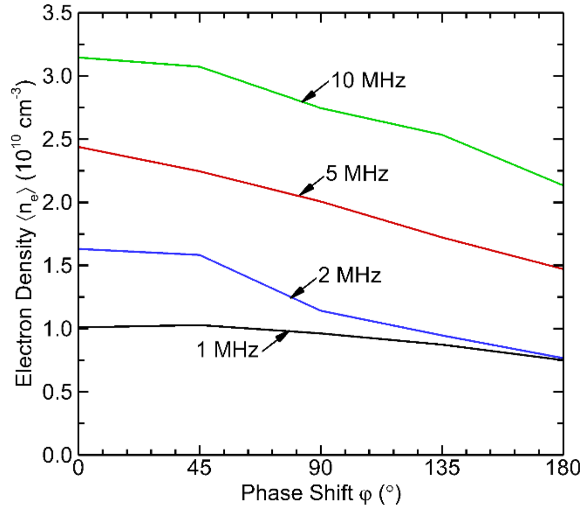

Figure 5.4: Average electron density as a function of phase shift φ for fundamental frequencies f_0 = 1 MHz to 10 MHz at constant applied voltage.

The decrease in electron density with increasing phase angle is at least partially the consequence of less efficient electron confinement. Electrons are largely confined to the bulk plasma by electric fields in the sheaths which point towards surfaces during the majority of the RF cycle. Electrons typically reach the surface (to balance positive ion current) by diffusion across the sheath during a short period during the anodic portion of the cycle. If transport by diffusion is insufficient to balance currents, an electric field reversal may occur to accelerate electrons towards the surface [13]. For $\varphi = 0°$ (peak waveform), the plasma sheath is nearly at its maximum width with the most negative sheath potential for the majority of the RF cycle, allowing electron transport to the surface only during the brief collapse in the sheath at the peak of the anodic portion of the

cycle. The opposite is true for φ = 180° where the plasma sheath is collapsed (anode-like) for most of the RF period, allowing electrons to transport to the bottom surface for a significantly longer fraction of the cycle.

With constant voltage (V_T = 300 V, V_0 = 1500 V), power deposition from the top electrode is a function of the bulk plasma properties and not independent of the bottom electrode power coupling. Power deposition as a function of phase angle φ and fundamental frequency f_0 are shown in Figure 5.5a for the top electrode (P_T) and Figure 5.5b for the bottom electrode (P_0).

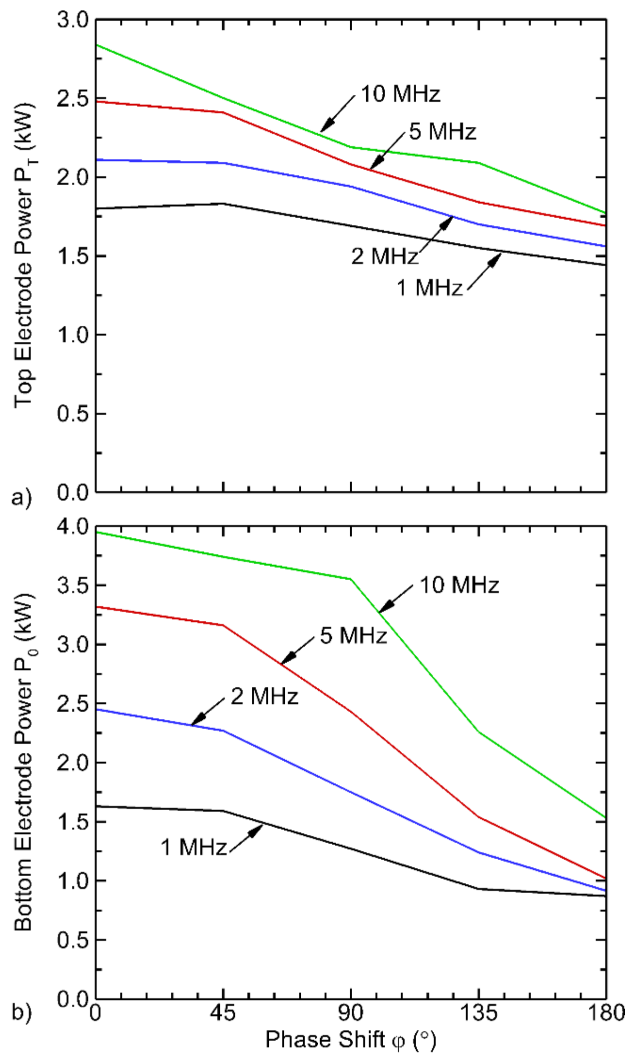

Figure 5.5: Power deposition for a) top electrode and b) bottom electrode as a function of phase shift φ for fundamental frequencies f_0 = 1 MHz to 10 MHz.

Higher fundamental frequencies f_0 on the bottom electrode produce more efficient electron heating and higher power deposition for a fixed voltage. For our conditions, electron power deposition is dominated by stochastic heating resulting from sheath expansion (or sheath speed) which is more rapid and occurs more often at higher frequencies. Increasing the fundamental frequency f_0 of the voltage on the bottom electrode therefore leads to a significant increase in power deposition, P_B. However, this relation is non-linear. A ten-fold increase in frequency f_0 (1 MHz to 10 MHz) only results in a 1.5 ($\varphi = 180°$) to 2 ($\varphi = 0°$) increase in P_B. These trends in power deposition with frequency directly translate to the corresponding trends in n_e as shown in Figure 5.4. Smaller phase angles have more rapidly expanding sheaths producing more electron heating, leading to an increase in P_B. With constant top voltage V_T, additional electron heating produced by P_B which increases electron density translates to an increase in power deposition by the top electrode, P_T.

As described in Chapter 1, the dependence of V_{dc} on the shape of the applied waveform through the generation of the electrical asymmetry effect (EAE) given by Eq. (1.53) [14–17]. This relation implies that the magnitude of V_{dc} is largest (most negative) for $\varphi = 0°$ and decreases with increasing φ (becoming more positive). The values of V_{dc} produced by the model, shown in Figure 5.6a as a function of phase shift φ for fundamental frequencies $f_0 = 1$, 2, 5 and 10 MHz, generally verify this scaling. $|V_{dc}|$ tends to decrease with increasing φ for all frequencies (the negative V_{dc} becoming more positive). A few discrete exceptions occur, for example $f_0 = 5$ MHz, $\varphi = 0°$; and $f_0 = 1$ MHz, $\varphi = 180°$. These exceptions are likely due to effects such as contributions of V_{dc} to secondary electron emission produced ionization, relative contributions of conduction and displacement current in a geometrically complex reactor and electronegativity of the plasma which are not explicitly included in the theory leading to Eq. (1.53).

The mean ion energies striking the wafer are shown in Figure 5.6b as a function of phase shift φ for fundamental frequencies f_0 = 1, 2, 5 and 10 MHz. The expectation is that mean ion energy should closely track the magnitude of V_{dc} with a change phase shift φ. This expectation is met for the highest frequency 10 MHz. At lower frequencies, beginning with 5 MHz, the correlation of mean ion energy with magnitude of V_{dc} as a function of phase shift φ begins to break down. At 1 MHz, the mean ion energy increases with phase shift while magnitude of V_{dc} is constant or is decreasing.

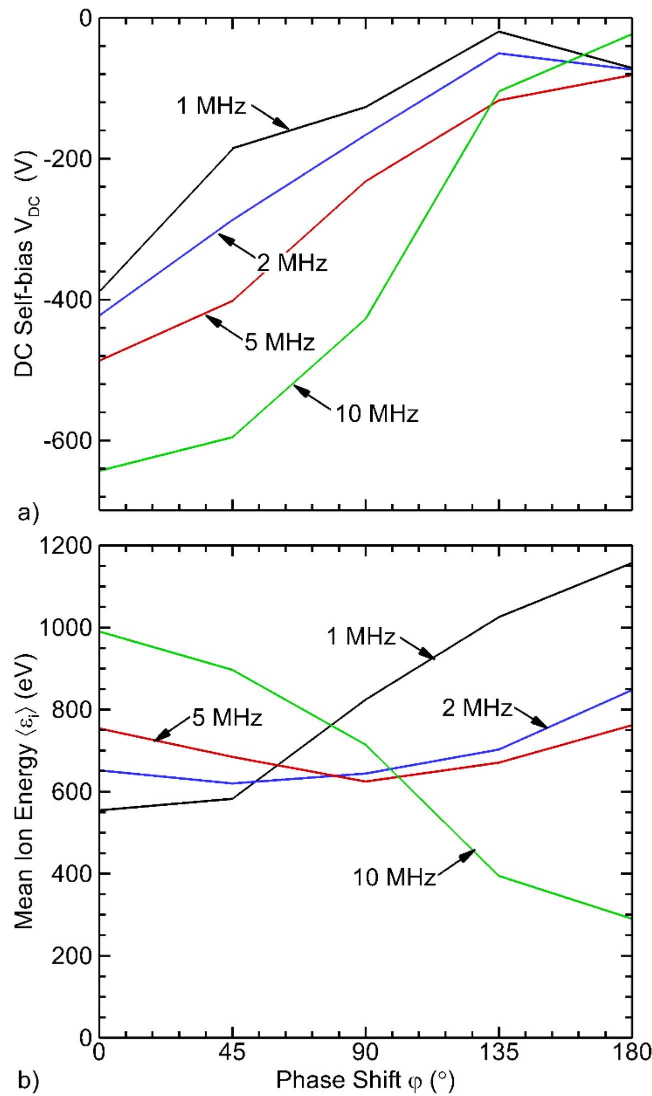

Figure 5.6: Plasma properties as a function of phase shift φ for different fundamental frequencies f_0 = 1 MHz to 10 MHz for constant voltage. a) V_{dc}. b) Mean ion energy incident onto the wafer.

Recall that V_{dc} results from the requirement that the current flowing to each electrode (powered and grounded) be equal over the RF cycle. In our model, currents are computed at the electrode surface. If that surface is in direct contact with the plasma, the current consists of both conduction current (charged particles flowing to the surface) and displacement current ($\vec{j}_D = \partial\left(\varepsilon\vec{E}\right)/\partial t$). If the electrode is in contact with a conductive material that is in contact with the plasma, such as the wafer, the current collected by the electrode consists of conduction current (through the wafer) and displacement current. If the electrode is buried beneath or within non-conducting dielectrics, the current the electrode collects is only displacement current. Contributions of displacement current to the bottom electrode may originate from charging of the top and sides of the focus ring. With the ratio of conduction to displacement current being functions of frequency which differs for top and bottom electrodes, there is no expectation that V_{dc} should be independent of frequency.

Another factor that may affect V_{dc} with frequency is electron heating. With electron heating being dominated by sheath expansion, higher bias frequencies f_0 produce more electron heating adjacent to the sheath at the bottom electrode for any given voltage amplitude. With increasing f_0 this increase in local as well as bulk electron density n_e leads to a decrease in shielding lengths λ_D and a decrease in the sheath width d_s at the bottom electrode. The end result is a change in the ratio of surface adjacent ion densities ($n_{sp} \setminus n_{sg}$). As described by Eq. 1.51 and 1.53 this change directly translates to a change in the V_{dc}.

An ion's ability to react to temporally changing electric fields in the sheath is related to the time required for the ion to cross the sheath, ΔT, compared to the RF period, $1/\nu_{RF}$, described by the sheath ion inertia coefficient,

$$S = \Delta T \nu_{RF} = \nu_{RF} \left(\frac{2 d_s^2 m_i}{q V_S} \right)^{1/2} \tag{5.1}$$

where d_s is the average sheath thickness, V_S is the average sheath potential, m_i is the ion mass and q is the elementary charge. For S > 1, ions typically do not dynamically respond to changes in the electric field that occur in the sheath (high frequency, large mass, thick sheath). Ions transiting through sheaths whose oscillation frequency produces S >> 1 arrive at the surface with an energy close to the average sheath potential. Although this scaling assumes a sinusoidal voltage with a single ion species, it can nevertheless serve as a general guide to understanding the frequency dependent trends in average ion energy onto the wafer shown in Figure 5.6b.

S depends on the value of the sheath width. Defining a precise criterion for location of the sheath-bulk plasma transition is an active area of research [18–27] and beyond the scope of this work. In this work the sheath edge is defined as the location at which the sheath electric field has decayed to 10^{-3} of its maximum value. The resulting sheath thickness is shown in Figure 5.7a as a function of the fundamental frequency f_0 with $\varphi = 0°$.

Since the sheath thickness is generally inversely proportional to plasma density at the sheath edge, which increases with f_0, the sheath thickness decreases with increasing frequency. S as a function of f_0 for $\varphi = 0°$ is shown in Figure 5.7b. Consistent with the premise above, non-dynamic ion transport through the sheath with S > 1 occurs for $f_0 = 10$ MHz. Dynamic transport behavior where ions react to time variations of electric field in the sheath with S < 1 occurs for $f_0 = 1$ MHz. As such, at the high end of frequencies the ion dynamics are dominated by time averaged sheath properties, such as the DC self-bias, V_{dc}. It is for that reason, that mean ion energy as a function of phase angle for $f_0 = 10$ MHz scales proportionally to the magnitude of V_{dc}, as shown in Figure 5.6b.

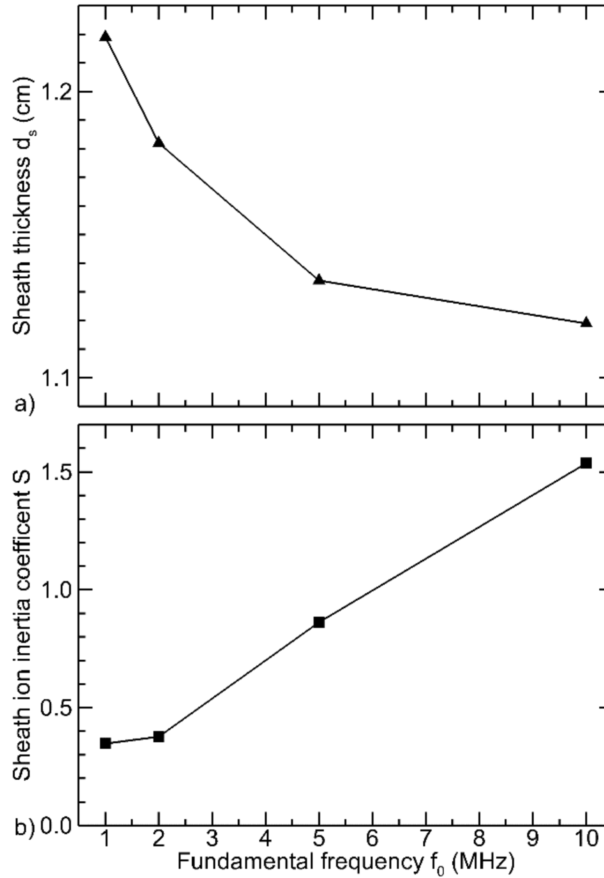

Figure 5.7: Sheath properties as a function of fundamental frequency f_0 for $\varphi = 0°$ at constant voltage. a) Sheath thickness ds and b) sheath ion inertia coefficient S.

Moving to lower fundamental frequencies f_0 the trend for average ion energy as a function of phase angle φ reverses. At low f_0 the average ion energy increases with increasing φ. Lowering the fundamental frequency results in the sheath modulation time scales approaching a regime in which ions can dynamically react to transients in the electric fields. For example, compare the voltage waveforms shown in Figure 1.14 for $\varphi = 0°$ (peak) and $\varphi = 180°$ (valley). Assuming dynamically reacting (positive) ions ($S < 1$), the maximum ion flux to the electrode occurs when the applied voltage is most negative. At $\varphi = 0°$ the applied potential is negative with respect to the plasma for most of the RF period. However, the minimum sheath potential, V_{min}, has a smaller magnitude than for $\varphi = 180°$. It is this ability of the ions to (at least partially) react to applied

voltage transients that results in their incident energy onto the surface to scale with the DC self-bias at high frequencies and the applied minimum potential at low frequencies.

The incident average energies of select ion species as a function of atomic mass for f_0 = 1 MHz and φ = 180° are shown in Figure 5.8.

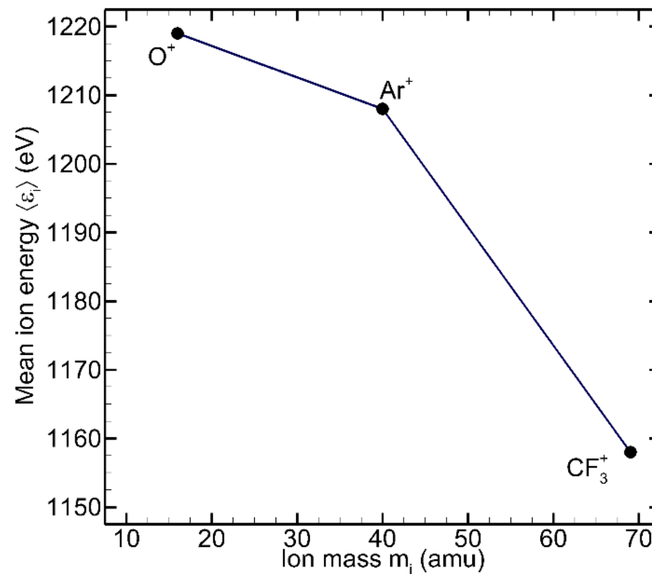

Figure 5.8: Incident average energy of select ion species as a function of mass.

Due to their lower inertia, the lighter O^+ ions can more rapidly react to changes in the electric field than heavier species such as CF_3^+. Consequently, the lighter ions can reach an energy closer to the maximum sheath potential drop during the small fraction of the RF period when the potential is most negative. While the average ion energies differ by approximately 60 eV which is only about 5% of the total, these trends illustrate the relation between the average ion energy and the ion's ability to dynamically react to transient fields. This scaling is also shown by the trends in the IEADs collected at the wafer surface shown in Figure 5.9 for f_0 = 1 MHz and 10 MHz for phase shifts φ = 0, 45, 90, 135 and 180°. At the lowest frequency the increase average energy with φ is mirrored in the IEAD where the mean energy is roughly equal to $-V_{dc} - |V_{min}|$.

As with the respective average energies onto the surface, there are significant differences in the trends for IEADs as a function of φ between the low and high fundamental frequencies. Overall, with f_0 = 10 MHz both maximum and average energies trend downwards with increasing φ while maintaining an approximately constant spread in energy.

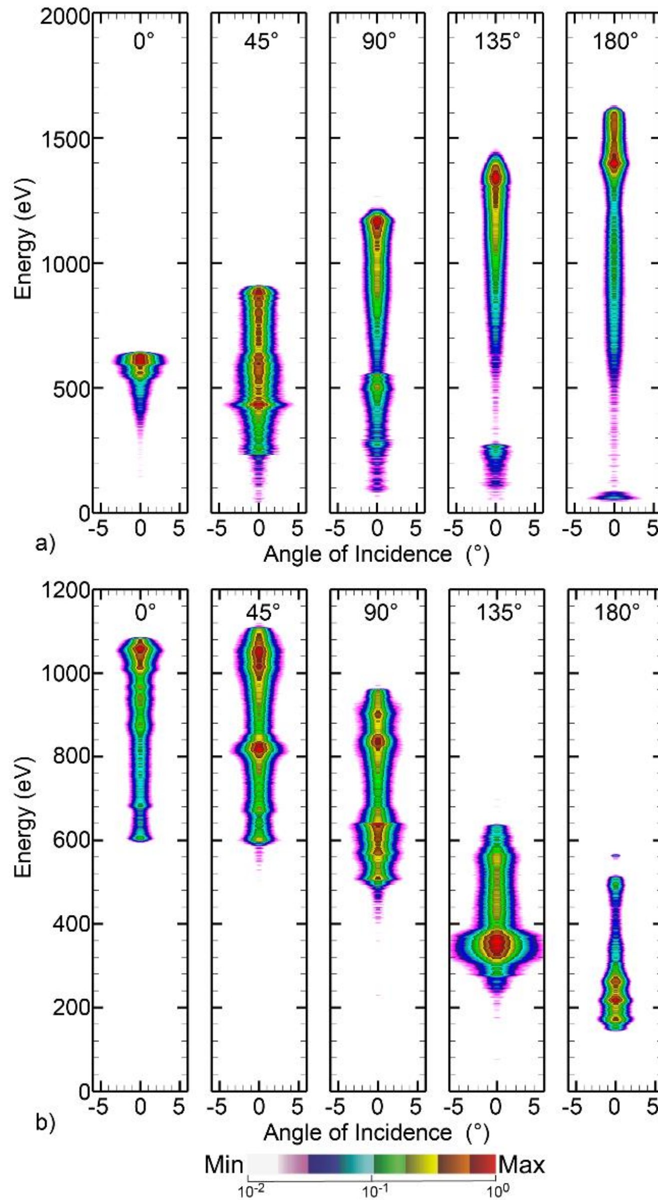

Figure 5.9: IEADs as a function of phase shift φ for fundamental frequencies a) f_0 = 1 MHz and b) f_0 = 10 MHz at constant applied voltage. Values are plotted on a 2-decade log scale.

Two distinct regimes for the behavior of average ion energy and IEAD with respect to the `phase angle (and V_{dc}) can be defined: The first is the *steady state ion regime* having S >1 (large f_0) in which average ion energy onto the surface is well correlated to the magnitude of V_{dc}, with the average energy being maximum at $\varphi = 0°$ and minimum at $\varphi = 180°$. The second is the *dynamic ion regime* having S < 1 (small f_0) where average ion energy and the IEAD are dominated by the temporal response of the ions to the applied voltage waveforms – with the average ion energy being minimum at $\varphi = 0°$ and maximum at $\varphi = 180°$.

5.4 Reactor Scale Plasma Properties with Constant Applied Power

To better align with industry practice where power (as opposed to voltage) is the control variable, simulations were performed in which the total power deposition was held constant for both electrodes while varying frequency and phase angle of the waveform on the bottom electrode. This was achieved by adjusting the voltage on the top electrode, V_T and bottom electrode, V_0, to deliver power depositions of $P_T = P_0 = 2000$ W.

The voltage amplitudes applied to the top electrode V_T are shown in Figure 5.10a as a function of phase shift φ for fundamental frequencies f_0 = 1 MHz to 10 MHz. The mean electron density as a function of φ for f_0 = 1 to 10 MHz is shown in Figure 5.11. When delivering constant power, V_T is a weak function of φ for a given f_0. However, the V_T decreases with increasing f_0. For a given f_0 with power delivered though the bottom electrode being held constant, the plasma density and so total impedance of the system does not significantly vary with φ. Consequently, the change in V_T with φ to deliver constant power is small. However, with increasing f_0, the fraction of power delivered by the bottom electrode devoted to ion acceleration decreases and that delivered to electron heating increases, which for constant power, produces an increase in electron density and decrease in impedance. A lower V_T is then required to deliver constant power.

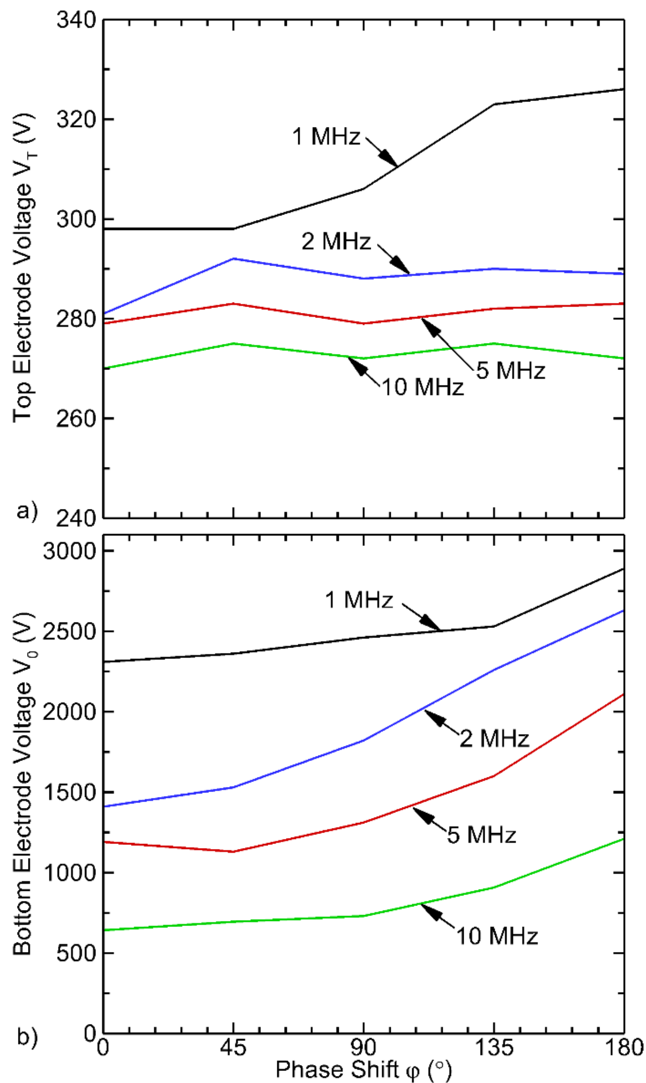

Figure 5.10: Applied voltage for constant power (2000 W) as function of phase shift φ for fundamental frequencies f_0 = 1 to 10 MHz applied to the bottom electrode. a) Top electrode and b) bottom electrode.

The voltage applied to the bottom electrode, V_0, with respect to f_0 and φ is shown in Figure 5.10b for constant power deposition. Power deposition for constant voltage and f_0 generally decreases with increasing φ, as shown in Figure 5.5. To recoup this decrease in power to maintain constant power, V_0 increases with increasing φ. The thickness of the sheath adjacent to the bottom electrode d_s and the sheath ion inertia coefficient S as a function of f_0 are shown in Figure 5.12 for $\varphi = 0°$ at constant voltage. With d_s being a function of the electron density, which increases with

f_0, the sheath thickness decreases. This reduction in d_s contributes to a decrease in S. However, this effect is dominated by the changes in f_0 and V_s, ultimately resulting in an increase of S with f_0. This trend indicates that with constant power, a transition also occurs from the *steady state ion regime* to the *dynamic ion regime* occurs as a function of f_0.

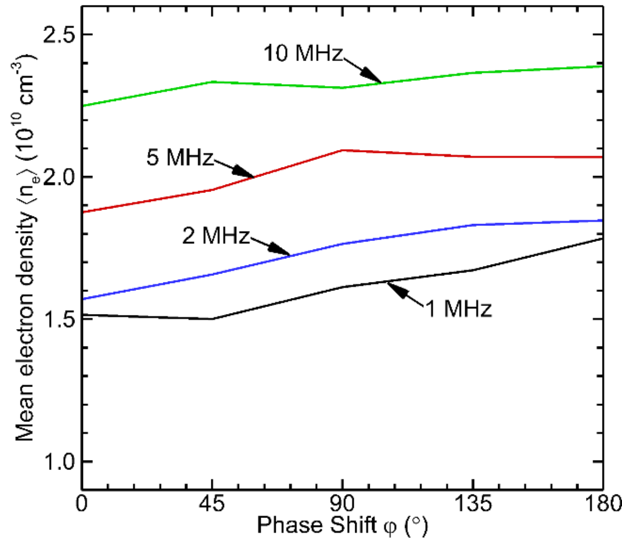

Figure 5.11: Mean electron density as a function of phase shift φ for fundamental frequencies f_0 = 1 MHz to 10 MHz at constant applied power.

The DC self-bias V_{dc} as a function of phase angle φ for f_0 = 1 MHz to 10 MHz is shown in Figure 5.13a while maintaining constant power. The trends with φ are similar to those when keeping voltage constant, shown in Figure 5.6a, where the magnitude of V_{dc} decreases (becomes more positive) with φ due to the electrical asymmetry effect. However, when holding power constant, the amplitude of V_0 decreases with increasing f_0 due to there being a larger proportion of power being more efficiently dissipated by electron heating. With a decrease in amplitude of V_0, the magnitude of V_{dc} decreases, becoming more positive.

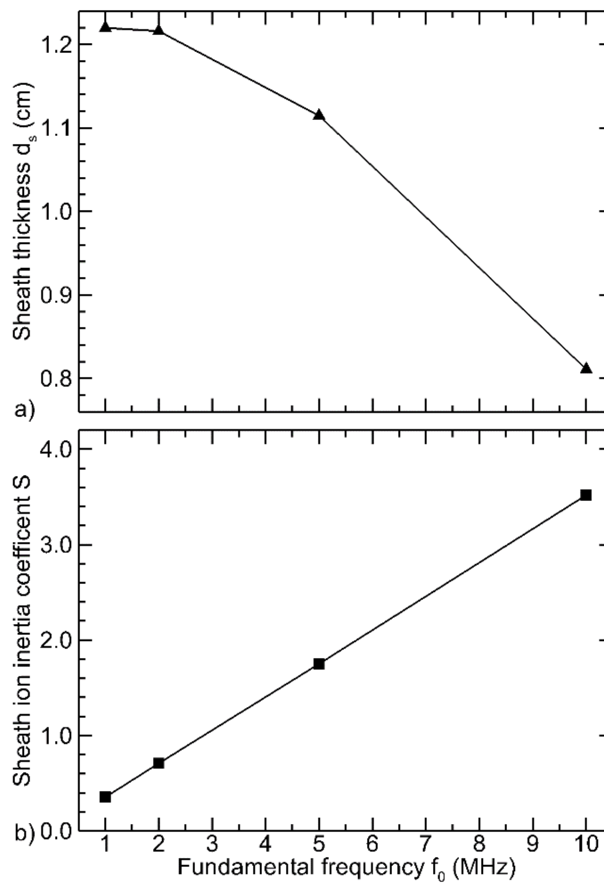

Figure 5.12: Sheath properties as a function of fundamental frequency f_0 for $\varphi = 0°$ at constant power. a) Sheath thickness d_s and b) sheath ion inertia coefficient S.

The average ion energies onto the wafer are shown in Figure 5.13b as a function of phase shift φ for $f_0 = 1$ MHz to 10 MHz. The corresponding IEADs as a function of phase shift φ for $f_0 =$ 1 MHz and $f_0 =$10 MHz are shown in Figure 5.14. As when holding V_0 constant, for higher frequencies the average ion energies scale with the magnitude of V_{dc} due to the inability of the ions to dynamically react to the transients in applied voltage. For $f_0 = 10$ MHz and $f_0 = 5$ MHz this leads to a decrease in average energy onto the wafer with increasing phase angle. As with constant voltage, at low frequencies f_0, the average ion energies are poorly correlated (and, in fact, anti-correlated) with V_{dc} and instead reflect the maximum sheath potentials.

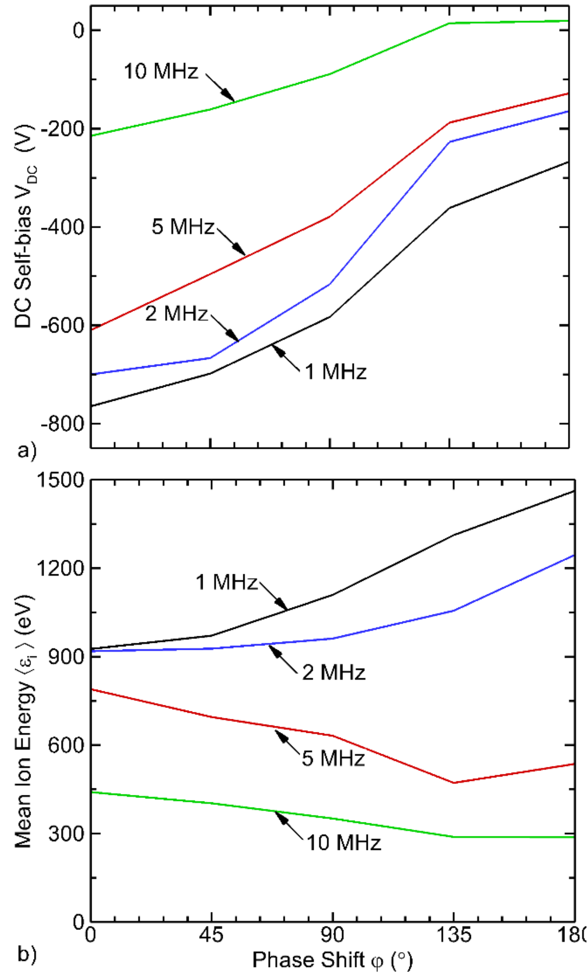

Figure 5.13: Plasma parameters as a function of phase shift φ for fundamental frequencies f_0 = 1 MHz to 10 MHz at constant power. a) DC self-bias and b) Mean ion energy delivered to the wafer.

As a result of the applied voltage no longer being constant, the resulting average ion energies are strong functions of phase shift φ for fundamental frequencies f_0. For example, the mean energies at 1 MHz are larger than those at 10 MHz by a factor of 2 for $\varphi = 0$ ° and 4.5 at φ = 180 °. These similarities and differences in mean ion energy between the constant voltage and constant power cases translate to the respective IEADs. At the lowest frequency (f_0 = 1 MHz) the IEADs for φ = 0 and 180° are more monoenergetic, reflecting the applied waveforms. The shapes of the applied voltage for these phase shifts roughly consist of a plateau and a singular well-defined short excursion to a maximum at $\varphi = 0°$ and to a minimum at $\varphi = 180°$. The intermediate cases (φ

= 45, 90 and 135°) do not have similar monoenergetic structures as the applied waveforms themselves do not predominantly consist of a stable voltage plateau or singular peak.

Desired anisotropic etch profiles require a balance of polymer deposition and activation energy delivered by ions and hot neutrals whose rates are largely determined but the magnitude of the reactive fluxes arriving on the surface.

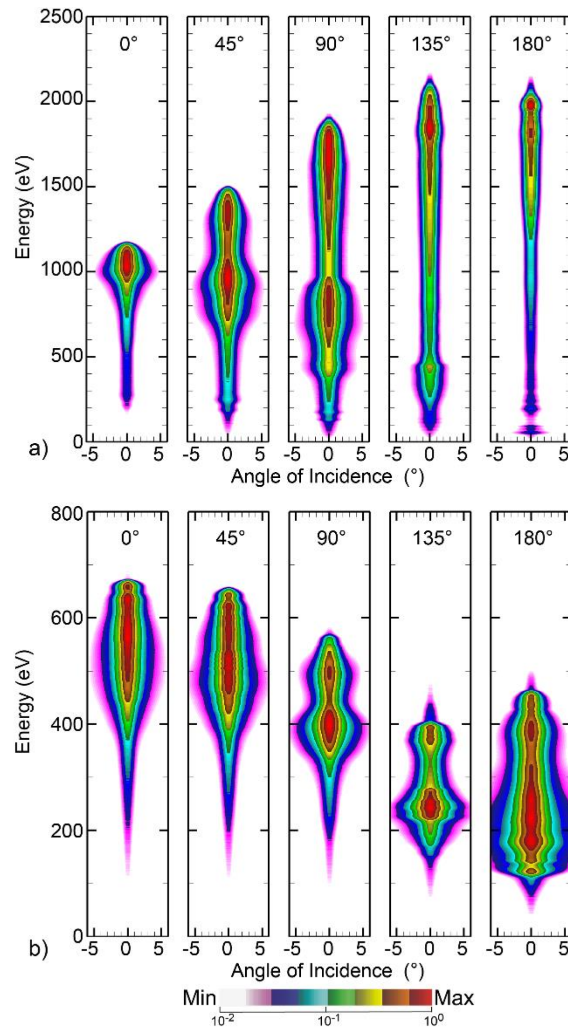

Figure 5.14: IEADs as a function of phase shift φ with constant power for fundamental frequencies a) f_0 = 1 and b) 10 MHz. Values are plotted on a 2-decade log scale.

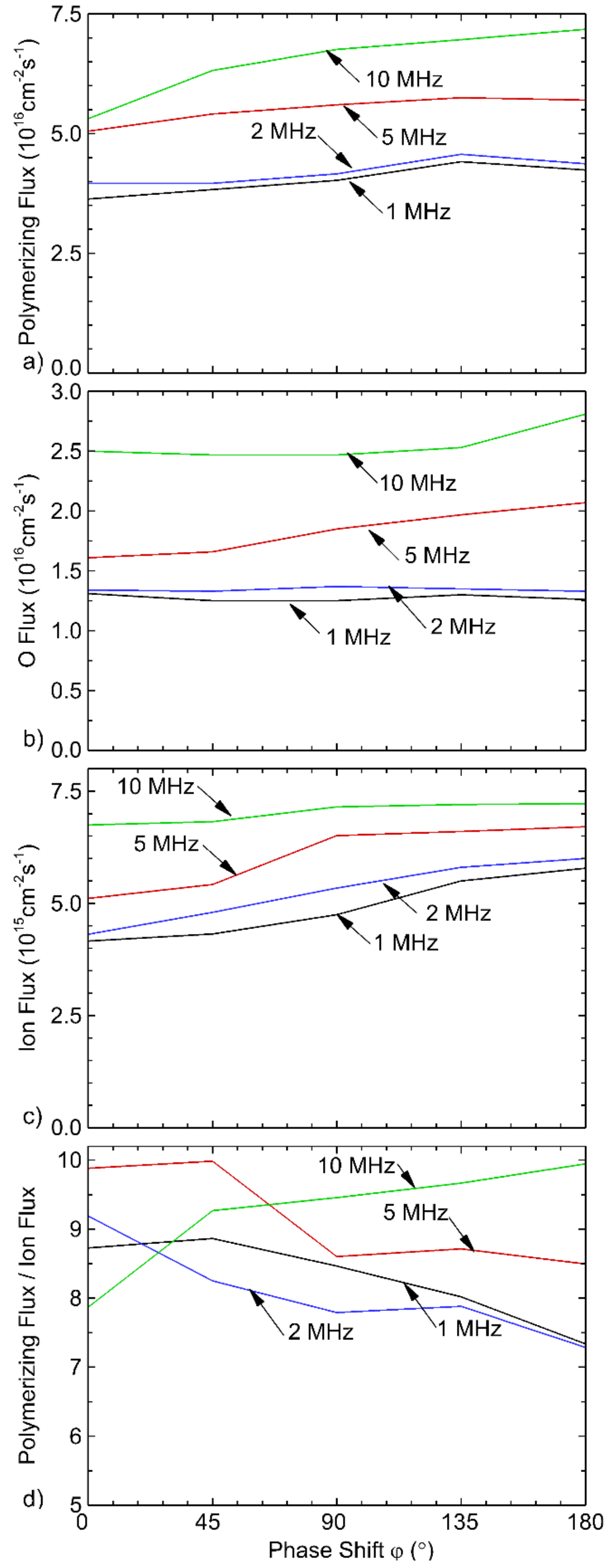

Figure 5.15: Fluxes to the wafer as a function of phase shift φ for fundamental frequencies f_0 = 1 to 10 MHz while keeping power constant. a) Total polymerizing flux, b) O-atom flux, c) total ion flux and d) ratio of polymerizing flux to ion flux.

The generation of oxide-polymer-complexes which enables selective removal of the SiO_2 is correlated to the incident flux of the polymerizing C_xF_y gas phase species, which are shown as a function of φ and f_0 in Figure 5.15a. The overall trends are that polymerizing fluxes are weak functions of phase angle φ while generally increasing with increasing f_0 on the bottom electrode. With increasing f_0, a larger proportion of bias power is dissipated by electron heating, which then produces a larger rate of dissociation of the CF_4 feedstock gas. With increasing phase angle, the sheath is collapsed for a greater fraction of the cycle, thereby moving the effective (time average) sheath edge closer to the wafer. This shift in sheath edge places radical production closer to the wafer, and so increases fluxes.

The thickness of the polymer layer by deposition is balanced by chemical, isotropic etching by O radicals and anisotropic sputtering by directional ions. The time and spatial average fluxes to the wafer of atomic oxygen, O, the most prevalent oxygen radical are shown in Figure 5.15b. The general trends reflect those of the polymerizing fluxes (Fig 16a), fluxes that increase with φ and f_0.

The magnitude of the ion flux, shown in Figure 5.15c, has a first order effect on etch rates and feature quality. Applied electric fields directly influence charged particle transport, whereas electron impact dissociation, excitation and ionization are at least one step removed as these phenomena occur as a result of electron collisions following their acceleration by electric fields. The dominant mechanism for ion power deposition is through sheath acceleration which, assuming a collision-less sheath, is proportional to the product of ion flux and incident ion energy. Assuming a constant fraction of power deposition by ion acceleration, a decrease in incident ion energy would necessitate an increase in ion flux to maintain the desired power. This is the trend for f_0 =5 MHz and 10 MHz in which the trend of ion-flux with phase angle is opposite that of the ion energy. This

explanation fails to capture the low frequency behavior in ion flux where an increasing fraction of the constant power deposition is due to electron heating.

5.5 SiO_2 Etching at Constant Power

To characterize the consequences of reactant fluxes and IEADs on SiO_2 etch properties, profile simulations were performed for f_0 = 1 MHz and 10 MHz for phase angles φ = 0° to 180° while maintaining constant power. The resulting features for f_0 = 1 MHz are shown in Figure 5.16.

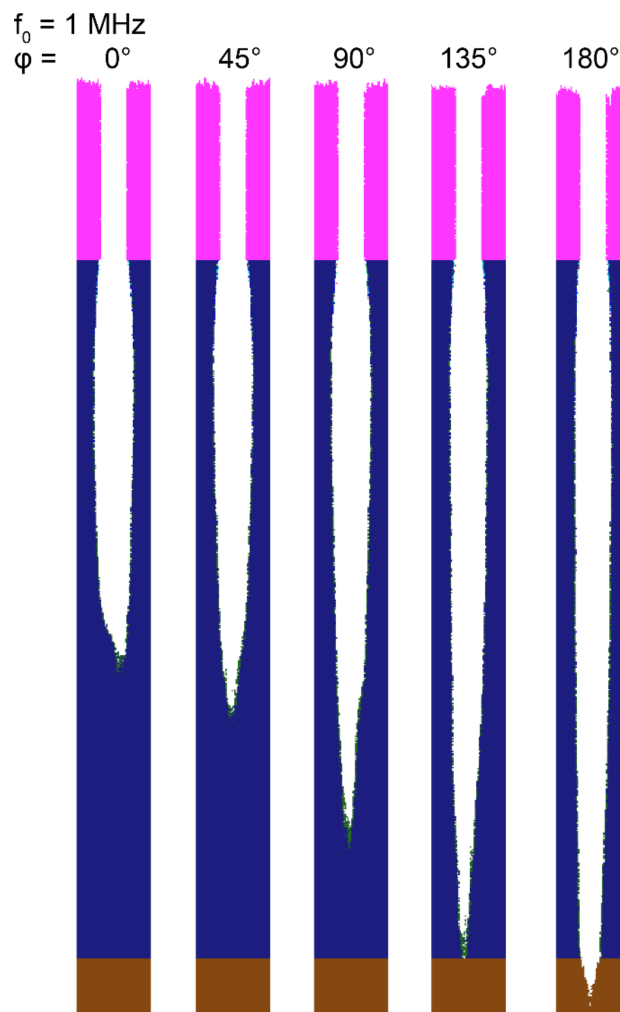

Figure 5.16: Predictions for etch profiles in SiO_2 at constant power with fundamental frequency f_0 = 1 MHz and varying phase angles φ.

For constant processing time, etching through the entire 3000 nm thick SiO_2 layer only occurred for $\varphi = 180°$ while for $\varphi = 0°$ the final etch depth is 1600 nm. The total relative etch rates are 0.53, 0.6, 0.78, 0.93 and 1.0 for $\varphi = 0°$, 45°, 90°, 135°, and 180° respectively. This trend is directly correlated to the trend in incident ion energy. Higher ion energies generally more rapidly remove SiO_2 by direct or chemically enhanced sputtering and retain their ability to do so after losing energy to grazing sidewall collisions. The profiles produced by IEADs at higher φ have more desirable characteristics such as straighter sidewalls and less overall bowing. This benefit is a direct consequence of the narrower angular distribution of the incident ions. The SiO_2 etch mechanism contains a SiO_2-polymer complex which requires fluorocarbon radical fluxes as reactants. Since these fluxes have a small increase with φ (Figure 5.15a), the increased availability of reactants could also play a role in the increased etch rate if the etch progression is flux limited as is often the case in HAR features.

The results of the feature etching for f_0 = 10 MHz are shown in Figure 5.17. The overall etch rates are similar to those at f_0 =1 MHz while the incident ion energies are significantly lower overall. The trend in etch depth with phase angle is the opposite to that for f_0 = 1 MHz. With f_0 = 10 MHz, etch rates mildly decrease with increasing phase angle φ while increasing for f_0 = 1 MHz. These trends most directly follow from both the average ion energies and maximum ion energies trending higher with increasing phase angle φ at f_0 = 1 MHz while decreasing at f_0 = 10 MHz. A secondary effect is that ion fluxes are nearly constant with increasing phase angle at f_0 = 10 MHz while increasing at f_0 = 1 MHz. With chemical and physical sputtering rates depending on ion energy as $\varepsilon^{1/2}$, large increases in ion energy are required for significant increases in etch rates. That said, the likelihood for specular scattering from side walls increases with increasing ion energy, and so more energy is retained deeper into the feature upon grazing collisions with sidewalls. On

the other hand, for otherwise constant, non-rate limiting conditions, etch rates increase linearly with increases in ion flux.

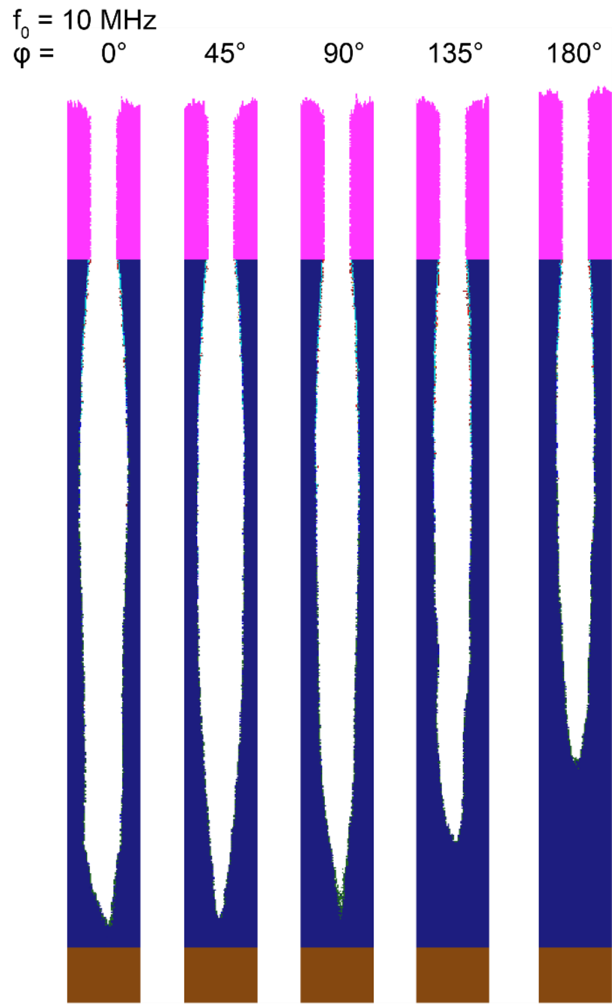

Figure 5.17: Predictions for etch profiles in SiO_2 at constant power with fundamental frequency f_0 = 10 MHz and varying phase angles φ.

While certainly an important parameter, ion energy is not the sole determining factor for etch rate. The etch process is based on a sensitive balance of surface passivation, activation and removal by fluxes of neutrals, ions and hot neutrals (generated by ions neutralizing during surface collisions). For each fundamental frequency, the ratio of these fluxes as function of φ is relatively constant, as shown in Figure 5.15d. Although ion energy and fluxes determine overall rate of

etching, the shape of the feature (e.g., sidewall slope, bowing) depend on relative rates of passivation by deposition, etching and sputtering. For example, for f_0 = 10 MHz, in spite of the higher etch rate with increasing phase angle, the features generally have less bowing, an effect that may be attributable to a larger ratio of polymerizing flux to ion flux. Large fluxes of passivating species typically produce more tapered features.

5.6 Concluding Remarks

Coupled reactor and feature scale simulations were performed to investigate the consequences of the fundamental driving frequency f_0 on the relation between DC self-bias V_{dc}, incident ion energy onto the wafer and reactive fluxes in dielectric etch processes using tailored voltage waveforms as a power source. For a set of waveforms based on consecutive harmonics for which the relative phase angle φ was varied from 0 to 180°, gas phase simulations were performed using fundamental frequencies f_0 = 1, 2, 5 and 10 MHz. While plasma conditions were found to differ when holding either voltage or power constant, the trends in V_{dc}, were qualitatively similar for the two scenarios. The magnitude of V_{dc} decreases (a negative bias becoming more positive) with increasing φ for all f_0 at constant voltage as well as power. Due to ion inertia, in the high frequency regime ion fluxes to the substrate are dominated by time average quantities such as the V_{dc} self. At low f_0, the ions are able to react transient characteristics in the sheath such as local extremes in the sheath potential directly produced by the applied tailored voltage waveforms.

The consequences of inertial effects on IEADs as a function of sinusoidal bias frequency are well known. The thick sheath regime corresponding to high frequency and large ion mass produces a single peaked IEAD. The thick sheath regime corresponding to low frequency and small mass produces a double peaked IEAD. The extension of these dependencies to VWT power sources is not straight forward due to the intrinsically more complex sheath structure and harmonic

content. The results of this study suggest that scaling of V_{dc} produced by processes akin to electrical asymmetry, a common goal sought when using voltage waveform tailoring, is particularly sensitive to the frequency regime of f_0. Low values of f_0 can result in significantly different trends of incident ion energy as a function of phase angle compared to high values of f_0. Incident ion energy is closely correlated to the V_{dc} self-bias at high values of f_0, maximum at $\varphi = 0°$ and minimum at $\varphi = 180°$. For low values of f_0, this correlation dissipates, and incident ion energy is instead dominated by the sheath dynamics of the applied voltage waveforms, maximum at $\varphi = 180°$ and minimum at $\varphi = 0°$.

The trends in ion energy (and IEADs) as a function of f_0 and φ directly impact the HAR etch process. Although the observations and conclusions made in this work are highly dependent on power deposition, plasma density, chemical composition and geometry, these observations also open additional avenues for process control. With 3-dimensional structures and atomic layer resolution already dominating industrial plasma etching processes, additional control strategies are required to achieve the desired critical dimensions. With frequency agile power supplies becoming more available, the combination of using VWT while varying fundamental frequency and phase angle provide new control opportunities.

5.7 References

[1] G. A. Skarphedinsson and J. T. Gudmundsson, Plasma Sources Sci Technol **29,** 084004 (2020).

[2] S. Brandt, B. Berger, E. Schüngel, I. Korolov, A. Derzsi, B. Bruneau, E. Johnson, T. Lafleur, D. O'Connell, M. Koepke, T. Gans, J. P. Booth, Z. Donkó and J. Schulze, Plasma Sources Sci Technol **25,** 17 (2016).

[3] P. Hartmann, L. Wang, K. Nösges, B. Berger, S. Wilczek, R. P. Brinkmann, T. Mussenbrock, Z. Juhasz, Z. Donkó, A. Derzsi, E. Lee and J. Schulze, J Phys D Appl Phys **54,** 255202 (2021).

[4] Z. Donkó, A. Derzsi, M. Vass, J. Schulze, E. Schuengel and S. Hamaguchi, Plasma Sources Sci Technol **27,** 104008 (2018).

[5] T. Lafleur, Plasma Sources Sci Technol **25,** 013001 (2015).

[6] J. Wang, S. Dine, J.-P. Booth and E. V. Johnson, Journal of Vacuum Science & Technology A: Vacuum, Surfaces, and Films **37,** 021303 (2019).

[7] F. Schmidt, J. Schulze, E. Johnson, J. P. Booth, D. Keil, D. M. French, J. Trieschmann and T. Mussenbrock, Plasma Sources Sci Technol **27,** 095012 (2018).

[8] C. Qu, Y. Sakiyama, P. Agarwal and M. J. Kushner, Journal of Vacuum Science & Technology A: Vacuum, Surfaces, and Films **39,** 52403 (2021).

[9] S. J. Lanham, J. Polito, Z. Xiong, U. R. Kortshagen and M. J. Kushner, J Appl Phys **132,** 73301 (2022).

[10] S. Huang, S. Shim, S. K. Nam and M. J. Kushner, Journal of Vacuum Science & Technology A: Vacuum, Surfaces, and Films **38,** 023001 (2020).

[11] S. Huang, C. Huard, S. Shim, S. K. Nam, I.-C. Song, S. Lu and M. J. Kushner, Journal of Vacuum Science & Technology A **37,** 031304 (2019).

[12] C. M. Huard, S. Sriraman, A. Paterson and M. J. Kushner, Journal of Vacuum Science & Technology A: Vacuum, Surfaces, and Films **36,** 06B101 (2018).

[13] J. Schulze, Z. Donkó, B. G. Heil, D. Luggenhölscher, T. Mussenbrock, R. P. Brinkmann and U. Czarnetzki, J Phys D Appl Phys **41,** 105214 (2008).

[14] B. G. Heil, U. Czarnetzki, R. P. Brinkmann and T. Mussenbrock, J Phys D Appl Phys **41,** 165202 (2008).

[15] U. Czarnetzki, J. Schulze, E. Schüngel and Z. Donkó, Plasma Sources Sci Technol **20,** 024010 (2011).

[16] J. Schulze, E. Schüngel, Z. Donkó and U. Czarnetzki, Plasma Sources Sci Technol **20,** 15017 (2011).

[17] S. J. Doyle, A. R. Gibson, R. W. Boswell, C. Charles and J. P. Dedrick, Plasma Sources Sci Technol **29,** 124002 (2020).

[18] L. P. Beving, M. M. Hopkins and S. D. Baalrud, Plasma Sources Sci Technol **31,** 084009 (2022).

[19] B. G. Heil, R. P. Brinkmann and U. Czarnetzki, J Phys D Appl Phys **41,** 225208 (2008).

[20] T. Shirafuji and K. Denpoh, Jpn J Appl Phys **57,** 06JG02 (2018).

[21] B. Mancinelli, L. Prevosto, J. C. Chamorro, F. O. Minotti and H. Kelly, Plasma Chemistry and Plasma Processing **38,** 147 (2018).

[22] O. Murillo, A. S. Mustafaev and V. S. Sukhomlinov, Technical Physics **64,** 1308 (2019).

[23] M. S. Benilov and N. A. Almeida, Phys Plasmas **26,** 123505 (2019).

[24] S. D. Baalrud, B. Scheiner, B. T. Yee, M. M. Hopkins and E. Barnat, Plasma Sources Sci Technol **29,** 053001 (2020).

[25] R. P. Brinkmann, J Phys D Appl Phys **42,** 194009 (2009).

[26] R. P. Brinkmann, J Phys D Appl Phys **44,** 042002 (2011).

[27] M. Klich, J. Löwer, S. Wilczek, T. Mussenbrock and R. P. Brinkmann, Plasma Sources Sci Technol **31,** 045014 (2022).

Chapter 6 Autonomous Hybrid Optimization of a SiO_2 Plasma Etching Mechanism

6.1 Introduction

The computational modeling of plasma etching processes is receiving new interest at least in part due to its ability to aid in the design and understanding of semiconductor device manufacturing and provide the basis for machine learning based optimization of processes [1–5]. In simulation of plasma etching, the framework typically includes a reactor scale model and a feature scale model [6–8]. The reactor scale model provides reactive fluxes, including their energy and angular distributions, that are used as input to the feature scale model [9][10]. There are several classes of feature scale models – using level-set-methods [11–14], statistical voxel approaches [15–17], and molecular dynamics (MD) [18,19]. Although MD methods are the most fundamental, they are currently computationally limited in the size of the feature that can be simulated and by availability of inter-particle potentials for complex chemistries. As a result, most full-feature scale capable models employ level set or statistical voxel methods with, in most cases, less fundamental reaction mechanisms.

Due to limits resulting from computational complexity and sometimes incomplete understanding of the physical process involved in plasma etching, feature profile simulations typically make use of simplified or reduce reaction mechanisms that use rate coefficients, reaction probabilities, threshold energies and energy and angular scaling to represent reactions between gas phase and surface species. The outcome of these reactions are the addition of material (deposition), removal of material (etching or sputtering) and its modification (passivation, implantation) [16,20,21]. The reaction mechanism and the coefficients and parameters that quantify the

mechanism are ideally based on either experimental observations or more complex computational models that do not allow for an efficient real-time evaluation.

Rapidly and accurately producing reaction mechanisms for profile simulation for novel materials, gas mixtures and temperature regimes, as in cryogenic etch processes [22–24], is challenging. This is particularly the case in data starved regimes, and so there is a need to robustly and efficiently adjust and improve reaction mechanisms. Classical optimization techniques as well as machine learning (ML) based approaches is an area of active research [4,25–28].

Applying ML techniques for process design is an expanding area of research where the increasing number of tunable parameters and complexity as well as highly non-linear behavior has rendered exhaustive sampling and rudimentary 'design of experiment' methods ineffective. Model-based feedback has proven effective at enabling precise, repeatable and stable process control [29–31]. Here the same issues with respect to data availability and consistency apply and the control models, too, are sometimes based on machine learning methods as well. This approach to virtual metrology has proven fairly effective as the efficient models often allow for rapid real time evaluation [32–36]. Other applications include the development of surrogate methods where statistical models are trained on actual experimental data or synthetically computed data to simulate the process as a whole or act as a sub model in a larger context [37,38], a practice especially common in large scale simulations of fusion plasmas [39–45]. Ideally, these models are capable of reproducing reactor and feature scale etch processes either directly as an outcome of the surrogate model or by interpolating between known results [46,47]. Generally, these types of approaches have underlying model structures that are valid in their training parameters space, however the parameters that are the outcome of the underlying model do not provide physical insight. Many of these data driven ML approaches are themselves fundamentally limited by the

availability or accuracy of the data used for training purposes. Producing this data is itself costly and time consuming, while the resulting trained ML based model may have limited applicability to process conditions outside the training set.

The challenge of needing large training sets of data has led to the use of physics informed ML and optimizations techniques where a lack of data is, to some degree, mitigated by the explicit use of physical formulations and models to reduce the degrees of freedom in the ML-derived model. Using this approach, a reaction mechanism can be built using known forms of probabilities of gas-surface interactions which may have poorly known coefficients. Using ML-methods to derive the physics-based coefficients should, in principle, produce a reaction mechanism that extends between the conditions of the training set.

These challenges specifically apply to the modeling of high aspect ratio (HAR) plasma etch processes [48–51]. The aspect ratio (AR) is the ratio of depth and to the width, most often given by the opening of a mask material. These processes are of relevance to the creation of vias, contact holes and isolation trenches [50]. Features are now produced for 3D memory devices having ARs approaching 100. Ideal HAR features have vertical side walls with widths replicating the mask with a minimum of bowing [52] or tapering [53]. There are many process-dependent challenges with make these outcomes difficult. For example, polymer deposition is a critical process in dielectric plasma etching in fluorocarbon gas mixtures [54,55]. A critical process challenge is the control polymer deposition in the upper regions of the mask during the etch process, which may result in necking and clogging [46,56,57]. *Necking* is the narrowing of the opening in the mask by polymer deposition. *Clogging* is closing of the mask opening by the deposition. Both necking and clogging result from the same processes with different degrees of severity. Clogging will stop etching while necking can limit neutral gas transport to the bottom,

trap etched surface species and shadow ions and photons into the feature. Modeling these processes, critical to feature optimization, is additionally challenged by lack of fundamental data.

Physics informed ML approaches to process development have taken the form of compact or reduced models. For example, through ML methods, reduced reaction mechanisms can be generated [58–60]. In a reduced reaction mechanism, species or reactions for which the outcome is weakly dependent are removed from a comprehensive mechanism, resulting in a model that is computationally more efficient. Reduced reaction mechanisms, though more rapidly executing, are generally valid over a limited range of operation, such as power, gas mixture or pressure.

The optimization of the reaction mechanism itself has been investigated previously by similar means for simulations based on Monte Carlo approaches as well as simulations based on cellular automatons [61–65]. Optimization schemes such as evolutionary algorithms and particle swarm methods can require many evaluations of the model. This large number of evaluations can lead to a large computational expense or needing to reduce the domain over which the optimization is being performed, either spatially or in terms of interaction complexity (e.g. limiting the number of species).

In this paper, we discuss the development and application of a semi-autonomous optimization technique using a coupled gradient descent – Nelder Mead approach to derive physics-based coefficients for reactions mechanisms used in voxel-based feature simulation of plasma etching. The demonstration system is SiO_2 HAR plasma etching in a fluorocarbon gas mixture. The reactor scale simulations that provide reactant fluxes were performed with the Hybrid Plasma Equipment Model (HPEM). The feature scale simulations were performed with the Monte Carlo Feature Profile Model (MCFPM) described in Chapter 2.

A high-level overview of the optimization scheme is given in Section 6.2. The process to

be optimized as well as the simulation tools used for the gas phase and feature scale simulation are discussed in Section 6.3 and 6.4. Metrics for the optimization process are defined in Section 6.5. The optimization schemes are described in Sections 6.6 and 6.7 and the hybrid approach is motivated. Results of the optimization combined optimization are discussed in Section 6.8. To test the transferability of the derived mechanism, etch processes outside its original training regime were simulated, with those results being presented in 6.9. The simultaneous optimization of multiple features is investigated in Section 6.10. Concluding remarks are in Sec. 6.11.

6.2 Description of the Optimization Scheme

The goal of this work is to optimize the reaction mechanism that describes plasma-surface interactions for SiO_2 etching to best replicate experimental data, which is provided in the form of scanning electron microscopy (SEM) images. The optimization is centered around adjusting physics parameters, in the reaction mechanism, represented by scalar values p_i, each representing a physical quantity, contained in a parameter set

$$\mathbf{p} = \begin{pmatrix} p_1 \\ p_2 \\ \vdots \\ p_n \end{pmatrix} \qquad (6.1)$$

The size of the parameter space scales like $O(c^n)$ making exhaustive search algorithms impractical for even moderately large numbers of parameters. Enforcing constraints and relations based on prior physical knowledge of the likely range of p_i can help to reduce the total parameter space and enable the use of conventional optimization techniques. This physical knowledge is, in our case, implemented by using a well-established surface mechanism having poorly known reaction probabilities, and applying physically reasonable boundaries to those poorly known coefficients. The optimization scheme is based on a hybrid approach, combining a gradient descent

method [27,66,67] with a Nelder-Mead optimization scheme [68–70]. A top-level overview of the method is shown in Figure 6.1.

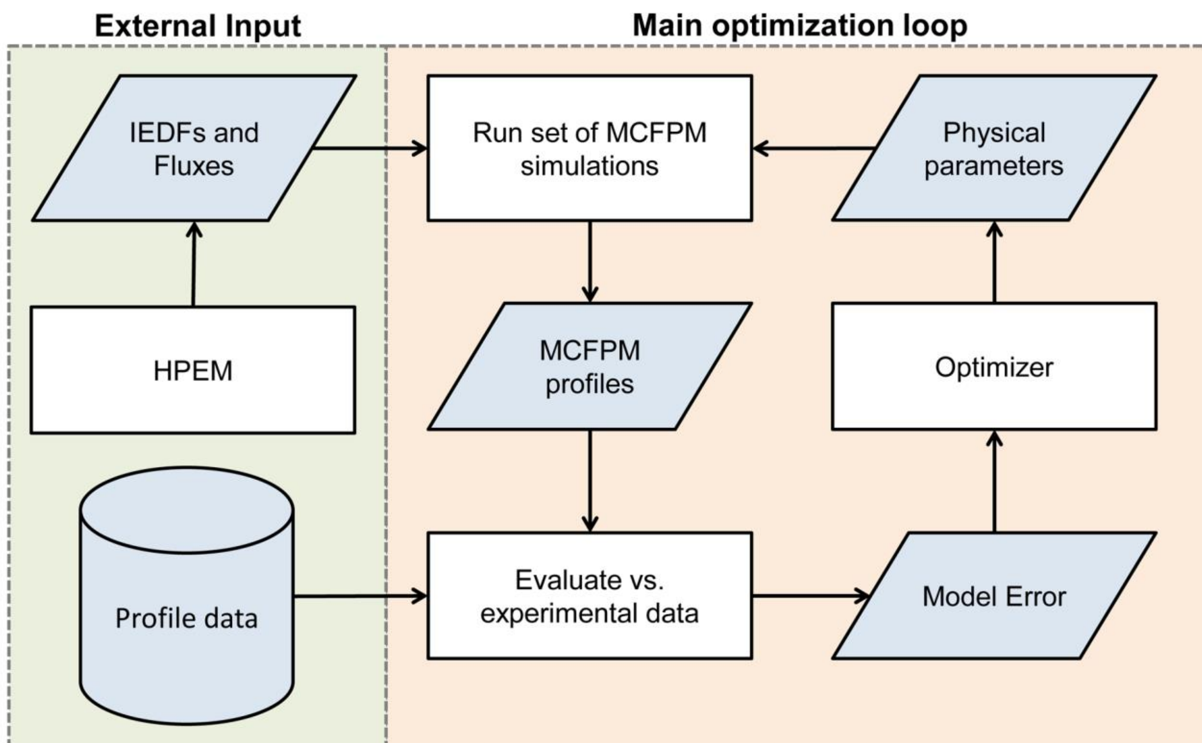

Figure 6.1: Global schematic of the optimization process.

The optimization setup requires external input (located on the left-hand side of Figure 6.1) which in the case are the reactant fluxes of radicals and ions, and their energy and angular distributions (EADs), that are incident onto the wafer being processed. These fluxes and EADs were provided by the HPEM using reactor conditions that produced the features that were imaged by the SEMS. A legitimate issue is the sensitivity of the optimized feature scale reaction mechanism to the accuracy of fluxes and EADs provided by the HPEM. Although this is an important discussion, it is beyond the scope of this particular investigation which is focused on developing the feature scale reaction mechanism. As such, the fluxes and EADs from the HPEM are treated as the *ground truth*. Details of the experiment and gas phase simulation are provided in

Section 6.3.

The gas phase fluxes and EADS are fed into MCFPM which performs the etch process simulations outlined in Section 6.4. The result of these simulations is compared to the features in the SEM images. Based on a set of geometric metrics, discussed in Section 6.5, a model error is determined. The data produced by the MCFPM and their differences to experimental data effectively act as the loss function to be minimized. The model error is used as the basis for the optimizer which iteratively adjusts the model parameters **p** to minimize the loss. This loop is repeated until the system converges.

6.3 Reactor Scale Plasma Simulation

The reactor scale gas phase simulations were performed using the Hybrid Plasma Equipment Model (HPEM), which is described in Section 2.1. The HPEM was used to model a capacitively coupled plasma sustained in a $C_4F_6/Ar/O_2$ gas mixture at 10 mTorr. In the base case the total gas flows were $C_4F_6/Ar/O_2$ = 140/100/105 sccm. The reactor configuration is shown in Figure 6.2.

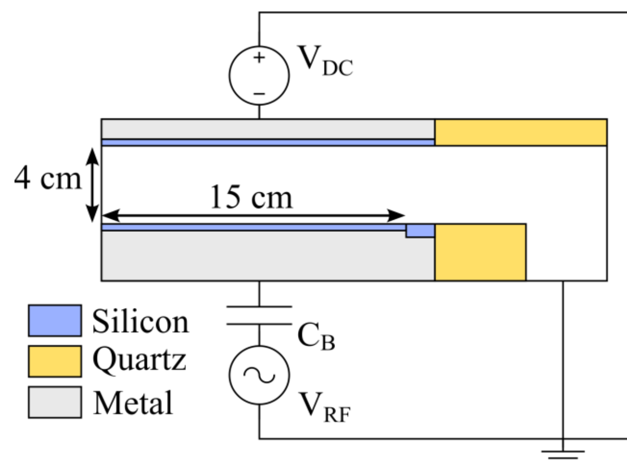

Figure 6.2: CCP reactor geometry and circuit.

Two electrodes with a radius of 15 cm are separated by a 4 cm gap. Dual radio frequency (RF) power V_{RF} is applied to the bottom electrode. The voltage waveform consists of low and high frequency components, $V_{rf}(t) = V_{lf} \sin(2\pi f_{lf} t) + V_{hf} \sin(2\pi f_{hf} t)$ with $f_{lf} = 1$ MHz and $f_{hf} = 40$ MHz. For the base case low frequency voltage, V_{lf} and high frequency voltage V_{hf}, were adjusted to supply powers of $P_{lf} = 8.0$ kW and $P_{hf} = 2.5$ kW. A negative DC bias of -500 V was applied to the top electrode, to deliver 650 W. The reaction mechanism is based on previous work [16,51].

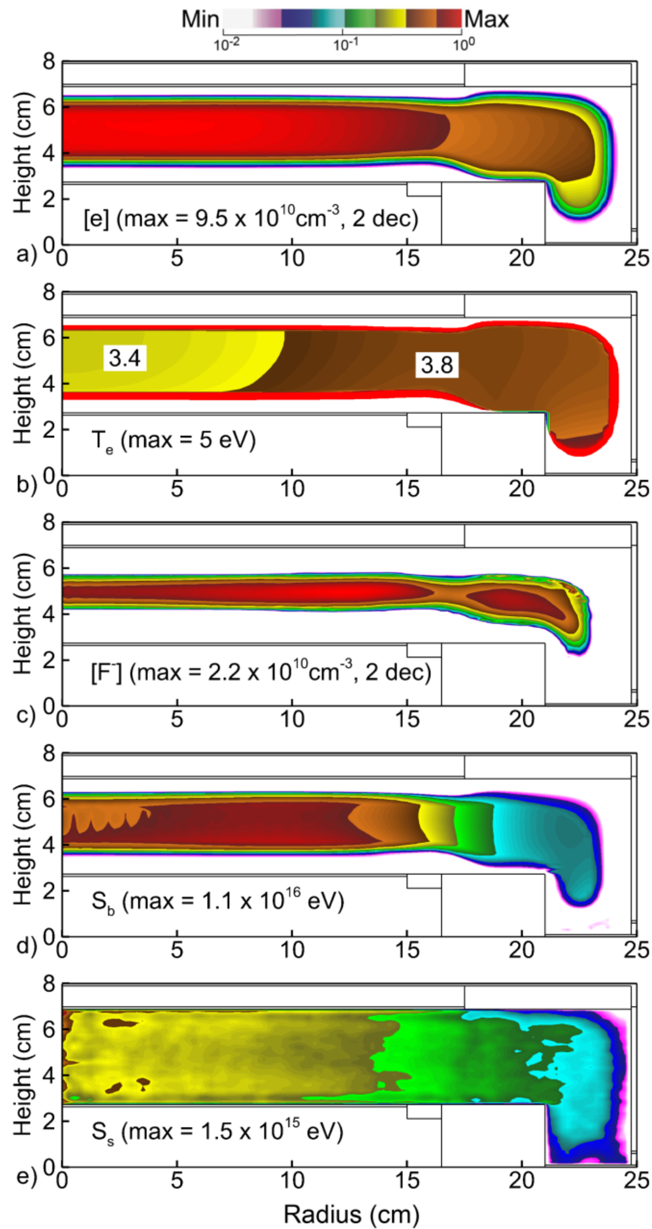

Figure 6.3: Plasma properties for the base case: a) Electron density [e], b) electron temperature T_e and c) negative fluorine ion Density [F^-], d) ionization rate by bulk electrons, e) ionization rate by secondary electrons.

The spatial distributions of the electron density [e], electron temperature, T_e, negative fluorine ion density [F^-], ionization by bulk electrons S_b, and ionization by secondary electrons S_s are shown in Figure 6.3.

Due to the large power input, the electron density is high, with a maximum value of 9.5 x 10^{10} cm^{-3}. The bulk electron temperature, shown for electron densities > 1.0×10^9 cm^3, is 3.4 to 3.8 eV over the wafer. High energy electrons are initially produced by secondary electron emission by ion bombardment, followed by acceleration in the sheaths. The electron source generated by bulk electrons S_b, mirrors that of [e] and T_e. Most of the ionization is produced by bulk processes. Ionization produced by sheath accelerated beam electrons plays a secondary but nevertheless important role in the overall ionization dynamics. Fluorine and oxygen containing plasmas can have significant densities of negative ions. The density of F^-, shown in Figure 6.3c, has the largest density of negative ion in this process with a maximum density of 2.2 x 10^{10} cm^{-3}. Due to the plasma having on the average, a positive electric potential, the F^- ions are confined to the center of the plasma. The negative ions have only a small overall effect on plasma transport dynamics to the wafer due to its negligible density close to the sheath region where its effect on electron heating dynamic would be the most important.

Plasma-surface interactions are almost entirely described by the fluxes of reactive species and ions, and their energy and angular distributions onto the surface. The fluxes of the most significant neutral and ion species incident onto the wafer at a radial position of 7.5 cm are listed in Table 6.1.

Table 6.1: Base case fluxes to wafer

Species	Flux ($cm^{-2}s^{-1}$)
C_3F_4	9.5×10^{16}
C_2F_3	6.8×10^{16}
CF	4.4×10^{16}
CF_2	9.4×10^{16}
CF_3	8.4×10^{15}
O	7.7×10^{16}

These fluxes include the fluorocarbons radicals most responsible for polymer deposition as well as atomic oxygen which etches and removes the polymer. The ratio of the flux of ions and neutrals to the wafer is an important parameter in the overall process dynamics. The anisotropy of the process is almost solely enabled by the directionality of ions incident onto the surface whereas the fluxes of neutral fluorocarbon radicals determine passivation. This is especially true for HAR processes in which the overall performance requires a precise balance of deposition and removal of polymerizing radical fluxes, both of which are either indirectly or directly dependent on the ion flux. neutral as well as ion fluxes.

In addition to the magnitude of the ion flux, the influence of energetic positive ion fluxes incident onto the surface and their transport through HAR features is sensitive to their energy and angular distribution (IEAD). The combined IEAD of all positive ion species is shown in Figure 6.4. Due to the large applied low frequency power, the sheath potential and commensurate DC self-bias, positive ions are accelerated vertically into the wafer while traversing the sheath. This leads to a narrow angular distribution of ions striking the wafer with energies up to 4800 eV, both properties being desirable in the context of HAR etch processes.

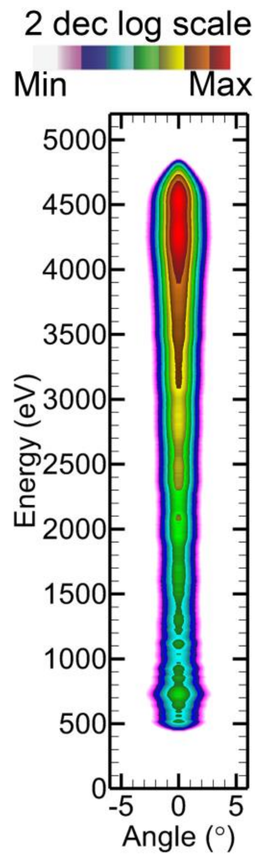

Figure 6.4: Ion Energy-Angular Distribution sampled at the wafer surface during the base case.

6.4 Surface Simulation Setup

The process investigated in this work is a HAR plasma etch into SiO_2 using an amorphous carbon (AC) mask, schematically shown in Figure 6.5. A SiO_2 substrate is covered by a 850 nm thick AC film patterned to contain an ideal, straight walled, opening with an initial width of 90 nm. The etch was performed for 60 seconds.

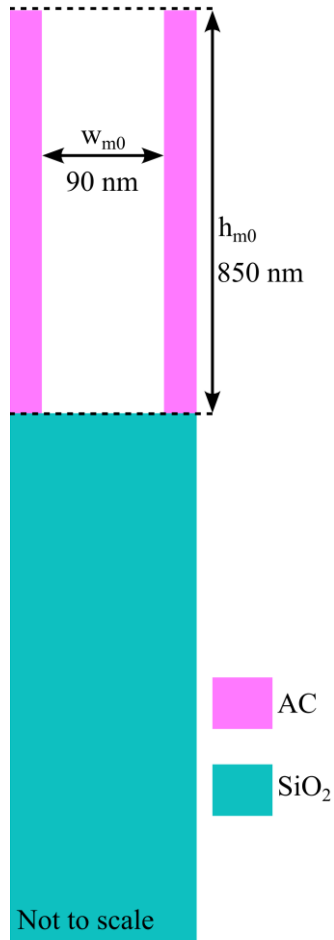

Figure 6.5: Feature scale simulation setup consisting of a SiO_2 substrate with an amorphous carbon mask.

The surface simulations were performed using the Monte Carlo Feature Scale Model (MCFPM) [16,50,74,75]. MCFPM is described in Section 2.2. The SiO_2 reaction mechanism is based on previous work by Huang et al [51] and is described in detail in [16]. A high-level overview of the mechanism is listed in Table 6.2. SiO_2 can be removed through physical sputtering by energetic ions and hot neutrals. The sputtered products can be redeposited on other surfaces. Unsaturated fluorocarbons can chemisorb on the SiO_2 to form an oxide -fluorocarbon complex. This complex is in turn easier to sputter based on a modified threshold (reduced total binding energy) and an overall higher reaction probability as the site has a lower binding energy. Additional

polymer can be deposited on top of the complex as well as other surfaces, providing a physical barrier to further etching and providing sidewall passivation. The polymer can be removed by physical sputtering or chemical etching by oxygen radicals. The only O-containing radical having significant fluxes to the surface is ground state atomic oxygen.

The gas phase reactions with the mask and substrate are ultimately contained in a single global reaction mechanism where they interact and share certain reactions, such as polymer deposition. A high-level overview of the AC mask reaction mechanism is in Table 2 and the full mechanism is described in Appendix B. The mechanism includes polymer deposition by C_xF_y precursors on AC and on prior deposited polymer. Similar to the etch mechanism for SiO_2, polymer is removed by oxygen radicals and physical sputtering. The AC can be sputtered by ions and hot neutrals as well.

The polymer, as deposited, consists of individual C_xF_y radicals and so is strictly an assembly of monomers. This radical based film can subsequently crosslink to create an actual polymeric material that is more resistant to sputtering. Ion bombardment can then break bonds (chain scission) to produce lower molecular weight polymer.

A polymer's physical and chemical properties can be dependent on crosslinks with neighboring species. The manner of linkage determines the reactivity of the polymer due to, for example, a lack of available radical sites for or more resistance to physical processes due to an increase in total bond strength. These crosslinks can be broken by exposure to energetic particles or radiation, for example through exposure to plasma. Since these energetic particles are typically delivered anisotropically to the surface, this spatially discriminate activation can result in shaping of the polymer deposition. The developed crosslinking mechanism used in this work is described in Section 2.2.3.

Since the control of necking and clogging by polymer deposition is of special interest, we discuss it as an important control parameter. The amount of polymer growth is determined by the ratio of deposition and removal. A steady state polymer thickness occurs when these contributions balance. Polymer removal occurs by sputtering and O-radical based etching. In oxygen rich gas mixtures, polymer removal can be dominated by O-radical based etching, mostly ground state atomic oxygen.

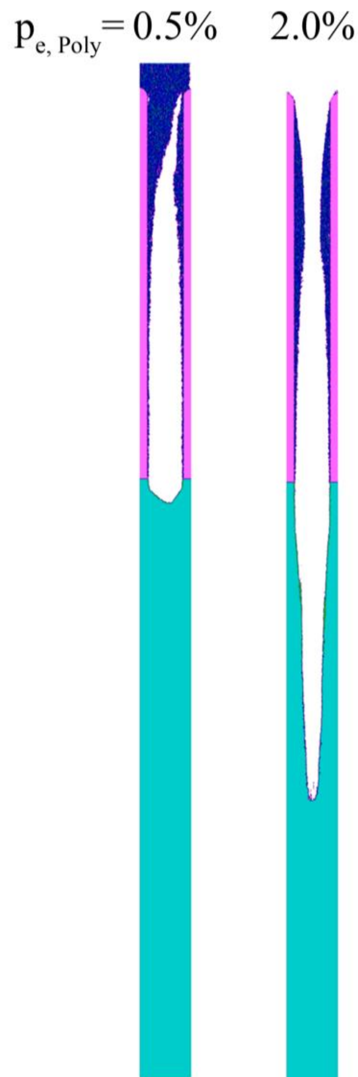

Figure 6.6: Etch features for different O based polymer etch probabilities 0.5% (left) and 2.0% (right).

In the mechanism discussed here, necking and clogging (the amount of polymer deposition in the mask region) can ultimately be controlled by the reaction probability of the O based polymer etch. The final etch profiles for otherwise identical process conditions are shown in Figure 6.6 while varying the probability of polymer etching by O-atoms. An etch probability of 0.5% results in net polymer growth which ultimately leads to a complete clog at the top of the feature. Higher removal probabilities, while still producing significant necking, does not fully clog the feature and allows for continued etching throughout the entire process.

Table 6.2: High-level description of the SiO_2 and AC etch mechanism.

Species	
M Ion or hot neutral	AC Amorphous carbon mask
S Surface Site	(g) Gas phase
P Polymer	(s) Solid
PC Crosslinked polymer	

Reaction			Description
$SiO_{2(s)} + M_{(g)}$	→	$SiO_{2(g)} + M_{(g)}$	Physical sputtering of SiO_2
$SiO_{2(g)} + S_{(s)}$	→	$SiO_{2(s)} + S_{(s)}$	SiO_2 redeposition
$SiO_{2(s)} + C_xF_{y(g)}$	→	$SiO_2C_xF_{y(s)}$	SiO_2 -Fluorocarbon complex formation
$SiO_2C_xF_{y(s)} + M_{(g)}$	→	$SiO_2C_xF_{y(g)} + M_{(g)}$	Complex sputtering
$S_{(s)} + C_xF_{y(g)}$	→	$S_{(s)} + P_{(s)}$	Polymer deposition on Surfaces
$P_{(s)} + C_xF_{y(g)}$	→	$P_{(s)} + P_{(s)}$	Polymer deposition on Polymer
$P_{(s)} + O_{(g)}$	→	$COF_{y(g)}$	Polymer etch by O
$AC_{(s)} + C_xF_{y(g)}$	→	$AC_{(s)} + P_{(s)}$	Polymer deposition on AC
$P_{(s)} + M_{(g)}$	→	$P_{(g)} + M_{(g)}$	Polymer sputtering
$AC_{(s)} + M_{(g)}$	→	$AC_{(g)} + M_{(g)}$	AC sputtering
$P_{(s)} + P_{(s)}$	→	$PC_{(s)} + PC_{(s)}$	Crosslinking
$P_{(s)} + P_{(s)} + M_{(g)}$	→	$P_{(s)} + P_{(s)} + M_{(g)}$	Breaking of Crosslinking

6.5 Target Metrics and Loss Function

A scalar metric is needed to evaluate the quality of the simulation-experiment matching when tuning the reaction mechanism. In this work the loss function $L(\mathbf{p})$ of a given parameter set $\mathbf{p}$ is the RMS error between the simulation and experiment of geometric measures, or shape parameters, of the shape of the etched feature, shown in Figure 6.7.

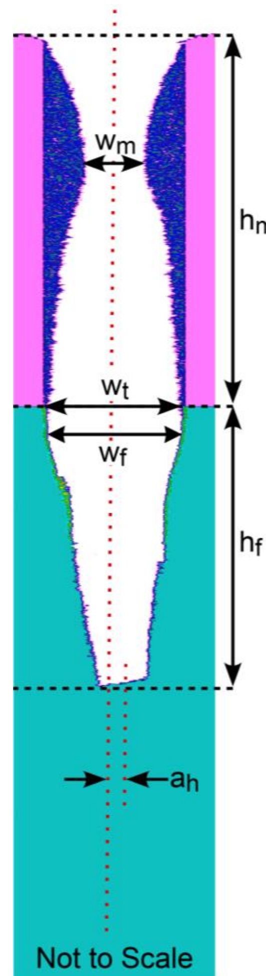

Figure 6.7: Target metrics used to evaluate the experimental matching.

While these shape parameters are not independent of each other, they nevertheless each aim to represent a specific characteristic of the feature that is of technical relevance. The width of the mask opening w_m including deposition stands as a measure of the necking and clogging, a

process which is dependent on the ration of the fluxes of polymer depositing to removing species. The narrowed opening can impede neutral gas transport into the feature, trap etch products inside the feature and shadow the trajectories ions and photons. Although the shape (curvature) of the polymer deposition is not a shape parameter in this investigation, the curvature of the polymer affects the angle of the trajectory with which ions (hot neutrals) reflect from its surface deeper into the surface. An improved approach might include shape (curvature) in the optimization process.

The width at the top of the feature, w_t, aims to capture undercutting (etching under the mask) that mostly occurs with excessive isotropic etching of the substrate or with there being insufficient passivation of the surface of the substrate compared to that of the mask material. The maximum width of the feature w_f, captures the occurrence of bowing, which can be caused by lack of passivation or broad ion angular distributions (bowing).

Mask selectivity refers to the relative rate of etching of the mask compared to the substrate. Masks for HAR etching must have high selectivity (low etch rate) compared to the substrate so that that the mask has a reasonable small thickness. The height of the mask h_m (height is thickness of the mask plus thickness of the substrate) must be controlled to ensure that the mask has a critical thickness at the end of the etch. The thickness of the mask determines the degree to which ions having broad angular spread are shadowed by and reflect off the mask prior to entering the feature.

The depth of the final feature, h_f, fundamentally defines the characteristics of HAR features and for a given process time determines the etch rate. Undesired etch defects such as twisting [76] can be captured by measuring the asymmetry, a_h, across the vertical center axis (dotted vertical line in Figure 6.7.

The loss function is then

$$L(\boldsymbol{p}) = \sqrt{a_{wm}(\hat{w}_m - w_m)^2 + a_{wt}(\hat{w}_t - w_t)^2 + a_{wf}(\hat{w}_f - w_f)^2 + a_{hm}(\hat{h}_m - h_m)^2 + a_{hf}(\hat{h}_f - h_f)^2 + a_{ah}(\hat{a}_h - a_h)^2} \quad (6.2)$$

where the hat accent (^) denotes the target value of a property. Each singular error component can be weighted in accordance with its importance or sensitivity by the respective weight factors a_i. In this work all components are equally weighted with the exception of the total asymmetry which has a higher weighting. The total asymmetry is computed based on the total number of asymmetric cells which has a substantially different scale.

For any given evaluation of the loss function $L(\boldsymbol{p})$, MCFPM has to be executed to simulate a full etch, which carries with it a computational cost. The method of evaluating and minimizing $L(\boldsymbol{p})$ through the optimization algorithm should have the goal of minimizing the number of evaluations. In this work, the target metrics are based on the scanning electron microscopy (SEM) image, shown in Figure 6.8. This image was produced after the process described in Section 6.3 was performed in a reactor that on which the simulated geometry was based.

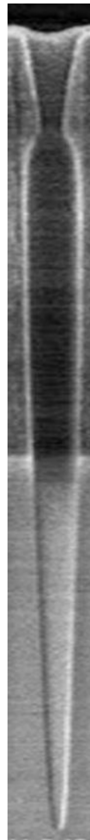

Figure 6.8: SEM image resulting from the base case experiment.

6.6 Gradient Descent

Gradient descent (GD) is a method for minimizing a multivariate error function, which is convenient due to its conceptual simplicity, universality and fast convergence. The GD method has been applied to a wide variety of physical and engineering problems [66,67,77–81]. In short, GD is based on following the gradient of a loss function L to its minimum as shown in Figure 6.9.

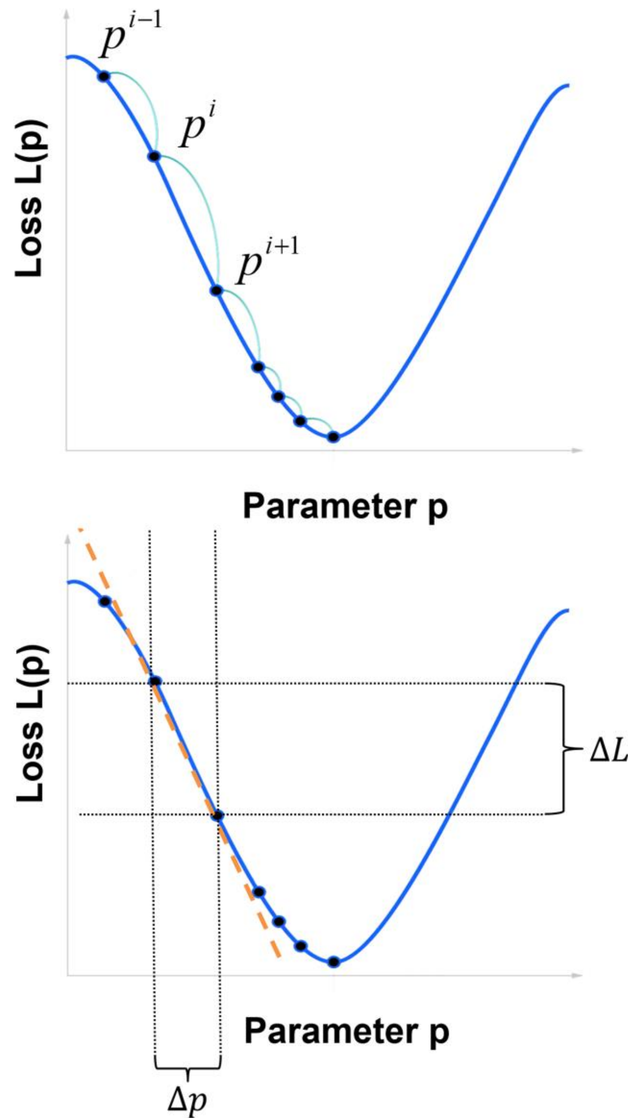

Figure 6.9: Outline of the gradient descent method for a 1D parameter space.

For a given set of parameters $\mathbf{p}^i$ the selection of the next set of parameters be expressed as

$$\mathbf{p}^{i+1} = \mathbf{p}^i - \eta \nabla L(\mathbf{p}^i), \tag{6.3}$$

where η is the learning rate which controls the effective step size and the rate of descent. The loss function consists of a set of discrete points that results from successive runs of the MCFPM and so is not natively differentiable. A finite difference scheme was used to estimate the partial gradients in every dimension by evaluating L(**p**) at a test location L(**p′**)

$$L(\mathbf{p}'_j) = L(\mathbf{p} + \mathbf{x}_j p'_j) \tag{6.4}$$

for every dimension of the parameter space n and computing the relative delta $\Delta L / \Delta p_j$. Effectively, the discrete gradient descent formulation becomes

$$\mathbf{p}^{i+1} = \mathbf{p}^i - \eta \sum_{j=1}^{n} \mathbf{x}_j \frac{\Delta L}{\Delta p_j} = \mathbf{p}^i - \eta \sum_{j=1}^{n} \mathbf{x}_j \frac{L(\mathbf{p}^i) - L(\mathbf{p}'^i)}{p_j^i - p_j'^i} \tag{6.5}$$

A useful modification to the gradient descent method is the addition of a momentum term, that enables the method to overcome local extrema and avoid convergence around a non-global minimum. Analogous to the momentum in Newtonian physics, momentum in GD adds an inertia term to the updated parameters. The previous gradient is remembered and the update on the next iteration is determined by the effective gradient g^i which is a linear combination of the actual gradient and the previous update:

$$\mathbf{p}^{i+1} = \mathbf{p}^i - \eta \mathbf{g}^i \tag{6.6}$$

with

$$\mathbf{g}^i = \delta \mathbf{g}^{i-1} + \nabla L(\mathbf{p}^i) \tag{6.7}$$

where δ is the momentum decay coefficient which determines the overall strength of the momentum term. Akin to a heavy ball, rolling down a gravitational potential (referred to as heavy

ball method) the gradient descent is less affected by small scale perturbation or "roughness" of the loss function surface.

Based on this methodology, an initial optimization was performed. The tuning parameters as well as their intervals are listed in Table 6.3. The target metrics obtained from experimental data are listed in Table 6.4. The optimization was performed for a total of 100 epochs. (An epoch is single round of evaluating the loss function with a given set of parameters.)

Table 6.3: Tuning parameters for gradient descent optimization

Symbol	Description	Min. value	Max. value
$p_{s,SiO2}$	Sputter probability of SiO_2	0.0	0.3
$p_{s,SiO2CFXY}$	Sputter probability of SiO_2-polymer complex	0.1	0.5
$p_{p,SiO2}$	SiO_2-polymer-complex formation probability	0.1	0.5
$p_{e,poly}$	O based polymer etch	0.0	0.5
$p_{d,poly-AC}$	Polymer deposition probability on mask	0.0	0.5

Table 6.4:Target metrics for gradient descent optimization

Symbol	Description	Target value
w_m	Width of mask opening	45 nm
w_t	Width at the top of the feature	90 nm
w_f	Maximum width of the feature	90 nm
h_f	Etch depth	825 nm
h_m	Remaining mask height	850 nm
a_h	Asymmetry	0

The evolution of the total loss function is shown in Figure 6.10a) as a function of elapsed epochs. The total loss quickly decreased during the first 20 epochs which indicates a partially successful optimization. This convergence mirrored by the evolution of the target metrics, shown in Figure 6.10b). The three metrics, etch depth h_f (blue squares), minimum mask opening w_m (red pyramid) and maximum feature width w_f (green delta) quickly approach their target values, represented by dashed horizontal lines. Some of the trends are correlated to the underlying adjustments to the parameters defining the etching mechanism, a selection of which are shown in Figure 6.10c).

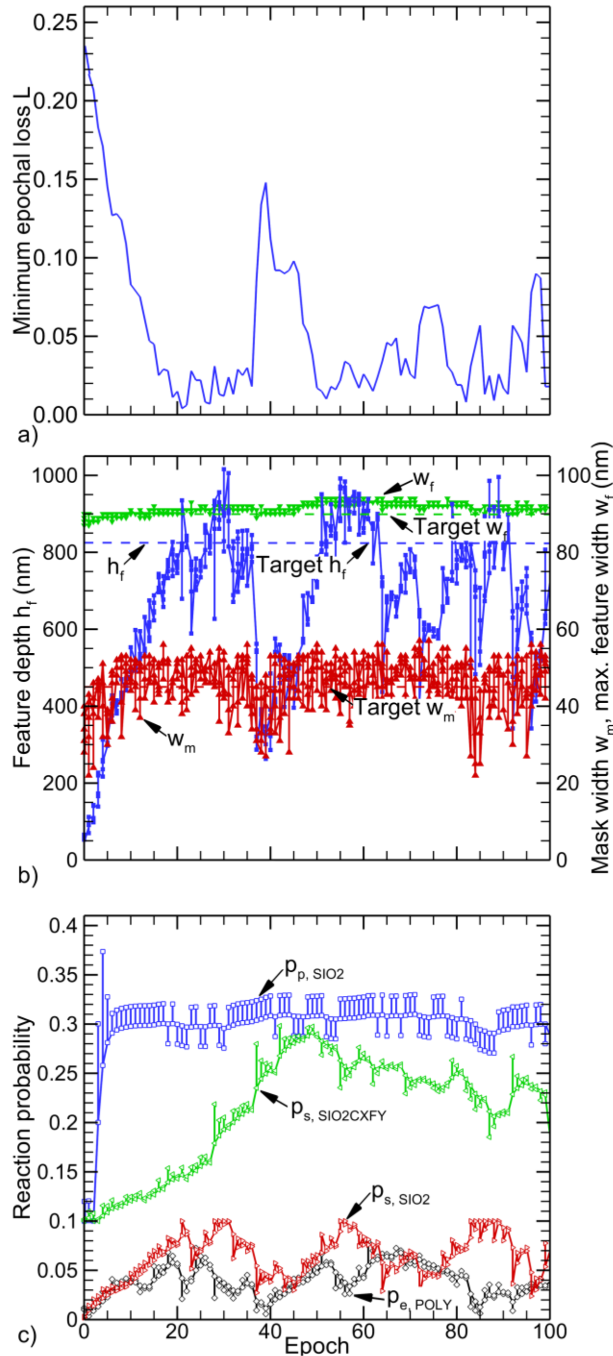

Figure 6.10: Results from the gradient descent optimization. a) minimal epochal loss. b) values of select metrics as a function of epochs. c) select tuning parameters as a function of epochs.

The increase in final predicted etch depth, for example, can be explained by changes to the complex formation probability and its sputter probability both of which increase in tandem with the increase in final etch depth. However, beyond epoch 20, however, the clear trend towards error

minimization breaks down and instabilities both in the model error as well as in the metrics emerge. This breakdown results from the underlying definition of the loss function.

The step size with which the parameter space is traversed is inherently tied to the size of the gradient (Eq. (6.6)) and should diminish as one approaches the minimum (zero gradient). L(**p**) is derived from predicted profiles produced by the MCFPM which has finite grid resolution – the dimension of the voxel. As the step size diminishes, producing a small change in the physics coefficients, the physical change in the predicted profile may not exceed the size of the voxel. At this point, the loss function is no longer differentiable, as shown in Figure 6.11.

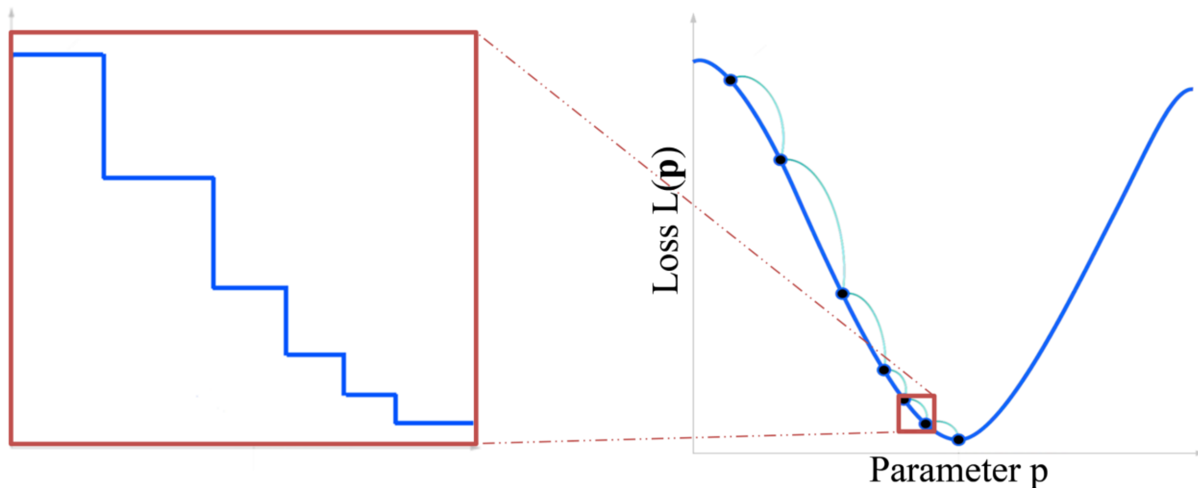

Figure 6.11: The finite resolution of the loss function leads to convergence issues.

This condition can lead to an absence of a gradient when the change in the profile stays within a single voxel, producing a breakdown of the functional relation between **p** and L(**p**) = L = constant. Another outcome is an overestimation of the gradient when a small change **p** causes the previous static profile t change to a different voxel.

The GD method provides rapid initial convergence but is potentially erratic when approaching the optimum. The behavior of the GD and control of the speed of the initial descent

speed is a function of the learning rate η. The evolution of L(**p**) for different learning rates η = $1x10^{-4}$, $5x10^{-4}$, $1x10^{-3}$ and $5x10^{-3}$ is shown in Figure 6.12.

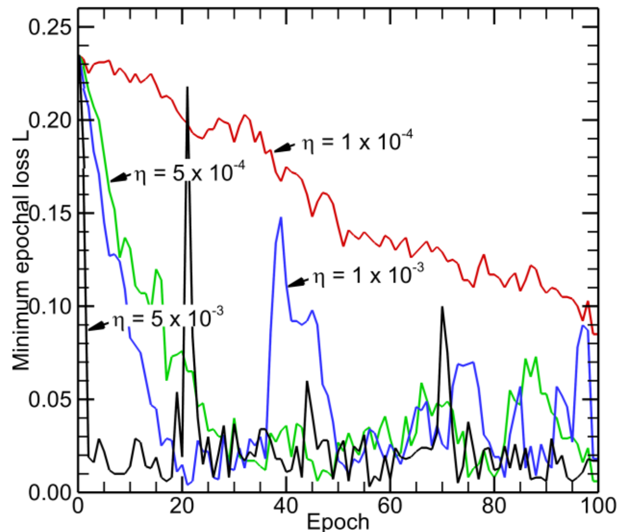

Figure 6.12: Evolution of the total loss for different learning rates η = $1x10^{-4}$, $5x10^{-4}$, $1x10^{-3}$ and $5x10^{-3}$.

The rate of descent is correlated to η – a smaller learning rate leads to smaller step sizes used to traverse across the parameter space and, consequently, a slower overall descent. Due to the limitations of the method that result from the erratic differentiation near convergence (an outcome of the finite voxel size), all optimizations eventually result in a convergence failure, independent of the learning rate.

Despite the limitations imposed by the finite difference approach, the GD method has the ability to overcome local minima (to some degree) while having rapid and controllable initial descent. This rapid initial convergence is particularly important in minimizing the number of loss function evaluations and so minimizing computational cost). As a result, one is motivated to retain the GD method to approach the optimized values, followed by a more robust, though possible more slowly converging, optimization method. In this work the Nelder-Mead method was selected to perform this task.

6.7 Nelder-Mead Optimization

The Nelder-Mead method is a gradient free optimization algorithm that has been used in a wide variety of optimization problems [82–88]. Conceptually, the Nelder-Mead (NM) method represents the tuning parameters as a point in n-dimensional solution space, where n is the number of tuning parameters to be optimized. A simplex, an object with n+1 vertices, each representing a different set of parameters, is employed to traverse the solution space through geometric transformations along its centroid $\mathbf{x_0}$.

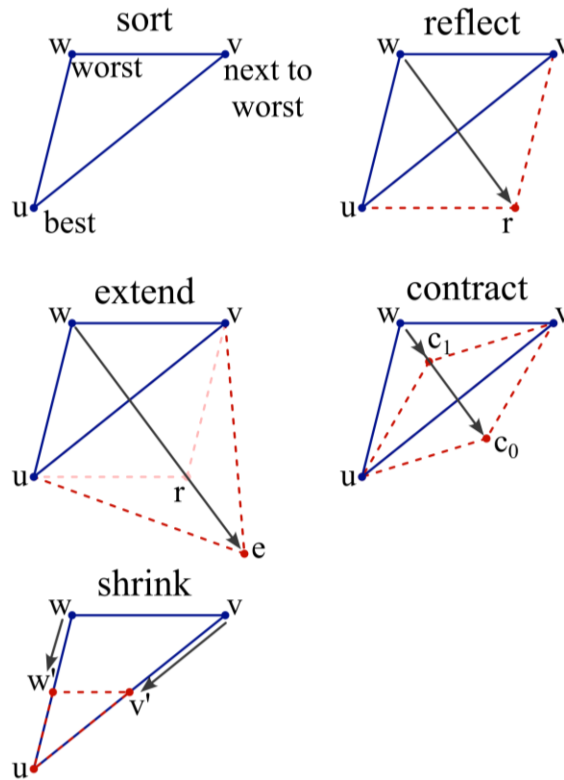

Figure 6.13: Examples of the geometric transformations of the parameter simplex in a 2D parameter space; reflection, extension; contraction; shrinkage.

An example scenario is shown in Figure 6.13 with n = 2 – a 2D solution space where the simplex is a triangle:

- **Sorting:** The points are sorted according to their loss function from best (lowest loss) to worst (highest loss): $L(\mathbf{u}) < L(\mathbf{v}) < L(\mathbf{w})$
- **Reflection:** Reflect the worst point, **w,** across the centroid; $\mathbf{r} = \mathbf{x}_0 + \alpha(\mathbf{x}_0 - \mathbf{w})$, with $\alpha > 0$.
- **Extension:** Extend the reflection beyond point **r**; $\mathbf{e} = \mathbf{x}_0 + \gamma(\mathbf{r} - \mathbf{x}_0)$, with $\gamma > 1$.
- **Contraction**: Generate two points, $\mathbf{c}_0$ and $\mathbf{c}_1$, that represent contractions of **r** towards **w**; $\mathbf{c}_0 = \mathbf{x}_0 + \rho(\mathbf{r} - \mathbf{x}_0)$ and $\mathbf{c}_0 = \mathbf{x}_0 + \rho(\mathbf{w} - \mathbf{x}_0)$ with $0 < \rho < 0.5$
- **Shrinkage:** Shrink the simplex towards the best point; $\mathbf{w}' = \mathbf{u} + \sigma(\mathbf{w} - \mathbf{u})$ and $\mathbf{v}' = \mathbf{u} + \sigma(\mathbf{v} - \mathbf{u})$, with $0 < \sigma < 1$

Using these simple geometric transformations, the NM algorithm consists of a specific set of decisions, which leads to an iterative loop that requires at least one successive evaluation of the loss function per step and a maximum of 4 per epoch. A flow chart of the Nelder-Mead algorithm is shown in Figure 6.14. Every epoch begins by sorting the simplex points according to their loss function value, with $L(\mathbf{u}) < L(\mathbf{v}) < L(\mathbf{w})$. Reflection is always the first geometric operation to be tested. If the reflected point, **r**, is better than the previous second point but worse than the best ($L(\mathbf{u}) < L(\mathbf{r}) < L(\mathbf{v})$), the reflected point replaces the previously worst point ($\mathbf{w} = \mathbf{r}$) and the epoch ends. If **r** is better than the previously most preferred point ($L(\mathbf{r}) < L(\mathbf{u})$) the extension point **e** is tested and added to the simplex if it outperforms **r** ($L(\mathbf{e}) < L(\mathbf{r})$). If the reflected point **r** is worse than all other simplex points, the contraction is performed. If neither $\mathbf{c}_0$ nor $\mathbf{c}_1$ have a lower loss than **r**, the simplex is shrunk and the next epoch is initiated. This loop continues until the maximum number of iterations is reached or the specified convergence has been reached. Since the individual parameters represent physical quantities, additional constraints can be placed on the values of the parameters. For example, sputter yields less than zero or reaction probabilities greater than one can be accounted for by limiting respective transformations to valid ranges.

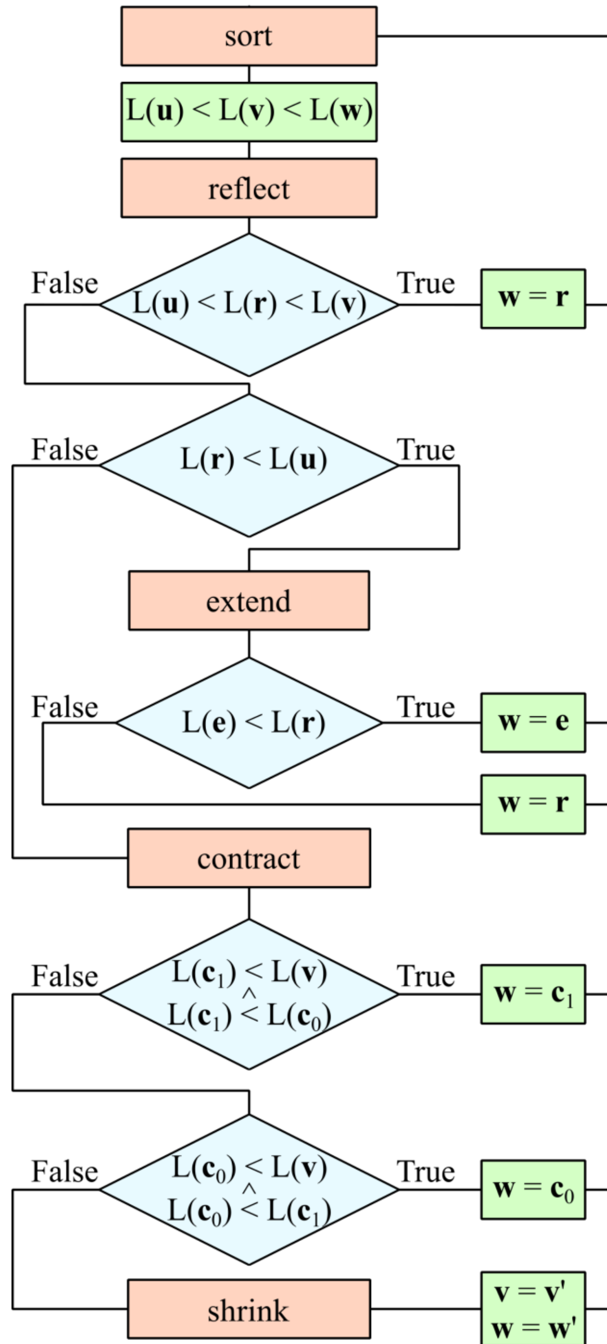

Figure 6.14: Flow chart describing the Nelder-Mead optimization algorithm.

Since NM is a direct search method (only relies on direct evaluations of the loss function itself), NM does not suffer from the same issues that arise with GD which relies on discrete differentiation. NM is regarded as heuristic optimization in this context. Although convergence is

technically not formally guaranteed, from a practical perspective NM does nearly always converge. This convergence results from the finite grid size. The loss function effectively becomes insensitive to perturbations below a certain threshold. Once the optimization process switches from GD to NM, no instabilities or non-stationary convergences were encountered.

The use of NM as the only convergence method is somewhat vulnerable to the presence of local minima. That is, NM may converge around a non-global minimum. This propensity for local convergence increases for higher order problems as the size of the parameter space increases. This tendency for local convergence is greatly reduced by initializing the first simplex in the vicinity of the absolute minimum as provided by the initial GD method. That is, the first simplex is not initialized at a random location. As a result, the NM portion of the optimization does not need to sample complete coverage of the parameter space nor conduct an exhaustive search has to be required. For our conditions, the sequential GD-NM approach minimized the computational load by reducing the number of loss function evaluations compared to random scatter initialization or swarm optimization methods.[89]

6.8 Hybrid GD-NM Optimization

Subsequently executing GD and NM optimization algorithms produces a hybrid scheme whose goal is to address the weakness of each singular approach while capturing their positive qualities. The convergence and output parameters produced by the hybrid optimization scheme are shown in Figure 6.15 as a function of epoch for the same conditions as Figure 6.10 a) minimum epochal error, b) selected metrics and c) evolution of the tuning parameters.

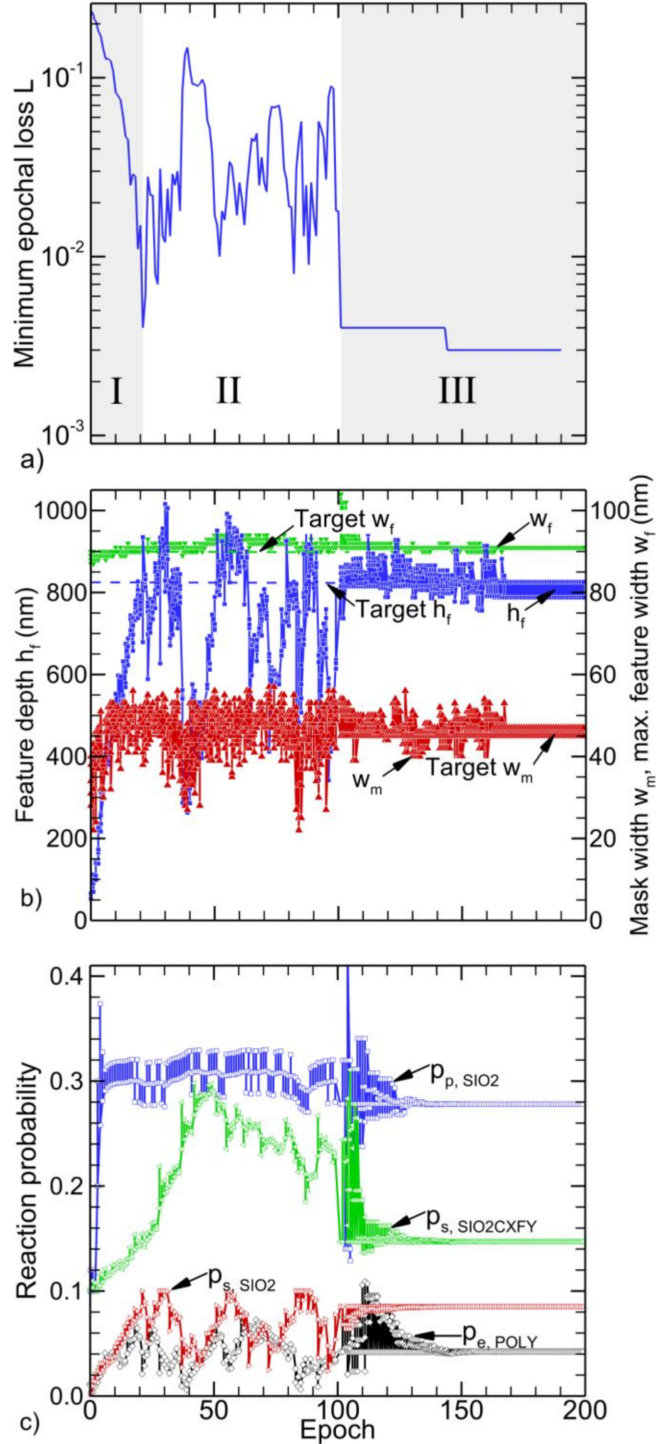

Figure 6.15: Results from the combined gradient descent and Nelder-Mead optimization. a) minimal epochal loss. b) values of select metrics as a function of epochs. c) select model parameters as a function of epochs.

The evolution of the total model error has 3 stages. The first stage, I, consists of the initial rapid descent and nearly monotonic reduction of the loss function, enabled by the gradient descent with an appropriate learning rate. Starting at approximately epoch 20, stage II suffers from convergence instabilities which is reflected in fluctuations in the target metrics (Figure 6.15b) and model parameters (Figure 6.15c). At epoch 100, stage III, the gradient descent is terminated and based on its results, the NM algorithm is initiated. The fluctuations are rapidly dampened, and a stable convergence commences. The error drops to approximately 3×10^{-3} which given the grid resolution is on the order of a single cell or less. This minimization in error is mirrored in the target metrics (Figure 6.15b) which converge to the desired values. The final parameter set is listed in Table 6.5.

Table 6.5: Final tuning parameters after coupled optimization.

Tuning Parameter	Value
$p_{s,SiO2}$	0.0852
$p_{s,SiO2CFXY}$	0.1471
$p_{p,SiO2}$	0.278
$p_{e,poly}$	0.0423
$p_{d,poly\text{-}AC}$	0.094

The definition of model physics parameters based on this optimizer algorithm is based on the reduced scalar representation of the feature. The method will not capture effects that are not included in the target metrics. For example, select features produced by MCFPM after the full etch process are shown in Figure 6.16 as a function of epochal progression. (These features are predictions at the end of the full etch period for a particular set of model parameters corresponding to an epoch. The sequence of features is not the temporal evolution of the feature itself). The SEM from which the target metrics were extracted is also shown (grayscale).

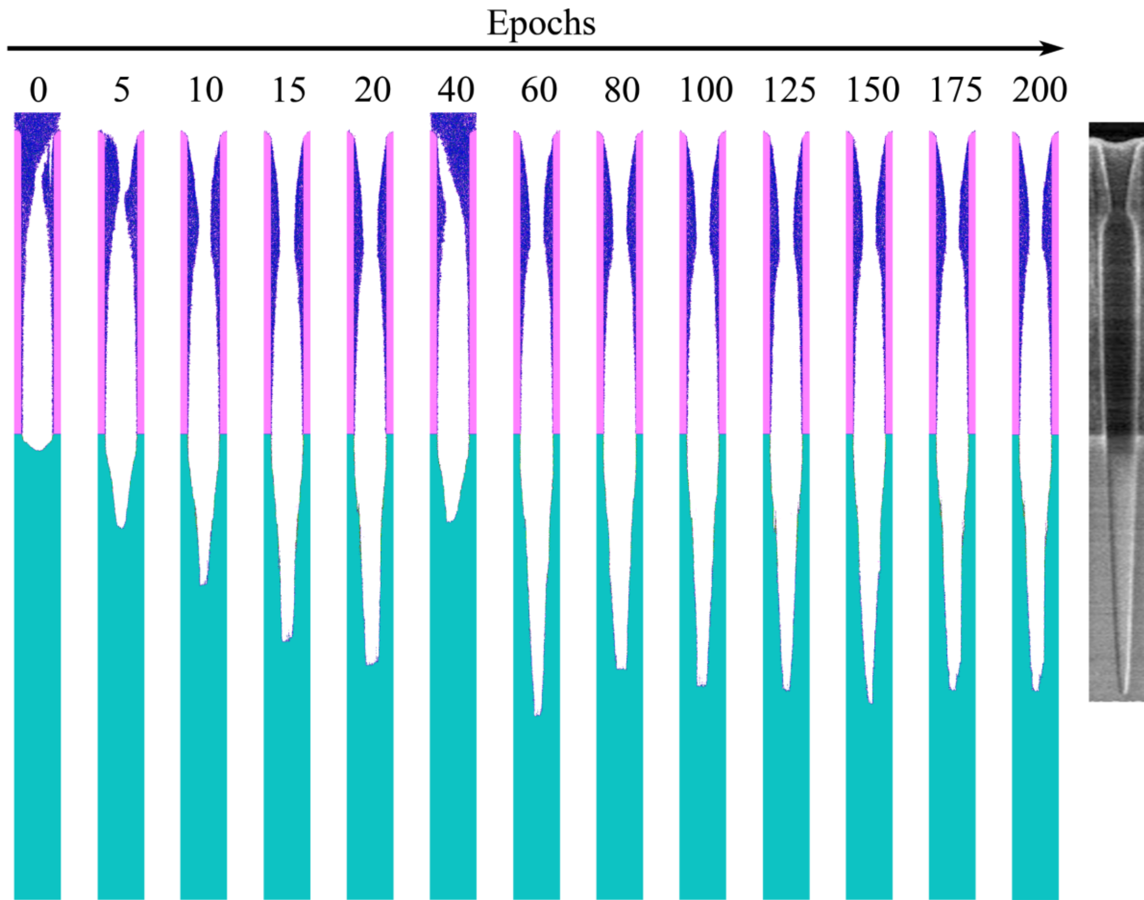

Figure 6.16: Final features after etch completion for different parameter sets as a function of epochal evolution and the actual experimental target feature.

Here, too, the optimization stages can be identified. During epochs 0 – 20, belonging to stage I (initial descent), the monotonic behavior is reflected in the increasing etch depth and widening of the necking. The increased etch rate directly correlates with increasing oxide-polymer complex formation, its removal and increases in the SiO_2 sputter rate. The decreased polymer deposition at the top of the mask is a consequence of the increasing polymer etch by oxygen.

Stage II (instabilities) produces erratic behavior in the predicted profiles with an absence of clear trends. Between epochs 20 and 100 the etch depth and polymer deposition vary seemingly randomly without clear trends. With stage III and the change to the Nelder-Mead algorithm for epochs 100-200 mechanism converges, with a lack of non-monotonic evolution of the metrics.

Overall, the final simulated etch feature at epoch 200 is in good agreement with the experimental counterpart in terms of the metrics used in the optimization process. There are, however, some key differences between the predicted profiles and the experimental SEM. For example, there are differences in the vertical position of the minimum in necking and the taper of the mask. The mismatch in these properties is due to the fact that they were not part of the optimization metrics. Assuming that the optimization process produced *good model parameters*, these differences indicate might that a) the mechanism lacks processes that would otherwise determine necking location or taper, b) the non-optimized physics parameters are not accurate and/or c) the solution is not unique and a second solution might better capture these phenomena. These results stress the importance of including metrics that address the most critical properties of the features in the optimization process, as well as the physics in the reaction mechanism that correlate to those properties. For example, taper of the feature is known to be sensitive to the chemical sputtering probability as a function of angle of incidence of energetic particles. This physics parameter was included in our mechanism but was not part of the optimization process.

In this context, metrics and the optimization processes are as a whole coupled, requiring at least a partial simultaneous evaluation. That is, independently optimizing each metric will not produce the desired result. This coupling can be demonstrated by the relationship between necking and clogging and feature evolution. Necking or, in the extreme, clogging reduces or entirely impedes the transport of reactive species and ions into the feature, slowing the etch process. In the event of clogging, the etch process is stopped which prevents evaluation and optimization of the etch process as a whole. Since in this work metrics are only derived from the final feature, there is no mechanism to differentiate between two fully clogged features based on the mask metrics alone. The width of mask opening is $w_m = 0$ in both cases even if the rate of the deposition were different

and the clogging occurred at different times during the etch. However, differences in rates of, for example, deposition can affect the time during which the feature is not clogged, which translates to differences in total etch depth. Through this mechanism, the etch depth acts as a secondary metric for the clogging mechanism, without which prior attempts to optimize the isolated mask mechanism failed.

Overall, the hybrid optimization scheme performed satisfactory in that it produced a mechanism that reproduces the desired feature with high accuracy. However, aspects of the process have potential for improvement. The epoch at which switching between GD and NM methods should be carefully chosen. Epochs spent in Stage II produce little additional information and are not a good use of computing resources. Such hybrid optimization schemes should include a mechanism or criterion to identify convergence failure of the GD and automatically switch to the secondary algorithm. A careful choice of the needed convergence would also minimize the number of epochs spent in Stage III.

6.9 Transferability of the Converged Mechanism

A test of whether the derived model parameters are physically relevant is to evaluate their transferability to *related processes.* Given the small sample set, overfitting or circumstantial unphysical results are of major concern. The term *related processes* was used deliberately. The parameters that have been derived from the optimization process are physics parameters that should, in principle, apply to a wide range of process conditions. However, there is a practical limit. For example, introduction of new gases or new method of excitation (inductively coupled vs capacitively coupled) would likely exceed that limit or require additional parameters in the optimization process.

6.9.1 Variation of O_2 in Flow

To test the applicability of the derived model parameters, a process with different input power (P_{lf} = 6.0 kW and P_{hf} = 2.5 kW) was simulated with differing oxygen to fluorocarbon feedstock gas ratios (O_2/C_4F_6 = 0.5, 1, 1.5 and 2.5). All other conditions were kept the same as the base case. The most significant changes compared to the base case were in the particle fluxes incident on the wafer surface, which are shown as function of the feed gas ratio in Figure 6.17.

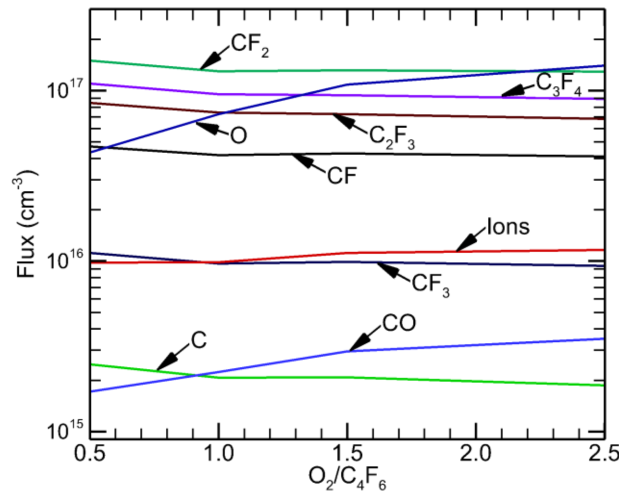

Figure 6.17: Fluxes incident on the wafer as a function of the O_2/C_4F_6 feedstock gas ratio.

The variation in the O_2/C_4F_6 ratio was achieved, experimentally and in the simulation, by adjusting the oxygen inflow only. As a consequence, the fluxes of the major contributing fluorocarbons remain nearly constant. The O flux increases from 4.1 x 10^{16} to 1.5 x 10^{17} $cm^{-2}s^{-1}$, a factor of 3.6, with increase of the oxygen inflow by factor of 5. These trends indicate that mole fractions of feedstock gases do not translate one-to-one to the surface fluxes. The features generated by MCFPM and their experimental counterparts are shown in Figure 6.18.

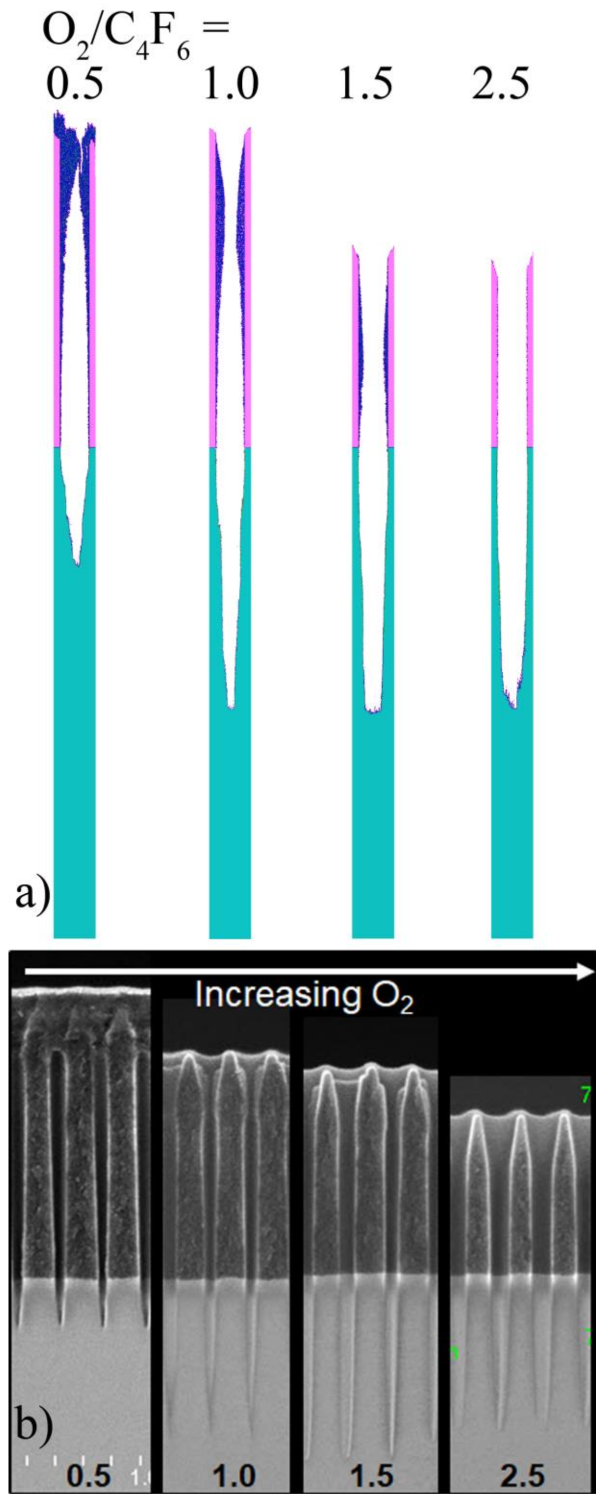

Figure 6.18: a) MCFPM features resulting from the O_2/C_4F_6 variation. b) SEM images of the features resulting from the corresponding experiment.

Although the reaction mechanism used in MCFPM was not specifically tuned for these process conditions, relevant trends were qualitatively reproduced qualitatively. Trends in polymer deposition on the mask are reproduced. At low O_2 fraction and low O-flux, the O based etching of deposited polymer is low which leads to full clogging of the feature in both the experiment and simulation. With increasing O_2 the rate at which polymer is removed increases and the necking is reduced, being essentially absent for the $O_2/C_4F_6 = 2.5$ case.

The lack of polymer film on the mask leads to increased mask erosion with increasing O_2 inflow. The amount of mask erosion in the simulated features is not in quantitative agreement with the experimental results. This lack of quantitative agreement is likely due to not having the necessary physical processes in the mechanism despite not being specifically required for the initial optimization process. For example, direct oxidation of the AC mask by O_2 was not included in the mechanism but may become important at larger O_2 flow rates. The etch depth is related to the mask necking through reduction in particle transport into the feature and through etch stop with full clogging. The full clogging of the feature for $O_2/C_4F_6 = 0.5$ is reproduced by the simulation, however, etch depth for the fully clogged feature is not reproduced as this depth depends on when the feature was clogged. The experiments show maximum etch depth for $O_2/C_4F_6 = 1.5$, which is not the case for the simulation. Overall, however, the predicted trends generally agree with experiments, which is not necessarily the expectation given the fact that the mechanism was tuned for only a single different process. The emergence of these untrained trends is a consequence of using a ‘physics informed’ optimization approach where the derived parameters are physics parameters and not simply fitting parameters. These trends also rely on the fluxes produced by the HPEM being *truth* and accurately representing experimental fluxes, which adds additional variability to the process.

6.9.2 Variation of Low Frequency Power

As second test of the model parameters derived from the optimization process was prediction of feature profiles while varying the low frequency power, P_{lf} = 0, 4, 6 and 8 kW. Low frequency power is often used to control the ion energy at the wafer surface. IEADs onto the wafer are a first-order concern in HAR etching.

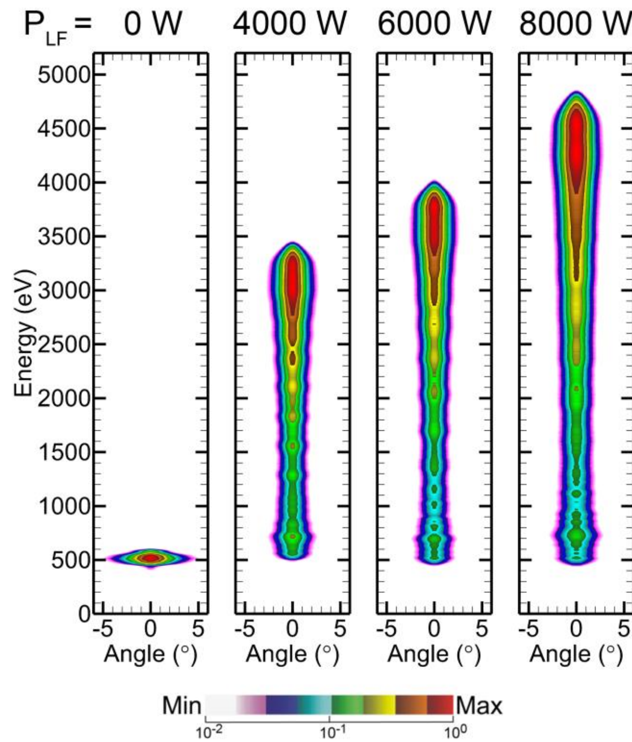

Figure 6.19: IEADs resulting from the P_{lf} variation with P_{lf} = 0, 4, 6 and 8 kW.

The IEADs produced by HPEM for this range of P_{lf} are shown in Figure 6.19 with there being direct correlation between P_{lf} and the mean and maximum energies of ions at the wafer. While the IEAD for P_{lf} = 0 kW has the lowest energies, with electrons exceeding 500 eV the high frequency RF power alone nevertheless produces high energy ions. The maximum angular spread has little variation as a function of P_{lf}, with the exception of P_{lf} = 0 kW which has significant

broadening of the angular distribution. Using the derived model parameters, MCFPM simulations were performed for the different values of P_{lf} = 0. Those results and the experimental SEM references are shown in Figure 6.20.

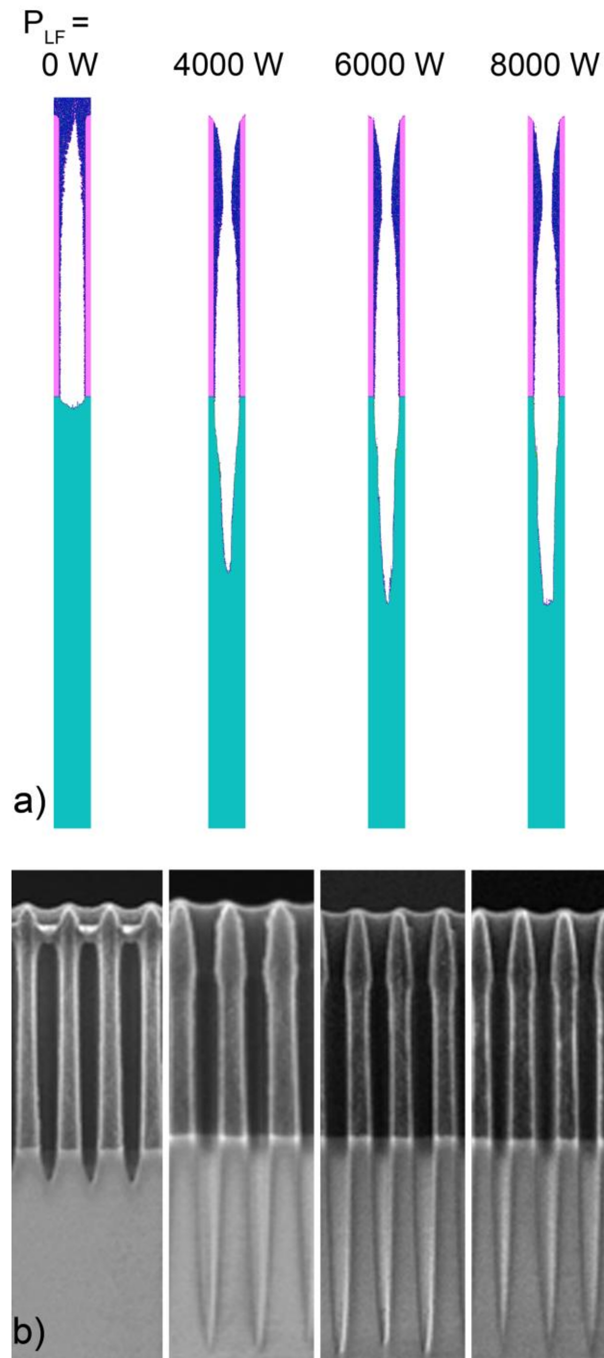

Figure 6.20: a) MCFPM features resulting from the P_{lf} variation. b) SEM images of the features resulting from the corresponding experiment.

The profiles, experiment and simulation, for P_{lf} = 0 kW produce total clogging of the mask opening, indicating that ion energy plays an important role in removing excess polymer. The remaining cases (P_{lf} = 4, 6 and 8 kW) have unclogged features and full etching with unexpected little variation as a function of LF power. In the experimental data a doubling of the P_{lf} (4 kW to 8 kW) produces few differences in the final features. These trends indicate that above a certain threshold energy the etch progression and the mask removal process are not ion starved, but rather limited by neutral gas transport. To some degree this trend is reproduced by the simulations where etch depth does increase with increasing low frequency power however the rate of increase is substantially sublinear. These outcomes indicate that the effect of ion energy (for example in sputter yield or related processes) might be overestimated in the mechanism. Again, this assumes that the results produced by the HPEM are *truth*.

6.10 Optimization Based on Multiple Features

Because Monte Carlo based simulations are inherently subject to statistical variations, the fact that the loss function is based on a single feature's geometry can result in overfitting and misinterpretation of the target metrics. To partially mitigate and roughly estimate the level of overfitting, instead of matching to a single features etch profile, the optimization was performed on a set of four features arranged in a grid as shown in Figure 6.21.

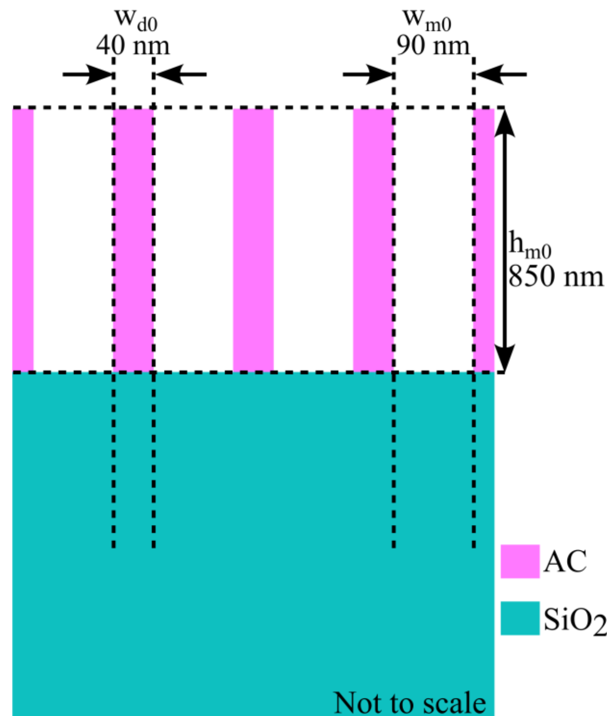

Figure 6.21: Feature scale simulation setup consisting of a SiO_2 substrate with an amorphous carbon mask and four separate features in a regular grid.

The individual features are Identical to those used earlier in this work and the distance between them is 40 nm. Using this geometry, the total loss is set to be the average of the individual features. Because the particles launched from the top of the simulation domain are launched based on a shared random number pool, this effectively induces statistical variation between the features. Apart from the changes in feature geometry, the optimization setup remains unchanged. Analogous to the results depicted in Section 6.8, the epochal evolution of the loss function is depicted in Figure 6.22a. As with the single feature optimization, 3 distinct stages in the optimization can be identified. The initial descent (Stage I) seems to commence more rapidly, despite identical learning rates. This might be the result of the result of the induced statistical variation that, to a degree, remedies some of the initial overfitting to statistical noise and enables a smoother gradient descent. While the convergence failure (Stage II) still occurs, the random oscillation of the loss seems to

be significantly dampened compared to Figure 6.15a. This is likely due to the fact that the incorrect gradient calculations are partially negated, as they are unlikely to occur in all features at the same time. The final convergence (Stage III), too, is similar to the single feature optimization in that it rapidly converges to a stable value and although the final loss is slightly larger, it is still on the order of a single cell. This behavior is confirmed by considering the average of the metrics. Shown in Figure 6.22b. All considered metrics reach very good final parity with the respective targets while their initial approach is faster and the intermediate non-convergence oscillations are less erratic and of smaller magnitude. The same set of tuning parameters is shown in Figure 6.22c. and while their temporal evolution is very different from that observed in the single feature case the final values are very close. The final values of the feature grid-based simulation are listed in Table 6.6.

Table 6.6: Final tuning parameters after coupled optimization of feature grid.

Tuning Parameter	Value
$p_{s,SiO2}$	0.0909
$p_{s,SiO2CFXY}$	0.1384
$p_{p,SiO2}$	0.2729
$p_{e,poly}$	0.0628
$p_{d,poly\text{-}AC}$	0.0842

The features produced as a function of epoch are depicted in Figure 6.23. As with the single feature optimization the initial mechanism produces clogged features, caused by insufficient polymer etching, which leads to an early etch stop. With progressing epochs (left to right in Figure 6.23), the net polymer deposition is reduced and the etch rate and etch depth increased. At epoch 100, immediately before stage III, the scalar metrics (Figure 6.22b) and 2d feature representation both indicate a good match in etch depth but excessive feature bowing that is effectively removed with subsequent ongoing optimization.

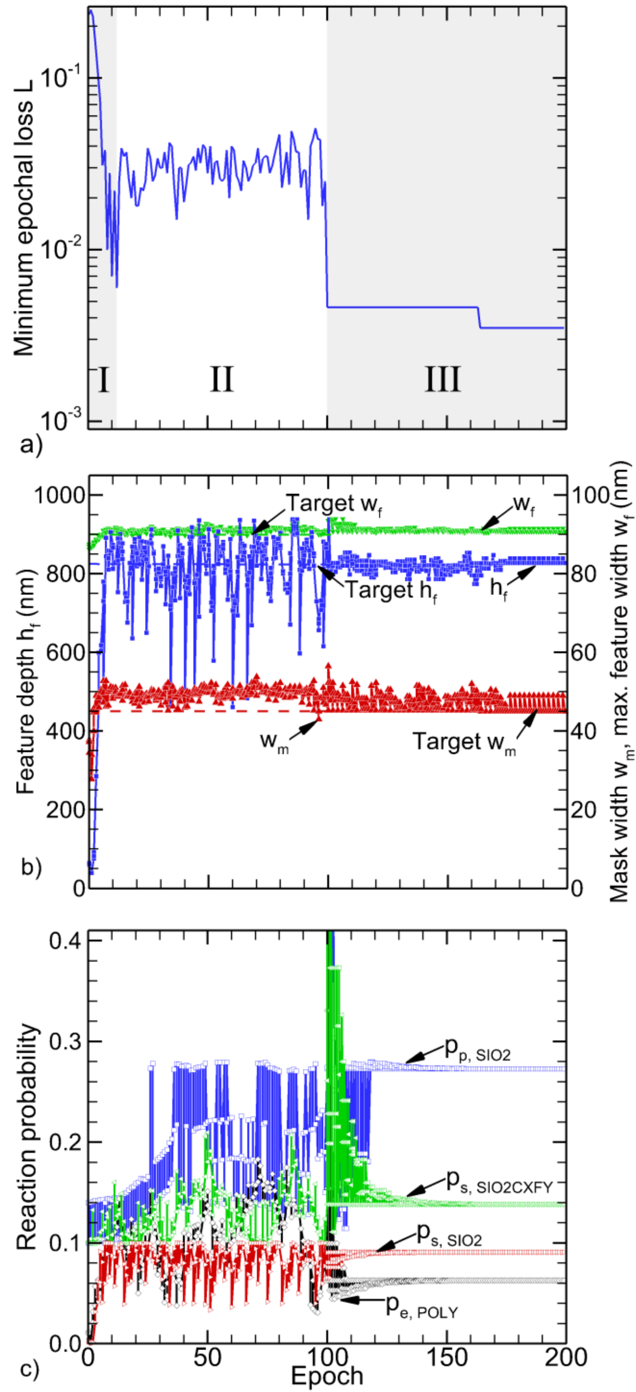

Figure 6.22: Results of the feature array optimization. a) minimal epochal loss. b) values of select metrics as a function of epochs. c) select model parameters as a function of epochs.

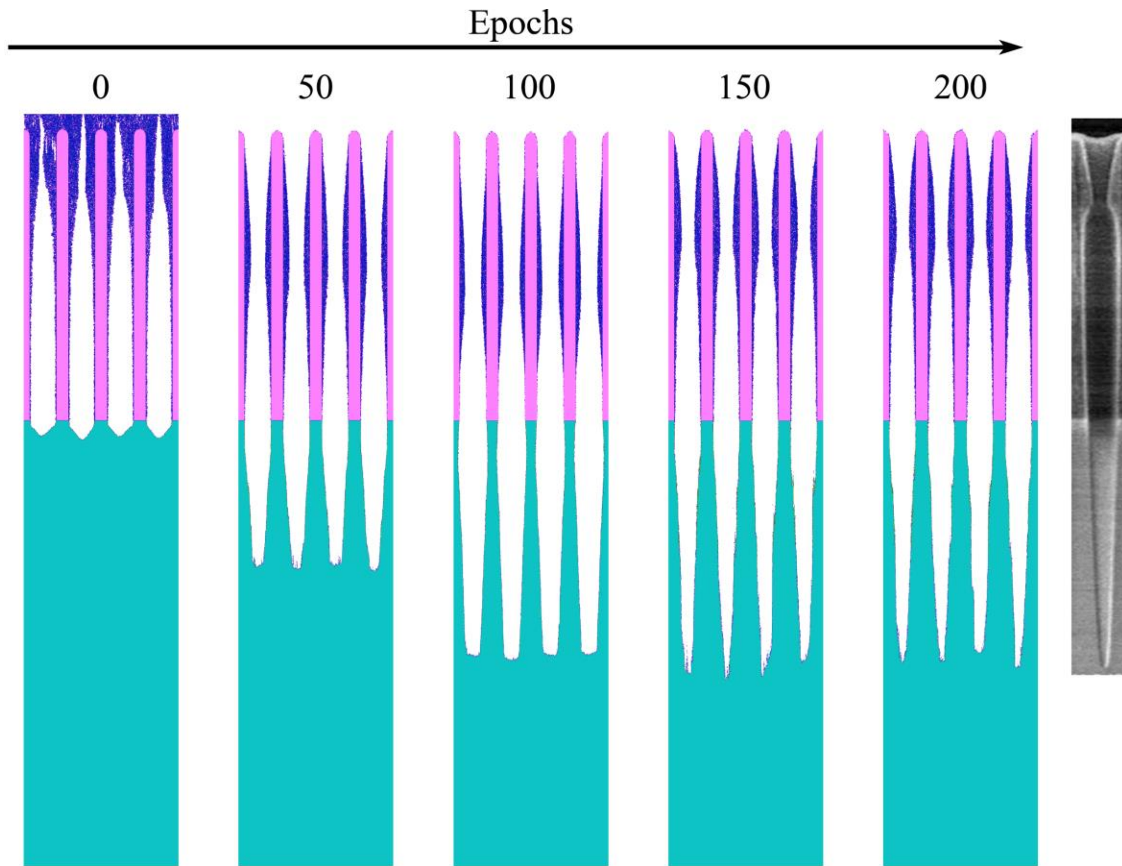

Figure 6.23: Final feature grids after etch completion for different parameter sets as a function of epochal evolution and the actual experimental target feature.

While these findings indicate that the optimization based on feature grids is generally preferable to that using only a single feature, these improvements must be weighed against the increase in computational cost that is incurred by the larger geometry and subsequent increase in total cells. A detailed investigation of this relation could be of considerable interest but is beyond the scope of the presented work.

6.11 Concluding Remarks

This chapter presented a two-stage hybrid optimization scheme aimed at optimizing physical parameters in a reaction mechanism that is used in profile simulations of a high aspect ratio etch into a SiO_2 substrate using a $C_4F_6/Ar/O_2$ gas mixture. The process is performed in a dual frequency capacitively coupled plasma reactor with independently controlled high frequency and low frequency powers applied to the bottom electrode. The employed optimization scheme consisted of consecutive execution of a finite difference gradient descent and Nelder-Mead algorithm. Doing so allowed taking advantage of some of the respective desirable qualities while at least partially negating some of the respective drawbacks. The fast, initial descent of the GD method was maintained while its inevitable instability was dampened by the successive NM process. The mechanism was matched to best represent geometric properties of the final etched feature extracted from scanning electron microscopy images. Using appropriate target metrics, the optimization produced a mechanism that was able to reproduce the experimental reference with sub 1% error, based on the employed metrics.

Outside the training parameter space using different gas compositions and power, the mechanism captured relevant trends. In a variation of the O_2/C_4F_6 ratio it reproduced feature clogging onsets and, to a lesser degree, necking and mask erosion trends. Similarly, a variation of the low frequency power produced a comparable onset of clogging at low enough powers which was also captured by the mechanism. Trends in feature etch rate (or lack thereof) are reproduced to a lesser degree.

Overall, the presented approach shows promising potential in that with a very limited set of data, just a single SEM image, it was able to reproduce a good match to the training target and was able to reproduce some relevant trends outside of its immediate training regime.

This is thanks to the 'physics informed' optimization approach which, in this given scenario, employed a base mechanism that already contained explicit formulations of the relevant physical processes and was thus conceptually more universal than the singular case to which it was matched.

Despite the given encouraging results this should only be considered a proof of concept as many details of the optimization scheme still require improvement. This includes a more effective criterion for the algorithm switching as well as a robust formulation to detect convergence and initiate an early stoppage to reduce unnecessary computing overhead. Another potentially worthwhile improvement would be the expansion of the metrics to include not only a single process condition but rather match to one or more parametric sweeps. Alternatively, the inclusion of multiple different etch times per process condition could proof useful to include data about the temporal feature evolution and, since the data set is effectively increased, partially mitigate overfitting which is of great concern whenever only a small set of data is used.

6.12 References

[1] V. M. Donnelly and A. Kornblit, Journal of Vacuum Science & Technology A: Vacuum, Surfaces, and Films **31,** 050825 (2013).

[2] I. Adamovich, S. D. Baalrud, A. Bogaerts, P. J. Bruggeman, M. Cappelli, V. Colombo, U. Czarnetzki, U. Ebert, J. G. Eden, P. Favia, D. B. Graves, S. Hamaguchi, G. Hieftje, M. Hori, I. D. Kaganovich, U. Kortshagen, M. J. Kushner, N. J. Mason, S. Mazouffre, S. M. Thagard, H. R. Metelmann, A. Mizuno, E. Moreau, A. B. Murphy, B. A. Niemira, G. S. Oehrlein, Z. L. Petrovic, L. C. Pitchford, Y. K. Pu, S. Rauf, O. Sakai, S. Samukawa, S. Starikovskaia, J. Tennyson, K. Terashima, M. M. Turner, M. C. M. Van De Sanden and A. Vardelle, Journal of Physics D: Applied Physics **50,** 323001 (2017).

[3] G. Packard, A. Rosenfeld, G. S. Oehrlein and S. Hamaguchi, Plasma Sources Science and Technology **27,** 023001 (2018).

[4] Y. Suzuki, S. Iwashita, T. Sato, H. Yonemichi, H. Moki and T. Moriya, 2018 International Symposium on Semiconductor Manufacturing (ISSM), **2018-Decem,** 1–4 (2018).

[5] R. Anirudh, R. Archibald, M. S. Asif, M. M. Becker, S. Benkadda, P. T. Bremer, R. H. S. Bude, X. Zhang, et al., IEEE Transactions on Plasma Science **51,** 1750 (2023).

[6] A. Sankaran and M. J. Kushner, Journal of Vacuum Science & Technology A **22,** 1242 (2004).

[7] R. J. Hoekstra, M. J. Grapperhaus and M. J. Kushner, Journal of Vacuum Science & Technology A: Vacuum, Surfaces, and Films **15,** 1913 (1998).

[8] C. M. Huard, Y. Zhang, S. Sriraman, A. Paterson and M. J. Kushner, Journal of Vacuum Science & Technology A: Vacuum, Surfaces, and Films **35,** 05C301 (2017).

[9] T. Iwase, Y. Kamaji, S. Y. Kang, K. Koga, N. Kuboi, M. Nakamura, N. Negishi, T. Nozaki, S. Nunomura, D. Ogawa, M. Omura, T. Shimizu, K. Shinoda, Y. Sonoda, H. Suzuki, K. Takahashi, T. Tsutsumi, K. Yoshikawa, T. Ishijima and K. Ishikawa, Japanese Journal of Applied Physics **58,** SE0802 (2019).

[10] N. Kuboi, https://doi.org/10.1117/1.JMM.22.4.041502 **22,** 041502 (2023).

[11] J. A. Sethian and D. Adalsteinsson, IEEE Transactions on Semiconductor Manufacturing **10,** 167 (1997).

[12] M. Chopra, S. Helpert, R. Verma, Z. Zhang, X. Zhu, al Meghali Chopra and R. Bonnecaze, https://doi.org/10.1117/12.2297482 **10588,** 132 (2018).

[13] T. Shimada, T. Yagisawa and T. Makabe, Japanese Journal of Applied Physics, Part 2: Letters **45,** L132 (2006).

[14] Y. G. Yook, H. S. You, J. H. Park, W. S. Chang, D. C. Kwon, J. S. Yoon, K. H. Yoon, S. S. Shin, D. H. Yu and Y. H. Im, Journal of Physics D: Applied Physics **55,** 255202 (2022).

[15] H. Tsuda, Y. Takao, K. Eriguchi and K. Ono, Japanese Journal of Applied Physics **51,** 08HC01 (2012).

[16] S. Huang, C. Huard, S. Shim, S. K. Nam, I.-C. Song, S. Lu and M. J. Kushner, Journal of Vacuum Science & Technology A **37,** 031304 (2019).

[17] C. M. Huard, Y. Zhang, S. Sriraman, A. Paterson, K. J. Kanarik and M. J. Kushner, Journal of Vacuum Science & Technology A: Vacuum, Surfaces, and Films **35,** 031306 (2017).

[18] H. Tsuda, K. Eriguchi, K. Ono and H. Ohta, Applied Physics Express **2,** 116501 (2009).

[19] N. A. Mauchamp and S. Hamaguchi, Journal of Vacuum Science & Technology A **40,** 53004 (2022).

[20] C. M. Huard, S. Sriraman, A. Paterson and M. J. Kushner, Journal of Vacuum Science & Technology A: Vacuum, Surfaces, and Films **36,** 6 (2018).

[21] C. Qu, Y. Sakiyama, P. Agarwal and M. J. Kushner, Journal of Vacuum Science & Technology A: Vacuum, Surfaces, and Films **39,** 52403 (2021).

[22] R. Dussart, R. Ettouri, J. Nos, G. Antoun, T. Tillocher and P. Lefaucheux, Journal of Applied Physics **133,** 113306 (2023).

[23] G. Antoun, T. Tillocher, P. Lefaucheux, J. Faguet, K. Maekawa and R. Dussart, Scientific Reports 2021 11:1 **11,** 1 (2021).

[24] R. Dussart, T. Tillocher, P. Lefaucheux and M. Boufnichel, Journal of Physics D: Applied Physics **47,** 123001 (2014).

[25] A. Mesbah and D. B. Graves, Journal of Physics D: Applied Physics **52,** 30LT02 (2019).

[26] A. D. Bonzanini, K. Shao, D. B. Graves, S. Hamaguchi and A. Mesbah, Plasma Sources Science and Technology **32,** 024003 (2023).

[27] R. Anirudh, R. Archibald, M. S. Asif, M. M. Becker, S. Benkadda, P. T. Bremer, R. H. S. Bude, X. Zhang, et al., IEEE Transactions on Plasma Science **51,** 1750 (2023).

[28] J. Moyne and J. Iskandar, Processes 2017, Vol. 5, Page 39 **5,** 39 (2017).

[29] D. Gidon, D. B. Graves and A. Mesbah, Plasma Sources Science and Technology **26,** 085005 (2017).

[30] T. F. Edgar, S. W. Butler, W. J. Campbell, C. Pfeiffer, C. Bode, S. B. Hwang, K. S. Balakrishnan and J. Hahn, Automatica **36,** 1567 (2000).

[31] M. Hankinson, T. Vincent, K. B. Irani and P. P. Khargonekar, IEEE Transactions on Semiconductor Manufacturing **10,** 121 (1997).

[32] D. Stokes and G. S. May, IEEE Transactions on Semiconductor Manufacturing **13,** 469 (2000).

[33] J. H. Xia, Rusli and A. S. Kumta, IEEE Transactions on Plasma Science **38,** 142 (2010).

[34] W. Q. Xiong, Y. Qiao, L. P. Bai, M. Ghahramani, N. Q. Wu, P. H. Hsieh and B. Liu, IEEE Transactions on Semiconductor Manufacturing **34,** 207 (2021).

[35] J. H. Xia, Rusli and A. Kumta, IEEE Transactions on Plasma Science **38,** 1091 (2010).

[36] C. E. Davis and G. S. May, IEEE Transactions on Electronics Packaging Manufacturing **31,** 104 (2008).

[37] P. Seleson, M. Mustafa, D. Curreli, C. D. Hauck, M. Stoyanov and D. E. Bernholdt, Computer Physics Communications **279,** 108436 (2022).

[38] T. Gergs, B. Borislavov and J. Trieschmann, Journal of Vacuum Science & Technology B **40,** 12802 (2022).

[39] G. Dong, X. Wei, J. Bao, G. Brochard, Z. Lin and W. Tang, Nuclear Fusion **61,** 126061 (2021).

[40] S. Morosohk and E. Schuster, Contributions to Plasma Physics **63,** e202200153 (2023).

[41] C. Ma, B. Zhu, X. Q. Xu and W. Wang, Physics of Plasmas **27,** 42502 (2020).

[42] A. Merlo, D. Böckenhoff, J. Schilling, U. Höfel, S. Kwak, J. Svensson, A. Pavone, S. A. Lazerson and T. S. Pedersen, Nuclear Fusion **61,** 096039 (2021).

[43] J. C. Martínez-Loyola, A. A. Siller-Ceniceros, M. E. Sánchez-Castro, al -, S. M. Alia, S. Pylypenko, Y. Liu, C. Akcay, L. L. Lao and X. Sun, Nuclear Fusion **62,** 126067 (2022).

[44] P. Rodriguez-Fernandez, A. E. White, A. J. Creely, M. J. Greenwald, N. T. Howard, F. Sciortino and J. C. Wright, Fusion Science and Technology **74,** 65 (2018).

[45] S. Dasbach and S. Wiesen, Nuclear Materials and Energy **34,** 101396 (2023).

[46] Y. Kim, S. Lee, T. Jung, B. Lee, N. Kwak and al Yongjin Kim, https://doi.org/10.1117/12.2087765 **9428,** 9 (2015).

[47] Y. Yang and Y. Xu, Journal of Vacuum Science & Technology B **41,** 52602 (2023).

[48] M. Omura, J. Hashimoto, T. Adachi, Y. Kondo, M. Ishikawa, J. Abe, I. Sakai, H. Hayashi, M. Sekine and M. Hori, Japanese Journal of Applied Physics **58,** SEEB02 (2019).

[49] K. J. Owen, B. VanDerElzen, R. L. Peterson and K. Najafi, Proceedings of the IEEE International Conference on Micro Electro Mechanical Systems (MEMS) 251 (2012).

[50] B. Wu, A. Kumar and S. Pamarthy, Journal of Applied Physics **108,** 51101 (2010).

[51] S. Huang, S. Shim, S. K. Nam and M. J. Kushner, Journal of Vacuum Science & Technology A: Vacuum, Surfaces, and Films **38,** 023001 (2020).

[52] Z. Hu, H. Shao, J. Li, P. Lai, W. Wang, C. Li, Q. Yan, X. He, J. Li, T. Yang, R. Chen and Y. Wei, Journal of Vacuum Science & Technology A **41,** 63113 (2023).

[53] J. Bobinac, T. Reiter, J. Piso, X. Klemenschits, O. Baumgartner, Z. Stanojevic, G. Strof, M. Karner and L. Filipovic, Micromachines 2023, Vol. 14, Page 665 **14,** 665 (2023).

[54] R. P. Brinkmann, J Phys D Appl Phys **44,** 042002 (2011).

[55] W. Park, J. Han, S. Park and S. Y. Moon, Vacuum **216,** 112466 (2023).

[56] X. Xiao, X. Ke, B. Su and H.-Y. Zhang, ECS Transactions **104,** 201 (2021).

[57] T. Matsushita, T. Matsumoto, H. Mukai, S. Kyoh, K. Hashimoto Takaya Matsushita and K. Hashimoto, https://doi.org/10.1117/12.2085628 **9428,** 15 (2015).

[58] A. A. Kaptanoglu, K. D. Morgan, C. J. Hansen and S. L. Brunton, Physical Review E **104,** 015206 (2021).

[59] E. P. Alves and F. Fiuza, Physical Review Research **4,** (2020).

[60] K. Willcox and J. Peraire, https://doi.org/10.2514/2.1570 **40,** 2323 (2012).

[61] Y. Xing, M. A. Gosálvez, K. Sato, M. Tian and H. Yi, Journal of Micromechanics and Microengineering **22,** 085020 (2012).

[62] M. A. Goslvez, N. Ferrando, Y. Xing, P. Pal, K. Sato, J. Cerdá and R. Gadea, Journal of Micromechanics and Microengineering **21,** 065017 (2011).

[63] Y. Li, Y. Xing, M. A. Gosalvez, P. Pal and Y. Zhou, 2013 Transducers and Eurosensors XXVII: The 17th International Conference on Solid-State Sensors, Actuators and Microsystems, TRANSDUCERS and EUROSENSORS 2013 1087 (2013).

[64] C. C. Liu, Y. Li, Y. S. Yang, C. Y. Chen and M. H. Chuang, International Conference on Simulation of Semiconductor Processes and Devices, SISPAD **2020-September,** 355 (2020).

[65] T. Xiao and D. Ni, Processes 2021, Vol. 9, Page 151 **9,** 151 (2021).

[66] M. S. Daoud, M. Shehab, H. M. Al-Mimi, L. Abualigah, R. A. Zitar and M. K. Y. Shambour, Archives of Computational Methods in Engineering 2022 30:4 **30,** 2431 (2022).

[67] M. Jalalitabar, I. G. Tsoulos, Y. Tian, Y. Zhang and H. Zhang, Mathematics 2023, Vol. 11, Page 682 **11,** 682 (2023).

[68] L. ; Zhou, X. ; Zhou, C. A. Yi, L. Zhou, X. Zhou and C. Yi, Electronics 2023, Vol. 12, Page 994 **12,** 994 (2023).

[69] S. Takenaga, Y. Ozaki and M. Onishi, Optimization Letters **17,** 283 (2023).

[70] Z. Huang, S. Yan, M. Rosenbusch, S. Yan and Z. Huang, Authorea Preprints (2023).

[71] M. J. Kushner, Journal of Physics D: Applied Physics **42,** 194013 (2009).

[72] T. Piskin, Y. Qian, P. Pribyl, W. Gekelman and M. J. Kushner, Journal of Applied Physics **133,** 173302 (2023).

[73] C. Qu, S. J. Lanham, S. C. Shannon, S. K. Nam and M. J. Kushner, Journal of Applied Physics **127,** 133302 (2020).

[74] D. Zhang, S. Rauf and T. Sparks, IEEE Transactions on Plasma Science **30,** 114 (2002).

[75] R. J. Hoekstra, M. J. Kushner, V. Sukharev and P. Schoenborn, Journal of Vacuum Science & Technology B: Microelectronics and Nanometer Structures Processing, Measurement, and Phenomena **16,** 2102 (1998).

[76] M. Shen, T. Lill, J. Hoang, H. Chi, A. Routzahn, J. Church, P. Subramonium, R. Puthenkovilakam, S. Reddy, S. Bhadauriya, S. Roberts and G. Kamarthy, Japanese Journal of Applied Physics **62,** SI0801 (2023).

[77] H. J. M. Shi, M. Qiming Xuan, F. Oztoprak and J. Nocedal, Optimization Methods and Software **38,** 289 (2023).

[78] E. J. Paul, M. Landreman and T. Antonsen, Journal of Plasma Physics **87,** 905870214 (2021).

[79] D. Shin and S. J. Hong, Journal of Vacuum Science & Technology B **41,** 64002 (2023).

[80] J. A. Désidéri, Comptes Rendus Mathematique **350,** 313 (2012).

[81] S. Ruder, (2016).

[82] R. R. Barton and J. S. Ivey, https://doi.org/10.1287/mnsc.42.7.954 **42,** 954 (1996).

[83] K. R. Mahmoud, Electromagnetics **31,** 578 (2011).

[84] I. Fajfar, Á. Bűrmen and J. Puhan, Optimization Letters **13,** 1011 (2019).

[85] C. Audet and C. Tribes, Computational Optimization and Applications **71,** 331 (2018).

[86] M. A. Luersen and R. Le Riche, Computers & Structures **82,** 2251 (2004).

[87] Y. Ozaki, M. Yano and M. Onishi, IPSJ Transactions on Computer Vision and Applications **9,** 1 (2017).

[88] Y. Lee, A. Resiga, S. Yi and C. Wern, Journal of Manufacturing and Materials Processing 2020, Vol. 4, Page 66 **4,** 66 (2020).

[89] E. Zahara and Y. T. Kao, Expert Systems with Applications **36,** 3880 (2009).

[90] J. D. Kress, ; D E Hanson, ; A F Voter, ; C L Liu, X.-Y. Liu, ; D G Coronell,) D E Hanson, A. F. Voter, C. L. Liu and D. G. Coronell, Journal of Vacuum Science & Technology A **17,** 2819 (1999).

[91] J. P. Chang and H. H. Sawin, Journal of Vacuum Science & Technology A **15,** 610 (1997).

Chapter 7 Summary and Outlook

7.1 Summary

In Chapter 1, an overview of physical properties and mechanisms relevant to plasma-based etching of semiconductors was given. This included basic plasma and surface etch phenomena as well as specific applications such as CCPs powered by tailored voltage waveforms operated in Fluorocarbon gas mixtures. A brief literature overview of the field of semiconductor manufacturing and the narrow subject of this thesis was given. Finally, the role of computational modeling as well as current challenges with respect to the fundamental data availability was presented to motivate the content of this thesis.

In Chapter 2, the computational models utilized in this work were introduced. The Hybrid Plasmas Equipment Model, HPEM, was used to simulate the gas phase as well as discharge dynamics and collect the magnitude as well as energy and angular distributions of fluxes to the wafer surface. These fluxes were used as input for the surface simulations using the Monte Carlo Feature Profile Model, MCFPM, which determines the temporal evolution of the surface during the etch process based on a predefined reaction mechanism.

In Chapter 3, the use of tailored voltage waveforms in geometrically asymmetric capacitively coupled plasmas sustained in Ar/O_2 at 40 mTorr was computationally investigated with the goal of shaping the EAD of electrons and ions incident onto the substrate to address differential charging. The tailored waveform consisted of a sinusoidal wave and its higher harmonics with a fundamental frequency of 1 MHz. It was found that electric field reversals in the

sheath and presheath can occur during the anodic portion of the cycle. The electric field reversal increases the energy and decreases the angular spread of electrons incident onto the substrate. The magnitude of the electric field reversal can be controlled by the phase angle of the even harmonics and the gas composition. Due to its electronegative nature, increasing mole fractions of O_2 impedes electron transport to the surface which further increases the electric field reversal.

In Chapter 4, the previous results were expanded upon by investigating the plasma etching of HAR features into SiO_2 in a similar geometry and power delivery configuration but using a $Ar/CF_4/O_2$ mixture. It was similarly found that some degree of control of the IEADs and EEADs is possible by adjusting the phase of higher harmonics φ through the resulting generation of electrical asymmetry and electric field reversal. However, the IEADs and EEADs cannot easily be separately controlled. The control of IEADs and EEADs are inherently linked. The highest quality feature was obtained with a phase angle $\varphi = 0°$ as this value generated the largest (most negative) DC self-bias and largest electric field reversal for accelerating electrons into the feature. That said, the consequences of voltage waveform tailoring (VWT) on etched features was dominated by the change in the IEADs. Although VWT does produce EEADs with higher energy and narrower angular spread, the effect of these electrons on the feature compared to thermal electrons is not large. This smaller impact of VWT produced EEADs is attributed to thermal electrons being accelerated into the feature by electric fields produced by the positive in-feature charging.

In Chapter 5, the relation between ion energy and DC self-bias was investigated in the context of a varying fundamental frequency f_0 for capacitively coupled plasmas sustained in $Ar/CF_4/O_2$ and how those trends translate to a high aspect ratio etching of trenches in SiO_2. f_0, was varied from 1 MHz to 10 MHz, and the relative phase from 0 to 180°. Two distinct regimes were identified. Average ion energy onto the wafer is strongly correlated to the DC self-bias at high f_0,

with there being a maximum at $\varphi = 0°$ and minimum at $\varphi = 180°$. In the low frequency regime this correlation is weak. Average ion energy onto the wafer is instead dominated by dynamic transients in the applied voltage waveforms, with a maximum at $\varphi = 180°$ and minimum at $\varphi = 0°$. The trends in ion energy translate to etch properties. In both the high and low frequency regimes, higher ion energies translate to higher etch rates and generally preferable final features, though behaving differently with phase angle.

In Chapter 6, an autonomous optimization scheme for reaction mechanisms was introduced to address the issue of data availability and accurate reproduction of physical etch processes. A method to automate the selection of fundamental data in a reduced reaction mechanism for feature scale SiO_2 plasma etching using a fluorocarbon gas mixture was discussed. This was done by matching predictions of etch profiles, obtained from MCFPM simulations to experimental data using a gradient descent / Nelder-Mead method hybrid optimization scheme. These methods produce a reaction mechanism that replicates the experimental training data as well as experimental data using a related but different etch processes.

7.2 Future Work

While this thesis has presented promising evidence to highlight the upside potential for technological applications of voltage waveform tailoring, further research will certainly be required to solidify these observations. It would be instructive to expand upon this work by broadening the parameter space in terms of pressure, power, reactor geometry, and gas composition. The use of VWT was aimed at improving etch dynamics in Fluorocarbon etching of SiO_2, but the gained insights could potentially translate to other related systems in which the control of electron and ion EADs is of great importance. This may include similar etch processes of dielectrics or other materials using entirely different gas compositions.

The use of tailored voltage waveforms has been intensely studied using a host of theoretical and computational approaches. While many of these have shown great promise with respect to the possible their technological applications, many challenges remain with respect to a widespread use of this or related techniques. One of these challenges is the adequate matching of these complex voltages which is only further compounded by recent trends to very high powers that limit the tolerable relative amount of reflected power.

Conceptually, the use of complex waveforms is not limited to planar CCPs as presented in this work. Since many other kinds of technological plasmas rely on RF power coupling as a source of plasma heating it is not unreasonable to expect useful applications of similar techniques in a host of different plasma sources and operating regimes. In closely related systems, like for example inductively coupled plasmas with RF biases, similar behavior when non sinusoidal waveforms are applied, could open up analogues avenues for process control. However, this may not be true for other types of discharges that operate in entirely different regimes with respect to the density and temperature of the plasma as well as neutral feedstock gas. So, while it is unlikely that the same working principles produce identical effects, it is nevertheless possible that voltage waveform tailoring can produce significant effects in these systems as well that warrant further investigations.

The optimization scheme presented in Chapter 6 should at this stage be considered a proof of concept, giving many potential areas of improvement.

The target metrics used in this work were able to represent certain aspects of the etch simulation with high accuracy but were lacking in others. The optimization scheme would greatly benefit from the inclusion of metrics that better capture the mask necking and the geometry in the lower echelons of the feature such as micro trenches and flatness of the etch front. The metrics considered in this work were based on a 2-dimensional representation of a vertical slice through

the feature. It might prove useful to implement 3-dimensional target metrics such as symmetry along the y-axis (normal to the current viewing plane) or changes in feature circularity, where applicable.

For the optimization itself the testing and direct comparison of other algorithms might provide additional improvements in terms of accuracy and convergence behavior. Additionally, the formulation and implementation of a rigorous convergence criterion will likely prove very effective in reducing the overall computational expense of the optimization process.

Finally, the optimization of the surface reaction mechanism has relied on the assumption that the HPEM data accurately represents the physical ground truth. To some degree, HPEM is subject to the same fundamental issues with respect to its parameterized data and imperfect benchmarking to experiments. Thus, a natural progression of this work could be the extensions of a similar optimization scheme to include gas phase reaction mechanisms and tune it using HPEM and appropriate target metrics.

Appendices

Appendix A: Statistical Variation in Predicted Feature Profiles

The Monte-Carlo method employed in the MCFPM produces profiles that are inherently subject to statistical variations. This is especially the case when charging processes are included which can act as a feedback loop which amplifies statistical variations. These variations result from the sequence of random numbers that are used to initially generate particle trajectories towards the surface. Quantitatively different features are produced by changing the *seed* that is used to initialize the random number generators. Even when keeping the same seeds, when executing the simulation in a parallel computing environment, there are nearly unavoidable differences in sequencing of the particle trajectories tracked on different processors. Different random number generators are used for each parallel thread to minimize these sequencing issues, but they will occur.

To ensure the overall validity of results produced when statistical variations occur, it is imperative to verify that the random run-to-run variations are of significantly smaller magnitude than the effects discussed. This includes the overall trends in feature properties as a function of phase angle φ as well as the isolated effects produced by surface charge neutralization by the incident electron flux, perhaps most sensitive to these statistical variations.

To assess the statistical variations, a series of identical simulations was performed while varying the random number seed. These cases also include the inherent statistical variations that occur in the parallel computing environment. The resulting profiles for the $\varphi = 0°$, $P_{VWT} = 1000$ W series are shown in Figure A.0.1a for 15 minutes of etching. The maximum difference from the mean etch depth for this series is less than 5% of the total etch. This variation is less than the change in etch depth and profile shape produced by the change in IEADs as a function of φ observed in this work. Similar conclusions extend to variation between the profiles produced with VWT produced and thermal EEADs.

Statistical variations of this type are not limited to numerical simulations but also occur in actual etch processes, producing a certain degree of feature-to-feature non-uniformity. This statistical feature-to-feature variation results from the small size of features, which in turn produces statistically different fluxes of reactant species into the feature. A common approach to remedy these unwanted statistical variations in HVM processes is *over-etching*. In over-etching, a terminal or etch stop layer is located at the desired final etch depth. For any given process, the etch rate into this layer is significantly lower than for the overlying substrate. This means that once the stop layer is reached during the process, vertical etching effectively stops (or is significantly slowed) while etching of the tapered side walls continues. Extending the etch process beyond this contact time, over-etching, partially remedies some of the statistical variations in feature profile by straightening the sidewalls of the feature. A series of profiles are shown in Figure A.0.1b produced with different random number seeds, analogous to Figure A.0.1a, while etching to the stop layer and over-etching for a total of 30 minutes. Through this over-etching, the variations in etch depth and profile are reduced. Where applicable, etch stop layers and over-etching can suppress the statistical run to run differences in feature properties.

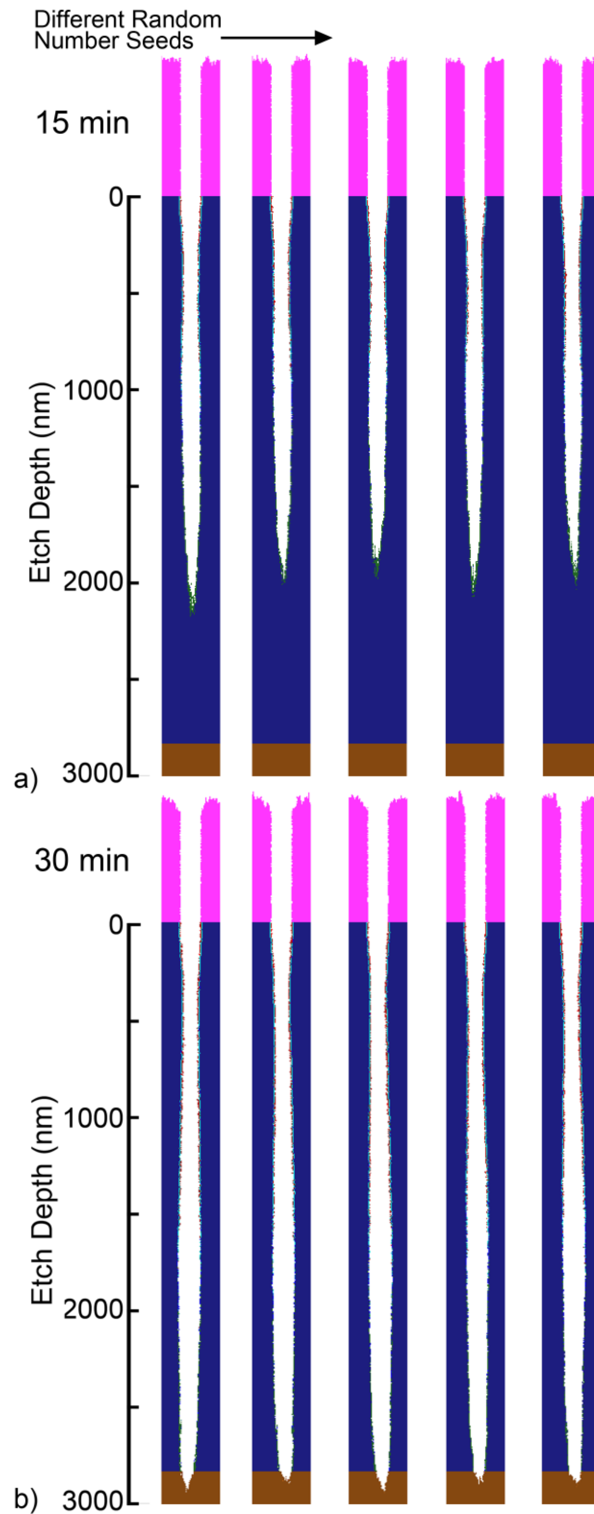

Figure A.0.1: Statistical run-to-run variation of the final etch profiles for the P_{VWT} = 1000 W and φ = 0° case. a) 15 min run and b) 30 min to produce over etch into the stop layer. For each series of profiles, each case had a different seed for the random number generators, in addition to having the inherent statistical variations in the parallel computing environment.

Appendix B: Surface Reaction Mechanism

Table B.0.1 contains the surface reaction mechanism used in this work after convergence. The reaction probability p_0 is modified according to Eq. (2.40) if angular or energy dependence of the reaction is present. In that case, $\varepsilon_{th}, \varepsilon_0$ and q define the energy dependence and ∠ defines the nature of the angular dependence, with ∠=1 corresponding to the results obtained by [1] and ∠=2 corresponding to the results obtained by [2].

If no values for p_0 , ε_0 , ε_{th} n and ∠ are provided, the reaction has not energy or angular dependence. The superscripts '+', '#' and '*' identify positive ions, hot neutrals and exited species, respectively.

The subscript '(s)' refers to a surface species, while '(xs)' is a crosslinked surface species. Not listed below are surface neutralization reactions that occur for every charge species. EP is a generic etch product that is assumed to be inert and not tracked further.

Table B.0.1: Complete surface reaction mechanism

Reaction	p_0	ε_{th}	n	ε_0	∠
$CF_{(s)}$ + CF → $CF_{(s)}$ + $CF_{(s)}$	0.1				
$CF_{(s)}$ + CF_2 → $CF_{(s)}$ + $CF_{2(s)}$	0.1				
$CF_{(s)}$ + CF_3 → $CF_{(s)}$ + $CF_{3(s)}$	0.1				
$CF_{(s)}$ + C_2F_3 → $CF_{(s)}$ + $C_2F_{3(s)}$	0.1				
$CF_{2(s)}$ + CF → $CF_{2(s)}$ + $CF_{(s)}$	0.1				
$CF_{2(s)}$ + CF_2 → $CF_{2(s)}$ + $CF_{2(s)}$	0.1				
$CF_{2(s)}$ + CF_3 → $CF_{2(s)}$ + $CF_{3(s)}$	0.1				
$CF_{2(s)}$ + C_2F_3 → $CF_{2(s)}$ + $C_2F_{3(s)}$	0.1				
$CF_{3(s)}$ + CF → $CF_{3(s)}$ + $CF_{(s)}$	0.1				

Reaction					
$CF_{3(s)} + CF_2 \rightarrow CF_{3(s)} + CF_{2(s)}$	0.1				
$CF_{3(s)} + CF_3 \rightarrow CF_{3(s)} + CF_{3(s)}$	0.1				
$CF_{3(s)} + C_2F_3 \rightarrow CF_{3(s)} + C_2F_{3(s)}$	0.1				
$C_2F_{3(s)} + CF \rightarrow C_2F_{3(s)} + CF_{(s)}$	0.03				
$C_2F_{3(s)} + CF_2 \rightarrow C_2F_{3(s)} + CF_{2(s)}$	0.03				
$C_2F_{3(s)} + CF_3 \rightarrow C_2F_{3(s)} + CF_{3(s)}$	0.03				
$C_2F_{3(s)} + C_2F_3 \rightarrow C_2F_{3(s)} + C_2F_{3(s)}$	0.03				
$AC_{(s)} + CF \rightarrow AC_{(s)} + CF_{(s)}$	0.2				
$AC_{(s)} + CF_2 \rightarrow AC_{(s)} + CF_{2(s)}$	0.2				
$AC_{(s)} + CF_3 \rightarrow AC_{(s)} + CF_{3(s)}$	0.2				
$AC_{(s)} + C_2F_3 \rightarrow AC_{(s)} + C_2F_{3(s)}$	0.2				
$AC_{(xs)} + CF \rightarrow AC_{(xs)} + CF_{(s)}$	0.2				
$AC_{(xs)} + CF_2 \rightarrow AC_{(xs)} + CF_{2(s)}$	0.2				
$AC_{(xs)} + CF_3 \rightarrow AC_{(xs)} + CF_{3(s)}$	0.2				
$AC_{(xs)} + C_2F_3 \rightarrow AC_{(xs)} + C_2F_{3(s)}$	0.2				
$CF_{(xs)} + CF \rightarrow CF_{(xs)} + CF_{(s)}$	0.02				
$CF_{(xs)} + CF_2 \rightarrow CF_{(xs)} + CF_{2(s)}$	0.02				
$CF_{(xs)} + CF_3 \rightarrow CF_{(xs)} + CF_{3(s)}$	0.02				
$CF_{(xs)} + C_2F_3 \rightarrow CF_{(xs)} + C_2F_{3(s)}$	0.02				
$CF_{2(xs)} + CF \rightarrow CF_{2(xs)} + CF_{(s)}$	0.02				
$CF_{2(xs)} + CF_2 \rightarrow CF_{2(xs)} + CF_{2(s)}$	0.02				
$CF_{2(xs)} + CF_3 \rightarrow CF_{2(xs)} + CF_{3(s)}$	0.02				
$CF_{2(xs)} + C_2F_3 \rightarrow CF_{2(xs)} + C_2F_{3(s)}$	0.02				
$CF_{3(xs)} + CF \rightarrow CF_{3(xs)} + CF_{(s)}$	0.02				
$CF_{3(xs)} + CF_2 \rightarrow CF_{3(xs)} + CF_{2(s)}$	0.02				
$CF_{3(xs)} + CF_3 \rightarrow CF_{3(xs)} + CF_{3(s)}$	0.02				
$CF_{3(xs)} + C_2F_3 \rightarrow CF_{3(xs)} + C_2F_{3(s)}$	0.02				
$CF_{(s)} + O \rightarrow EP$	0.0423				
$CF_{2(s)} + O \rightarrow EP$	0.0423				
$CF_{3(s)} + O \rightarrow EP$	0.0423				
$C_2F_{3(s)} + O \rightarrow EP$	0.0423				
$CF_{(xs)} + O \rightarrow EP$	0.0423				
$CF_{2(xs)} + O \rightarrow EP$	0.0423				
$CF_{3(xs)} + O \rightarrow EP$	0.0423				
$AC_{(s)} + O \rightarrow CO$	1.00E-05				
$AC_{(xs)} + O \rightarrow CO$	1.00E-05				
$AC_{(s)} + Ar^{+} \rightarrow C + Ar^{\#}$	0.001	200	0.4	250	1
$AC_{(s)} + F_2^{+} \rightarrow C + F_2^{\#}$	0.001	200	0.4	250	1
$AC_{(s)} + F^{+} \rightarrow C + F^{\#}$	0.001	200	0.4	250	1
$AC_{(s)} + O_2^{+} \rightarrow C + O_2^{\#}$	0.001	200	0.4	250	1
$AC_{(s)} + O^{+} \rightarrow C + O^{\#}$	0.001	200	0.4	250	1

$AC_{(s)}$	$+ CF_3^+$	→	C	$+ CF_3^\#$	0.001	200	0.4	250	1
$AC_{(s)}$	$+ CF_2^+$	→	C	$+ CF_2^\#$	0.001	200	0.4	250	1
$AC_{(s)}$	$+ CF^+$	→	C	$+ CF^\#$	0.001	200	0.4	250	1
$AC_{(s)}$	$+ C_2F_3^+$	→	C	$+ C_2F_3^\#$	0.001	200	0.4	250	1
$AC_{(s)}$	$+ C_2F_4^+$	→	C	$+ C_2F_4^\#$	0.001	200	0.4	250	1
$AC_{(s)}$	$+ C_2F_5^+$	→	C	$+ C_2F_5^\#$	0.001	200	0.4	250	1
$AC_{(s)}$	$+ C_3F_5^+$	→	C	$+ C_3F_5^\#$	0.001	200	0.4	250	1
$AC_{(s)}$	$+ C_3F_6^+$	→	C	$+ C_3F_6^\#$	0.001	200	0.4	250	1
$AC_{(s)}$	$+ C_3F_7^+$	→	C	$+ C_3F_7^\#$	0.001	200	0.4	250	1
$AC_{(s)}$	$+ C_4F_7^+$	→	C	$+ C_4F_7^\#$	0.001	200	0.4	250	1
$AC_{(s)}$	$+ C_4F_8^+$	→	C	$+ C_4F_8^\#$	0.001	200	0.4	250	1
$AC_{(s)}$	$+ Ar^\#$	→	C	$+ Ar^\#$	0.001	200	0.4	250	1
$AC_{(s)}$	$+ F_2^\#$	→	C	$+ F_2^\#$	0.001	200	0.4	250	1
$AC_{(s)}$	$+ F^\#$	→	C	$+ F^\#$	0.001	200	0.4	250	1
$AC_{(s)}$	$+ O_2^\#$	→	C	$+ O_2^\#$	0.001	200	0.4	250	1
$AC_{(s)}$	$+ O^\#$	→	C	$+ O^\#$	0.001	200	0.4	250	1
$AC_{(s)}$	$+ CF_3^\#$	→	C	$+ CF_3^\#$	0.001	200	0.4	250	1
$AC_{(s)}$	$+ CF_2^\#$	→	C	$+ CF_2^\#$	0.001	200	0.4	250	1
$AC_{(s)}$	$+ CF^\#$	→	C	$+ CF^\#$	0.001	200	0.4	250	1
$AC_{(s)}$	$+ C_2F_3^\#$	→	C	$+ C_2F_3^\#$	0.001	200	0.4	250	1
$AC_{(s)}$	$+ C_2F_4^\#$	→	C	$+ C_2F_4^\#$	0.001	200	0.4	250	1
$AC_{(s)}$	$+ C_2F_5^\#$	→	C	$+ C_2F_5^\#$	0.001	200	0.4	250	1
$AC_{(s)}$	$+ C_3F_5^\#$	→	C	$+ C_3F_5^\#$	0.001	200	0.4	250	1
$AC_{(s)}$	$+ C_3F_6^\#$	→	C	$+ C_3F_6^\#$	0.001	200	0.4	250	1
$AC_{(s)}$	$+ C_3F_7^\#$	→	C	$+ C_3F_7^\#$	0.001	200	0.4	250	1
$AC_{(s)}$	$+ C_4F_7^\#$	→	C	$+ C_4F_7^\#$	0.001	200	0.4	250	1
$AC_{(s)}$	$+ C_4F_8^\#$	→	C	$+ C_4F_8^\#$	0.001	200	0.4	250	1
$AC_{(xs)}$	$+ Ar^+$	→	C	$+ Ar^\#$	0.001	200	0.4	250	1
$AC_{(xs)}$	$+ F_2^+$	→	C	$+ F_2^\#$	0.001	200	0.4	250	1
$AC_{(xs)}$	$+ F^+$	→	C	$+ F^\#$	0.001	200	0.4	250	1
$AC_{(xs)}$	$+ O_2^+$	→	C	$+ O_2^\#$	0.001	200	0.4	250	1
$AC_{(xs)}$	$+ O^+$	→	C	$+ O^\#$	0.001	200	0.4	250	1
$AC_{(xs)}$	$+ CF_3^+$	→	C	$+ CF_3^\#$	0.001	200	0.4	250	1
$AC_{(xs)}$	$+ CF_2^+$	→	C	$+ CF_2^\#$	0.001	200	0.4	250	1
$AC_{(xs)}$	$+ CF^+$	→	C	$+ CF^\#$	0.001	200	0.4	250	1
$AC_{(xs)}$	$+ C_2F_3^+$	→	C	$+ C_2F_3^\#$	0.001	200	0.4	250	1
$AC_{(xs)}$	$+ C_2F_4^+$	→	C	$+ C_2F_4^\#$	0.001	200	0.4	250	1
$AC_{(xs)}$	$+ C_2F_5^+$	→	C	$+ C_2F_5^\#$	0.001	200	0.4	250	1
$AC_{(xs)}$	$+ C_3F_5^+$	→	C	$+ C_3F_5^\#$	0.001	200	0.4	250	1
$AC_{(xs)}$	$+ C_3F_6^+$	→	C	$+ C_3F_6^\#$	0.001	200	0.4	250	1
$AC_{(xs)}$	$+ C_3F_7^+$	→	C	$+ C_3F_7^\#$	0.001	200	0.4	250	1

$AC_{(xs)} + C_4F_7^+ \rightarrow C + C_4F_7^\#$	0.001	200	0.4	250	1
$AC_{(xs)} + C_4F_8^+ \rightarrow C + C_4F_8^\#$	0.001	200	0.4	250	1
$AC_{(xs)} + Ar^\# \rightarrow C + Ar^\#$	0.001	200	0.4	250	1
$AC_{(xs)} + F_2^\# \rightarrow C + F_2^\#$	0.001	200	0.4	250	1
$AC_{(xs)} + F^\# \rightarrow C + F^\#$	0.001	200	0.4	250	1
$AC_{(xs)} + O_2^\# \rightarrow C + O_2^\#$	0.001	200	0.4	250	1
$AC_{(xs)} + O^\# \rightarrow C + O^\#$	0.001	200	0.4	250	1
$AC_{(xs)} + CF_3^\# \rightarrow C + CF_3^\#$	0.001	200	0.4	250	1
$AC_{(xs)} + CF_2^\# \rightarrow C + CF_2^\#$	0.001	200	0.4	250	1
$AC_{(xs)} + CF^\# \rightarrow C + CF^\#$	0.001	200	0.4	250	1
$AC_{(xs)} + C_2F_3^\# \rightarrow C + C_2F_3^\#$	0.001	200	0.4	250	1
$AC_{(xs)} + C_2F_4^\# \rightarrow C + C_2F_4^\#$	0.001	200	0.4	250	1
$AC_{(xs)} + C_2F_5^\# \rightarrow C + C_2F_5^\#$	0.001	200	0.4	250	1
$AC_{(xs)} + C_3F_5^\# \rightarrow C + C_3F_5^\#$	0.001	200	0.4	250	1
$AC_{(xs)} + C_3F_6^\# \rightarrow C + C_3F_6^\#$	0.001	200	0.4	250	1
$AC_{(xs)} + C_3F_7^\# \rightarrow C + C_3F_7^\#$	0.001	200	0.4	250	1
$AC_{(xs)} + C_4F_7^\# \rightarrow C + C_4F_7^\#$	0.001	200	0.4	250	1
$AC_{(xs)} + C_4F_8^\# \rightarrow C + C_4F_8^\#$	0.001	200	0.4	250	1
$CF_{(s)} + Ar^+ \rightarrow EP + Ar^\#$	0.9	20	0.5	500	1
$CF_{(s)} + Ar^+ \rightarrow AC_{(s)} + F + Ar^\#$	0.01	20	0.5	500	1
$CF_{(s)} + Ar^\# \rightarrow EP + Ar^\#$	0.9	20	0.5	500	1
$CF_{(s)} + Ar^\# \rightarrow AC_{(s)} + F + Ar^\#$	0.01	20	0.5	500	1
$CF_{(s)} + CF_3^+ \rightarrow EP + CF_3^\#$	0.9	20	0.5	500	1
$CF_{(s)} + CF_3^+ \rightarrow AC_{(s)} + F + CF_3^\#$	0.01	20	0.5	500	1
$CF_{(s)} + CF_3^\# \rightarrow EP + CF_3^\#$	0.9	20	0.5	500	1
$CF_{(s)} + CF_3^\# \rightarrow AC_{(s)} + F + CF_3^\#$	0.01	20	0.5	500	1
$CF_{(s)} + CF_2^+ \rightarrow EP + CF_2^\#$	0.9	20	0.5	500	1
$CF_{(s)} + CF_2^+ \rightarrow AC_{(s)} + F + CF_2^\#$	0.01	20	0.5	500	1
$CF_{(s)} + CF_2^\# \rightarrow EP + CF_2^\#$	0.9	20	0.5	500	1
$CF_{(s)} + CF_2^\# \rightarrow AC_{(s)} + F + CF_2^\#$	0.01	20	0.5	500	1
$CF_{(s)} + CF^+ \rightarrow EP + CF^\#$	0.9	20	0.5	500	1
$CF_{(s)} + CF^+ \rightarrow AC_{(s)} + F + CF^\#$	0.01	20	0.5	500	1
$CF_{(s)} + CF^\# \rightarrow EP + CF^\#$	0.9	20	0.5	500	1
$CF_{(s)} + CF^\# \rightarrow AC_{(s)} + F + CF^\#$	0.01	20	0.5	500	1
$CF_{(s)} + F^+ \rightarrow EP + F^\#$	0.9	20	0.5	500	1
$CF_{(s)} + F^+ \rightarrow AC_{(s)} + F + F^\#$	0.01	20	0.5	500	1
$CF_{(s)} + F^\# \rightarrow EP + F^\#$	0.9	20	0.5	500	1
$CF_{(s)} + F^\# \rightarrow AC_{(s)} + F + F^\#$	0.01	20	0.5	500	1
$CF_{(s)} + F_2^+ \rightarrow EP + F_2^\#$	0.9	20	0.5	500	1
$CF_{(s)} + F_2^+ \rightarrow AC_{(s)} + F + F_2^\#$	0.01	20	0.5	500	1
$CF_{(s)} + F_2^\# \rightarrow EP + F_2^\#$	0.9	20	0.5	500	1

$CF_{(s)} + F_2^{\#} \rightarrow AC_{(s)} + F + F_2^{\#}$	0.01	20	0.5	500	1
$CF_{(s)} + C_2F_5^{+} \rightarrow EP + C_2F_5^{\#}$	0.9	20	0.5	500	1
$CF_{(s)} + C_2F_5^{+} \rightarrow AC_{(s)} + F + C_2F_5^{\#}$	0.01	20	0.5	500	1
$CF_{(s)} + C_2F_5^{\#} \rightarrow EP + C_2F_5^{\#}$	0.9	20	0.5	500	1
$CF_{(s)} + C_2F_5^{\#} \rightarrow AC_{(s)} + F + C_2F_5^{\#}$	0.01	20	0.5	500	1
$CF_{(s)} + C_2F_4^{+} \rightarrow EP + C_2F_4^{\#}$	0.9	20	0.5	500	1
$CF_{(s)} + C_2F_4^{+} \rightarrow AC_{(s)} + F + C_2F_4^{\#}$	0.01	20	0.5	500	1
$CF_{(s)} + C_2F_4^{\#} \rightarrow EP + C_2F_4^{\#}$	0.9	20	0.5	500	1
$CF_{(s)} + C_2F_4^{\#} \rightarrow AC_{(s)} + F + C_2F_4^{\#}$	0.01	20	0.5	500	1
$CF_{(s)} + C_2F_3^{+} \rightarrow EP + C_2F_3^{\#}$	0.9	20	0.5	500	1
$CF_{(s)} + C_2F_3^{+} \rightarrow AC_{(s)} + F + C_2F_3^{\#}$	0.01	20	0.5	500	1
$CF_{(s)} + C_2F_3^{\#} \rightarrow EP + C_2F_3^{\#}$	0.9	20	0.5	500	1
$CF_{(s)} + C_2F_3^{\#} \rightarrow AC_{(s)} + F + C_2F_3^{\#}$	0.01	20	0.5	500	1
$CF_{(s)} + C_3F_5^{+} \rightarrow EP + C_3F_5^{\#}$	0.9	20	0.5	500	1
$CF_{(s)} + C_3F_5^{+} \rightarrow AC_{(s)} + F + C_3F_5^{\#}$	0.01	20	0.5	500	1
$CF_{(s)} + C_3F_5^{\#} \rightarrow EP + C_3F_5^{\#}$	0.9	20	0.5	500	1
$CF_{(s)} + C_3F_5^{\#} \rightarrow AC_{(s)} + F + C_3F_5^{\#}$	0.01	20	0.5	500	1
$CF_{(s)} + C_3F_6^{+} \rightarrow EP + C_3F_6^{\#}$	0.9	20	0.5	500	1
$CF_{(s)} + C_3F_6^{+} \rightarrow AC_{(s)} + F + C_3F_6^{\#}$	0.01	20	0.5	500	1
$CF_{(s)} + C_3F_6^{\#} \rightarrow EP + C_3F_6^{\#}$	0.9	20	0.5	500	1
$CF_{(s)} + C_3F_6^{\#} \rightarrow AC_{(s)} + F + C_3F_6^{\#}$	0.01	20	0.5	500	1
$CF_{(s)} + C_3F_7^{+} \rightarrow EP + C_3F_7^{\#}$	0.9	20	0.5	500	1
$CF_{(s)} + C_3F_7^{+} \rightarrow AC_{(s)} + F + C_3F_7^{\#}$	0.01	20	0.5	500	1
$CF_{(s)} + C_3F_7^{\#} \rightarrow EP + C_3F_7^{\#}$	0.9	20	0.5	500	1
$CF_{(s)} + C_3F_7^{\#} \rightarrow AC_{(s)} + F + C_3F_7^{\#}$	0.01	20	0.5	500	1
$CF_{(s)} + C_4F_7^{+} \rightarrow EP + C_4F_7^{\#}$	0.9	20	0.5	500	1
$CF_{(s)} + C_4F_7^{+} \rightarrow AC_{(s)} + F + C_4F_7^{\#}$	0.01	20	0.5	500	1
$CF_{(s)} + C_4F_7^{\#} \rightarrow EP + C_4F_7^{\#}$	0.9	20	0.5	500	1
$CF_{(s)} + C_4F_7^{\#} \rightarrow AC_{(s)} + F + C_4F_7^{\#}$	0.01	20	0.5	500	1
$CF_{(s)} + C_4F_8^{+} \rightarrow EP + C_4F_8^{\#}$	0.9	20	0.5	500	1
$CF_{(s)} + C_4F_8^{+} \rightarrow AC_{(s)} + F + C_4F_8^{\#}$	0.01	20	0.5	500	1
$CF_{(s)} + C_4F_8^{\#} \rightarrow EP + C_4F_8^{\#}$	0.9	20	0.5	500	1
$CF_{(s)} + C_4F_8^{\#} \rightarrow AC_{(s)} + F + C_4F_8^{\#}$	0.01	20	0.5	500	1
$CF_{(s)} + O^{+} \rightarrow EP + O^{\#}$	0.9	20	0.5	500	1
$CF_{(s)} + O^{+} \rightarrow AC_{(s)} + F + O^{\#}$	0.01	20	0.5	500	1
$CF_{(s)} + O_2^{+} \rightarrow EP + O_2^{\#}$	0.9	20	0.5	500	1
$CF_{(s)} + O_2^{+} \rightarrow AC_{(s)} + F + O_2^{\#}$	0.01	20	0.5	500	1
$CF_{(s)} + O^{\#} \rightarrow EP + O^{\#}$	0.9	20	0.5	500	1
$CF_{(s)} + O^{\#} \rightarrow AC_{(s)} + F + O^{\#}$	0.01	20	0.5	500	1
$CF_{(s)} + O^{\#} \rightarrow CF + O^{\#}$	0.1				
$CF_{(s)} + O_2^{\#} \rightarrow EP + O_2^{\#}$	0.9	20	0.5	500	1

$CF_{(s)} + O_2^{\#} \rightarrow AC_{(s)} + F + O_2^{\#}$	0.01	20	0.5	500	1
$CF_{2(s)} + Ar^{+} \rightarrow EP + Ar^{\#}$	0.9	20	0.5	500	1
$CF_{2(s)} + Ar^{+} \rightarrow CF_{(s)} + F + Ar^{\#}$	0.01	20	0.5	500	1
$CF_{2(s)} + Ar^{\#} \rightarrow EP + Ar^{\#}$	0.9	20	0.5	500	1
$CF_{2(s)} + Ar^{\#} \rightarrow CF_{(s)} + F + Ar^{\#}$	0.01	20	0.5	500	1
$CF_{2(s)} + CF_3^{+} \rightarrow EP + CF_3^{\#}$	0.9	20	0.5	500	1
$CF_{2(s)} + CF_3^{+} \rightarrow CF_{(s)} + F + CF_3^{\#}$	0.01	20	0.5	500	1
$CF_{2(s)} + CF_3^{\#} \rightarrow EP + CF_3^{\#}$	0.9	20	0.5	500	1
$CF_{2(s)} + CF_3^{\#} \rightarrow CF_{(s)} + F + CF_3^{\#}$	0.01	20	0.5	500	1
$CF_{2(s)} + CF_2^{+} \rightarrow EP + CF_2^{\#}$	0.9	20	0.5	500	1
$CF_{2(s)} + CF_2^{+} \rightarrow CF_{(s)} + F + CF_2^{\#}$	0.01	20	0.5	500	1
$CF_{2(s)} + CF_2^{\#} \rightarrow EP + CF_2^{\#}$	0.9	20	0.5	500	1
$CF_{2(s)} + CF_2^{\#} \rightarrow CF_{(s)} + F + CF_2^{\#}$	0.01	20	0.5	500	1
$CF_{2(s)} + CF^{+} \rightarrow EP + CF^{\#}$	0.9	20	0.5	500	1
$CF_{2(s)} + CF^{+} \rightarrow CF_{(s)} + F + CF^{\#}$	0.01	20	0.5	500	1
$CF_{2(s)} + CF^{\#} \rightarrow EP + CF^{\#}$	0.9	20	0.5	500	1
$CF_{2(s)} + CF^{\#} \rightarrow CF_{(s)} + F + CF^{\#}$	0.01	20	0.5	500	1
$CF_{2(s)} + F^{+} \rightarrow EP + F^{\#}$	0.9	20	0.5	500	1
$CF_{2(s)} + F^{+} \rightarrow CF_{(s)} + F + F^{\#}$	0.01	20	0.5	500	1
$CF_{2(s)} + F^{\#} \rightarrow EP + F^{\#}$	0.9	20	0.5	500	1
$CF_{2(s)} + F^{\#} \rightarrow CF_{(s)} + F + F^{\#}$	0.01	20	0.5	500	1
$CF_{2(s)} + F_2^{+} \rightarrow EP + F_2^{\#}$	0.9	20	0.5	500	1
$CF_{2(s)} + F_2^{+} \rightarrow CF_{(s)} + F + F_2^{\#}$	0.01	20	0.5	500	1
$CF_{2(s)} + F_2^{\#} \rightarrow EP + F_2^{\#}$	0.9	20	0.5	500	1
$CF_{2(s)} + F_2^{\#} \rightarrow CF_{(s)} + F + F_2^{\#}$	0.01	20	0.5	500	1
$CF_{2(s)} + C_2F_5^{+} \rightarrow EP + C_2F_5^{\#}$	0.9	20	0.5	500	1
$CF_{2(s)} + C_2F_5^{+} \rightarrow CF_{(s)} + F + C_2F_5^{\#}$	0.01	20	0.5	500	1
$CF_{2(s)} + C_2F_5^{\#} \rightarrow EP + C_2F_5^{\#}$	0.9	20	0.5	500	1
$CF_{2(s)} + C_2F_5^{\#} \rightarrow CF_{(s)} + F + C_2F_5^{\#}$	0.01	20	0.5	500	1
$CF_{2(s)} + C_2F_4^{+} \rightarrow EP + C_2F_4^{\#}$	0.9	20	0.5	500	1
$CF_{2(s)} + C_2F_4^{+} \rightarrow CF_{(s)} + F + C_2F_4^{\#}$	0.01	20	0.5	500	1
$CF_{2(s)} + C_2F_4^{\#} \rightarrow EP + C_2F_4^{\#}$	0.9	20	0.5	500	1
$CF_{2(s)} + C_2F_4^{\#} \rightarrow CF_{(s)} + F + C_2F_4^{\#}$	0.01	20	0.5	500	1
$CF_{2(s)} + C_2F_3^{+} \rightarrow EP + C_2F_3^{\#}$	0.9	20	0.5	500	1
$CF_{2(s)} + C_2F_3^{+} \rightarrow CF_{(s)} + F + C_2F_3^{\#}$	0.01	20	0.5	500	1
$CF_{2(s)} + C_2F_3^{\#} \rightarrow EP + C_2F_3^{\#}$	0.9	20	0.5	500	1
$CF_{2(s)} + C_2F_3^{\#} \rightarrow CF_{(s)} + F + C_2F_3^{\#}$	0.01	20	0.5	500	1
$CF_{2(s)} + C_3F_5^{+} \rightarrow EP + C_3F_5^{\#}$	0.9	20	0.5	500	1
$CF_{2(s)} + C_3F_5^{+} \rightarrow CF_{(s)} + F + C_3F_5^{\#}$	0.01	20	0.5	500	1
$CF_{2(s)} + C_3F_5^{\#} \rightarrow EP + C_3F_5^{\#}$	0.9	20	0.5	500	1
$CF_{2(s)} + C_3F_5^{\#} \rightarrow CF_{(s)} + F + C_3F_5^{\#}$	0.01	20	0.5	500	1

$CF_{2(s)} + C_3F_6^+ \rightarrow EP + C_3F_6^\#$	0.9	20	0.5	500	1
$CF_{2(s)} + C_3F_5^\# \rightarrow CF_{(s)} + F + C_3F_5^\#$	0.01	20	0.5	500	1
$CF_{2(s)} + C_3F_6^\# \rightarrow EP + C_3F_6^\#$	0.9	20	0.5	500	1
$CF_{2(s)} + C_3F_6^\# \rightarrow CF_{(s)} + F + C_3F_6^\#$	0.01	20	0.5	500	1
$CF_{2(s)} + C_3F_7^+ \rightarrow EP + C_3F_7^\#$	0.9	20	0.5	500	1
$CF_{2(s)} + C_3F_7^+ \rightarrow CF_{(s)} + F + C_3F_7^\#$	0.01	20	0.5	500	1
$CF_{2(s)} + C_3F_7^\# \rightarrow EP + C_3F_7^\#$	0.9	20	0.5	500	1
$CF_{2(s)} + C_3F_7^\# \rightarrow CF_{(s)} + F + C_3F_7^\#$	0.01	20	0.5	500	1
$CF_{2(s)} + C_4F_7^+ \rightarrow EP + C_4F_7^\#$	0.9	20	0.5	500	1
$CF_{2(s)} + C_4F_7^+ \rightarrow CF_{(s)} + F + C_4F_7^\#$	0.01	20	0.5	500	1
$CF_{2(s)} + C_4F_7^\# \rightarrow EP + C_4F_7^\#$	0.9	20	0.5	500	1
$CF_{2(s)} + C_4F_7^\# \rightarrow CF_{(s)} + F + C_4F_7^\#$	0.01	20	0.5	500	1
$CF_{2(s)} + C_4F_8^+ \rightarrow EP + C_4F_8^\#$	0.9	20	0.5	500	1
$CF_{2(s)} + C_4F_8^+ \rightarrow CF_{(s)} + F + C_4F_8^\#$	0.01	20	0.5	500	1
$CF_{2(s)} + C_4F_8^\# \rightarrow EP + C_4F_8^\#$	0.9	20	0.5	500	1
$CF_{2(s)} + C_4F_8^\# \rightarrow CF_{(s)} + F + C_4F_8^\#$	0.01	20	0.5	500	1
$CF_{2(s)} + O^+ \rightarrow EP + O^\#$	0.9	20	0.5	500	1
$CF_{2(s)} + O^+ \rightarrow CF_{(s)} + F + O^\#$	0.01	20	0.5	500	1
$CF_{2(s)} + O_2^+ \rightarrow EP + O_2^\#$	0.9	20	0.5	500	1
$CF_{2(s)} + O_2^+ \rightarrow CF_{(s)} + F + O_2^\#$	0.01	20	0.5	500	1
$CF_{2(s)} + O^\# \rightarrow EP + O^\#$	0.9	20	0.5	500	1
$CF_{2(s)} + O^\# \rightarrow CF_{(s)} + F + O^\#$	0.01	20	0.5	500	1
$CF_{2(s)} + O^\# \rightarrow CF + O^\#$	0.1				
$CF_{2(s)} + O_2^\# \rightarrow EP + O_2^\#$	0.9	20	0.5	500	1
$CF_{2(s)} + O_2^\# \rightarrow CF_{(s)} + F + O_2^\#$	0.01	20	0.5	500	1
$CF_{3(s)} + Ar^+ \rightarrow EP + Ar^\#$	0.9	20	0.5	500	1
$CF_{3(s)} + Ar^+ \rightarrow CF_{2(s)} + F + Ar^\#$	0.01	20	0.5	500	1
$CF_{3(s)} + Ar^\# \rightarrow EP + Ar^\#$	0.9	20	0.5	500	1
$CF_{3(s)} + Ar^\# \rightarrow CF_{2(s)} + F + Ar^\#$	0.01	20	0.5	500	1
$CF_{3(s)} + CF_3^+ \rightarrow EP + CF_3^\#$	0.9	20	0.5	500	1
$CF_{3(s)} + CF_3^+ \rightarrow CF_{2(s)} + F + CF_3^\#$	0.01	20	0.5	500	1
$CF_{3(s)} + CF_3^\# \rightarrow EP + CF_3^\#$	0.9	20	0.5	500	1
$CF_{3(s)} + CF_3^\# \rightarrow CF_{2(s)} + F + CF_3^\#$	0.01	20	0.5	500	1
$CF_{3(s)} + CF_2^+ \rightarrow EP + CF_2^\#$	0.9	20	0.5	500	1
$CF_{3(s)} + CF_2^+ \rightarrow CF_{2(s)} + F + CF_2^\#$	0.01	20	0.5	500	1
$CF_{3(s)} + CF_2^\# \rightarrow EP + CF_2^\#$	0.9	20	0.5	500	1
$CF_{3(s)} + CF_2^\# \rightarrow CF_{2(s)} + F + CF_2^\#$	0.01	20	0.5	500	1
$CF_{3(s)} + CF^+ \rightarrow EP + CF^\#$	0.9	20	0.5	500	1
$CF_{3(s)} + CF^+ \rightarrow CF_{2(s)} + F + CF^\#$	0.01	20	0.5	500	1
$CF_{3(s)} + CF^\# \rightarrow EP + CF^\#$	0.9	20	0.5	500	1
$CF_{3(s)} + CF^\# \rightarrow CF_{2(s)} + F + CF^\#$	0.01	20	0.5	500	1

$CF_{3(s)}$	$+ F^+$	→	EP	$+ F^\#$		0.9	20	0.5	500	1
$CF_{3(s)}$	$+ F^+$	→	$CF_{2(s)}$	+ F	$+ F^\#$	0.01	20	0.5	500	1
$CF_{3(s)}$	$+ F^\#$	→	EP	$+ F^\#$		0.9	20	0.5	500	1
$CF_{3(s)}$	$+ F^\#$	→	$CF_{2(s)}$	+ F	$+ F^\#$	0.01	20	0.5	500	1
$CF_{3(s)}$	$+ F_2^+$	→	EP	$+ F_2^\#$		0.9	20	0.5	500	1
$CF_{3(s)}$	$+ F_2^+$	→	$CF_{2(s)}$	+ F	$+ F_2^\#$	0.01	20	0.5	500	1
$CF_{3(s)}$	$+ F_2^\#$	→	EP	$+ F_2^\#$		0.9	20	0.5	500	1
$CF_{3(s)}$	$+ F_2^\#$	→	$CF_{2(s)}$	+ F	$+ F_2^\#$	0.01	20	0.5	500	1
$CF_{3(s)}$	$+ C_2F_5^+$	→	EP	$+ C_2F_5^\#$		0.9	20	0.5	500	1
$CF_{3(s)}$	$+ C_2F_5^+$	→	$CF_{2(s)}$	+ F	$+ C_2F_5^\#$	0.01	20	0.5	500	1
$CF_{3(s)}$	$+ C_2F_5^\#$	→	EP	$+ C_2F_5^\#$		0.9	20	0.5	500	1
$CF_{3(s)}$	$+ C_2F_5^\#$	→	$CF_{2(s)}$	+ F	$+ C_2F_5^\#$	0.01	20	0.5	500	1
$CF_{3(s)}$	$+ C_2F_4^+$	→	EP	$+ C_2F_4^\#$		0.9	20	0.5	500	1
$CF_{3(s)}$	$+ C_2F_4^+$	→	$CF_{2(s)}$	+ F	$+ C_2F_4^\#$	0.01	20	0.5	500	1
$CF_{3(s)}$	$+ C_2F_4^\#$	→	EP	$+ C_2F_4^\#$		0.9	20	0.5	500	1
$CF_{3(s)}$	$+ C_2F_4^\#$	→	$CF_{2(s)}$	+ F	$+ C_2F_4^\#$	0.01	20	0.5	500	1
$CF_{3(s)}$	$+ C_2F_3^+$	→	EP	$+ C_2F_3^\#$		0.9	20	0.5	500	1
$CF_{3(s)}$	$+ C_2F_3^+$	→	$CF_{2(s)}$	+ F	$+ C_2F_3^\#$	0.01	20	0.5	500	1
$CF_{3(s)}$	$+ C_2F_3^\#$	→	EP	$+ C_2F_3^\#$		0.9	20	0.5	500	1
$CF_{3(s)}$	$+ C_2F_3^\#$	→	$CF_{2(s)}$	+ F	$+ C_2F_3^\#$	0.01	20	0.5	500	1
$CF_{3(s)}$	$+ C_3F_5^+$	→	EP	$+ C_3F_5^\#$		0.9	20	0.5	500	1
$CF_{3(s)}$	$+ C_3F_5^+$	→	$CF_{2(s)}$	+ F	$+ C_3F_5^\#$	0.01	20	0.5	500	1
$CF_{3(s)}$	$+ C_3F_5^\#$	→	EP	$+ C_3F_5^\#$		0.9	20	0.5	500	1
$CF_{3(s)}$	$+ C_3F_5^\#$	→	$CF_{2(s)}$	+ F	$+ C_3F_5^\#$	0.01	20	0.5	500	1
$CF_{3(s)}$	$+ C_3F_6^+$	→	EP	$+ C_3F_6^\#$		0.9	20	0.5	500	1
$CF_{3(s)}$	$+ C_3F_5^\#$	→	$CF_{2(s)}$	+ F	$+ C_3F_5^\#$	0.01	20	0.5	500	1
$CF_{3(s)}$	$+ C_3F_6^\#$	→	EP	$+ C_3F_6^\#$		0.9	20	0.5	500	1
$CF_{3(s)}$	$+ C_3F_6^\#$	→	$CF_{2(s)}$	+ F	$+ C_3F_6^\#$	0.01	20	0.5	500	1
$CF_{3(s)}$	$+ C_3F_7^+$	→	EP	$+ C_3F_7^\#$		0.9	20	0.5	500	1
$CF_{3(s)}$	$+ C_3F_7^+$	→	$CF_{2(s)}$	+ F	$+ C_3F_7^\#$	0.01	20	0.5	500	1
$CF_{3(s)}$	$+ C_3F_7^\#$	→	EP	$+ C_3F_7^\#$		0.9	20	0.5	500	1
$CF_{3(s)}$	$+ C_3F_7^\#$	→	$CF_{2(s)}$	+ F	$+ C_3F_7^\#$	0.01	20	0.5	500	1
$CF_{3(s)}$	$+ C_4F_7^+$	→	EP	$+ C_4F_7^\#$		0.9	20	0.5	500	1
$CF_{3(s)}$	$+ C_4F_7^+$	→	$CF_{2(s)}$	+ F	$+ C_4F_7^\#$	0.01	20	0.5	500	1
$CF_{3(s)}$	$+ C_4F_7^\#$	→	EP	$+ C_4F_7^\#$		0.9	20	0.5	500	1
$CF_{3(s)}$	$+ C_4F_7^\#$	→	$CF_{2(s)}$	+ F	$+ C_4F_7^\#$	0.01	20	0.5	500	1
$CF_{3(s)}$	$+ C_4F_8^+$	→	EP	$+ C_4F_8^\#$		0.9	20	0.5	500	1
$CF_{3(s)}$	$+ C_4F_8^+$	→	$CF_{2(s)}$	+ F	$+ C_4F_8^\#$	0.01	20	0.5	500	1
$CF_{3(s)}$	$+ C_4F_8^\#$	→	EP	$+ C_4F_8^\#$		0.9	20	0.5	500	1
$CF_{3(s)}$	$+ C_4F_8^\#$	→	$CF_{2(s)}$	+ F	$+ C_4F_8^\#$	0.01	20	0.5	500	1
$CF_{3(s)}$	$+ O^+$	→	EP	$+ O^\#$		0.9	20	0.5	500	1

$CF_{3(s)}$ + O^+ → $CF_{2(s)}$ + F + $O^\#$	0.01	20	0.5	500	1
$CF_{3(s)}$ + O_2^+ → EP + $O_2^\#$	0.9	20	0.5	500	1
$CF_{3(s)}$ + O_2^+ → $CF_{2(s)}$ + F + $O_2^\#$	0.01	20	0.5	500	1
$CF_{3(s)}$ + $O^\#$ → EP + $O^\#$	0.9	20	0.5	500	1
$CF_{3(s)}$ + $O^\#$ → $CF_{2(s)}$ + F + $O^\#$	0.01	20	0.5	500	1
$CF_{3(s)}$ + $O^\#$ → CF + $O^\#$	0.1				
$CF_{3(s)}$ + $O_2^\#$ → EP + $O_2^\#$	0.9	20	0.5	500	1
$CF_{3(s)}$ + $O_2^\#$ → $CF_{2(s)}$ + F + $O_2^\#$	0.01	20	0.5	500	1
$C_2F_{3(s)}$ + Ar^+ → EP + $Ar^\#$	0.8	50	0.5	500	1
$C_2F_{3(s)}$ + $Ar^\#$ → EP + $Ar^\#$	0.8	50	0.5	500	1
$C_2F_{3(s)}$ + CF_3^+ → EP + $CF_3^\#$	0.8	50	0.5	500	1
$C_2F_{3(s)}$ + $CF_3^\#$ → EP + $CF_3^\#$	0.8	50	0.5	500	1
$C_2F_{3(s)}$ + CF_2^+ → EP + $CF_2^\#$	0.8	50	0.5	500	1
$C_2F_{3(s)}$ + $CF_2^\#$ → EP + $CF_2^\#$	0.8	50	0.5	500	1
$C_2F_{3(s)}$ + CF^+ → EP + $CF^\#$	0.8	50	0.5	500	1
$C_2F_{3(s)}$ + $CF^\#$ → EP + $CF^\#$	0.8	50	0.5	500	1
$C_2F_{3(s)}$ + F^+ → EP + $F^\#$	0.8	50	0.5	500	1
$C_2F_{3(s)}$ + $F^\#$ → EP + $F^\#$	0.8	50	0.5	500	1
$C_2F_{3(s)}$ + F_2^+ → EP + $F_2^\#$	0.8	50	0.5	500	1
$C_2F_{3(s)}$ + $F_2^\#$ → EP + $F_2^\#$	0.8	50	0.5	500	1
$C_2F_{3(s)}$ + $C_2F_5^+$ → EP + $C_2F_5^\#$	0.8	50	0.5	500	1
$C_2F_{3(s)}$ + $C_2F_5^\#$ → EP + $C_2F_5^\#$	0.8	50	0.5	500	1
$C_2F_{3(s)}$ + $C_2F_4^+$ → EP + $C_2F_4^\#$	0.8	50	0.5	500	1
$C_2F_{3(s)}$ + $C_2F_4^\#$ → EP + $C_2F_4^\#$	0.8	50	0.5	500	1
$C_2F_{3(s)}$ + $C_2F_3^+$ → EP + $C_2F_3^\#$	0.8	50	0.5	500	1
$C_2F_{3(s)}$ + $C_2F_3^\#$ → EP + $C_2F_3^\#$	0.8	50	0.5	500	1
$C_2F_{3(s)}$ + $C_3F_5^+$ → EP + $C_3F_5^\#$	0.8	50	0.5	500	1
$C_2F_{3(s)}$ + $C_3F_5^\#$ → EP + $C_3F_5^\#$	0.8	50	0.5	500	1
$C_2F_{3(s)}$ + $C_3F_6^+$ → EP + $C_3F_6^\#$	0.8	50	0.5	500	1
$C_2F_{3(s)}$ + $C_3F_6^\#$ → EP + $C_3F_6^\#$	0.8	50	0.5	500	1
$C_2F_{3(s)}$ + $C_3F_7^+$ → EP + $C_3F_7^\#$	0.8	50	0.5	500	1
$C_2F_{3(s)}$ + $C_3F_7^\#$ → EP + $C_3F_7^\#$	0.8	50	0.5	500	1
$C_2F_{3(s)}$ + $C_4F_7^+$ → EP + $C_4F_7^\#$	0.8	50	0.5	500	1
$C_2F_{3(s)}$ + $C_4F_7^\#$ → EP + $C_4F_7^\#$	0.8	50	0.5	500	1
$C_2F_{3(s)}$ + $C_4F_8^+$ → EP + $C_4F_8^\#$	0.8	50	0.5	500	1
$C_2F_{3(s)}$ + $C_4F_8^\#$ → EP + $C_4F_8^\#$	0.8	50	0.5	500	1
$C_2F_{3(s)}$ + O^+ → EP + $O^\#$	0.8	50	0.5	500	1
$C_2F_{3(s)}$ + O_2^+ → EP + $O_2^\#$	0.8	50	0.5	500	1
$C_2F_{3(s)}$ + $O^\#$ → EP + $O^\#$	0.8	50	0.5	500	1
$C_2F_{3(s)}$ + $O_2^\#$ → EP + $O_2^\#$	0.8	50	0.5	500	1
$CF_{(xs)}$ + Ar^+ → EP + $Ar^\#$	0.6	50	0.5	500	1

$CF_{(xs)} + Ar^{+} \rightarrow CF_{(s)} + Ar^{\#}$	0.3	8	0.5	500	1
$CF_{(xs)} + Ar^{\#} \rightarrow EP + Ar^{\#}$	0.6	50	0.5	500	1
$CF_{(xs)} + Ar^{\#} \rightarrow CF_{(s)} + Ar^{\#}$	0.3	8	0.5	500	1
$CF_{(xs)} + CF_3^{+} \rightarrow EP + CF_3^{\#}$	0.6	50	0.5	500	1
$CF_{(xs)} + CF_3^{+} \rightarrow CF_{(s)} + CF_3^{\#}$	0.3	8	0.5	500	1
$CF_{(xs)} + CF_3^{\#} \rightarrow EP + CF_3^{\#}$	0.6	50	0.5	500	1
$CF_{(xs)} + CF_3^{\#} \rightarrow CF_{(s)} + CF_3^{\#}$	0.3	8	0.5	500	1
$CF_{(xs)} + CF_2^{+} \rightarrow EP + CF_2^{\#}$	0.6	50	0.5	500	1
$CF_{(xs)} + CF_2^{+} \rightarrow CF_{(s)} + CF_2^{\#}$	0.3	8	0.5	500	1
$CF_{(xs)} + CF_2^{\#} \rightarrow EP + CF_2^{\#}$	0.6	50	0.5	500	1
$CF_{(xs)} + CF_2^{\#} \rightarrow CF_{(s)} + CF_2^{\#}$	0.3	8	0.5	500	1
$CF_{(xs)} + CF^{+} \rightarrow EP + CF^{\#}$	0.6	50	0.5	500	1
$CF_{(xs)} + CF^{+} \rightarrow CF_{(s)} + CF^{\#}$	0.3	8	0.5	500	1
$CF_{(xs)} + CF^{\#} \rightarrow EP + CF^{\#}$	0.6	50	0.5	500	1
$CF_{(xs)} + CF^{\#} \rightarrow CF_{(s)} + CF^{\#}$	0.3	8	0.5	500	1
$CF_{(xs)} + F^{+} \rightarrow EP + F^{\#}$	0.6	50	0.5	500	1
$CF_{(xs)} + F^{+} \rightarrow CF_{(s)} + F^{\#}$	0.3	8	0.5	500	1
$CF_{(xs)} + F^{\#} \rightarrow EP + F^{\#}$	0.6	50	0.5	500	1
$CF_{(xs)} + F^{\#} \rightarrow CF_{(s)} + F^{\#}$	0.3	8	0.5	500	1
$CF_{(xs)} + F_2^{+} \rightarrow EP + F_2^{\#}$	0.6	50	0.5	500	1
$CF_{(xs)} + F_2^{+} \rightarrow CF_{(s)} + F_2^{\#}$	0.3	8	0.5	500	1
$CF_{(xs)} + F_2^{\#} \rightarrow EP + F_2^{\#}$	0.6	50	0.5	500	1
$CF_{(xs)} + F_2^{\#} \rightarrow CF_{(s)} + F_2^{\#}$	0.3	8	0.5	500	1
$CF_{(xs)} + C_2F_5^{+} \rightarrow EP + C_2F_5^{\#}$	0.6	50	0.5	500	1
$CF_{(xs)} + C_2F_5^{+} \rightarrow CF_{(s)} + C_2F_5^{\#}$	0.3	8	0.5	500	1
$CF_{(xs)} + C_2F_5^{\#} \rightarrow EP + C_2F_5^{\#}$	0.6	50	0.5	500	1
$CF_{(xs)} + C_2F_5^{\#} \rightarrow CF_{(s)} + C_2F_5^{\#}$	0.3	8	0.5	500	1
$CF_{(xs)} + C_2F_4^{+} \rightarrow EP + C_2F_4^{\#}$	0.6	50	0.5	500	1
$CF_{(xs)} + C_2F_4^{+} \rightarrow CF_{(s)} + C_2F_4^{\#}$	0.3	8	0.5	500	1
$CF_{(xs)} + C_2F_4^{\#} \rightarrow EP + C_2F_4^{\#}$	0.6	50	0.5	500	1
$CF_{(xs)} + C_2F_4^{\#} \rightarrow CF_{(s)} + C_2F_4^{\#}$	0.3	8	0.5	500	1
$CF_{(xs)} + C_2F_3^{+} \rightarrow EP + C_2F_3^{\#}$	0.6	50	0.5	500	1
$CF_{(xs)} + C_2F_3^{+} \rightarrow CF_{(s)} + C_2F_3^{\#}$	0.3	8	0.5	500	1
$CF_{(xs)} + C_2F_3^{\#} \rightarrow EP + C_2F_3^{\#}$	0.6	50	0.5	500	1
$CF_{(xs)} + C_2F_3^{\#} \rightarrow CF_{(s)} + C_2F_3^{\#}$	0.3	8	0.5	500	1
$CF_{(xs)} + C_3F_5^{+} \rightarrow EP + C_3F_5^{\#}$	0.6	50	0.5	500	1
$CF_{(xs)} + C_3F_5^{+} \rightarrow CF_{(s)} + C_3F_5^{\#}$	0.3	8	0.5	500	1
$CF_{(xs)} + C_3F_5^{\#} \rightarrow EP + C_3F_5^{\#}$	0.6	50	0.5	500	1
$CF_{(xs)} + C_3F_5^{\#} \rightarrow CF_{(s)} + C_3F_5^{\#}$	0.3	8	0.5	500	1
$CF_{(xs)} + C_3F_6^{+} \rightarrow EP + C_3F_6^{\#}$	0.6	50	0.5	500	1
$CF_{(xs)} + C_3F_6^{+} \rightarrow CF_{(s)} + C_3F_6^{\#}$	0.3	8	0.5	500	1

$CF_{(xs)} + C_3F_6^{\#} \rightarrow EP + C_3F_6^{\#}$	0.6	50	0.5	500	1
$CF_{(xs)} + C_3F_6^{\#} \rightarrow CF_{(s)} + C_3F_6^{\#}$	0.3	8	0.5	500	1
$CF_{(xs)} + C_3F_7^{+} \rightarrow EP + C_3F_7^{\#}$	0.6	50	0.5	500	1
$CF_{(xs)} + C_3F_7^{+} \rightarrow CF_{(s)} + C_3F_7^{\#}$	0.3	8	0.5	500	1
$CF_{(xs)} + C_3F_7^{\#} \rightarrow EP + C_3F_7^{\#}$	0.6	50	0.5	500	1
$CF_{(xs)} + C_3F_7^{\#} \rightarrow CF_{(s)} + C_3F_7^{\#}$	0.3	8	0.5	500	1
$CF_{(xs)} + C_4F_7^{+} \rightarrow EP + C_4F_7^{\#}$	0.6	50	0.5	500	1
$CF_{(xs)} + C_4F_7^{+} \rightarrow CF_{(s)} + C_4F_7^{\#}$	0.3	8	0.5	500	1
$CF_{(xs)} + C_4F_7^{\#} \rightarrow EP + C_4F_7^{\#}$	0.6	50	0.5	500	1
$CF_{(xs)} + C_4F_7^{\#} \rightarrow CF_{(s)} + C_4F_7^{\#}$	0.3	8	0.5	500	1
$CF_{(xs)} + C_4F_8^{+} \rightarrow EP + C_4F_8^{\#}$	0.6	50	0.5	500	1
$CF_{(xs)} + C_4F_8^{+} \rightarrow CF_{(s)} + C_4F_8^{\#}$	0.3	8	0.5	500	1
$CF_{(xs)} + C_4F_8^{\#} \rightarrow EP + C_4F_8^{\#}$	0.6	50	0.5	500	1
$CF_{(xs)} + C_4F_8^{\#} \rightarrow CF_{(s)} + C_4F_8^{\#}$	0.3	8	0.5	500	1
$CF_{(xs)} + O^{+} \rightarrow EP + O^{\#}$	0.6	50	0.5	500	1
$CF_{(xs)} + O^{+} \rightarrow CF_{(s)} + O^{\#}$	0.3	8	0.5	500	1
$CF_{(xs)} + O_2^{+} \rightarrow EP + O_2^{\#}$	0.6	50	0.5	500	1
$CF_{(xs)} + O_2^{+} \rightarrow CF_{(s)} + O_2^{\#}$	0.3	8	0.5	500	1
$CF_{(xs)} + O^{\#} \rightarrow EP + O^{\#}$	0.6	50	0.5	500	1
$CF_{(xs)} + O^{\#} \rightarrow CF_{(s)} + O^{\#}$	0.3	8	0.5	500	1
$CF_{(xs)} + O^{\#} \rightarrow CF + O^{\#}$	0.1				
$CF_{(xs)} + O_2^{\#} \rightarrow EP + O_2^{\#}$	0.6	50	0.5	500	1
$CF_{(xs)} + O_2^{\#} \rightarrow CF_{(s)} + O_2^{\#}$	0.3	8	0.5	500	1
$CF_{2(xs)} + Ar^{+} \rightarrow EP + Ar^{\#}$	0.6	50	0.5	500	1
$CF_{2(xs)} + Ar^{+} \rightarrow CF_{2(s)} + Ar^{\#}$	0.3	8	0.5	500	1
$CF_{2(xs)} + Ar^{\#} \rightarrow EP + Ar^{\#}$	0.6	50	0.5	500	1
$CF_{2(xs)} + Ar^{\#} \rightarrow CF_{2(s)} + Ar^{\#}$	0.3	8	0.5	500	1
$CF_{2(xs)} + CF_3^{+} \rightarrow EP + CF_3^{\#}$	0.6	50	0.5	500	1
$CF_{2(xs)} + CF_3^{+} \rightarrow CF_{2(s)} + CF_3^{\#}$	0.3	8	0.5	500	1
$CF_{2(xs)} + CF_3^{\#} \rightarrow EP + CF_3^{\#}$	0.6	50	0.5	500	1
$CF_{2(xs)} + CF_3^{\#} \rightarrow CF_{2(s)} + CF_3^{\#}$	0.3	8	0.5	500	1
$CF_{2(xs)} + CF_2^{+} \rightarrow EP + CF_2^{\#}$	0.6	50	0.5	500	1
$CF_{2(xs)} + CF_2^{+} \rightarrow CF_{2(s)} + CF_3^{\#}$	0.3	8	0.5	500	1
$CF_{2(xs)} + CF_2^{\#} \rightarrow EP + CF_2^{\#}$	0.6	50	0.5	500	1
$CF_{2(xs)} + CF_2^{\#} \rightarrow CF_{2(s)} + CF_2^{\#}$	0.3	8	0.5	500	1
$CF_{2(xs)} + CF^{+} \rightarrow EP + CF^{\#}$	0.6	50	0.5	500	1
$CF_{2(xs)} + CF^{+} \rightarrow CF_{2(s)} + CF^{\#}$	0.3	8	0.5	500	1
$CF_{2(xs)} + CF^{\#} \rightarrow EP + CF^{\#}$	0.6	50	0.5	500	1
$CF_{2(xs)} + CF^{\#} \rightarrow CF_{2(s)} + CF^{\#}$	0.3	8	0.5	500	1
$CF_{2(xs)} + F^{+} \rightarrow EP + F^{\#}$	0.6	50	0.5	500	1
$CF_{2(xs)} + F^{+} \rightarrow CF_{2(s)} + F^{\#}$	0.3	8	0.5	500	1

$CF_{2(xs)} + F^{\#} \rightarrow EP + F^{\#}$	0.6	50	0.5	500	1
$CF_{2(xs)} + F^{\#} \rightarrow CF_{2(s)} + F^{\#}$	0.3	8	0.5	500	1
$CF_{2(xs)} + F_2^{+} \rightarrow EP + F_2^{\#}$	0.6	50	0.5	500	1
$CF_{2(xs)} + F_2^{+} \rightarrow CF_{2(s)} + F_2^{\#}$	0.3	8	0.5	500	1
$CF_{2(xs)} + F_2^{\#} \rightarrow EP + F_2^{\#}$	0.6	50	0.5	500	1
$CF_{2(xs)} + F_2^{\#} \rightarrow CF_{2(s)} + F_2^{\#}$	0.3	8	0.5	500	1
$CF_{2(xs)} + C_2F_5^{+} \rightarrow EP + C_2F_5^{\#}$	0.6	50	0.5	500	1
$CF_{2(xs)} + C_2F_5^{+} \rightarrow CF_{2(s)} + C_2F_5^{\#}$	0.3	8	0.5	500	1
$CF_{2(xs)} + C_2F_5^{\#} \rightarrow EP + C_2F_5^{\#}$	0.6	50	0.5	500	1
$CF_{2(xs)} + C_2F_5^{\#} \rightarrow CF_{2(s)} + C_2F_5^{\#}$	0.3	8	0.5	500	1
$CF_{2(xs)} + C_2F_4^{+} \rightarrow EP + C_2F_4^{\#}$	0.6	50	0.5	500	1
$CF_{2(xs)} + C_2F_4^{+} \rightarrow CF_{2(s)} + C_2F_4^{\#}$	0.3	8	0.5	500	1
$CF_{2(xs)} + C_2F_4^{\#} \rightarrow EP + C_2F_4^{\#}$	0.6	50	0.5	500	1
$CF_{2(xs)} + C_2F_4^{\#} \rightarrow CF_{2(s)} + C_2F_4^{\#}$	0.3	8	0.5	500	1
$CF_{2(xs)} + C_2F_3^{+} \rightarrow EP + C_2F_3^{\#}$	0.6	50	0.5	500	1
$CF_{2(xs)} + C_2F_3^{+} \rightarrow CF_{2(s)} + C_2F_3^{\#}$	0.3	8	0.5	500	1
$CF_{2(xs)} + C_2F_3^{\#} \rightarrow EP + C_2F_3^{\#}$	0.6	50	0.5	500	1
$CF_{2(xs)} + C_2F_3^{\#} \rightarrow CF_{2(s)} + C_2F_3^{\#}$	0.3	8	0.5	500	1
$CF_{2(xs)} + C_3F_5^{+} \rightarrow EP + C_3F_5^{\#}$	0.6	50	0.5	500	1
$CF_{2(xs)} + C_3F_5^{+} \rightarrow CF_{2(s)} + C_3F_5^{\#}$	0.3	8	0.5	500	1
$CF_{2(xs)} + C_3F_5^{\#} \rightarrow EP + C_3F_5^{\#}$	0.6	50	0.5	500	1
$CF_{2(xs)} + C_3F_5^{\#} \rightarrow CF_{2(s)} + C_3F_5^{\#}$	0.3	8	0.5	500	1
$CF_{2(xs)} + C_3F_6^{+} \rightarrow EP + C_3F_6^{\#}$	0.6	50	0.5	500	1
$CF_{2(xs)} + C_3F_6^{+} \rightarrow CF_{2(s)} + C_3F_6^{\#}$	0.3	8	0.5	500	1
$CF_{2(xs)} + C_3F_6^{\#} \rightarrow EP + C_3F_6^{\#}$	0.6	50	0.5	500	1
$CF_{2(xs)} + C_3F_6^{+} \rightarrow CF_{2(s)} + C_3F_6^{\#}$	0.3	8	0.5	500	1
$CF_{2(xs)} + C_3F_7^{+} \rightarrow EP + C_3F_7^{\#}$	0.6	50	0.5	500	1
$CF_{2(xs)} + C_3F_7^{+} \rightarrow CF_{2(s)} + C_3F_7^{\#}$	0.3	8	0.5	500	1
$CF_{2(xs)} + C_3F_7^{\#} \rightarrow EP + C_3F_7^{\#}$	0.6	50	0.5	500	1
$CF_{2(xs)} + C_3F_7^{\#} \rightarrow CF_{2(s)} + C_3F_7^{\#}$	0.3	8	0.5	500	1
$CF_{2(xs)} + C_4F_7^{+} \rightarrow EP + C_4F_7^{\#}$	0.6	50	0.5	500	1
$CF_{2(xs)} + C_4F_7^{+} \rightarrow CF_{2(s)} + C_4F_7^{\#}$	0.3	8	0.5	500	1
$CF_{2(xs)} + C_4F_7^{\#} \rightarrow EP + C_4F_7^{\#}$	0.6	50	0.5	500	1
$CF_{2(xs)} + C_4F_7^{\#} \rightarrow CF_{2(s)} + C_4F_7^{\#}$	0.3	8	0.5	500	1
$CF_{2(xs)} + C_4F_8^{+} \rightarrow EP + C_4F_8^{\#}$	0.6	50	0.5	500	1
$CF_{2(xs)} + C_4F_8^{+} \rightarrow CF_{2(s)} + C_4F_8^{\#}$	0.3	8	0.5	500	1
$CF_{2(xs)} + C_4F_8^{\#} \rightarrow EP + C_4F_8^{\#}$	0.6	50	0.5	500	1
$CF_{2(xs)} + C_4F_8^{\#} \rightarrow CF_{2(s)} + C_4F_8^{\#}$	0.3	8	0.5	500	1
$CF_{2(xs)} + O^{+} \rightarrow EP + O^{\#}$	0.6	50	0.5	500	1
$CF_{2(xs)} + O^{+} \rightarrow CF_{2(s)} + O^{\#}$	0.3	8	0.5	500	1
$CF_{2(xs)} + O_2^{+} \rightarrow EP + O_2^{\#}$	0.6	50	0.5	500	1

$CF_{2(xs)} + O_2^{+} \rightarrow CF_{2(s)} + O_2^{\#}$	0.3	8	0.5	500	1
$CF_{2(xs)} + O^{\#} \rightarrow EP + O^{\#}$	0.6	50	0.5	500	1
$CF_{2(xs)} + O_2^{+} \rightarrow CF_{2(s)} + O_2^{\#}$	0.3	8	0.5	500	1
$CF_{2(xs)} + O^{\#} \rightarrow CF + O^{\#}$	0.1				
$CF_{2(xs)} + O_2^{\#} \rightarrow EP + O_2^{\#}$	0.6	50	0.5	500	1
$CF_{2(xs)} + O_2^{+} \rightarrow CF_{2(s)} + O_2^{\#}$	0.3	8	0.5	500	1
$CF_{3(xs)} + Ar^{+} \rightarrow EP + Ar^{\#}$	0.6	50	0.5	500	1
$CF_{3(xs)} + Ar^{+} \rightarrow CF_{3(s)} + Ar^{\#}$	0.3	8	0.5	500	1
$CF_{3(xs)} + Ar^{\#} \rightarrow EP + Ar^{\#}$	0.6	50	0.5	500	1
$CF_{3(xs)} + Ar^{\#} \rightarrow CF_{3(s)} + Ar^{\#}$	0.3	8	0.5	500	1
$CF_{3(xs)} + CF_3^{+} \rightarrow EP + CF_3^{\#}$	0.6	50	0.5	500	1
$CF_{3(xs)} + CF_3^{+} \rightarrow CF_{3(s)} + CF_3^{\#}$	0.3	8	0.5	500	1
$CF_{3(xs)} + CF_3^{\#} \rightarrow EP + CF_3^{\#}$	0.6	50	0.5	500	1
$CF_{3(xs)} + CF_3^{\#} \rightarrow CF_{3(s)} + CF_3^{\#}$	0.3	8	0.5	500	1
$CF_{3(xs)} + CF_2^{+} \rightarrow EP + CF_2^{\#}$	0.6	50	0.5	500	1
$CF_{3(xs)} + CF_2^{+} \rightarrow CF_{3(s)} + CF_3^{\#}$	0.3	8	0.5	500	1
$CF_{3(xs)} + CF_2^{\#} \rightarrow EP + CF_2^{\#}$	0.6	50	0.5	500	1
$CF_{3(xs)} + CF_2^{\#} \rightarrow CF_{3(s)} + CF_2^{\#}$	0.3	8	0.5	500	1
$CF_{3(xs)} + CF^{+} \rightarrow EP + CF^{\#}$	0.6	50	0.5	500	1
$CF_{3(xs)} + CF^{+} \rightarrow CF_{3(s)} + CF^{\#}$	0.3	8	0.5	500	1
$CF_{3(xs)} + CF^{\#} \rightarrow EP + CF^{\#}$	0.6	50	0.5	500	1
$CF_{3(xs)} + CF^{\#} \rightarrow CF_{3(s)} + CF^{\#}$	0.3	8	0.5	500	1
$CF_{3(xs)} + F^{+} \rightarrow EP + F^{\#}$	0.6	50	0.5	500	1
$CF_{3(xs)} + F^{+} \rightarrow CF_{3(s)} + F^{\#}$	0.3	8	0.5	500	1
$CF_{3(xs)} + F^{\#} \rightarrow EP + F^{\#}$	0.6	50	0.5	500	1
$CF_{3(xs)} + F^{\#} \rightarrow CF_{3(s)} + F^{\#}$	0.3	8	0.5	500	1
$CF_{3(xs)} + F_2^{+} \rightarrow EP + F_2^{\#}$	0.6	50	0.5	500	1
$CF_{3(xs)} + F_2^{+} \rightarrow CF_{3(s)} + F_2^{\#}$	0.3	8	0.5	500	1
$CF_{3(xs)} + F_2^{\#} \rightarrow EP + F_2^{\#}$	0.6	50	0.5	500	1
$CF_{3(xs)} + F_2^{\#} \rightarrow CF_{3(s)} + F_2^{\#}$	0.3	8	0.5	500	1
$CF_{3(xs)} + C_2F_5^{+} \rightarrow EP + C_2F_5^{\#}$	0.6	50	0.5	500	1
$CF_{3(xs)} + C_2F_5^{+} \rightarrow CF_{3(s)} + C_2F_5^{\#}$	0.3	8	0.5	500	1
$CF_{3(xs)} + C_2F_5^{\#} \rightarrow EP + C_2F_5^{\#}$	0.6	50	0.5	500	1
$CF_{3(xs)} + C_2F_5^{\#} \rightarrow CF_{3(s)} + C_2F_5^{\#}$	0.3	8	0.5	500	1
$CF_{3(xs)} + C_2F_4^{+} \rightarrow EP + C_2F_4^{\#}$	0.6	50	0.5	500	1
$CF_{3(xs)} + C_2F_4^{+} \rightarrow CF_{3(s)} + C_2F_4^{\#}$	0.3	8	0.5	500	1
$CF_{3(xs)} + C_2F_4^{\#} \rightarrow EP + C_2F_4^{\#}$	0.6	50	0.5	500	1
$CF_{3(xs)} + C_2F_4^{\#} \rightarrow CF_{3(s)} + C_2F_4^{\#}$	0.3	8	0.5	500	1
$CF_{3(xs)} + C_2F_3^{+} \rightarrow EP + C_2F_3^{\#}$	0.6	50	0.5	500	1
$CF_{3(xs)} + C_2F_3^{+} \rightarrow CF_{3(s)} + C_2F_3^{\#}$	0.3	8	0.5	500	1
$CF_{3(xs)} + C_2F_3^{\#} \rightarrow EP + C_2F_3^{\#}$	0.6	50	0.5	500	1

$CF_{3(xs)}$	$+ C_2F_3^{\#}$	$\rightarrow$	$CF_{3(s)}$	$+ C_2F_3^{\#}$	0.3	8	0.5	500	1
$CF_{3(xs)}$	$+ C_3F_5^{+}$	$\rightarrow$	EP	$+ C_3F_5^{\#}$	0.6	50	0.5	500	1
$CF_{3(xs)}$	$+ C_3F_5^{+}$	$\rightarrow$	$CF_{3(s)}$	$+ C_3F_5^{\#}$	0.3	8	0.5	500	1
$CF_{3(xs)}$	$+ C_3F_5^{\#}$	$\rightarrow$	EP	$+ C_3F_5^{\#}$	0.6	50	0.5	500	1
$CF_{3(xs)}$	$+ C_3F_5^{\#}$	$\rightarrow$	$CF_{3(s)}$	$+ C_3F_5^{\#}$	0.3	8	0.5	500	1
$CF_{3(xs)}$	$+ C_3F_6^{+}$	$\rightarrow$	EP	$+ C_3F_6^{\#}$	0.6	50	0.5	500	1
$CF_{3(xs)}$	$+ C_3F_6^{+}$	$\rightarrow$	$CF_{3(s)}$	$+ C_3F_6^{\#}$	0.3	8	0.5	500	1
$CF_{3(xs)}$	$+ C_3F_6^{\#}$	$\rightarrow$	EP	$+ C_3F_6^{\#}$	0.6	50	0.5	500	1
$CF_{3(xs)}$	$+ C_3F_6^{+}$	$\rightarrow$	$CF_{3(s)}$	$+ C_3F_6^{\#}$	0.3	8	0.5	500	1
$CF_{3(xs)}$	$+ C_3F_7^{+}$	$\rightarrow$	EP	$+ C_3F_7^{\#}$	0.6	50	0.5	500	1
$CF_{3(xs)}$	$+ C_3F_7^{+}$	$\rightarrow$	$CF_{3(s)}$	$+ C_3F_7^{\#}$	0.3	8	0.5	500	1
$CF_{3(xs)}$	$+ C_3F_7^{\#}$	$\rightarrow$	EP	$+ C_3F_7^{\#}$	0.6	50	0.5	500	1
$CF_{3(xs)}$	$+ C_3F_7^{\#}$	$\rightarrow$	$CF_{3(s)}$	$+ C_3F_7^{\#}$	0.3	8	0.5	500	1
$CF_{3(xs)}$	$+ C_4F_7^{+}$	$\rightarrow$	EP	$+ C_4F_7^{\#}$	0.6	50	0.5	500	1
$CF_{3(xs)}$	$+ C_4F_7^{+}$	$\rightarrow$	$CF_{3(s)}$	$+ C_4F_7^{\#}$	0.3	8	0.5	500	1
$CF_{3(xs)}$	$+ C_4F_7^{\#}$	$\rightarrow$	EP	$+ C_4F_7^{\#}$	0.6	50	0.5	500	1
$CF_{3(xs)}$	$+ C_4F_7^{\#}$	$\rightarrow$	$CF_{3(s)}$	$+ C_4F_7^{\#}$	0.3	8	0.5	500	1
$CF_{3(xs)}$	$+ C_4F_8^{+}$	$\rightarrow$	EP	$+ C_4F_8^{\#}$	0.6	50	0.5	500	1
$CF_{3(xs)}$	$+ C_4F_8^{+}$	$\rightarrow$	$CF_{3(s)}$	$+ C_4F_8^{\#}$	0.3	8	0.5	500	1
$CF_{3(xs)}$	$+ C_4F_8^{\#}$	$\rightarrow$	EP	$+ C_4F_8^{\#}$	0.6	50	0.5	500	1
$CF_{3(xs)}$	$+ C_4F_8^{\#}$	$\rightarrow$	$CF_{3(s)}$	$+ C_4F_8^{\#}$	0.3	8	0.5	500	1
$CF_{3(xs)}$	$+ O^{+}$	$\rightarrow$	EP	$+ O^{\#}$	0.6	50	0.5	500	1
$CF_{3(xs)}$	$+ O^{+}$	$\rightarrow$	$CF_{3(s)}$	$+ O^{\#}$	0.3	8	0.5	500	1
$CF_{3(xs)}$	$+ O_2^{+}$	$\rightarrow$	EP	$+ O_2^{\#}$	0.6	50	0.5	500	1
$CF_{3(xs)}$	$+ O_2^{+}$	$\rightarrow$	$CF_{3(s)}$	$+ O_2^{\#}$	0.3	8	0.5	500	1
$CF_{3(xs)}$	$+ O^{\#}$	$\rightarrow$	EP	$+ O^{\#}$	0.6	50	0.5	500	1
$CF_{3(xs)}$	$+ O_2^{+}$	$\rightarrow$	$CF_{3(s)}$	$+ O_2^{\#}$	0.3	8	0.5	500	1
$CF_{3(xs)}$	$+ O^{\#}$	$\rightarrow$	CF	$+ O^{\#}$	0.1				
$CF_{3(xs)}$	$+ O_2^{\#}$	$\rightarrow$	EP	$+ O_2^{\#}$	0.6	50	0.5	500	1
$CF_{3(xs)}$	$+ O_2^{+}$	$\rightarrow$	$CF_{3(s)}$	$+ O_2^{\#}$	0.3	8	0.5	500	1
$AC_{(s)}$	+ F	$\rightarrow$	$CF_{(s)}$		0.01				
$AC_{(xs)}$	+ F	$\rightarrow$	$CF_{(s)}$		0.001				
$CF_{(s)}$	+ F	$\rightarrow$	$CF_{2(s)}$		0.01				
$CF_{2(s)}$	+ F	$\rightarrow$	$CF_{3(s)}$		0.01				
$CF_{3(s)}$	+ F	$\rightarrow$	CF_4		0.01				
$AC_{(s)}$	+ C	$\rightarrow$	$AC_{(s)}$	$+ AC_{(s)}$	0.01				
$SiO_{2(s)}$	+ C	$\rightarrow$	$SiO_{2(s)}$	$+ AC_{(s)}$	0.01				
$CF_{2(s)}$	+ C	$\rightarrow$	$CF_{2(s)}$	$+ AC_{(s)}$	0.01				
$SiO_{2(s)}$	$+ Ar^{+}$	$\rightarrow$	$SiO_2*_{(s)}$	$+ Ar^{\#}$	0.9				
$SiO_{2(s)}$	$+ Ar^{+}$	$\rightarrow$	$Ar^{\#}$	$+ SiO_2$	0.0852	70	1	140	1
$SiO_{2(s)}$	$+ F^{+}$	$\rightarrow$	$SiO_2*_{(s)}$	$+ F^{\#}$	0.9				

$SiO_{2(s)} + F^{+} \rightarrow F^{\#} + SiO_2$	0.0852	70	1	140	1
$SiO_{2(s)} + F_2^{+} \rightarrow SiO_2*_{(s)} + F_2^{\#}$	0.9				
$SiO_{2(s)} + F_2^{+} \rightarrow F_2^{\#}\ SiO_2 + F_2^{\#}$	0.0852	70	1	140	1
$SiO_{2(s)} + O_2^{+} \rightarrow SiO_2*_{(s)} + O_2^{\#}$	0.9				
$SiO_{2(s)} + O_2^{+} \rightarrow O_2^{\#} + SiO_2$	0.0852	70	1	140	1
$SiO_{2(s)} + O^{+} \rightarrow SiO_2*_{(s)} + O^{\#}$	0.9				
$SiO_{2(s)} + O^{+} \rightarrow O^{\#} + SiO_2$	0.0852	70	1	140	1
$SiO_{2(s)} + CF_3^{+} \rightarrow SiO_2*_{(s)} + CF_3^{\#}$	0.9				
$SiO_{2(s)} + CF_3^{+} \rightarrow CF_3^{\#} + SiO_2$	0.0852	70	1	140	1
$SiO_{2(s)} + CF_2^{+} \rightarrow SiO_2*_{(s)} + CF_2^{\#}$	0.9				
$SiO_{2(s)} + CF_2^{+} \rightarrow CF_2^{\#} + SiO_2$	0.0852	70	1	140	1
$SiO_{2(s)} + CF^{+} \rightarrow SiO_2*_{(s)} + CF^{\#}$	0.9				
$SiO_{2(s)} + CF^{+} \rightarrow CF^{\#} + SiO_2$	0.0852	70	1	140	1
$SiO_{2(s)} + C_2F_5^{+} \rightarrow SiO_2*_{(s)} + C_2F_5^{\#}$	0.9				
$SiO_{2(s)} + C_2F_5^{+} \rightarrow C_2F_5^{\#} + SiO_2$	0.0852	70	1	140	1
$SiO_{2(s)} + C_2F_4^{+} \rightarrow SiO_2*_{(s)} + C_2F_4^{\#}$	0.9				
$SiO_{2(s)} + C_2F_4^{+} \rightarrow C_2F_4^{\#} + SiO_2$	0.0852	70	1	140	1
$SiO_{2(s)} + C_2F_3^{+} \rightarrow SiO_2*_{(s)} + C_2F_3^{\#}$	0.9				
$SiO_{2(s)} + C_2F_3^{+} \rightarrow C_2F_3^{\#} + SiO_2$	0.0852	70	1	140	1
$SiO_{2(s)} + C_3F_5^{+} \rightarrow SiO_2*_{(s)} + C_3F_5^{\#}$	0.9				
$SiO_{2(s)} + C_3F_5^{+} \rightarrow C_3F_5^{\#} + SiO_2$	0.0852	70	1	140	1
$SiO_{2(s)} + C_3F_6^{+} \rightarrow SiO_2*_{(s)} + C_3F_6^{\#}$	0.9				
$SiO_{2(s)} + C_3F_6^{+} \rightarrow C_3F_6^{\#} + SiO_2$	0.0852	70	1	140	1
$SiO_{2(s)} + C_3F_7^{+} \rightarrow SiO_2*_{(s)} + C_3F_7^{\#}$	0.9				
$SiO_{2(s)} + C_3F_7^{+} \rightarrow C_3F_7^{\#} + SiO_2$	0.0852	70	1	140	1
$SiO_{2(s)} + C_4F_7^{+} \rightarrow SiO_2*_{(s)} + C_4F_7^{\#}$	0.9				
$SiO_{2(s)} + C_4F_7^{+} \rightarrow SiO_2 + C_4F_7^{\#}$	0.0852	70	1	140	1
$SiO_{2(s)} + C_4F_8^{+} \rightarrow SiO_2*_{(s)} + C_4F_8^{\#}$	0.9				
$SiO_{2(s)} + C_4F_8^{+} \rightarrow C_4F_8^{\#} + SiO_2$	0.0852	70	1	140	1
$SiO_{2(s)} + Ar^{\#} \rightarrow SiO_2*_{(s)} + Ar^{\#}$	0.9				
$SiO_{2(s)} + Ar^{\#} \rightarrow Ar^{\#} + SiO_2$	0.0852	70	1	140	1
$SiO_{2(s)} + F^{\#} \rightarrow SiO_2*_{(s)} + F^{\#}$	0.9				
$SiO_{2(s)} + F^{\#} \rightarrow F^{\#} + SiO_2$	0.0852	70	1	140	1
$SiO_{2(s)} + F_2^{\#} \rightarrow SiO_2*_{(s)} + F_2^{\#}$	0.9				
$SiO_{2(s)} + F_2^{\#} \rightarrow F_2^{\#}\ SiO_2 + F_2^{\#}$	0.0852	70	1	140	1
$SiO_{2(s)} + O_2^{\#} \rightarrow SiO_2*_{(s)} + O_2^{\#}$	0.9				
$SiO_{2(s)} + O_2^{\#} \rightarrow O_2^{\#} + SiO_2$	0.0852	70	1	140	1
$SiO_{2(s)} + O^{\#} \rightarrow SiO_2*_{(s)} + O^{\#}$	0.9				
$SiO_{2(s)} + O^{\#} \rightarrow O^{\#} + SiO_2$	0.0852	70	1	140	1
$SiO_{2(s)} + CF_3^{\#} \rightarrow SiO_2*_{(s)} + CF_3^{\#}$	0.9				
$SiO_{2(s)} + CF_3^{\#} \rightarrow CF_3^{\#} + SiO_2$	0.0852	70	1	140	1

$SiO_{2(s)} + CF_2^{\#} \rightarrow SiO_2^{*}{}_{(s)} + CF_2^{\#}$	0.9				
$SiO_{2(s)} + CF_2^{\#} \rightarrow CF_2^{\#} + SiO_2$	0.0852	70	1	140	1
$SiO_{2(s)} + CF^{\#} \rightarrow SiO_2^{*}{}_{(s)} + CF^{\#}$	0.9				
$SiO_{2(s)} + CF^{\#} \rightarrow CF^{\#} + SiO_2$	0.0852	70	1	140	1
$SiO_{2(s)} + C_2F_5^{\#} \rightarrow SiO_2^{*}{}_{(s)} + C_2F_5^{\#}$	0.9				
$SiO_{2(s)} + C_2F_5^{\#} \rightarrow C_2F_5^{\#} + SiO_2$	0.0852	70	1	140	1
$SiO_{2(s)} + C_2F_4^{\#} \rightarrow SiO_2^{*}{}_{(s)} + C_2F_4^{\#}$	0.9				
$SiO_{2(s)} + C_2F_4^{\#} \rightarrow C_2F_4^{\#} + SiO_2$	0.0852	70	1	140	1
$SiO_{2(s)} + C_2F_3^{\#} \rightarrow SiO_2^{*}{}_{(s)} + C_2F_3^{\#}$	0.9				
$SiO_{2(s)} + C_2F_3^{\#} \rightarrow C_2F_3^{\#} + SiO_2$	0.0852	70	1	140	1
$SiO_{2(s)} + C_3F_5^{\#} \rightarrow SiO_2^{*}{}_{(s)} + C_3F_5^{\#}$	0.9				
$SiO_{2(s)} + C_3F_5^{\#} \rightarrow C_3F_5^{\#} + SiO_2$	0.0852	70	1	140	1
$SiO_{2(s)} + C_3F_6^{\#} \rightarrow SiO_2^{*}{}_{(s)} + C_3F_6^{\#}$	0.9				
$SiO_{2(s)} + C_3F_6^{\#} \rightarrow C_3F_6^{\#} + SiO_2$	0.0852	70	1	140	1
$SiO_{2(s)} + C_3F_7^{\#} \rightarrow SiO_2^{*}{}_{(s)} + C_3F_7^{\#}$	0.9				
$SiO_{2(s)} + C_3F_7^{\#} \rightarrow C_3F_7^{\#} + SiO_2$	0.0852	70	1	140	1
$SiO_{2(s)} + C_4F_7^{\#} \rightarrow SiO_2^{*}{}_{(s)} + C_4F_7^{\#}$	0.9				
$SiO_{2(s)} + C_4F_7^{\#} \rightarrow SiO_2 + C_4F_7^{\#}$	0.0852	70	1	140	1
$SiO_{2(s)} + C_4F_8^{\#} \rightarrow SiO_2^{*}{}_{(s)} + C_4F_8^{\#}$	0.9				
$SiO_{2(s)} + C_4F_8^{\#} \rightarrow C_4F_8^{\#} + SiO_2$	0.0852	70	1	140	1
$SiO_2^{*}{}_{(s)} + Ar^{+} \rightarrow Ar^{\#} + SiO_2$	0.0852	70	1	140	1
$SiO_2^{*}{}_{(s)} + CF_3^{+} \rightarrow CF_3^{\#} + SiO_2$	0.0852	70	1	140	1
$SiO_2^{*}{}_{(s)} + CF_2^{+} \rightarrow CF_2^{\#} + SiO_2$	0.0852	70	1	140	1
$SiO_2^{*}{}_{(s)} + CF^{+} \rightarrow CF^{\#} + SiO_2$	0.0852	70	1	140	1
$SiO_2^{*}{}_{(s)} + F_2^{+} \rightarrow F_2^{\#} + SiO_2$	0.0852	70	1	140	1
$SiO_2^{*}{}_{(s)} + F^{+} \rightarrow F^{\#} + SiO_2$	0.0852	70	1	140	1
$SiO_2^{*}{}_{(s)} + O_2^{+} \rightarrow O_2^{\#} + SiO_2$	0.0852	70	1	140	1
$SiO_2^{*}{}_{(s)} + O^{+} \rightarrow SiO_2 + O^{\#}$	0.0852	70	1	140	1
$SiO_2^{*}{}_{(s)} + O^{+} \rightarrow O^{\#} + SiO_2$	0.0852	70	1	140	1
$SiO_2^{*}{}_{(s)} + C_2F_4^{+} \rightarrow C_2F_4^{\#} + SiO_2$	0.0852	70	1	140	1
$SiO_2^{*}{}_{(s)} + C_2F_3^{+} \rightarrow C_2F_3^{\#} + SiO_2$	0.0852	70	1	140	1
$SiO_2^{*}{}_{(s)} + C_2F_3^{+} \rightarrow SiO_2 + C_2F_3^{\#}$	0.0852	70	1	140	1
$SiO_2^{*}{}_{(s)} + C_2F_5^{+} \rightarrow C_2F_5^{\#} + SiO_2$	0.0852	70	1	140	1
$SiO_2^{*}{}_{(s)} + C_3F_5^{+} \rightarrow C_3F_5^{\#} + SiO_2$	0.0852	70	1	140	1
$SiO_2^{*}{}_{(s)} + C_3F_6^{+} \rightarrow C_3F_6^{\#} + SiO_2$	0.0852	70	1	140	1
$SiO_2^{*}{}_{(s)} + C_3F_7^{+} \rightarrow C_3F_7^{\#} + SiO_2$	0.0852	70	1	140	1
$SiO_2^{*}{}_{(s)} + C_4F_7^{+} \rightarrow C_4F_7^{\#} + SiO_2$	0.0852	70	1	140	1
$SiO_2^{*}{}_{(s)} + C_4F_8^{+} \rightarrow C_4F_8^{\#} + SiO_2$	0.0852	70	1	140	1
$SiO_2^{*}{}_{(s)} + Ar^{\#} \rightarrow Ar^{\#} + SiO_2$	0.0852	70	1	140	1
$SiO_2^{*}{}_{(s)} + CF_3^{\#} \rightarrow CF_3^{\#} + SiO_2$	0.0852	70	1	140	1
$SiO_2^{*}{}_{(s)} + CF_2^{\#} \rightarrow CF_2^{\#} + SiO_2$	0.0852	70	1	140	1

$SiO_2{}^*{}_{(s)} + CF^{\#} \rightarrow CF^{\#} + SiO_2$	0.0852	70	1	140	1
$SiO_2{}^*{}_{(s)} + F_2{}^{\#} \rightarrow F_2{}^{\#} + SiO_2$	0.0852	70	1	140	1
$SiO_2{}^*{}_{(s)} + F^{\#} \rightarrow F^{\#} + SiO_2$	0.0852	70	1	140	1
$SiO_2{}^*{}_{(s)} + O_2{}^{\#} \rightarrow O_2{}^{\#} + SiO_2$	0.0852	70	1	140	1
$SiO_2{}^*{}_{(s)} + O^{\#} \rightarrow SiO_2 + O^{\#}$	0.0852	70	1	140	1
$SiO_2{}^*{}_{(s)} + O^{\#} \rightarrow O^{\#} + SiO_2$	0.0852	70	1	140	1
$SiO_2{}^*{}_{(s)} + C_2F_4{}^{\#} \rightarrow C_2F_4{}^{\#} + SiO_2$	0.0852	70	1	140	1
$SiO_2{}^*{}_{(s)} + C_2F_3{}^{\#} \rightarrow C_2F_3{}^{\#} + SiO_2$	0.0852	70	1	140	1
$SiO_2{}^*{}_{(s)} + C_2F_3{}^{\#} \rightarrow SiO_2 + C_2F_3{}^{\#}$	0.0852	70	1	140	1
$SiO_2{}^*{}_{(s)} + C_2F_5{}^{\#} \rightarrow C_2F_5{}^{\#} + SiO_2$	0.0852	70	1	140	1
$SiO_2{}^*{}_{(s)} + C_3F_5{}^{\#} \rightarrow C_3F_5{}^{\#} + SiO_2$	0.0852	70	1	140	1
$SiO_2{}^*{}_{(s)} + C_3F_6{}^{\#} \rightarrow C_3F_6{}^{\#} + SiO_2$	0.0852	70	1	140	1
$SiO_2{}^*{}_{(s)} + C_3F_7{}^{\#} \rightarrow C_3F_7{}^{\#} + SiO_2$	0.0852	70	1	140	1
$SiO_2{}^*{}_{(s)} + C_4F_7{}^{\#} \rightarrow C_4F_7{}^{\#} + SiO_2$	0.0852	70	1	140	1
$SiO_2{}^*{}_{(s)} + C_4F_8{}^{\#} \rightarrow C_4F_8{}^{\#} + SiO_2$	0.0852	70	1	140	1
$SiO_{2(s)} + CF \rightarrow SiO_2CF_{(s)}$	0.278				
$SiO_{2(s)} + CF_2 \rightarrow SiO_2CF_{2(s)}$	0.278				
$SiO_{2(s)} + CF_3 \rightarrow SiO_2CF_{3(s)}$	0.2				
$SiO_{2(s)} + C_2F_3 \rightarrow SiO_2C_2F_{3(s)}$	0.2				
$SiO_{2(s)} + C_2F_4 \rightarrow SiO_2C_2F_{4(s)}$	0.001				
$SiO_{2(s)} + C_3F_5 \rightarrow SiO_2C_3F_{5(s)}$	0.001				
$SiO_{2(s)} + C_3F_6 \rightarrow SiO_2C_3F_{6(s)}$	0.001				
$SiO_2{}^*{}_{(s)} + CF \rightarrow SiO_2CF_{(s)}$	0.8				
$SiO_2{}^*{}_{(s)} + CF \rightarrow SiO_{2(s)} + CF$	0.2				
$SiO_2{}^*{}_{(s)} + CF_2 \rightarrow SiO_2CF_{2(s)}$	0.85				
$SiO_2{}^*{}_{(s)} + CF_2 \rightarrow SiO_{2(s)} + CF_2$	0.15				
$SiO_2{}^*{}_{(s)} + CF_3 \rightarrow SiO_2CF_{3(s)}$	0.9				
$SiO_2{}^*{}_{(s)} + CF_3 \rightarrow SiO_{2(s)} + CF_3$	0.1				
$SiO_2{}^*{}_{(s)} + C_2F_3 \rightarrow SiO_2C_2F_{3(s)}$	0.9				
$SiO_2{}^*{}_{(s)} + C_2F_3 \rightarrow SiO_{2(s)} + C_2F_3$	0.1				
$SiO_2{}^*{}_{(s)} + F \rightarrow SiO_{2(s)} + F$	1				
$SiO_2{}^*{}_{(s)} + O \rightarrow SiO_{2(s)} + O$	1				
$SiO_2CF_{(s)} + Ar^+ \rightarrow SiF + CO_2 + Ar^{\#}$	0.1471	35	1	140	2
$SiO_2CF_{2(s)} + Ar^+ \rightarrow CO_2 + Ar^{\#} + SiF_2$	0.1471	35	1	140	2
$SiO_2CF_{3(s)} + Ar^+ \rightarrow CO_2 + Ar^{\#} + SiF_3$	0.1471	35	1	140	2
$SiO_2C_2F_{3(s)} + Ar^+ \rightarrow SiOCF_{3(s)} + CO + Ar^{\#}$	0.1471	35	1	140	2
$SiO_2C_2F_{4(s)} + Ar^+ \rightarrow SiOCF_{3(s)} + COF + Ar^{\#}$	0.1471	35	1	140	2
$SiO_2C_3F_{5(s)} + Ar^+ \rightarrow SiO_2CF_{(s)} + C_2F_4 + Ar^{\#}$	0.1471	35	1	140	2
$SiO_2C_3F_{6(s)} + Ar^+ \rightarrow SiO_2CF_{3(s)} + C_2F_3 + Ar^{\#}$	0.1471	35	1	140	2
$SiO_2CF^*{}_{(s)} + Ar^+ \rightarrow CO_2 + Ar^{\#} + SiF$	0.1471	35	1	140	2
$SiO_2CF_2{}^*{}_{(s)} + Ar^+ \rightarrow CO_2 + Ar^{\#} + SiF_2$	0.1471	35	1	140	2

$SiO_2CF_3{*}_{(s)} + Ar^+ \rightarrow CO_2 + Ar^\# + SiF_3$	0.1471	35	1	140	2
$SiO_2C_2F_3{*}_{(s)} + Ar^+ \rightarrow SiOCF_3{*}_{(s)} + CO + Ar^\#$	0.1471	35	1	140	2
$SiO_2C_2F_4{*}_{(s)} + Ar^+ \rightarrow SiOCF_3{*}_{(s)} + COF + Ar^\#$	0.1471	35	1	140	2
$SiO_2C_3F_5{*}_{(s)} + Ar^+ \rightarrow SiO_2CF{*}_{(s)} + C_2F_4 + Ar^\#$	0.1471	35	1	140	2
$SiO_2C_3F_6{*}_{(s)} + Ar^+ \rightarrow SiO_2CF_3{*}_{(s)} + C_2F_3 + Ar^\#$	0.1471	35	1	140	2
$SiO_2CF_{(s)} + Ar^\# \rightarrow SiF + CO_2 + Ar^\#$	0.1471	35	1	140	2
$SiO_2CF_{2(s)} + Ar^\# \rightarrow CO_2 + Ar^\# + SiF_2$	0.1471	35	1	140	2
$SiO_2CF_{3(s)} + Ar^\# \rightarrow CO_2 + Ar^\# + SiF_3$	0.1471	35	1	140	2
$SiO_2C_2F_{3(s)} + Ar^\# \rightarrow SiOCF_{3(s)} + CO + Ar^\#$	0.1471	35	1	140	2
$SiO_2C_2F_{4(s)} + Ar^\# \rightarrow SiOCF_{3(s)} + COF + Ar^\#$	0.1471	35	1	140	2
$SiO_2C_3F_{5(s)} + Ar^\# \rightarrow SiO_2CF_{(s)} + C_2F_4 + Ar^\#$	0.1471	35	1	140	2
$SiO_2C_3F_{6(s)} + Ar^\# \rightarrow SiO_2CF_{3(s)} + C_2F_3 + Ar^\#$	0.1471	35	1	140	2
$SiO_2CF{*}_{(s)} + Ar^\# \rightarrow CO_2 + Ar^\# + SiF$	0.1471	35	1	140	2
$SiO_2CF_2{*}_{(s)} + Ar^\# \rightarrow CO_2 + Ar^\# + SiF_2$	0.1471	35	1	140	2
$SiO_2CF_3{*}_{(s)} + Ar^\# \rightarrow CO_2 + Ar^\# + SiF_3$	0.1471	35	1	140	2
$SiO_2C_2F_3{*}_{(s)} + Ar^\# \rightarrow SiOCF_3{*}_{(s)} + CO + Ar^\#$	0.1471	35	1	140	2
$SiO_2C_2F_4{*}_{(s)} + Ar^\# \rightarrow SiOCF_3{*}_{(s)} + COF + Ar^\#$	0.1471	35	1	140	2
$SiO_2C_3F_5{*}_{(s)} + Ar^\# \rightarrow SiO_2CF{*}_{(s)} + C_2F_4 + Ar^\#$	0.1471	35	1	140	2
$SiO_2C_3F_6{*}_{(s)} + Ar^\# \rightarrow SiO_2CF_3{*}_{(s)} + C_2F_3 + Ar^\#$	0.1471	35	1	140	2
$SiO_2CF_{(s)} + O^+ \rightarrow SiF + CO_2 + O^\#$	0.1471	35	1	140	2
$SiO_2CF_{2(s)} + O^+ \rightarrow CO_2 + O^\# + SiF_2$	0.1471	35	1	140	2
$SiO_2CF_{3(s)} + O^+ \rightarrow CO_2 + O^\# + SiF_3$	0.1471	35	1	140	2
$SiO_2C_2F_{3(s)} + O^+ \rightarrow SiOCF_{3(s)} + CO + O^\#$	0.1471	35	1	140	2
$SiO_2C_2F_{4(s)} + O^+ \rightarrow SiOCF_{3(s)} + COF + O^\#$	0.1471	35	1	140	2
$SiO_2C_3F_{5(s)} + O^+ \rightarrow SiO_2CF_{(s)} + C_2F_4 + O^\#$	0.1471	35	1	140	2
$SiO_2C_3F_{6(s)} + O^+ \rightarrow SiO_2CF_{3(s)} + C_2F_3 + O^\#$	0.1471	35	1	140	2
$SiO_2CF{*}_{(s)} + O^+ \rightarrow CO_2 + O^\# + SiF$	0.1471	35	1	140	2
$SiO_2CF_2{*}_{(s)} + O^+ \rightarrow CO_2 + O^\# + SiF_2$	0.1471	35	1	140	2
$SiO_2CF_3{*}_{(s)} + O^+ \rightarrow CO_2 + O^\# + SiF_3$	0.1471	35	1	140	2
$SiO_2C_2F_3{*}_{(s)} + O^+ \rightarrow SiOCF_3{*}_{(s)} + CO + O^\#$	0.1471	35	1	140	2
$SiO_2C_2F_4{*}_{(s)} + O^+ \rightarrow SiOCF_3{*}_{(s)} + COF + O^\#$	0.1471	35	1	140	2
$SiO_2C_3F_5{*}_{(s)} + O^+ \rightarrow SiO_2CF{*}_{(s)} + C_2F_4 + O^\#$	0.1471	35	1	140	2
$SiO_2C_3F_6{*}_{(s)} + O^+ \rightarrow SiO_2CF_3{*}_{(s)} + C_2F_3 + O^\#$	0.1471	35	1	140	2
$SiO_2CF_{(s)} + O^\# \rightarrow SiF + CO_2 + O^\#$	0.1471	35	1	140	2
$SiO_2CF_{2(s)} + O^\# \rightarrow CO_2 + O^\# + SiF_2$	0.1471	35	1	140	2
$SiO_2CF_{3(s)} + O^\# \rightarrow CO_2 + O^\# + SiF_3$	0.1471	35	1	140	2
$SiO_2C_2F_{3(s)} + O^\# \rightarrow SiOCF_{3(s)} + CO + O^\#$	0.1471	35	1	140	2
$SiO_2C_2F_{4(s)} + O^\# \rightarrow SiOCF_{3(s)} + COF + O^\#$	0.1471	35	1	140	2
$SiO_2C_3F_{5(s)} + O^\# \rightarrow SiO_2CF_{(s)} + C_2F_4 + O^\#$	0.1471	35	1	140	2
$SiO_2C_3F_{6(s)} + O^\# \rightarrow SiO_2CF_{3(s)} + C_2F_3 + O^\#$	0.1471	35	1	140	2
$SiO_2CF{*}_{(s)} + O^\# \rightarrow CO_2 + O^\# + SiF$	0.1471	35	1	140	2

Reaction				
$SiO_2CF_2*_{(s)} + O^{\#} \rightarrow CO_2 + O^{\#} + SiF_2$	0.1471	35	1	140	2
$SiO_2CF_3*_{(s)} + O^{\#} \rightarrow CO_2 + O^{\#} + SiF_3$	0.1471	35	1	140	2
$SiO_2C_2F_3*_{(s)} + O^{\#} \rightarrow SiOCF_3*_{(s)} + CO + O^{\#}$	0.1471	35	1	140	2
$SiO_2C_2F_4*_{(s)} + O^{\#} \rightarrow SiOCF_3*_{(s)} + COF + O^{\#}$	0.1471	35	1	140	2
$SiO_2C_3F_5*_{(s)} + O^{\#} \rightarrow SiO_2CF*_{(s)} + C_2F_4 + O^{\#}$	0.1471	35	1	140	2
$SiO_2C_3F_6*_{(s)} + O^{\#} \rightarrow SiO_2CF_3*_{(s)} + C_2F_3 + O^{\#}$	0.1471	35	1	140	2
$SiO_2CF_{(s)} + O_2^{+} \rightarrow SiF + CO_2 + O_2^{\#}$	0.1471	35	1	140	2
$SiO_2CF_{2(s)} + O_2^{+} \rightarrow CO_2 + O_2^{\#} + SiF_2$	0.1471	35	1	140	2
$SiO_2CF_{3(s)} + O_2^{+} \rightarrow CO_2 + O_2^{\#} + SiF_3$	0.1471	35	1	140	2
$SiO_2C_2F_{3(s)} + O_2^{+} \rightarrow SiOCF_{3(s)} + CO + O_2^{\#}$	0.1471	35	1	140	2
$SiO_2C_2F_{4(s)} + O_2^{+} \rightarrow SiOCF_{3(s)} + COF + O_2^{\#}$	0.1471	35	1	140	2
$SiO_2C_3F_{5(s)} + O_2^{+} \rightarrow SiO_2CF_{(s)} + C_2F_4 + O_2^{\#}$	0.1471	35	1	140	2
$SiO_2C_3F_{6(s)} + O_2^{+} \rightarrow SiO_2CF_{3(s)} + C_2F_3 + O_2^{\#}$	0.1471	35	1	140	2
$SiO_2CF*_{(s)} + O_2^{+} \rightarrow CO_2 + O_2^{\#} + SiF$	0.1471	35	1	140	2
$SiO_2CF_2*_{(s)} + O_2^{+} \rightarrow CO_2 + O_2^{\#} + SiF_2$	0.1471	35	1	140	2
$SiO_2CF_3*_{(s)} + O_2^{+} \rightarrow CO_2 + O_2^{\#} + SiF_3$	0.1471	35	1	140	2
$SiO_2C_2F_3*_{(s)} + O_2^{+} \rightarrow SiOCF_3*_{(s)} + CO + O_2^{\#}$	0.1471	35	1	140	2
$SiO_2C_2F_4*_{(s)} + O_2^{+} \rightarrow SiOCF_3*_{(s)} + COF + O_2^{\#}$	0.1471	35	1	140	2
$SiO_2C_3F_5*_{(s)} + O_2^{+} \rightarrow SiO_2CF*_{(s)} + C_2F_4 + O_2^{\#}$	0.1471	35	1	140	2
$SiO_2C_3F_6*_{(s)} + O_2^{+} \rightarrow SiO_2CF_3*_{(s)} + C_2F_3 + O_2^{\#}$	0.1471	35	1	140	2
$SiO_2CF_{(s)} + O_2^{\#} \rightarrow SiF + CO_2 + O_2^{\#}$	0.1471	35	1	140	2
$SiO_2CF_{2(s)} + O_2^{\#} \rightarrow CO_2 + O_2^{\#} + SiF_2$	0.1471	35	1	140	2
$SiO_2CF_{3(s)} + O_2^{\#} \rightarrow CO_2 + O_2^{\#} + SiF_3$	0.1471	35	1	140	2
$SiO_2C_2F_{3(s)} + O_2^{\#} \rightarrow SiOCF_{3(s)} + CO + O_2^{\#}$	0.1471	35	1	140	2
$SiO_2C_2F_{4(s)} + O_2^{\#} \rightarrow SiOCF_{3(s)} + COF + O_2^{\#}$	0.1471	35	1	140	2
$SiO_2C_3F_{5(s)} + O_2^{\#} \rightarrow SiO_2CF_{(s)} + C_2F_4 + O_2^{\#}$	0.1471	35	1	140	2
$SiO_2C_3F_{6(s)} + O_2^{\#} \rightarrow SiO_2CF_{3(s)} + C_2F_3 + O_2^{\#}$	0.1471	35	1	140	2
$SiO_2CF*_{(s)} + O_2^{\#} \rightarrow CO_2 + O_2^{\#} + SiF$	0.1471	35	1	140	2
$SiO_2CF_2*_{(s)} + O_2^{\#} \rightarrow CO_2 + O_2^{\#} + SiF_2$	0.1471	35	1	140	2
$SiO_2CF_3*_{(s)} + O_2^{\#} \rightarrow CO_2 + O_2^{\#} + SiF_3$	0.1471	35	1	140	2
$SiO_2C_2F_3*_{(s)} + O_2^{\#} \rightarrow SiOCF_3*_{(s)} + CO + O_2^{\#}$	0.1471	35	1	140	2
$SiO_2C_2F_4*_{(s)} + O_2^{\#} \rightarrow SiOCF_3*_{(s)} + COF + O_2^{\#}$	0.1471	35	1	140	2
$SiO_2C_3F_5*_{(s)} + O_2^{\#} \rightarrow SiO_2CF*_{(s)} + C_2F_4 + O_2^{\#}$	0.1471	35	1	140	2
$SiO_2C_3F_6*_{(s)} + O_2^{\#} \rightarrow SiO_2CF_3*_{(s)} + C_2F_3 + O_2^{\#}$	0.1471	35	1	140	2
$SiO_2CF_{(s)} + CF_3^{+} \rightarrow SiF + CO_2 + CF_3^{\#}$	0.1471	35	1	140	2
$SiO_2CF_{2(s)} + CF_3^{+} \rightarrow CO_2 + CF_3^{\#} + SiF_2$	0.1471	35	1	140	2
$SiO_2CF_{3(s)} + CF_3^{+} \rightarrow CO_2 + CF_3^{\#} + SiF_3$	0.1471	35	1	140	2
$SiO_2C_2F_{3(s)} + CF_3^{+} \rightarrow SiOCF_{3(s)} + CO + CF_3^{\#}$	0.1471	35	1	140	2
$SiO_2C_2F_{4(s)} + CF_3^{+} \rightarrow SiOCF_{3(s)} + COF + CF_3^{\#}$	0.1471	35	1	140	2
$SiO_2C_3F_{5(s)} + CF_3^{+} \rightarrow SiO_2CF_{(s)} + C_2F_4 + CF_3^{\#}$	0.1471	35	1	140	2
$SiO_2C_3F_{6(s)} + CF_3^{+} \rightarrow SiO_2CF_{3(s)} + C_2F_3 + CF_3^{\#}$	0.1471	35	1	140	2

$SiO_2CF^*_{(s)} + CF_3^+ \rightarrow CO_2 + CF_3^\# + SiF$	0.1471	35	1	140	2
$SiO_2CF_2^*_{(s)} + CF_3^+ \rightarrow CO_2 + CF_3^\# + SiF_2$	0.1471	35	1	140	2
$SiO_2CF_3^*_{(s)} + CF_3^+ \rightarrow CO_2 + CF_3^\# + SiF_3$	0.1471	35	1	140	2
$SiO_2C_2F_3^*_{(s)} + CF_3^+ \rightarrow SiOCF_3^*_{(s)} + CO + CF_3^\#$	0.1471	35	1	140	2
$SiO_2C_2F_4^*_{(s)} + CF_3^+ \rightarrow SiOCF_3^*_{(s)} + COF + CF_3^\#$	0.1471	35	1	140	2
$SiO_2C_3F_5^*_{(s)} + CF_3^+ \rightarrow SiO_2CF^*_{(s)} + C_2F_4 + CF_3^\#$	0.1471	35	1	140	2
$SiO_2C_3F_6^*_{(s)} + CF_3^+ \rightarrow SiO_2CF_3^*_{(s)} + C_2F_3 + CF_3^\#$	0.1471	35	1	140	2
$SiO_2CF_{(s)} + CF_3^\# \rightarrow SiF + CO_2 + CF_3^\#$	0.1471	35	1	140	2
$SiO_2CF_{2(s)} + CF_3^\# \rightarrow CO_2 + CF_3^\# + SiF_2$	0.1471	35	1	140	2
$SiO_2CF_{3(s)} + CF_3^\# \rightarrow CO_2 + CF_3^\# + SiF_3$	0.1471	35	1	140	2
$SiO_2C_2F_{3(s)} + CF_3^\# \rightarrow SiOCF_{3(s)} + CO + CF_3^\#$	0.1471	35	1	140	2
$SiO_2C_2F_{4(s)} + CF_3^\# \rightarrow SiOCF_{3(s)} + COF + CF_3^\#$	0.1471	35	1	140	2
$SiO_2C_3F_{5(s)} + CF_3^\# \rightarrow SiO_2CF_{(s)} + C_2F_4 + CF_3^\#$	0.1471	35	1	140	2
$SiO_2C_3F_{6(s)} + CF_3^\# \rightarrow SiO_2CF_{3(s)} + C_2F_3 + CF_3^\#$	0.1471	35	1	140	2
$SiO_2CF^*_{(s)} + CF_3^\# \rightarrow CO_2 + CF_3^\# + SiF$	0.1471	35	1	140	2
$SiO_2CF_2^*_{(s)} + CF_3^\# \rightarrow CO_2 + CF_3^\# + SiF_2$	0.1471	35	1	140	2
$SiO_2CF_3^*_{(s)} + CF_3^\# \rightarrow CO_2 + CF_3^\# + SiF_3$	0.1471	35	1	140	2
$SiO_2C_2F_3^*_{(s)} + CF_3^\# \rightarrow SiOCF_3^*_{(s)} + CO + CF_3^\#$	0.1471	35	1	140	2
$SiO_2C_2F_4^*_{(s)} + CF_3^\# \rightarrow SiOCF_3^*_{(s)} + COF + CF_3^\#$	0.1471	35	1	140	2
$SiO_2C_3F_5^*_{(s)} + CF_3^\# \rightarrow SiO_2CF^*_{(s)} + C_2F_4 + CF_3^\#$	0.1471	35	1	140	2
$SiO_2C_3F_6^*_{(s)} + CF_3^\# \rightarrow SiO_2CF_3^*_{(s)} + C_2F_3 + CF_3^\#$	0.1471	35	1	140	2
$SiO_2CF_{(s)} + CF_2^+ \rightarrow SiF + CO_2 + CF_2^\#$	0.1471	35	1	140	2
$SiO_2CF_{2(s)} + CF_2^+ \rightarrow CO_2 + CF_2^\# + SiF_2$	0.1471	35	1	140	2
$SiO_2CF_{3(s)} + CF_2^+ \rightarrow CO_2 + CF_2^\# + SiF_3$	0.1471	35	1	140	2
$SiO_2C_2F_{3(s)} + CF_2^+ \rightarrow SiOCF_{3(s)} + CO + CF_2^\#$	0.1471	35	1	140	2
$SiO_2C_2F_{4(s)} + CF_2^+ \rightarrow SiOCF_{3(s)} + COF + CF_2^\#$	0.1471	35	1	140	2
$SiO_2C_3F_{5(s)} + CF_2^+ \rightarrow SiO_2CF_{(s)} + C_2F_4 + CF_2^\#$	0.1471	35	1	140	2
$SiO_2C_3F_{6(s)} + CF_2^+ \rightarrow SiO_2CF_{3(s)} + C_2F_3 + CF_2^\#$	0.1471	35	1	140	2
$SiO_2CF^*_{(s)} + CF_2^+ \rightarrow CO_2 + CF_2^\# + SiF$	0.1471	35	1	140	2
$SiO_2CF_2^*_{(s)} + CF_2^+ \rightarrow CO_2 + CF_2^\# + SiF_2$	0.1471	35	1	140	2
$SiO_2CF_3^*_{(s)} + CF_2^+ \rightarrow CO_2 + CF_2^\# + SiF_3$	0.1471	35	1	140	2
$SiO_2C_2F_3^*_{(s)} + CF_2^+ \rightarrow SiOCF_3^*_{(s)} + CO + CF_2^\#$	0.1471	35	1	140	2
$SiO_2C_2F_4^*_{(s)} + CF_2^+ \rightarrow SiOCF_3^*_{(s)} + COF + CF_2^\#$	0.1471	35	1	140	2
$SiO_2C_3F_5^*_{(s)} + CF_2^+ \rightarrow SiO_2CF^*_{(s)} + C_2F_4 + CF_2^\#$	0.1471	35	1	140	2
$SiO_2C_3F_6^*_{(s)} + CF_2^+ \rightarrow SiO_2CF_3^*_{(s)} + C_2F_3 + CF_2^\#$	0.1471	35	1	140	2
$SiO_2CF_{(s)} + CF_2^\# \rightarrow SiF + CO_2 + CF_2^\#$	0.1471	35	1	140	2
$SiO_2CF_{2(s)} + CF_2^\# \rightarrow CO_2 + CF_2^\# + SiF_2$	0.1471	35	1	140	2
$SiO_2CF_{3(s)} + CF_2^\# \rightarrow CO_2 + CF_2^\# + SiF_3$	0.1471	35	1	140	2
$SiO_2C_2F_{3(s)} + CF_2^\# \rightarrow SiOCF_{3(s)} + CO + CF_2^\#$	0.1471	35	1	140	2
$SiO_2C_2F_{4(s)} + CF_2^\# \rightarrow SiOCF_{3(s)} + COF + CF_2^\#$	0.1471	35	1	140	2
$SiO_2C_3F_{5(s)} + CF_2^\# \rightarrow SiO_2CF_{(s)} + C_2F_4 + CF_2^\#$	0.1471	35	1	140	2

$SiO_2C_3F_{6(s)} + CF_2^{\#}$	→	$SiO_2CF_{3(s)} + C_2F_3 + CF_2^{\#}$	0.1471	35	1	140	2
$SiO_2CF*_{(s)} + CF_2^{\#}$	→	$CO_2 + CF_2^{\#} + SiF$	0.1471	35	1	140	2
$SiO_2CF_2*_{(s)} + CF_2^{\#}$	→	$CO_2 + CF_2^{\#} + SiF_2$	0.1471	35	1	140	2
$SiO_2CF_3*_{(s)} + CF_2^{\#}$	→	$CO_2 + CF_2^{\#} + SiF_3$	0.1471	35	1	140	2
$SiO_2C_2F_3*_{(s)} + CF_2^{\#}$	→	$SiOCF_3*_{(s)} + CO + CF_2^{\#}$	0.1471	35	1	140	2
$SiO_2C_2F_4*_{(s)} + CF_2^{\#}$	→	$SiOCF_3*_{(s)} + COF + CF_2^{\#}$	0.1471	35	1	140	2
$SiO_2C_3F_5*_{(s)} + CF_2^{\#}$	→	$SiO_2CF*_{(s)} + C_2F_4 + CF_2^{\#}$	0.1471	35	1	140	2
$SiO_2C_3F_6*_{(s)} + CF_2^{\#}$	→	$SiO_2CF_3*_{(s)} + C_2F_3 + CF_2^{\#}$	0.1471	35	1	140	2
$SiO_2CF_{(s)} + CF^+$	→	$SiF + CO_2 + CF^{\#}$	0.1471	35	1	140	2
$SiO_2CF_{2(s)} + CF^+$	→	$CO_2 + CF^{\#} + SiF_2$	0.1471	35	1	140	2
$SiO_2CF_{3(s)} + CF^+$	→	$CO_2 + CF^{\#} + SiF_3$	0.1471	35	1	140	2
$SiO_2C_2F_{3(s)} + CF^+$	→	$SiOCF_{3(s)} + CO + CF^{\#}$	0.1471	35	1	140	2
$SiO_2C_2F_{4(s)} + CF^+$	→	$SiOCF_{3(s)} + COF + CF^{\#}$	0.1471	35	1	140	2
$SiO_2C_3F_{5(s)} + CF^+$	→	$SiO_2CF_{(s)} + C_2F_4 + CF^{\#}$	0.1471	35	1	140	2
$SiO_2C_3F_{6(s)} + CF^+$	→	$SiO_2CF_{3(s)} + C_2F_3 + CF^{\#}$	0.1471	35	1	140	2
$SiO_2CF*_{(s)} + CF^+$	→	$CO_2 + CF^{\#} + SiF$	0.1471	35	1	140	2
$SiO_2CF_2*_{(s)} + CF^+$	→	$CO_2 + CF^{\#} + SiF_2$	0.1471	35	1	140	2
$SiO_2CF_3*_{(s)} + CF^+$	→	$CO_2 + CF^{\#} + SiF_3$	0.1471	35	1	140	2
$SiO_2C_2F_3*_{(s)} + CF^+$	→	$SiOCF_3*_{(s)} + CO + CF^{\#}$	0.1471	35	1	140	2
$SiO_2C_2F_4*_{(s)} + CF^+$	→	$SiOCF_3*_{(s)} + COF + CF^{\#}$	0.1471	35	1	140	2
$SiO_2C_3F_5*_{(s)} + CF^+$	→	$SiO_2CF*_{(s)} + C_2F_4 + CF^{\#}$	0.1471	35	1	140	2
$SiO_2C_3F_6*_{(s)} + CF^+$	→	$SiO_2CF_3*_{(s)} + C_2F_3 + CF^{\#}$	0.1471	35	1	140	2
$SiO_2CF_{(s)} + CF^{\#}$	→	$SiF + CO_2 + CF^{\#}$	0.1471	35	1	140	2
$SiO_2CF_{2(s)} + CF^{\#}$	→	$CO_2 + CF^{\#} + SiF_2$	0.1471	35	1	140	2
$SiO_2CF_{3(s)} + CF^{\#}$	→	$CO_2 + CF^{\#} + SiF_3$	0.1471	35	1	140	2
$SiO_2C_2F_{3(s)} + CF^{\#}$	→	$SiOCF_{3(s)} + CO + CF^{\#}$	0.1471	35	1	140	2
$SiO_2C_2F_{4(s)} + CF^{\#}$	→	$SiOCF_{3(s)} + COF + CF^{\#}$	0.1471	35	1	140	2
$SiO_2C_3F_{5(s)} + CF^{\#}$	→	$SiO_2CF_{(s)} + C_2F_4 + CF^{\#}$	0.1471	35	1	140	2
$SiO_2C_3F_{6(s)} + CF^{\#}$	→	$SiO_2CF_{3(s)} + C_2F_3 + CF^{\#}$	0.1471	35	1	140	2
$SiO_2CF*_{(s)} + CF^{\#}$	→	$CO_2 + CF^{\#} + SiF$	0.1471	35	1	140	2
$SiO_2CF_2*_{(s)} + CF^{\#}$	→	$CO_2 + CF^{\#} + SiF_2$	0.1471	35	1	140	2
$SiO_2CF_3*_{(s)} + CF^{\#}$	→	$CO_2 + CF^{\#} + SiF_3$	0.1471	35	1	140	2
$SiO_2C_2F_3*_{(s)} + CF^{\#}$	→	$SiOCF_3*_{(s)} + CO + CF^{\#}$	0.1471	35	1	140	2
$SiO_2C_2F_4*_{(s)} + CF^{\#}$	→	$SiOCF_3*_{(s)} + COF + CF^{\#}$	0.1471	35	1	140	2
$SiO_2C_3F_5*_{(s)} + CF^{\#}$	→	$SiO_2CF*_{(s)} + C_2F_4 + CF^{\#}$	0.1471	35	1	140	2
$SiO_2C_3F_6*_{(s)} + CF^{\#}$	→	$SiO_2CF_3*_{(s)} + C_2F_3 + CF^{\#}$	0.1471	35	1	140	2
$SiO_2CF_{(s)} + F^+$	→	$SiF + CO_2 + F^{\#}$	0.1471	35	1	140	2
$SiO_2CF_{2(s)} + F^+$	→	$CO_2 + F^{\#} + SiF_2$	0.1471	35	1	140	2
$SiO_2CF_{3(s)} + F^+$	→	$CO_2 + F^{\#} + SiF_3$	0.1471	35	1	140	2
$SiO_2C_2F_{3(s)} + F^+$	→	$SiOCF_{3(s)} + CO + F^{\#}$	0.1471	35	1	140	2
$SiO_2C_2F_{4(s)} + F^+$	→	$SiOCF_{3(s)} + COF + F^{\#}$	0.1471	35	1	140	2

$SiO_2C_3F_{5(s)} + F^+ \rightarrow SiO_2CF_{(s)} + C_2F_4 + F^{\#}$	0.1471	35	1	140	2
$SiO_2C_3F_{6(s)} + F^+ \rightarrow SiO_2CF_{3(s)} + C_2F_3 + F^{\#}$	0.1471	35	1	140	2
$SiO_2CF*_{(s)} + F^+ \rightarrow CO_2 + F^{\#} + SiF$	0.1471	35	1	140	2
$SiO_2CF_2*_{(s)} + F^+ \rightarrow CO_2 + F^{\#} + SiF_2$	0.1471	35	1	140	2
$SiO_2CF_3*_{(s)} + F^+ \rightarrow CO_2 + F^{\#} + SiF_3$	0.1471	35	1	140	2
$SiO_2C_2F_3*_{(s)} + F^+ \rightarrow SiOCF_3*_{(s)} + CO + F^{\#}$	0.1471	35	1	140	2
$SiO_2C_2F_4*_{(s)} + F^+ \rightarrow SiOCF_3*_{(s)} + COF + F^{\#}$	0.1471	35	1	140	2
$SiO_2C_3F_5*_{(s)} + F^+ \rightarrow SiO_2CF*_{(s)} + C_2F_4 + F^{\#}$	0.1471	35	1	140	2
$SiO_2C_3F_6*_{(s)} + F^+ \rightarrow SiO_2CF_3*_{(s)} + C_2F_3 + F^{\#}$	0.1471	35	1	140	2
$SiO_2CF_{(s)} + F^{\#} \rightarrow SiF + CO_2 + F^{\#}$	0.1471	35	1	140	2
$SiO_2CF_{2(s)} + F^{\#} \rightarrow CO_2 + F^{\#} + SiF_2$	0.1471	35	1	140	2
$SiO_2CF_{3(s)} + F^{\#} \rightarrow CO_2 + F^{\#} + SiF_3$	0.1471	35	1	140	2
$SiO_2C_2F_{3(s)} + F^{\#} \rightarrow SiOCF_{3(s)} + CO + F^{\#}$	0.1471	35	1	140	2
$SiO_2C_2F_{4(s)} + F^{\#} \rightarrow SiOCF_{3(s)} + COF + F^{\#}$	0.1471	35	1	140	2
$SiO_2C_3F_{5(s)} + F^{\#} \rightarrow SiO_2CF_{(s)} + C_2F_4 + F^{\#}$	0.1471	35	1	140	2
$SiO_2C_3F_{6(s)} + F^{\#} \rightarrow SiO_2CF_{3(s)} + C_2F_3 + F^{\#}$	0.1471	35	1	140	2
$SiO_2CF*_{(s)} + F^{\#} \rightarrow CO_2 + F^{\#} + SiF$	0.1471	35	1	140	2
$SiO_2CF_2*_{(s)} + F^{\#} \rightarrow CO_2 + F^{\#} + SiF_2$	0.1471	35	1	140	2
$SiO_2CF_3*_{(s)} + F^{\#} \rightarrow CO_2 + F^{\#} + SiF_3$	0.1471	35	1	140	2
$SiO_2C_2F_3*_{(s)} + F^{\#} \rightarrow SiOCF_3*_{(s)} + CO + F^{\#}$	0.1471	35	1	140	2
$SiO_2C_2F_4*_{(s)} + F^{\#} \rightarrow SiOCF_3*_{(s)} + COF + F^{\#}$	0.1471	35	1	140	2
$SiO_2C_3F_5*_{(s)} + F^{\#} \rightarrow SiO_2CF*_{(s)} + C_2F_4 + F^{\#}$	0.1471	35	1	140	2
$SiO_2C_3F_6*_{(s)} + F^{\#} \rightarrow SiO_2CF_3*_{(s)} + C_2F_3 + F^{\#}$	0.1471	35	1	140	2
$SiO_2CF_{(s)} + F_2^+ \rightarrow SiF + CO_2 + F_2^{\#}$	0.1471	35	1	140	2
$SiO_2CF_{2(s)} + F_2^+ \rightarrow CO_2 + F_2^{\#} + SiF_2$	0.1471	35	1	140	2
$SiO_2CF_{3(s)} + F_2^+ \rightarrow CO_2 + F_2^{\#} + SiF_3$	0.1471	35	1	140	2
$SiO_2C_2F_{3(s)} + F_2^+ \rightarrow SiOCF_{3(s)} + CO + F_2^{\#}$	0.1471	35	1	140	2
$SiO_2C_2F_{4(s)} + F_2^+ \rightarrow SiOCF_{3(s)} + COF + F_2^{\#}$	0.1471	35	1	140	2
$SiO_2C_3F_{5(s)} + F_2^+ \rightarrow SiO_2CF_{(s)} + C_2F_4 + F_2^{\#}$	0.1471	35	1	140	2
$SiO_2C_3F_{6(s)} + F_2^+ \rightarrow SiO_2CF_{3(s)} + C_2F_3 + F_2^{\#}$	0.1471	35	1	140	2
$SiO_2CF*_{(s)} + F_2^+ \rightarrow CO_2 + F_2^{\#} + SiF$	0.1471	35	1	140	2
$SiO_2CF_2*_{(s)} + F_2^+ \rightarrow CO_2 + F_2^{\#} + SiF_2$	0.1471	35	1	140	2
$SiO_2CF_3*_{(s)} + F_2^+ \rightarrow CO_2 + F_2^{\#} + SiF_3$	0.1471	35	1	140	2
$SiO_2C_2F_3*_{(s)} + F_2^+ \rightarrow SiOCF_3*_{(s)} + CO + F_2^{\#}$	0.1471	35	1	140	2
$SiO_2C_2F_4*_{(s)} + F_2^+ \rightarrow SiOCF_3*_{(s)} + COF + F_2^{\#}$	0.1471	35	1	140	2
$SiO_2C_3F_5*_{(s)} + F_2^+ \rightarrow SiO_2CF*_{(s)} + C_2F_4 + F_2^{\#}$	0.1471	35	1	140	2
$SiO_2C_3F_6*_{(s)} + F_2^+ \rightarrow SiO_2CF_3*_{(s)} + C_2F_3 + F_2^{\#}$	0.1471	35	1	140	2
$SiO_2CF_{(s)} + F_2^{\#} \rightarrow SiF + CO_2 + F_2^{\#}$	0.1471	35	1	140	2
$SiO_2CF_{2(s)} + F_2^{\#} \rightarrow CO_2 + F_2^{\#} + SiF_2$	0.1471	35	1	140	2
$SiO_2CF_{3(s)} + F_2^{\#} \rightarrow CO_2 + F_2^{\#} + SiF_3$	0.1471	35	1	140	2
$SiO_2C_2F_{3(s)} + F_2^{\#} \rightarrow SiOCF_{3(s)} + CO + F_2^{\#}$	0.1471	35	1	140	2

$SiO_2C_2F_{4(s)} + F_2^{\#} \rightarrow SiOCF_{3(s)} + COF + F_2^{\#}$	0.1471	35	1	140	2
$SiO_2C_3F_{5(s)} + F_2^{\#} \rightarrow SiO_2CF_{(s)} + C_2F_4 + F_2^{\#}$	0.1471	35	1	140	2
$SiO_2C_3F_{6(s)} + F_2^{\#} \rightarrow SiO_2CF_{3(s)} + C_2F_3 + F_2^{\#}$	0.1471	35	1	140	2
$SiO_2CF^*_{(s)} + F_2^{\#} \rightarrow CO_2 + F_2^{\#} + SiF$	0.1471	35	1	140	2
$SiO_2CF_2^*{}_{(s)} + F_2^{\#} \rightarrow CO_2 + F_2^{\#} + SiF_2$	0.1471	35	1	140	2
$SiO_2CF_3^*{}_{(s)} + F_2^{\#} \rightarrow CO_2 + F_2^{\#} + SiF_3$	0.1471	35	1	140	2
$SiO_2C_2F_3^*{}_{(s)} + F_2^{\#} \rightarrow SiOCF_3^*{}_{(s)} + CO + F_2^{\#}$	0.1471	35	1	140	2
$SiO_2C_2F_4^*{}_{(s)} + F_2^{\#} \rightarrow SiOCF_3^*{}_{(s)} + COF + F_2^{\#}$	0.1471	35	1	140	2
$SiO_2C_3F_5^*{}_{(s)} + F_2^{\#} \rightarrow SiO_2CF^*_{(s)} + C_2F_4 + F_2^{\#}$	0.1471	35	1	140	2
$SiO_2C_3F_6^*{}_{(s)} + F_2^{\#} \rightarrow SiO_2CF_3^*{}_{(s)} + C_2F_3 + F_2^{\#}$	0.1471	35	1	140	2
$SiO_2CF_{(s)} + C_2F_5^+ \rightarrow SiF + CO_2 + C_2F_5^{\#}$	0.1471	35	1	140	2
$SiO_2CF_{2(s)} + C_2F_5^+ \rightarrow CO_2 + C_2F_5^{\#} + SiF_2$	0.1471	35	1	140	2
$SiO_2CF_{3(s)} + C_2F_5^+ \rightarrow CO_2 + C_2F_5^{\#} + SiF_3$	0.1471	35	1	140	2
$SiO_2C_2F_{3(s)} + C_2F_5^+ \rightarrow SiOCF_{3(s)} + CO + C_2F_5^{\#}$	0.1471	35	1	140	2
$SiO_2C_2F_{4(s)} + C_2F_5^+ \rightarrow SiOCF_{3(s)} + COF + C_2F_5^{\#}$	0.1471	35	1	140	2
$SiO_2C_3F_{5(s)} + C_2F_5^+ \rightarrow SiO_2CF_{(s)} + C_2F_4 + C_2F_5^{\#}$	0.1471	35	1	140	2
$SiO_2C_3F_{6(s)} + C_2F_5^+ \rightarrow SiO_2CF_{3(s)} + C_2F_3 + C_2F_5^{\#}$	0.1471	35	1	140	2
$SiO_2CF^*_{(s)} + C_2F_5^+ \rightarrow CO_2 + C_2F_5^{\#} + SiF$	0.1471	35	1	140	2
$SiO_2CF_2^*{}_{(s)} + C_2F_5^+ \rightarrow CO_2 + C_2F_5^{\#} + SiF_2$	0.1471	35	1	140	2
$SiO_2CF_3^*{}_{(s)} + C_2F_5^+ \rightarrow CO_2 + C_2F_5^{\#} + SiF_3$	0.1471	35	1	140	2
$SiO_2C_2F_3^*{}_{(s)} + C_2F_5^+ \rightarrow SiOCF_3^*{}_{(s)} + CO + C_2F_5^{\#}$	0.1471	35	1	140	2
$SiO_2C_2F_4^*{}_{(s)} + C_2F_5^+ \rightarrow SiOCF_3^*{}_{(s)} + COF + C_2F_5^{\#}$	0.1471	35	1	140	2
$SiO_2C_3F_5^*{}_{(s)} + C_2F_5^+ \rightarrow SiO_2CF^*_{(s)} + C_2F_4 + C_2F_5^{\#}$	0.1471	35	1	140	2
$SiO_2C_3F_6^*{}_{(s)} + C_2F_5^+ \rightarrow SiO_2CF_3^*{}_{(s)} + C_2F_3 + C_2F_5^{\#}$	0.1471	35	1	140	2
$SiO_2CF_{(s)} + C_2F_5^{\#} \rightarrow SiF + CO_2 + C_2F_5^{\#}$	0.1471	35	1	140	2
$SiO_2CF_{2(s)} + C_2F_5^{\#} \rightarrow CO_2 + C_2F_5^{\#} + SiF_2$	0.1471	35	1	140	2
$SiO_2CF_{3(s)} + C_2F_5^{\#} \rightarrow CO_2 + C_2F_5^{\#} + SiF_3$	0.1471	35	1	140	2
$SiO_2C_2F_{3(s)} + C_2F_5^{\#} \rightarrow SiOCF_{3(s)} + CO + C_2F_5^{\#}$	0.1471	35	1	140	2
$SiO_2C_2F_{4(s)} + C_2F_5^{\#} \rightarrow SiOCF_{3(s)} + COF + C_2F_5^{\#}$	0.1471	35	1	140	2
$SiO_2C_3F_{5(s)} + C_2F_5^{\#} \rightarrow SiO_2CF_{(s)} + C_2F_4 + C_2F_5^{\#}$	0.1471	35	1	140	2
$SiO_2C_3F_{6(s)} + C_2F_5^{\#} \rightarrow SiO_2CF_{3(s)} + C_2F_3 + C_2F_5^{\#}$	0.1471	35	1	140	2
$SiO_2CF^*_{(s)} + C_2F_5^{\#} \rightarrow CO_2 + C_2F_5^{\#} + SiF$	0.1471	35	1	140	2
$SiO_2CF_2^*{}_{(s)} + C_2F_5^{\#} \rightarrow CO_2 + C_2F_5^{\#} + SiF_2$	0.1471	35	1	140	2
$SiO_2CF_3^*{}_{(s)} + C_2F_5^{\#} \rightarrow CO_2 + C_2F_5^{\#} + SiF_3$	0.1471	35	1	140	2
$SiO_2C_2F_3^*{}_{(s)} + C_2F_5^{\#} \rightarrow SiOCF_3^*{}_{(s)} + CO + C_2F_5^{\#}$	0.1471	35	1	140	2
$SiO_2C_2F_4^*{}_{(s)} + C_2F_5^{\#} \rightarrow SiOCF_3^*{}_{(s)} + COF + C_2F_5^{\#}$	0.1471	35	1	140	2
$SiO_2C_3F_5^*{}_{(s)} + C_2F_5^{\#} \rightarrow SiO_2CF^*_{(s)} + C_2F_4 + C_2F_5^{\#}$	0.1471	35	1	140	2
$SiO_2C_3F_6^*{}_{(s)} + C_2F_5^{\#} \rightarrow SiO_2CF_3^*{}_{(s)} + C_2F_3 + C_2F_5^{\#}$	0.1471	35	1	140	2
$SiO_2CF_{(s)} + C_2F_4^+ \rightarrow SiF + CO_2 + C_2F_4^{\#}$	0.1471	35	1	140	2
$SiO_2CF_{2(s)} + C_2F_4^+ \rightarrow CO_2 + C_2F_4^{\#} + SiF_2$	0.1471	35	1	140	2
$SiO_2CF_{3(s)} + C_2F_4^+ \rightarrow CO_2 + C_2F_4^{\#} + SiF_3$	0.1471	35	1	140	2

$SiO_2C_2F_{3(s)} + C_2F_4^+ \rightarrow SiOCF_{3(s)} + CO + C_2F_4^{\#}$	0.1471	35	1	140	2
$SiO_2C_2F_{4(s)} + C_2F_4^+ \rightarrow SiOCF_{3(s)} + COF + C_2F_4^{\#}$	0.1471	35	1	140	2
$SiO_2C_3F_{5(s)} + C_2F_4^+ \rightarrow SiO_2CF_{(s)} + C_2F_4 + C_2F_4^{\#}$	0.1471	35	1	140	2
$SiO_2C_3F_{6(s)} + C_2F_4^+ \rightarrow SiO_2CF_{3(s)} + C_2F_3 + C_2F_4^{\#}$	0.1471	35	1	140	2
$SiO_2CF^*_{(s)} + C_2F_4^+ \rightarrow CO_2 + C_2F_4^{\#} + SiF$	0.1471	35	1	140	2
$SiO_2CF_2^*{}_{(s)} + C_2F_4^+ \rightarrow CO_2 + C_2F_4^{\#} + SiF_2$	0.1471	35	1	140	2
$SiO_2CF_3^*{}_{(s)} + C_2F_4^+ \rightarrow CO_2 + C_2F_4^{\#} + SiF_3$	0.1471	35	1	140	2
$SiO_2C_2F_3^*{}_{(s)} + C_2F_4^+ \rightarrow SiOCF_3^*{}_{(s)} + CO + C_2F_4^{\#}$	0.1471	35	1	140	2
$SiO_2C_2F_4^*{}_{(s)} + C_2F_4^+ \rightarrow SiOCF_3^*{}_{(s)} + COF + C_2F_4^{\#}$	0.1471	35	1	140	2
$SiO_2C_3F_5^*{}_{(s)} + C_2F_4^+ \rightarrow SiO_2CF^*_{(s)} + C_2F_4 + C_2F_4^{\#}$	0.1471	35	1	140	2
$SiO_2C_3F_6^*{}_{(s)} + C_2F_4^+ \rightarrow SiO_2CF_3^*{}_{(s)} + C_2F_3 + C_2F_4^{\#}$	0.1471	35	1	140	2
$SiO_2CF_{(s)} + C_2F_4^{\#} \rightarrow SiF + CO_2 + C_2F_4^{\#}$	0.1471	35	1	140	2
$SiO_2CF_{2(s)} + C_2F_4^{\#} \rightarrow CO_2 + C_2F_4^{\#} + SiF_2$	0.1471	35	1	140	2
$SiO_2CF_{3(s)} + C_2F_4^{\#} \rightarrow CO_2 + C_2F_4^{\#} + SiF_3$	0.1471	35	1	140	2
$SiO_2C_2F_{3(s)} + C_2F_4^{\#} \rightarrow SiOCF_{3(s)} + CO + C_2F_4^{\#}$	0.1471	35	1	140	2
$SiO_2C_2F_{4(s)} + C_2F_4^{\#} \rightarrow SiOCF_{3(s)} + COF + C_2F_4^{\#}$	0.1471	35	1	140	2
$SiO_2C_3F_{5(s)} + C_2F_4^{\#} \rightarrow SiO_2CF_{(s)} + C_2F_4 + C_2F_4^{\#}$	0.1471	35	1	140	2
$SiO_2C_3F_{6(s)} + C_2F_4^{\#} \rightarrow SiO_2CF_{3(s)} + C_2F_3 + C_2F_4^{\#}$	0.1471	35	1	140	2
$SiO_2CF^*_{(s)} + C_2F_4^{\#} \rightarrow CO_2 + C_2F_4^{\#} + SiF$	0.1471	35	1	140	2
$SiO_2CF_2^*{}_{(s)} + C_2F_4^{\#} \rightarrow CO_2 + C_2F_4^{\#} + SiF_2$	0.1471	35	1	140	2
$SiO_2CF_3^*{}_{(s)} + C_2F_4^{\#} \rightarrow CO_2 + C_2F_4^{\#} + SiF_3$	0.1471	35	1	140	2
$SiO_2C_2F_3^*{}_{(s)} + C_2F_4^{\#} \rightarrow SiOCF_3^*{}_{(s)} + CO + C_2F_4^{\#}$	0.1471	35	1	140	2
$SiO_2C_2F_4^*{}_{(s)} + C_2F_4^{\#} \rightarrow SiOCF_3^*{}_{(s)} + COF + C_2F_4^{\#}$	0.1471	35	1	140	2
$SiO_2C_3F_5^*{}_{(s)} + C_2F_4^{\#} \rightarrow SiO_2CF^*_{(s)} + C_2F_4 + C_2F_4^{\#}$	0.1471	35	1	140	2
$SiO_2C_3F_6^*{}_{(s)} + C_2F_4^{\#} \rightarrow SiO_2CF_3^*{}_{(s)} + C_2F_3 + C_2F_4^{\#}$	0.1471	35	1	140	2
$SiO_2CF_{(s)} + C_2F_3^+ \rightarrow SiF + CO_2 + C_2F_3^{\#}$	0.1471	35	1	140	2
$SiO_2CF_{2(s)} + C_2F_3^+ \rightarrow CO_2 + C_2F_3^{\#} + SiF_2$	0.1471	35	1	140	2
$SiO_2CF_{3(s)} + C_2F_3^+ \rightarrow CO_2 + C_2F_3^{\#} + SiF_3$	0.1471	35	1	140	2
$SiO_2C_2F_{3(s)} + C_2F_3^+ \rightarrow SiOCF_{3(s)} + CO + C_2F_3^{\#}$	0.1471	35	1	140	2
$SiO_2C_2F_{4(s)} + C_2F_3^+ \rightarrow SiOCF_{3(s)} + COF + C_2F_3^{\#}$	0.1471	35	1	140	2
$SiO_2C_3F_{5(s)} + C_2F_3^+ \rightarrow SiO_2CF_{(s)} + C_2F_4 + C_2F_3^{\#}$	0.1471	35	1	140	2
$SiO_2C_3F_{6(s)} + C_2F_3^+ \rightarrow SiO_2CF_{3(s)} + C_2F_3 + C_2F_3^{\#}$	0.1471	35	1	140	2
$SiO_2CF^*_{(s)} + C_2F_3^+ \rightarrow CO_2 + C_2F_3^{\#} + SiF$	0.1471	35	1	140	2
$SiO_2CF_2^*{}_{(s)} + C_2F_3^+ \rightarrow CO_2 + C_2F_3^{\#} + SiF_2$	0.1471	35	1	140	2
$SiO_2CF_3^*{}_{(s)} + C_2F_3^+ \rightarrow CO_2 + C_2F_3^{\#} + SiF_3$	0.1471	35	1	140	2
$SiO_2C_2F_3^*{}_{(s)} + C_2F_3^+ \rightarrow SiOCF_3^*{}_{(s)} + CO + C_2F_3^{\#}$	0.1471	35	1	140	2
$SiO_2C_2F_4^*{}_{(s)} + C_2F_3^+ \rightarrow SiOCF_3^*{}_{(s)} + COF + C_2F_3^{\#}$	0.1471	35	1	140	2
$SiO_2C_3F_5^*{}_{(s)} + C_2F_3^+ \rightarrow SiO_2CF^*_{(s)} + C_2F_4 + C_2F_3^{\#}$	0.1471	35	1	140	2
$SiO_2C_3F_6^*{}_{(s)} + C_2F_3^+ \rightarrow SiO_2CF_3^*{}_{(s)} + C_2F_3 + C_2F_3^{\#}$	0.1471	35	1	140	2
$SiO_2CF_{(s)} + C_2F_3^{\#} \rightarrow SiF + CO_2 + C_2F_3^{\#}$	0.1471	35	1	140	2
$SiO_2CF_{2(s)} + C_2F_3^{\#} \rightarrow CO_2 + C_2F_3^{\#} + SiF_2$	0.1471	35	1	140	2

$SiO_2CF_{3(s)} + C_2F_3^{\#} \rightarrow CO_2 + C_2F_3^{\#} + SiF_3$	0.1471	35	1	140	2
$SiO_2C_2F_{3(s)} + C_2F_3^{\#} \rightarrow SiOCF_{3(s)} + CO + C_2F_3^{\#}$	0.1471	35	1	140	2
$SiO_2C_2F_{4(s)} + C_2F_3^{\#} \rightarrow SiOCF_{3(s)} + COF + C_2F_3^{\#}$	0.1471	35	1	140	2
$SiO_2C_3F_{5(s)} + C_2F_3^{\#} \rightarrow SiO_2CF_{(s)} + C_2F_4 + C_2F_3^{\#}$	0.1471	35	1	140	2
$SiO_2C_3F_{6(s)} + C_2F_3^{\#} \rightarrow SiO_2CF_{3(s)} + C_2F_3 + C_2F_3^{\#}$	0.1471	35	1	140	2
$SiO_2CF^*_{(s)} + C_2F_3^{\#} \rightarrow CO_2 + C_2F_3^{\#} + SiF$	0.1471	35	1	140	2
$SiO_2CF_2^*{}_{(s)} + C_2F_3^{\#} \rightarrow CO_2 + C_2F_3^{\#} + SiF_2$	0.1471	35	1	140	2
$SiO_2CF_3^*{}_{(s)} + C_2F_3^{\#} \rightarrow CO_2 + C_2F_3^{\#} + SiF_3$	0.1471	35	1	140	2
$SiO_2C_2F_3^*{}_{(s)} + C_2F_3^{\#} \rightarrow SiOCF_3^*{}_{(s)} + CO + C_2F_3^{\#}$	0.1471	35	1	140	2
$SiO_2C_2F_4^*{}_{(s)} + C_2F_3^{\#} \rightarrow SiOCF_3^*{}_{(s)} + COF + C_2F_3^{\#}$	0.1471	35	1	140	2
$SiO_2C_3F_5^*{}_{(s)} + C_2F_3^{\#} \rightarrow SiO_2CF^*_{(s)} + C_2F_4 + C_2F_3^{\#}$	0.1471	35	1	140	2
$SiO_2C_3F_6^*{}_{(s)} + C_2F_3^{\#} \rightarrow SiO_2CF_3^*{}_{(s)} + C_2F_3 + C_2F_3^{\#}$	0.1471	35	1	140	2
$SiO_2CF_{(s)} + C_3F_5^+ \rightarrow SiF + CO_2 + C_3F_5^{\#}$	0.1471	35	1	140	2
$SiO_2CF_{2(s)} + C_3F_5^+ \rightarrow CO_2 + C_3F_5^{\#} + SiF_2$	0.1471	35	1	140	2
$SiO_2CF_{3(s)} + C_3F_5^+ \rightarrow CO_2 + C_3F_5^{\#} + SiF_3$	0.1471	35	1	140	2
$SiO_2C_2F_{3(s)} + C_3F_5^+ \rightarrow SiOCF_{3(s)} + CO + C_3F_5^{\#}$	0.1471	35	1	140	2
$SiO_2C_2F_{4(s)} + C_3F_5^+ \rightarrow SiOCF_{3(s)} + COF + C_3F_5^{\#}$	0.1471	35	1	140	2
$SiO_2C_3F_{5(s)} + C_3F_5^+ \rightarrow SiO_2CF_{(s)} + C_2F_4 + C_3F_5^{\#}$	0.1471	35	1	140	2
$SiO_2C_3F_{6(s)} + C_3F_5^+ \rightarrow SiO_2CF_{3(s)} + C_2F_3 + C_3F_5^{\#}$	0.1471	35	1	140	2
$SiO_2CF^*_{(s)} + C_3F_5^+ \rightarrow CO_2 + C_3F_5^{\#} + SiF$	0.1471	35	1	140	2
$SiO_2CF_2^*{}_{(s)} + C_3F_5^+ \rightarrow CO_2 + C_3F_5^{\#} + SiF_2$	0.1471	35	1	140	2
$SiO_2CF_3^*{}_{(s)} + C_3F_5^+ \rightarrow CO_2 + C_3F_5^{\#} + SiF_3$	0.1471	35	1	140	2
$SiO_2C_2F_3^*{}_{(s)} + C_3F_5^+ \rightarrow SiOCF_3^*{}_{(s)} + CO + C_3F_5^{\#}$	0.1471	35	1	140	2
$SiO_2C_2F_4^*{}_{(s)} + C_3F_5^+ \rightarrow SiOCF_3^*{}_{(s)} + COF + C_3F_5^{\#}$	0.1471	35	1	140	2
$SiO_2C_3F_5^*{}_{(s)} + C_3F_5^+ \rightarrow SiO_2CF^*_{(s)} + C_2F_4 + C_3F_5^{\#}$	0.1471	35	1	140	2
$SiO_2C_3F_6^*{}_{(s)} + C_3F_5^+ \rightarrow SiO_2CF_3^*{}_{(s)} + C_2F_3 + C_3F_5^{\#}$	0.1471	35	1	140	2
$SiO_2CF_{(s)} + C_3F_5^{\#} \rightarrow SiF + CO_2 + C_3F_5^{\#}$	0.1471	35	1	140	2
$SiO_2CF_{2(s)} + C_3F_5^{\#} \rightarrow CO_2 + C_3F_5^{\#} + SiF_2$	0.1471	35	1	140	2
$SiO_2CF_{3(s)} + C_3F_5^{\#} \rightarrow CO_2 + C_3F_5^{\#} + SiF_3$	0.1471	35	1	140	2
$SiO_2C_2F_{3(s)} + C_3F_5^{\#} \rightarrow SiOCF_{3(s)} + CO + C_3F_5^{\#}$	0.1471	35	1	140	2
$SiO_2C_2F_{4(s)} + C_3F_5^{\#} \rightarrow SiOCF_{3(s)} + COF + C_3F_5^{\#}$	0.1471	35	1	140	2
$SiO_2C_3F_{5(s)} + C_3F_5^{\#} \rightarrow SiO_2CF_{(s)} + C_2F_4 + C_3F_5^{\#}$	0.1471	35	1	140	2
$SiO_2C_3F_{6(s)} + C_3F_5^{\#} \rightarrow SiO_2CF_{3(s)} + C_2F_3 + C_3F_5^{\#}$	0.1471	35	1	140	2
$SiO_2CF^*_{(s)} + C_3F_5^{\#} \rightarrow CO_2 + C_3F_5^{\#} + SiF$	0.1471	35	1	140	2
$SiO_2CF_2^*{}_{(s)} + C_3F_5^{\#} \rightarrow CO_2 + C_3F_5^{\#} + SiF_2$	0.1471	35	1	140	2
$SiO_2CF_3^*{}_{(s)} + C_3F_5^{\#} \rightarrow CO_2 + C_3F_5^{\#} + SiF_3$	0.1471	35	1	140	2
$SiO_2C_2F_3^*{}_{(s)} + C_3F_5^{\#} \rightarrow SiOCF_3^*{}_{(s)} + CO + C_3F_5^{\#}$	0.1471	35	1	140	2
$SiO_2C_2F_4^*{}_{(s)} + C_3F_5^{\#} \rightarrow SiOCF_3^*{}_{(s)} + COF + C_3F_5^{\#}$	0.1471	35	1	140	2
$SiO_2C_3F_5^*{}_{(s)} + C_3F_5^{\#} \rightarrow SiO_2CF^*_{(s)} + C_2F_4 + C_3F_5^{\#}$	0.1471	35	1	140	2
$SiO_2C_3F_6^*{}_{(s)} + C_3F_5^{\#} \rightarrow SiO_2CF_3^*{}_{(s)} + C_2F_3 + C_3F_5^{\#}$	0.1471	35	1	140	2
$SiO_2CF_{(s)} + C_3F_6^+ \rightarrow SiF + CO_2 + C_3F_6^{\#}$	0.1471	35	1	140	2

Reaction					
$SiO_2CF_{2(s)} + C_3F_6^{+} \rightarrow CO_2 + C_3F_6^{\#} + SiF_2$	0.1471	35	1	140	2
$SiO_2CF_{3(s)} + C_3F_6^{+} \rightarrow CO_2 + C_3F_6^{\#} + SiF_3$	0.1471	35	1	140	2
$SiO_2C_2F_{3(s)} + C_3F_6^{+} \rightarrow SiOCF_{3(s)} + CO + C_3F_6^{\#}$	0.1471	35	1	140	2
$SiO_2C_2F_{4(s)} + C_3F_6^{+} \rightarrow SiOCF_{3(s)} + COF + C_3F_6^{\#}$	0.1471	35	1	140	2
$SiO_2C_3F_{5(s)} + C_3F_6^{+} \rightarrow SiO_2CF_{(s)} + C_2F_4 + C_3F_6^{\#}$	0.1471	35	1	140	2
$SiO_2C_3F_{6(s)} + C_3F_6^{+} \rightarrow SiO_2CF_{3(s)} + C_2F_3 + C_3F_6^{\#}$	0.1471	35	1	140	2
$SiO_2CF^*_{(s)} + C_3F_6^{+} \rightarrow CO_2 + C_3F_6^{\#} + SiF$	0.1471	35	1	140	2
$SiO_2CF_2^*{}_{(s)} + C_3F_6^{+} \rightarrow CO_2 + C_3F_6^{\#} + SiF_2$	0.1471	35	1	140	2
$SiO_2CF_3^*{}_{(s)} + C_3F_6^{+} \rightarrow CO_2 + C_3F_6^{\#} + SiF_3$	0.1471	35	1	140	2
$SiO_2C_2F_3^*{}_{(s)} + C_3F_6^{+} \rightarrow SiOCF_3^*{}_{(s)} + CO + C_3F_6^{\#}$	0.1471	35	1	140	2
$SiO_2C_2F_4^*{}_{(s)} + C_3F_6^{+} \rightarrow SiOCF_3^*{}_{(s)} + COF + C_3F_6^{\#}$	0.1471	35	1	140	2
$SiO_2C_3F_5^*{}_{(s)} + C_3F_6^{+} \rightarrow SiO_2CF^*{}_{(s)} + C_2F_4 + C_3F_6^{\#}$	0.1471	35	1	140	2
$SiO_2C_3F_6^*{}_{(s)} + C_3F_6^{+} \rightarrow SiO_2CF_3^*{}_{(s)} + C_2F_3 + C_3F_6^{\#}$	0.1471	35	1	140	2
$SiO_2CF_{(s)} + C_3F_6^{\#} \rightarrow SiF + CO_2 + C_3F_6^{\#}$	0.1471	35	1	140	2
$SiO_2CF_{2(s)} + C_3F_6^{\#} \rightarrow CO_2 + C_3F_6^{\#} + SiF_2$	0.1471	35	1	140	2
$SiO_2CF_{3(s)} + C_3F_6^{\#} \rightarrow CO_2 + C_3F_6^{\#} + SiF_3$	0.1471	35	1	140	2
$SiO_2C_2F_{3(s)} + C_3F_6^{\#} \rightarrow SiOCF_{3(s)} + CO + C_3F_6^{\#}$	0.1471	35	1	140	2
$SiO_2C_2F_{4(s)} + C_3F_6^{\#} \rightarrow SiOCF_{3(s)} + COF + C_3F_6^{\#}$	0.1471	35	1	140	2
$SiO_2C_3F_{5(s)} + C_3F_6^{\#} \rightarrow SiO_2CF_{(s)} + C_2F_4 + C_3F_6^{\#}$	0.1471	35	1	140	2
$SiO_2C_3F_{6(s)} + C_3F_6^{\#} \rightarrow SiO_2CF_{3(s)} + C_2F_3 + C_3F_6^{\#}$	0.1471	35	1	140	2
$SiO_2CF^*_{(s)} + C_3F_6^{\#} \rightarrow CO_2 + C_3F_6^{\#} + SiF$	0.1471	35	1	140	2
$SiO_2CF_2^*{}_{(s)} + C_3F_6^{\#} \rightarrow CO_2 + C_3F_6^{\#} + SiF_2$	0.1471	35	1	140	2
$SiO_2CF_3^*{}_{(s)} + C_3F_6^{\#} \rightarrow CO_2 + C_3F_6^{\#} + SiF_3$	0.1471	35	1	140	2
$SiO_2C_2F_3^*{}_{(s)} + C_3F_6^{\#} \rightarrow SiOCF_3^*{}_{(s)} + CO + C_3F_6^{\#}$	0.1471	35	1	140	2
$SiO_2C_2F_4^*{}_{(s)} + C_3F_6^{\#} \rightarrow SiOCF_3^*{}_{(s)} + COF + C_3F_6^{\#}$	0.1471	35	1	140	2
$SiO_2C_3F_5^*{}_{(s)} + C_3F_6^{\#} \rightarrow SiO_2CF^*{}_{(s)} + C_2F_4 + C_3F_6^{\#}$	0.1471	35	1	140	2
$SiO_2C_3F_6^*{}_{(s)} + C_3F_6^{\#} \rightarrow SiO_2CF_3^*{}_{(s)} + C_2F_3 + C_3F_6^{\#}$	0.1471	35	1	140	2
$SiO_2CF_{(s)} + C_3F_7^{+} \rightarrow SiF + CO_2 + C_3F_7^{\#}$	0.1471	35	1	140	2
$SiO_2CF_{2(s)} + C_3F_7^{+} \rightarrow CO_2 + C_3F_7^{\#} + SiF_2$	0.1471	35	1	140	2
$SiO_2CF_{3(s)} + C_3F_7^{+} \rightarrow CO_2 + C_3F_7^{\#} + SiF_3$	0.1471	35	1	140	2
$SiO_2C_2F_{3(s)} + C_3F_7^{+} \rightarrow SiOCF_{3(s)} + CO + C_3F_7^{\#}$	0.1471	35	1	140	2
$SiO_2C_2F_{4(s)} + C_3F_7^{+} \rightarrow SiOCF_{3(s)} + COF + C_3F_7^{\#}$	0.1471	35	1	140	2
$SiO_2C_3F_{5(s)} + C_3F_7^{+} \rightarrow SiO_2CF_{(s)} + C_2F_4 + C_3F_7^{\#}$	0.1471	35	1	140	2
$SiO_2C_3F_{6(s)} + C_3F_7^{+} \rightarrow SiO_2CF_{3(s)} + C_2F_3 + C_3F_7^{\#}$	0.1471	35	1	140	2
$SiO_2CF^*_{(s)} + C_3F_7^{+} \rightarrow CO_2 + C_3F_7^{\#} + SiF$	0.1471	35	1	140	2
$SiO_2CF_2^*{}_{(s)} + C_3F_7^{+} \rightarrow CO_2 + C_3F_7^{\#} + SiF_2$	0.1471	35	1	140	2
$SiO_2CF_3^*{}_{(s)} + C_3F_7^{+} \rightarrow CO_2 + C_3F_7^{\#} + SiF_3$	0.1471	35	1	140	2
$SiO_2C_2F_3^*{}_{(s)} + C_3F_7^{+} \rightarrow SiOCF_3^*{}_{(s)} + CO + C_3F_7^{\#}$	0.1471	35	1	140	2
$SiO_2C_2F_4^*{}_{(s)} + C_3F_7^{+} \rightarrow SiOCF_3^*{}_{(s)} + COF + C_3F_7^{\#}$	0.1471	35	1	140	2
$SiO_2C_3F_5^*{}_{(s)} + C_3F_7^{+} \rightarrow SiO_2CF^*{}_{(s)} + C_2F_4 + C_3F_7^{\#}$	0.1471	35	1	140	2
$SiO_2C_3F_6^*{}_{(s)} + C_3F_7^{+} \rightarrow SiO_2CF_3^*{}_{(s)} + C_2F_3 + C_3F_7^{\#}$	0.1471	35	1	140	2

$SiO_2CF_{(s)} + C_3F_7^{\#} \rightarrow SiF + CO_2 + C_3F_7^{\#}$	0.1471	35	1	140	2
$SiO_2CF_{2(s)} + C_3F_7^{\#} \rightarrow CO_2 + C_3F_7^{\#} + SiF_2$	0.1471	35	1	140	2
$SiO_2CF_{3(s)} + C_3F_7^{\#} \rightarrow CO_2 + C_3F_7^{\#} + SiF_3$	0.1471	35	1	140	2
$SiO_2C_2F_{3(s)} + C_3F_7^{\#} \rightarrow SiOCF_{3(s)} + CO + C_3F_7^{\#}$	0.1471	35	1	140	2
$SiO_2C_2F_{4(s)} + C_3F_7^{\#} \rightarrow SiOCF_{3(s)} + COF + C_3F_7^{\#}$	0.1471	35	1	140	2
$SiO_2C_3F_{5(s)} + C_3F_7^{\#} \rightarrow SiO_2CF_{(s)} + C_2F_4 + C_3F_7^{\#}$	0.1471	35	1	140	2
$SiO_2C_3F_{6(s)} + C_3F_7^{\#} \rightarrow SiO_2CF_{3(s)} + C_2F_3 + C_3F_7^{\#}$	0.1471	35	1	140	2
$SiO_2CF^*_{(s)} + C_3F_7^{\#} \rightarrow CO_2 + C_3F_7^{\#} + SiF$	0.1471	35	1	140	2
$SiO_2CF_2^*{}_{(s)} + C_3F_7^{\#} \rightarrow CO_2 + C_3F_7^{\#} + SiF_2$	0.1471	35	1	140	2
$SiO_2CF_3^*{}_{(s)} + C_3F_7^{\#} \rightarrow CO_2 + C_3F_7^{\#} + SiF_3$	0.1471	35	1	140	2
$SiO_2C_2F_3^*{}_{(s)} + C_3F_7^{\#} \rightarrow SiOCF_3^*{}_{(s)} + CO + C_3F_7^{\#}$	0.1471	35	1	140	2
$SiO_2C_2F_4^*{}_{(s)} + C_3F_7^{\#} \rightarrow SiOCF_3^*{}_{(s)} + COF + C_3F_7^{\#}$	0.1471	35	1	140	2
$SiO_2C_3F_5^*{}_{(s)} + C_3F_7^{\#} \rightarrow SiO_2CF^*_{(s)} + C_2F_4 + C_3F_7^{\#}$	0.1471	35	1	140	2
$SiO_2C_3F_6^*{}_{(s)} + C_3F_7^{\#} \rightarrow SiO_2CF_3^*{}_{(s)} + C_2F_3 + C_3F_7^{\#}$	0.1471	35	1	140	2
$SiO_2CF_{(s)} + C_4F_7^{+} \rightarrow SiF + CO_2 + C_4F_7^{\#}$	0.1471	35	1	140	2
$SiO_2CF_{2(s)} + C_4F_7^{+} \rightarrow CO_2 + C_4F_7^{\#} + SiF_2$	0.1471	35	1	140	2
$SiO_2CF_{3(s)} + C_4F_7^{+} \rightarrow CO_2 + C_4F_7^{\#} + SiF_3$	0.1471	35	1	140	2
$SiO_2C_2F_{3(s)} + C_4F_7^{+} \rightarrow SiOCF_{3(s)} + CO + C_4F_7^{\#}$	0.1471	35	1	140	2
$SiO_2C_2F_{4(s)} + C_4F_7^{+} \rightarrow SiOCF_{3(s)} + COF + C_4F_7^{\#}$	0.1471	35	1	140	2
$SiO_2C_3F_{5(s)} + C_4F_7^{+} \rightarrow SiO_2CF_{(s)} + C_2F_4 + C_4F_7^{\#}$	0.1471	35	1	140	2
$SiO_2C_3F_{6(s)} + C_4F_7^{+} \rightarrow SiO_2CF_{3(s)} + C_2F_3 + C_4F_7^{\#}$	0.1471	35	1	140	2
$SiO_2CF^*_{(s)} + C_4F_7^{+} \rightarrow CO_2 + C_4F_7^{\#} + SiF$	0.1471	35	1	140	2
$SiO_2CF_2^*{}_{(s)} + C_4F_7^{+} \rightarrow CO_2 + C_4F_7^{\#} + SiF_2$	0.1471	35	1	140	2
$SiO_2CF_3^*{}_{(s)} + C_4F_7^{+} \rightarrow CO_2 + C_4F_7^{\#} + SiF_3$	0.1471	35	1	140	2
$SiO_2C_2F_3^*{}_{(s)} + C_4F_7^{+} \rightarrow SiOCF_3^*{}_{(s)} + CO + C_4F_7^{\#}$	0.1471	35	1	140	2
$SiO_2C_2F_4^*{}_{(s)} + C_4F_7^{+} \rightarrow SiOCF_3^*{}_{(s)} + COF + C_4F_7^{\#}$	0.1471	35	1	140	2
$SiO_2C_3F_5^*{}_{(s)} + C_4F_7^{+} \rightarrow SiO_2CF^*_{(s)} + C_2F_4 + C_4F_7^{\#}$	0.1471	35	1	140	2
$SiO_2C_3F_6^*{}_{(s)} + C_4F_7^{+} \rightarrow SiO_2CF_3^*{}_{(s)} + C_2F_3 + C_4F_7^{\#}$	0.1471	35	1	140	2
$SiO_2CF_{(s)} + C_4F_7^{\#} \rightarrow SiF + CO_2 + C_4F_7^{\#}$	0.1471	35	1	140	2
$SiO_2CF_{2(s)} + C_4F_7^{\#} \rightarrow CO_2 + C_4F_7^{\#} + SiF_2$	0.1471	35	1	140	2
$SiO_2CF_{3(s)} + C_4F_7^{\#} \rightarrow CO_2 + C_4F_7^{\#} + SiF_3$	0.1471	35	1	140	2
$SiO_2C_2F_{3(s)} + C_4F_7^{\#} \rightarrow SiOCF_{3(s)} + CO + C_4F_7^{\#}$	0.1471	35	1	140	2
$SiO_2C_2F_{4(s)} + C_4F_7^{\#} \rightarrow SiOCF_{3(s)} + COF + C_4F_7^{\#}$	0.1471	35	1	140	2
$SiO_2C_3F_{5(s)} + C_4F_7^{\#} \rightarrow SiO_2CF_{(s)} + C_2F_4 + C_4F_7^{\#}$	0.1471	35	1	140	2
$SiO_2C_3F_{6(s)} + C_4F_7^{\#} \rightarrow SiO_2CF_{3(s)} + C_2F_3 + C_4F_7^{\#}$	0.1471	35	1	140	2
$SiO_2CF^*_{(s)} + C_4F_7^{\#} \rightarrow CO_2 + C_4F_7^{\#} + SiF$	0.1471	35	1	140	2
$SiO_2CF_2^*{}_{(s)} + C_4F_7^{\#} \rightarrow CO_2 + C_4F_7^{\#} + SiF_2$	0.1471	35	1	140	2
$SiO_2CF_3^*{}_{(s)} + C_4F_7^{\#} \rightarrow CO_2 + C_4F_7^{\#} + SiF_3$	0.1471	35	1	140	2
$SiO_2C_2F_3^*{}_{(s)} + C_4F_7^{\#} \rightarrow SiOCF_3^*{}_{(s)} + CO + C_4F_7^{\#}$	0.1471	35	1	140	2
$SiO_2C_2F_4^*{}_{(s)} + C_4F_7^{\#} \rightarrow SiOCF_3^*{}_{(s)} + COF + C_4F_7^{\#}$	0.1471	35	1	140	2
$SiO_2C_3F_5^*{}_{(s)} + C_4F_7^{\#} \rightarrow SiO_2CF^*_{(s)} + C_2F_4 + C_4F_7^{\#}$	0.1471	35	1	140	2

Reaction				
$SiO_2C_3F_6{*}_{(s)} + C_4F_7^{\#} \rightarrow SiO_2CF_3{*}_{(s)} + C_2F_3 + C_4F_7^{\#}$	0.1471	35	1	140	2
$SiO_2CF_{(s)} + C_4F_8^{+} \rightarrow SiF + CO_2 + C_4F_8^{\#}$	0.1471	35	1	140	2
$SiO_2CF_{2(s)} + C_4F_8^{+} \rightarrow CO_2 + C_4F_8^{\#} + SiF_2$	0.1471	35	1	140	2
$SiO_2CF_{3(s)} + C_4F_8^{+} \rightarrow CO_2 + C_4F_8^{\#} + SiF_3$	0.1471	35	1	140	2
$SiO_2C_2F_{3(s)} + C_4F_8^{+} \rightarrow SiOCF_{3(s)} + CO + C_4F_8^{\#}$	0.1471	35	1	140	2
$SiO_2C_2F_{4(s)} + C_4F_8^{+} \rightarrow SiOCF_{3(s)} + COF + C_4F_8^{\#}$	0.1471	35	1	140	2
$SiO_2C_3F_{5(s)} + C_4F_8^{+} \rightarrow SiO_2CF_{(s)} + C_2F_4 + C_4F_8^{\#}$	0.1471	35	1	140	2
$SiO_2C_3F_{6(s)} + C_4F_8^{+} \rightarrow SiO_2CF_{3(s)} + C_2F_3 + C_4F_8^{\#}$	0.1471	35	1	140	2
$SiO_2CF{*}_{(s)} + C_4F_8^{+} \rightarrow CO_2 + C_4F_8^{\#} + SiF$	0.1471	35	1	140	2
$SiO_2CF_2{*}_{(s)} + C_4F_8^{+} \rightarrow CO_2 + C_4F_8^{\#} + SiF_2$	0.1471	35	1	140	2
$SiO_2CF_3{*}_{(s)} + C_4F_8^{+} \rightarrow CO_2 + C_4F_8^{\#} + SiF_3$	0.1471	35	1	140	2
$SiO_2C_2F_3{*}_{(s)} + C_4F_8^{+} \rightarrow SiOCF_3{*}_{(s)} + CO + C_4F_8^{\#}$	0.1471	35	1	140	2
$SiO_2C_2F_4{*}_{(s)} + C_4F_8^{+} \rightarrow SiOCF_3{*}_{(s)} + COF + C_4F_8^{\#}$	0.1471	35	1	140	2
$SiO_2C_3F_5{*}_{(s)} + C_4F_8^{+} \rightarrow SiO_2CF{*}_{(s)} + C_2F_4 + C_4F_8^{\#}$	0.1471	35	1	140	2
$SiO_2C_3F_6{*}_{(s)} + C_4F_8^{+} \rightarrow SiO_2CF_3{*}_{(s)} + C_2F_3 + C_4F_8^{\#}$	0.1471	35	1	140	2
$SiO_2CF_{(s)} + C_4F_8^{\#} \rightarrow SiF + CO_2 + C_4F_8^{\#}$	0.1471	35	1	140	2
$SiO_2CF_{2(s)} + C_4F_8^{\#} \rightarrow CO_2 + C_4F_8^{\#} + SiF_2$	0.1471	35	1	140	2
$SiO_2CF_{3(s)} + C_4F_8^{\#} \rightarrow CO_2 + C_4F_8^{\#} + SiF_3$	0.1471	35	1	140	2
$SiO_2C_2F_{3(s)} + C_4F_8^{\#} \rightarrow SiOCF_{3(s)} + CO + C_4F_8^{\#}$	0.1471	35	1	140	2
$SiO_2C_2F_{4(s)} + C_4F_8^{\#} \rightarrow SiOCF_{3(s)} + COF + C_4F_8^{\#}$	0.1471	35	1	140	2
$SiO_2C_3F_{5(s)} + C_4F_8^{\#} \rightarrow SiO_2CF_{(s)} + C_2F_4 + C_4F_8^{\#}$	0.1471	35	1	140	2
$SiO_2C_3F_{6(s)} + C_4F_8^{\#} \rightarrow SiO_2CF_{3(s)} + C_2F_3 + C_4F_8^{\#}$	0.1471	35	1	140	2
$SiO_2CF{*}_{(s)} + C_4F_8^{\#} \rightarrow CO_2 + C_4F_8^{\#} + SiF$	0.1471	35	1	140	2
$SiO_2CF_2{*}_{(s)} + C_4F_8^{\#} \rightarrow CO_2 + C_4F_8^{\#} + SiF_2$	0.1471	35	1	140	2
$SiO_2CF_3{*}_{(s)} + C_4F_8^{\#} \rightarrow CO_2 + C_4F_8^{\#} + SiF_3$	0.1471	35	1	140	2
$SiO_2C_2F_3{*}_{(s)} + C_4F_8^{\#} \rightarrow SiOCF_3{*}_{(s)} + CO + C_4F_8^{\#}$	0.1471	35	1	140	2
$SiO_2C_2F_4{*}_{(s)} + C_4F_8^{\#} \rightarrow SiOCF_3{*}_{(s)} + COF + C_4F_8^{\#}$	0.1471	35	1	140	2
$SiO_2C_3F_5{*}_{(s)} + C_4F_8^{\#} \rightarrow SiO_2CF{*}_{(s)} + C_2F_4 + C_4F_8^{\#}$	0.1471	35	1	140	2
$SiO_2C_3F_6{*}_{(s)} + C_4F_8^{\#} \rightarrow SiO_2CF_3{*}_{(s)} + C_2F_3 + C_4F_8^{\#}$	0.1471	35	1	140	2
$SiOCF_{3(s)} + Ar^{+} \rightarrow Ar^{\#} + CO + SiF_3$	0.1471	35	1	140	2
$SiOCF_{3(s)} + Ar^{\#} \rightarrow Ar^{\#} + CO + SiF_3$	0.1471	35	1	140	2
$SiOCF_{3(s)} + CF_3^{+} \rightarrow CF_3^{\#} + CO + SiF_3$	0.1471	35	1	140	2
$SiOCF_{3(s)} + CF_3^{\#} \rightarrow CF_3^{\#} + CO + SiF_3$	0.1471	35	1	140	2
$SiOCF_{3(s)} + CF_2^{+} \rightarrow CF_2^{\#} + CO + SiF_3$	0.1471	35	1	140	2
$SiOCF_{3(s)} + CF_2^{\#} \rightarrow CF_2^{\#} + CO + SiF_3$	0.1471	35	1	140	2
$SiOCF_{3(s)} + CF^{+} \rightarrow CF^{\#} + CO + SiF_3$	0.1471	35	1	140	2
$SiOCF_{3(s)} + CF^{\#} \rightarrow CF^{\#} + CO + SiF_3$	0.1471	35	1	140	2
$SiOCF_{3(s)} + F^{+} \rightarrow F^{\#} + CO + SiF_3$	0.1471	35	1	140	2
$SiOCF_{3(s)} + F^{\#} \rightarrow F^{\#} + CO + SiF_3$	0.1471	35	1	140	2
$SiOCF_{3(s)} + F_2^{+} \rightarrow F_2^{\#} + CO + SiF_3$	0.1471	35	1	140	2
$SiOCF_{3(s)} + F_2^{\#} \rightarrow F_2^{\#} + CO + SiF_3$	0.1471	35	1	140	2

$SiOCF_{3(s)} + C_2F_5^+ \rightarrow C_2F_5^\# + CO + SiF_3$	0.1471	35	1	140	2
$SiOCF_{3(s)} + C_2F_5^\# \rightarrow C_2F_5^\# + CO + SiF_3$	0.1471	35	1	140	2
$SiOCF_{3(s)} + C_2F_4^+ \rightarrow C_2F_4^\# + CO + SiF_3$	0.1471	35	1	140	2
$SiOCF_{3(s)} + C_2F_4^\# \rightarrow C_2F_4^\# + CO + SiF_3$	0.1471	35	1	140	2
$SiOCF_{3(s)} + C_2F_3^+ \rightarrow C_2F_3^\# + CO + SiF_3$	0.1471	35	1	140	2
$SiOCF_{3(s)} + C_2F_3^\# \rightarrow C_2F_3^\# + CO + SiF_3$	0.1471	35	1	140	2
$SiOCF_{3(s)} + C_3F_5^+ \rightarrow C_3F_5^\# + CO + SiF_3$	0.1471	35	1	140	2
$SiOCF_{3(s)} + C_3F_5^\# \rightarrow C_3F_5^\# + CO + SiF_3$	0.1471	35	1	140	2
$SiOCF_{3(s)} + C_3F_6^+ \rightarrow C_3F_6^\# + CO + SiF_3$	0.1471	35	1	140	2
$SiOCF_{3(s)} + C_3F_6^\# \rightarrow C_3F_6^\# + CO + SiF_3$	0.1471	35	1	140	2
$SiOCF_{3(s)} + C_3F_7^+ \rightarrow C_3F_7^\# + CO + SiF_3$	0.1471	35	1	140	2
$SiOCF_{3(s)} + C_3F_7^\# \rightarrow C_3F_7^\# + CO + SiF_3$	0.1471	35	1	140	2
$SiOCF_{3(s)} + C_4F_7^+ \rightarrow C_4F_7^\# + CO + SiF_3$	0.1471	35	1	140	2
$SiOCF_{3(s)} + C_4F_7^\# \rightarrow C_4F_7^\# + CO + SiF_3$	0.1471	35	1	140	2
$SiOCF_{3(s)} + C_4F_8^+ \rightarrow C_4F_8^\# + CO + SiF_3$	0.1471	35	1	140	2
$SiOCF_{3(s)} + C_4F_8^\# \rightarrow C_4F_8^\# + CO + SiF_3$	0.1471	35	1	140	2
$SiOCF_{3(s)} + O^+ \rightarrow O^\# + CO + SiF_3$	0.1471	35	1	140	2
$SiOCF_{3(s)} + O^\# \rightarrow O^\# + CO + SiF_3$	0.1471	35	1	140	2
$SiOCF_{3(s)} + O_2^+ \rightarrow O_2^\# + CO + SiF_3$	0.1471	35	1	140	2
$SiOCF_{3(s)} + O_2^\# \rightarrow O_2^\# + CO + SiF_3$	0.1471	35	1	140	2
$SiOCF_3{}^*{}_{(s)} + Ar^+ \rightarrow Ar^\# + CO + SiF_3$	0.1471	35	1	140	2
$SiOCF_3{}^*{}_{(s)} + Ar^\# \rightarrow Ar^\# + CO + SiF_3$	0.1471	35	1	140	2
$SiOCF_3{}^*{}_{(s)} + CF_3^+ \rightarrow CF_3^\# + CO + SiF_3$	0.1471	35	1	140	2
$SiOCF_3{}^*{}_{(s)} + CF_3^\# \rightarrow CF_3^\# + CO + SiF_3$	0.1471	35	1	140	2
$SiOCF_3{}^*{}_{(s)} + CF_2^+ \rightarrow CF_2^\# + CO + SiF_3$	0.1471	35	1	140	2
$SiOCF_3{}^*{}_{(s)} + CF_2^\# \rightarrow CF_2^\# + CO + SiF_3$	0.1471	35	1	140	2
$SiOCF_3{}^*{}_{(s)} + CF^+ \rightarrow CF^\# + CO + SiF_3$	0.1471	35	1	140	2
$SiOCF_3{}^*{}_{(s)} + CF^\# \rightarrow CF^\# + CO + SiF_3$	0.1471	35	1	140	2
$SiOCF_3{}^*{}_{(s)} + F^+ \rightarrow F^\# + CO + SiF_3$	0.1471	35	1	140	2
$SiOCF_3{}^*{}_{(s)} + F^\# \rightarrow F^\# + CO + SiF_3$	0.1471	35	1	140	2
$SiOCF_3{}^*{}_{(s)} + F_2^+ \rightarrow F_2^\# + CO + SiF_3$	0.1471	35	1	140	2
$SiOCF_3{}^*{}_{(s)} + F_2^\# \rightarrow F_2^\# + CO + SiF_3$	0.1471	35	1	140	2
$SiOCF_3{}^*{}_{(s)} + C_2F_5^+ \rightarrow C_2F_5^\# + CO + SiF_3$	0.1471	35	1	140	2
$SiOCF_3{}^*{}_{(s)} + C_2F_5^\# \rightarrow C_2F_5^\# + CO + SiF_3$	0.1471	35	1	140	2
$SiOCF_3{}^*{}_{(s)} + C_2F_4^+ \rightarrow C_2F_4^\# + CO + SiF_3$	0.1471	35	1	140	2
$SiOCF_3{}^*{}_{(s)} + C_2F_4^\# \rightarrow C_2F_4^\# + CO + SiF_3$	0.1471	35	1	140	2
$SiOCF_3{}^*{}_{(s)} + C_2F_3^+ \rightarrow C_2F_3^\# + CO + SiF_3$	0.1471	35	1	140	2
$SiOCF_3{}^*{}_{(s)} + C_2F_3^\# \rightarrow C_2F_3^\# + CO + SiF_3$	0.1471	35	1	140	2
$SiOCF_3{}^*{}_{(s)} + C_3F_5^+ \rightarrow C_3F_5^\# + CO + SiF_3$	0.1471	35	1	140	2
$SiOCF_3{}^*{}_{(s)} + C_3F_5^\# \rightarrow C_3F_5^\# + CO + SiF_3$	0.1471	35	1	140	2
$SiOCF_3{}^*{}_{(s)} + C_3F_6^+ \rightarrow C_3F_6^\# + CO + SiF_3$	0.1471	35	1	140	2

$SiOCF_3{}^*_{(s)} + C_3F_6^{\#}$	$\rightarrow$	$C_3F_6^{\#} + CO + SiF_3$	0.1471	35	1	140	2
$SiOCF_3{}^*_{(s)} + C_3F_7^{+}$	$\rightarrow$	$C_3F_7^{\#} + CO + SiF_3$	0.1471	35	1	140	2
$SiOCF_3{}^*_{(s)} + C_3F_7^{\#}$	$\rightarrow$	$C_3F_7^{\#} + CO + SiF_3$	0.1471	35	1	140	2
$SiOCF_3{}^*_{(s)} + C_4F_7^{+}$	$\rightarrow$	$C_4F_7^{\#} + CO + SiF_3$	0.1471	35	1	140	2
$SiOCF_3{}^*_{(s)} + C_4F_7^{\#}$	$\rightarrow$	$C_4F_7^{\#} + CO + SiF_3$	0.1471	35	1	140	2
$SiOCF_3{}^*_{(s)} + C_4F_8^{+}$	$\rightarrow$	$C_4F_8^{\#} + CO + SiF_3$	0.1471	35	1	140	2
$SiOCF_3{}^*_{(s)} + C_4F_8^{\#}$	$\rightarrow$	$C_4F_8^{\#} + CO + SiF_3$	0.1471	35	1	140	2
$SiOCF_3{}^*_{(s)} + O^{+}$	$\rightarrow$	$O^{\#} + CO + SiF_3$	0.1471	35	1	140	2
$SiOCF_3{}^*_{(s)} + O^{\#}$	$\rightarrow$	$O^{\#} + CO + SiF_3$	0.1471	35	1	140	2
$SiOCF_3{}^*_{(s)} + O_2^{+}$	$\rightarrow$	$O_2^{\#} + CO + SiF_3$	0.1471	35	1	140	2
$SiOCF_3{}^*_{(s)} + O_2^{\#}$	$\rightarrow$	$O_2^{\#} + CO + SiF_3$	0.1471	35	1	140	2
$SiO_2CF_{(s)} + F$	$\rightarrow$	$SiO_2CF_{2(s)}$	0.1				
$SiO_2CF{}^*_{(s)} + F$	$\rightarrow$	$SiO_2CF_2{}^*_{(s)}$	0.1				
$SiO_2CF_{2(s)} + F$	$\rightarrow$	$SiO_2CF_{3(s)}$	0.1				
$SiO_2CF_2{}^*_{(s)} + F$	$\rightarrow$	$SiO_2CF_3{}^*_{(s)}$	0.1				
$SiO_2C_2F_{3(s)} + F$	$\rightarrow$	$SiO_2C_2F_{4(s)}$	0.1				
$SiO_2C_2F_3{}^*_{(s)} + F$	$\rightarrow$	$SiO_2C_2F_4{}^*_{(s)}$	0.1				
$SiO_2C_3F_{5(s)} + F$	$\rightarrow$	$SiO_2C_3F_{6(s)}$	0.1				
$SiO_2C_3F_5{}^*_{(s)} + F$	$\rightarrow$	$SiO_2C_3F_6{}^*_{(s)}$	0.1				
$SiO_2CF_{(s)} + CF$	$\rightarrow$	$SiO_2C_2F_{3(s)}$	0.0002				
$SiO_2CF{}^*_{(s)} + CF$	$\rightarrow$	$SiO_2CF{}^*_{(s)} + CF_{(s)}$	0.002				
$SiO_2CF_{2(s)} + CF$	$\rightarrow$	$SiO_2C_2F_{3(s)}$	0.0002				
$SiO_2CF_2{}^*_{(s)} + CF$	$\rightarrow$	$SiO_2CF_2{}^*_{(s)} + CF_{(s)}$	0.002				
$SiO_2CF_{3(s)} + CF$	$\rightarrow$	$SiO_2C_2F_{4(s)}$	0.0002				
$SiO_2CF_3{}^*_{(s)} + CF$	$\rightarrow$	$SiO_2CF_3{}^*_{(s)} + CF_{(s)}$	0.002				
$SiO_2C_2F_{3(s)} + CF$	$\rightarrow$	$SiO_2C_3F_{5(s)}$	0.002				
$SiO_2C_2F_3{}^*_{(s)} + CF$	$\rightarrow$	$SiO_2C_2F_3{}^*_{(s)} + CF_{(s)}$	0.002				
$SiO_2C_2F_{4(s)} + CF$	$\rightarrow$	$SiO_2C_3F_{5(s)}$	0.0002				
$SiO_2C_2F_4{}^*_{(s)} + CF$	$\rightarrow$	$SiO_2C_2F_4{}^*_{(s)} + CF_{(s)}$	0.002				
$SiO_2C_3F_5{}^*_{(s)} + CF$	$\rightarrow$	$SiO_2C_3F_5{}^*_{(s)} + CF_{(s)}$	0.002				
$SiO_2C_3F_6{}^*_{(s)} + CF$	$\rightarrow$	$SiO_2C_3F_6{}^*_{(s)} + CF_{(s)}$	0.002				
$SiOCF_{3(s)} + CF$	$\rightarrow$	$SiOCF_{3(s)} + CF_{(s)}$	0.002				
$SiOCF_3{}^*_{(s)} + CF$	$\rightarrow$	$SiOCF_3{}^*_{(s)} + CF_{(s)}$	0.002				
$SiO_2CF_{(s)} + CF_2$	$\rightarrow$	$SiO_2C_2F_{3(s)}$	0.00015				
$SiO_2CF{}^*_{(s)} + CF_2$	$\rightarrow$	$SiO_2CF{}^*_{(s)} + CF_{2(s)}$	0.0015				
$SiO_2CF_{2(s)} + CF_2$	$\rightarrow$	$SiO_2C_2F_{4(s)}$	0.00015				
$SiO_2CF_2{}^*_{(s)} + CF_2$	$\rightarrow$	$SiO_2CF_2{}^*_{(s)} + CF_{2(s)}$	0.0015				
$SiO_2CF_{3(s)} + CF_2$	$\rightarrow$	$SiO_2C_2F_{4(s)}$	0.00015				
$SiO_2CF_3{}^*_{(s)} + CF_2$	$\rightarrow$	$SiO_2CF_3{}^*_{(s)} + CF_{2(s)}$	0.0015				
$SiO_2C_2F_{3(s)} + CF_2$	$\rightarrow$	$SiO_2C_3F_{5(s)}$	0.00015				
$SiO_2C_2F_3{}^*_{(s)} + CF_2$	$\rightarrow$	$SiO_2C_2F_3{}^*_{(s)} + CF_{2(s)}$	0.0015				

$SiO_2C_2F_{4(s)} + CF_2 \rightarrow SiO_2C_3F_{6(s)}$	0.00015				
$SiO_2C_2F_4{*}_{(s)} + CF_2 \rightarrow SiO_2C_2F_4{*}_{(s)} + CF_{2(s)}$	0.0015				
$SiO_2C_3F_5{*}_{(s)} + CF_2 \rightarrow SiO_2C_3F_5{*}_{(s)} + CF_{2(s)}$	0.0015				
$SiO_2C_3F_6{*}_{(s)} + CF_2 \rightarrow SiO_2C_3F_6{*}_{(s)} + CF_{2(s)}$	0.0015				
$SiOCF_{3(s)} + CF_2 \rightarrow SiOCF_{3(s)} + CF_{2(s)}$	0.0015				
$SiOCF_3{*}_{(s)} + CF_2 \rightarrow SiOCF_3{*}_{(s)} + CF_{2(s)}$	0.0015				
$SiO_2CF_{(s)} + CF_3 \rightarrow SiO_2C_2F_{4(s)}$	0.0001				
$SiO_2CF{*}_{(s)} + CF_3 \rightarrow SiO_2CF{*}_{(s)} + CF_{3(s)}$	0.001				
$SiO_2CF_{2(s)} + CF_3 \rightarrow SiO_2C_2F_{4(s)}$	0.0001				
$SiO_2CF_2{*}_{(s)} + CF_3 \rightarrow SiO_2CF_2{*}_{(s)} + CF_{3(s)}$	0.001				
$SiO_2CF_{3(s)} + CF_3 \rightarrow SiO_2C_2F_{4(s)}$	0.0001				
$SiO_2CF_3{*}_{(s)} + CF_3 \rightarrow SiO_2CF_3{*}_{(s)} + CF_{3(s)}$	0.001				
$SiO_2C_2F_{3(s)} + CF_3 \rightarrow SiO_2C_3F_{6(s)}$	0.0001				
$SiO_2C_2F_3{*}_{(s)} + CF_3 \rightarrow SiO_2C_2F_3{*}_{(s)} + CF_{3(s)}$	0.001				
$SiO_2C_2F_4{*}_{(s)} + CF_3 \rightarrow SiO_2C_2F_4{*}_{(s)} + CF_{3(s)}$	0.001				
$SiO_2C_3F_5{*}_{(s)} + CF_3 \rightarrow SiO_2C_3F_5{*}_{(s)} + CF_{3(s)}$	0.001				
$SiO_2C_3F_6{*}_{(s)} + CF_3 \rightarrow SiO_2C_3F_6{*}_{(s)} + CF_{3(s)}$	0.001				
$SiOCF_{3(s)} + CF_3 \rightarrow SiOCF_{3(s)} + CF_{3(s)}$	0.001				
$SiOCF_3{*}_{(s)} + CF_3 \rightarrow SiOCF_3{*}_{(s)} + CF_{3(s)}$	0.001				
$SiO_2CF_{(s)} + C_2F_3 \rightarrow SiO_2C_3F_{5(s)}$	0.0001				
$SiO_2CF{*}_{(s)} + C_2F_3 \rightarrow SiO_2CF{*}_{(s)} + C_2F_{3(s)}$	0.001				
$SiO_2CF_{2(s)} + C_2F_3 \rightarrow SiO_2C_3F_{5(s)}$	0.0001				
$SiO_2CF_2{*}_{(s)} + C_2F_3 \rightarrow SiO_2CF_2{*}_{(s)} + C_2F_{3(s)}$	0.001				
$SiO_2CF_{3(s)} + C_2F_3 \rightarrow SiO_2C_3F_{6(s)}$	0.0001				
$SiO_2CF_3{*}_{(s)} + C_2F_3 \rightarrow SiO_2CF_3{*}_{(s)} + C_2F_{3(s)}$	0.001				
$SiO_2C_2F_3{*}_{(s)} + C_2F_3 \rightarrow SiO_2C_2F_3{*}_{(s)} + C_2F_{3(s)}$	0.001				
$SiO_2C_2F_4{*}_{(s)} + C_2F_3 \rightarrow SiO_2C_2F_4{*}_{(s)} + C_2F_{3(s)}$	0.001				
$SiO_2C_3F_5{*}_{(s)} + C_2F_3 \rightarrow SiO_2C_3F_5{*}_{(s)} + C_2F_{3(s)}$	0.001				
$SiO_2C_3F_6{*}_{(s)} + C_2F_3 \rightarrow SiO_2C_3F_6{*}_{(s)} + C_2F_{3(s)}$	0.001				
$SiOCF_{3(s)} + C_2F_3 \rightarrow SiOCF_{3(s)} + C_2F_{3(s)}$	0.001				
$SiOCF_3{*}_{(s)} + C_2F_3 \rightarrow SiOCF_3{*}_{(s)} + C_2F_{3(s)}$	0.001				

B.1 References

[1] J. D. Kress, ; D E Hanson, ; A F Voter, ; C L Liu, X.-Y. Liu, ; D G Coronell,) D E Hanson, A. F. Voter, C. L. Liu and D. G. Coronell, Journal of Vacuum Science & Technology A **17,** 2819 (1999).

[2] J. P. Chang and H. H. Sawin, Journal of Vacuum Science & Technology A **15,** 610 (1997).